UNIVERSITY OF SOUTHAMPTON

Faculty of Engineering, Science and Mathematics

School of Engineering Sciences

Finite element modelling for the assessment of residual stresses and failure mechanisms in welded connections

A thesis submitted to the University of Southampton for the degree of Doctor of Philosophy.

By

Aihui Wu

Materials Research Group

June 2004

UNIVERSITY OF SOUTHAMPTON

ABSTRACT

FACULTY OF ENGINEERING, SCIENCE AND MATHEMATICS
SCHOOL OF ENGINEERING SCIENCES
MATERIALS RESEARCH GROUP

Doctor of Philosophy

FINITE ELEMENT MODELLING FOR THE ASSESSMENT OF RESIDUAL STRESSES AND FAILURE MECHANISMS IN WELDED CONNECTIONS

by Aihui Wu

Despite the considerable amount of research on welded joints, their behaviour is still not fully understood due to their complexity. This research aims to contribute in this area with emphasis on some inherent features of the welded joints, namely welding-induced residual stresses and distortion, weld defects, geometric imperfections and material property variations in the weld area and HAZ, in order to improve understanding on welded joints and thus ensure a safer design.

FEM models of a fillet welded cruciform joint have been generated with emphasis on the modelling of mechanical property variation in base metal, weld metal and HAZ detected by hardness tests. The accuracy of the models were assessed by solving a benchmark problem and comparing their predictions with published experimental data. The results from these models showed that the assumptions made by various design codes that the weld throat is the critical plane and stresses are uniformly distributed over this area may not always be true. The strain distribution within and adjacent to the HAZ was found to be very sensitive to the accurate representation of the gradual change of material properties in this area. Such variation should therefore be accounted for when assessing joint failure mechanisms occurring at low stress levels.

A finite element simulation of the welding process has been carried out for a butt weld and assessed by comparison with experimental residual stress results and empirical distortion results. The sensitivity of residual stress results on variations of certain input parameters including martial properties, amount of heat input and boundary conditions was investigated. This exercise demonstrated the capacity of the available software to deal with the particular requirements of a rather complex thermo-mechanical problem. It also provided the opportunity for some preliminary investigation into the importance of the various input parameters thus suggesting a simplified but reliable modelling method for the more complex T-joint. Simulations of welding processes of T-joints carried out in the literature either assumed simultaneous welding of the two passes or modelled only one pass due to the complexity of the modelling process. A sequential welding of a T-joint, which is what really happens in practice, has been successfully simulated and assessed by comparison to available experiments and results from the literature. This simulation provided new information on the residual stress magnitude and distribution over the weld area of a T-joint and detailed residual stress results for further load-carrying analysis of welded T-joints.

Experiments and FE analyses have been carried out on two welded T-joints with very different manufacturing and geometric characteristics to study their behaviour under load. FE models have been developed and assessed by comparison with results from the experiments. The effect of geometry and defects has been studied on the generated models. Residual stresses have been obtained from the welding process simulation and input into the load-carrying model as initial stresses to study quantitatively their effect on the yielding behaviour of T-joints under bending.

CONTENTS

LIST OF FIGURES

LIST OF TABLES

PREFACE

This thesis is an account of the work which was carried out wholly by the author at the Materials Research Group, School of Engineering Sciences, University of Southampton, under the supervision of Dr. B. G. Mellor and Dr S. Syngellakis in the period of October, 1999 - June, 2004.

No part of this thesis has been submitted for a degree at any other university. The research work described here is original, although the work of others has been drawn upon freely with due acknowledgements in the text.

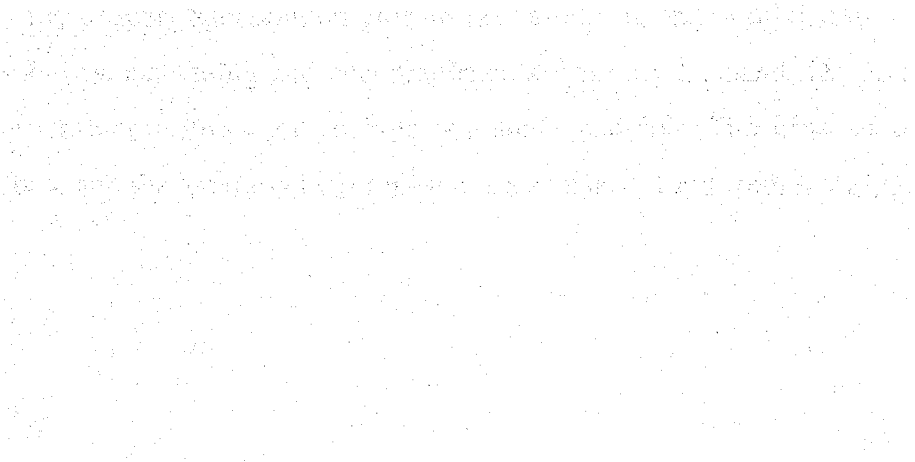

Acknowledgements

Firstly, I would like to express my sincere thanks and gratitude to my supervisors Dr. Stavros Syngellakis and Dr. Brian Mellor, whose valuable supervisions and patience have made this study possible. Not only have they taught me comprehensively, but they have also showed me what the right research attitude is and how to do research efficiently through their active supervisions.

The financial support of the University of Southampton and its School of Engineering Sciences is gratefully acknowledged.

I would also like to thank Mr. E. Bonner, Mr. D. Beckett, Mr. E. Roszkowiak, Mrs. S. Walker, Mrs. G. Skiller and Mrs. G. Rood whose kind helps make my study here much easier and happier. I wish to extend the same thanks to all of the staff at Southampton University's Materials Research Group. Many thanks go to Dr. Mark Joyce who helped me in doing the tensile test of specimen WT1-C while I was occupied in Cambridge.

Special thanks are due to Dr. Phillippa Reed and Dr. Anna Syngellakis for their great understanding and encouragements during my pregnancy and after the baby was born.

I wish to also thank all of my colleagues and personal friends for their support and friendship. Especially Jialin Yan, Jian Liu, Nong Gao, Yigeng Xu, Nihong Yang, K.H. Khor, H.T. Pang, P. Rometsch, A. Roques, D. Booth, and F. Lefebvre.

Finally, my deepest appreciation goes to my family for their continuous supports. The constant understanding and encouragements from my husband, Dr. Xianzhong Zhao, are extremely important to both my study and life. The birth of our son, Jianwu Zhao, and the great joy he brings me is a special reward from my PhD study.

Aihui Wu

June 2004

Notation

A Cross-sectional area of the groove of a butt joint

a Weld throat length

b The width of the tension zone of residual stress

c Specific heat

[C] Specific heat matrix

C1-C4 Coefficients

E Young's modulus

f_u The nominal ultimate tensile strength of the weaker part joined in a fillet weld

h Convection coefficient

h_p Depth of penetration

H Vickers hardness (kg/mm^2) / Enthalpy (J/m^3)

I Arc current, amperes

k Thermal conductivity

K Strength coefficient

[K] Stiffness matrix / Effective conductivity matrix;

K_0, K_1, K_2, K_a, K_w: Constants

L Weld length

M_Y Yielding moment

n Strain-hardening exponent

m Meyer index

Q Net heat input from the arc to the workpiece

Q^k Heat flow per unit time through conductivity

Q^h Heat loss per unit time through convection

q_G Rate of heat generated per volume

R_u Failure load of a transverse fillet weld

t Thickness of plate

T Temperature

T_e Effective throat dimension

V Arc voltage

v Welding speed

w Weld leg length

W The weight of deposited metal per unit weld length

w_0 The weight of deposited metal per unit weld length per welding of each pass

Y Dimensionless constant that depends on geometry and mode of loading

α Dilution factor / Thermal expansion coefficient

β Angular distortion

$\gamma_{Mw}, \gamma_m, \gamma_f, \gamma_{f3}, \beta$ partial safety factor

η_a Arc efficiency

ρ Density

$\sigma_{\perp}$ Normal stress perpendicular to the weld throat

σ_{per} Permissible stress

σ_m The maximum stress at weld region

σ_w, σ_p, σ_c, Tensile strength of weld metal, parent metal and deposited metal, respectively

σ_Y Yield strength

σ_u Ultimate strength of a material

σ_c Tensile strength of weld metal

τ Shear stress

τ_D Allowable stress

$\tau_{\perp}$ Shear stress transverse to the weld axis

$\tau_{//}$ Shear stress parallel to the weld axis

ε^T Thermal dilatation

Abbreviations

AISI	American Iron and Steel Institute
ANSYS	General-purpose FEM package
APDL	ANSYS Parametric Design Language
AWS	American Welding Society
BISRA	British Iron and Steel Research Association
BM	Base Metal
CTOD	Crack Tip Opening Displacement
FAC	Failure Assessment Curve
FE/FEA/FEM	Finite Element/Analysis/Method
GMAW	Gas metal arc welding
HAZ	Heat Affected Zone
IIW/IIS	International Institute of Welding
LBZ	Local Brittle Zone
MARCK/ABAQUS/SAPIV	Names of other commercial FE packages
SCF	Stress concentration factor
TMM	Thermal metallurgical and mechanical
WM	Weld Metal
2/3-D	Two/Three Dimensional

1. Introduction

1.1 Background

Welding offers a means of making continuous, load-bearing metallic joints between the components of a structure, which are physically and chemically indistinguishable from the bulk material, although this is not often achieved[1,2]. In 1921 the first all-welded, ocean-going ship was built[3]. Since then, welded joints have been widely used in structures in general engineering construction, and offshore and aeronautical industries. This raised the need for a better understanding of the behaviour of the weld material itself as well as the welded joints and welded structures. It also became necessary to develop methods for reliable design of welded joints and structures.

In addition to fusion welding, new welding techniques, such as friction stir welding and resistance welding have been developed. However, fusion welding techniques are still considered the most important in welding construction[4], of which arc welding is the most commonly used. This thesis is intended to focus on arc fusion welding only since, despite the considerable amount of research in this area, full understanding of this welding process and safe design of welded joints and structures arising from it are still far from complete.

Reliable structural design of welded structures requires the accurate assessment of the behaviour of the welded connections. To meet the requirement of properly designing various welded structures in practice, a number of design codes for welding and welded joints were developed in different countries and most of them are based on empirical studies. With the help of advanced computer technology, numerical methods such as the finite element method (FEM) have become increasingly popular in various engineering fields, and the design of welded joints and structures is no exception. By using FEM in particular, detailed stress and strain distributions can be obtained for welded joints under load and the complex welding process simulated. Although the static strength of welds in the welded structures is conventionally designed to be higher than that of other components of the structure, in the real world a large percentage of fracture failures are found to be in the weld.

This indicates that the behaviour of a welded joint is not yet fully understood due to its complexity although considerable research work has been done in this area in the last few decades[5]. Thus more studies need to be carried out on the behaviour of the welded joint itself with careful consideration of what factors may affect it and how.

Most conventional weld designs are based on knowledge of the stresses imposed on the weld joint. The design codes assume that the weld throat is the critical plane of failure, the throat stresses are therefore calculated for each type of load separately and then added vectorially to produce the combined stress, which is then compared with the allowable weld throat stress. The stresses are assumed to be uniformly distributed over the throat area[2,6,7]. However, calculations of these stresses are much more complicated than usually assumed due to (a) geometric imperfections arising from welding distortions, cutting and machining imperfections; (b) residual stresses and strains due to fit up errors and weld shrinkage; (c) geometric complexity within the connection. Investigations on such effects have shown that the assumptions of the design codes are often violated. For example, it has been found that the throat area is not the actual failure plane[8,9,10,11] and the stress distribution along the throat area is not uniform[12]. Thus it is necessary to study further the true load-carrying behaviour of welded joints with accurate geometry and material property representation in order to provide information to improve the current codes to ensure a safer design.

It is a well-known fact that during the welding process, an area in the parent metal adjacent to the deposited weld metal experiences rapid heating and cooling rates to form a heat-affected zone, and the metallurgical structure and mechanical material properties of the area from the centre of weld metal to the unaffected parent metal may vary considerably. Thus it is not adequate to consider the weld metal and parent metal as homogenous and isotropic. More studies need to be performed to look at the effect of this non-uniformity of material property distribution by considering more realistic assessments of material properties and then, based on these studies, to generate simple models of such property distributions with reasonable accuracy.

It has also been established that welding residual stresses can play an important role in the fracture behaviour of welded structures. Residual stresses may cause initial distortion the presence of which can make it difficult to maintain dimensional tolerances during weld fabrication and any misalignment in the welded joints may result in reaction stresses not considered at the design stage[13]. Conventionally, welding-induced residual stresses are regarded as secondary stresses and therefore not accounted for in the structural analysis. But this has been proved to be inadequate in practice[14]. One of the examples is the discovery of widespread brittle fracture in many pre-qualified welded joints during the 1994 Northridge earthquake. Welding-induced residual stresses are believed to constitute one of the factors contributing to this brittle fracture[14]. Their effect must therefore be taken into consideration in structural models of welded structures.

New welding techniques such as laser welding and friction stir welding have attracted a lot of research interest lately, however, as the residual stresses induced in arc welding are such a complex but important problem, research in that area is still very active. A number of experiments have been conducted by various researchers in which welding induced residual stresses and distortion are measured. Although they give an idea of how the residual stresses are distributed and affected by various factors, the results are limited to some particular sized and shaped welds and cannot be applied to welds other than those tested. Furthermore, most of these experiments are destructive and gave only residual stresses at discrete locations which may not be adequate in a fatigue or dynamic analysis as the residual stresses change rapidly over a small area.

Over the past two decades, the finite element method has been used in several attempts to predict distortion and residual stresses due to welding. However, the welding process itself is a very complex phenomenon which is not fully understood so that the distribution and magnitude of residual stresses is not readily available from the literature for all welding situations. It is, therefore, necessary to develop models for the welding process, which would produce not only qualitative but also quantitative information on residual stresses. Only then, based on this information,

the effect of residual stresses and distortion on the static strength of welded joints and welded structures can be accurately accessed. The distribution and magnitude of residual stresses is also vital in accessing the fatigue life of welded joints as it is well known that residual stresses, possibly up to yield stress level, may greatly affect fatigue crack initiation and growth rate in the region where tensile residual stresses exist.

1.2 Objectives and methodology

The aim of this research project is thus to generate models of the welded connections using FEM in order to study the behaviour of the welded connection itself with detailed consideration of the various factors affecting its performance under extreme loading. Emphasis has been given to the accurate representation of material properties of the weld metal, HAZ and base metal. Welding processes inducing residual stresses have been simulated and the effect of such stresses studied using FEM. The effect of another inherent problem in a weld, namely, a critically located defect, has also been studied. All these modelling and simulations can be achieved using commercial, general-purpose finite element (FE) packages, modern advanced computers and the knowledge gained from previous attempts in this area. FE models generated were assessed by comparing their predictions with experimental results carried out in parallel to the finite element analysis (FEA) or published in the literature as an FE model can only be trusted if it has been properly validated by other theory or experiments.

In view of the above general aims, the specific objectives of this research project were:

(a) to build an FEM model for a T-joint which is one of the most commonly encountered in engineering practice and has a more complex behaviour than a butt weld. Particular attention was paid to the accurate representation of material property variations from the base metal (BM), across the heat-affected zone (HAZ) to the weld metal (WM).

(b) to simulate the welding process for that joint so that the residual stresses and distortion can be predicted; this simulation differs from those published in the literature in the way that it simulated the sequential welding process of a T-joint which is what actually happens in practice while previous FE models simulate only one-side welding or assume simultaneous welding of the two passes due to the complexity of the modelling itself.

(c) to study the stress-strain development of the joint under external loading with and without the residual stresses as initial conditions; A number of previous investigations has been carried out simulating the behaviour of welded joints under load and the welding process separately, but little on combining simulation of these two processes to study the effect of residual stresses and distortion on the joint performance under service conditions.

(d) to build physical T-joint models and design arrangements for testing specimens cut from these joints. Room-temperature material property values for base and weld materials were obtained from tensile tests and a property gradient approach was applied, based on interpolating hardness data, to obtain such property estimates for the HAZ. Experimental measurements were eventually used to assess the reliability of the FEM models.

(e) to identify the most likely failure mechanism and thus the strength of joints with various geometric characteristics; and finally,

(f) to study analytically the effect of critically located defects on the potential failure mechanism of a T-joint.

1.3 Structure of the thesis

A literature review is presented in Chapter 2. This has been initially carried out in order to obtain a sound understanding of the behaviour of the welded joints and welded structures as well as to become aware of what other researchers in this area have achieved. Conventional design methods have been reviewed and the failure

mechanisms of welds discussed. In the literature review, emphasis has also been given to the most important factors that may affect the behaviour of both the welded joint and the overall structure, welding induced residual stresses and distortions.

The welding process needs to be modelled in order to obtain the distribution of residual stresses and distortion. As a first attempt, a thermal-stress FE analysis of a butt-welded plate was developed to predict the residual stresses and distortion. This geometry was chosen because of its relative simplicity compared with that of a fillet welded T joint. Results from the FE study were compared with those from experimental studies published in the literature to assess the reliability of the FE model. The analysis of the butt-weld presented in Chapter 3 provided the knowledge and expertise to tackle the more difficult T-joint modelling problem.

An FE model for analysing a fillet welded cruciform under static loading is presented in Chapter 4. This model was generated mainly because of the availability of the experimental results published in the literature for the purpose of assessing the FE model. The FE model was also assessed by comparing results with analytical calculations. In addition, the generation and assessment of a fillet-welded cruciform joint is similar to that for a fillet-welded T-joint. The effects of material property variation and size of the HAZ, as well as overall weld geometry have been studied.

A series of experiments have been performed on fillet welded T joints to study their behaviour under loading. The T joint was chosen because it is very common and has more complex load transfer behaviour than a butt weld. Two types of T-joints have been produced, one welded in the Engineering Design and Manufacture Centre of the University of Southampton, which has various visible defects, and one obtained from Cussons Technology Limited[15], which is a good quality weld. The experimental study can be split into three areas; monitoring the welding process itself for a T-joint, material property tests, and load-bearing behaviour tests. Chapter 5 presents all the details and output of the experimental work.

In Chapter 6, the same modelling methodologies as those described in Chapter 3 for a butt weld were applied to T-joints to simulate the welding process in order to obtain the welding induced residual stresses and distortion. In this study, FEM models of a sequentially welded two-sided T-joint were generated and the corresponding welding process simulated. A parallel experimental investigation was carried out as presented in Chapter 5. Particular attention was given to the accurate measurements of material properties at room temperature in the weld area that were introduced in the FEM model. Temperature history results obtained from the test were used to calibrate the thermal analysis in the FEM simulation. Residual stress distribution results obtained were compared with those published in the literature to assess the reliability of the FE model.

FE models of T-joint specimens under tension and bending with no residual stresses were developed and applied adopting the same methodologies as that for the cruciform joint and are presented in Chapter 7. The dimensions and material properties of those models were similar to the experimental models described in Chapter 5. Results from both the experimental study and the finite element modelling were compared and the FE model assessed. The effects of geometry and material properties of the local weld area were studied. From these results, the variation of failure mode observed in the experiments was explained. To study the effect of welding induced residual stresses, FE models with such initial conditions, obtained from the analysis described in Chapter 6, and then loaded under the experimental bending loads were also applied.

Finally Chapter 8 highlights the main results achieved from the research, the limitations of this study and the areas where further work is needed.

References

[1] Mellor B.G., Weld lecture handout, *University of Southampton*, 1999
[2] Hicks J.G., Welded Joint Design, **2**nd edition, *Abington Publishing*, 1997
[3] Masubuchi K., Analysis of Welded Structures, MIT, *Pergamon Press*, 1980
[4] Easterling K., Introduction to the Physical Metallurgy of Welding, *Butterworth-Heinemann*, 1993
[5] Mackerle J., Finite element analysis and simulation of welds: a bibliography (1976-1996), *Modelling Simulation of Materials Science and Engineering*, Vol. **4**, pp501-533, 1996
[6] DD ENV 1993-1-1:1992, Eurocode 3: Design of steel structures, Part 1-1: General rules and rules for buildings, European Committee for Standardization, 1992
[7] Higgins T.R., Preece F.R., Proposed working stress for fillet welds in building construction, *Welding Research Supplement*, **47**, pp429s-432s, 1968
[8] Commission XV "Fundamentals of design and fabrication for welding" of the IIW, Doc. IIS/IIW 504-76, *Welding in the World*, **14**(5/6), pp132-149, 1976
[9] Dawe J.L., Kulak G.L., Welded connections under combined shear and moment, *Journal of the Structural Division*, **100**, pp727-741, 1974
[10] Mellor B.G., Rainey R.C.T, & Kirk N.E., The static strength of end and T fillet weld connections, *Materials & Design*, **20**, pp193-205, 1999
[11] Kato B., Morita K., The strength of fillet welded joints, *Doc. XV-267-69, International Institute of Welding,* 1972
[12] Merriman H.B., Welding and the draughtsman, *British Welding Journal*, pp255-265, June, 1959
[13] Hong J.K., Dong P., Tsai C.L., Finite element simulation of residual stresses in multi-pass welds, *International Conference Proceedings on Modelling and Control of Joining Processes,* ed. T. Zacharia, AWS, pp470-476, 1993
[14] Zhang J., Dong P., Residual stresses in welded moment frames and implications for structural performance, *Journal of Structural Engineering*, **126**(3), pp306-315, 2000
[15] Burgess P. G., An investigation into crack propagation in fillet welds under collision loading conditions, B_{ENG} Dissertation, University of Southampton, 2000

2. Literature review

2.1 Introduction

Variation of material properties in the weld metal and heat affected zone in the base metal, the residual stress and distortion induced by the welding process, and the inevitable defects introduced in the weld are the most important factors that cause complications in the design process. To meet the requirement of designing various welded structures in practice, a number of design codes for welding and welded joints were developed in different countries and most of them are based on empirical studies. With the help of advanced computer technology, finite element analysis has become increasingly popular in simulating the welding process and in the design of welded joints and structures. Analyses based on the finite element method (FEM) have been applied to various aspects of the welding process and welded joint behaviour, including temperature distribution from which microstructure may be predicted[1,2], residual stresses and deformation induced by the welding process, static and fatigue strength.

In this chapter, a review of the relevant knowledge and important research results obtained from the literature on design methods and the behaviour of welded joints is presented. The review focuses on finite element applications to welding process simulation and welded joint failure analysis. Methods used in conventional weld design are first introduced. However, those calculation methods are based on various simplifying assumptions and do not fully account for the real behaviour of welded joints. The material and mechanical imperfections inherent in welds, such as the variable material properties of the heat-affected zone (HAZ), weld defects, welding induced residual stresses and deformations were considered in order to obtain a better and clearer picture of their effect on the behaviour of welded joints. Based on this review, problems needed to be studied in more depth and taken into consideration in a reliable and economic FEM analysis are identified.

2.2 Conventional design of welded connections

As a general rule of the American Iron and Steel Institute (AISI) Specification, all connections should be designed to transmit the maximum design force in the connected member with proper regard for eccentricity[3].

The weld metal is usually selected to be equal to or slightly stronger than the steel it joins. For a full penetration butt weld, the design strength of the weld can be taken as equal to the design resistance of the weaker of the parts joined, provided that the weld is made with electrodes of appropriate yield and tensile strengths. Hence the design is controlled by the elements joined, and no design procedures are required for the weld[4]. For a partial penetration butt weld, the minimum depth of penetration should be sufficient so that throughout the weld the stress does not exceed the relevant strength of the parent material[5].

The stress distribution in a fillet weld is complex and depends on the direction of loading as well as joint geometry. From the structural efficiency point of view, side fillet welds with the load applied parallel to the length of the weld are weaker than equal lengths of end welds with the load applied perpendicular to the length of the weld [3,6,7].

There are several methods of calculating the size or strength of fillet welds. A simple method for calculating a critical fillet weld stress was first presented by Dustin in 1927 by dividing the applied load by the effective throat area[8]. This method was consolidated and generalised during the 1930's by researchers in this area[8]. Jennings presented methods and equations in 1936, most of which are still in use today[6,8].

The simplest method assumes that the throat is in shear for all types of load, and the shear stress in the throat is the load divided by the throat area. The lack of stress uniformity in most engineering structures was taken into account by reducing the values of the recommended allowable stresses; the calculated shear stress should not be greater than the allowable shear stress[9]. In the American Welding Society

(AWS)[10] design code the allowable stress is taken as 30% of the nominal ultimate strength of the weld metal. BS 5400[11] specifies the allowable stress, τ_D, to be

$$\tau_D = \frac{k(\sigma_Y + 455)}{\gamma_m \gamma_{f3} 2\sqrt{3}} \text{ (MPa)} \qquad (2\text{-}1)$$

where σ_Y (in MPa) is the nominal yield strength of the weaker part joined; γ_m is the partial material factor defined as the product γ_{m1} γ_{m2} where γ_{m1} is the partial factor on the characteristic yield stress and γ_{m2} the partial factor for modelling uncertainties and other variables in the formulae for design resistance; γ_{f3} is partial safety factor for load that accounts for any inaccuracy in the assessment of the effect of loading, unforeseen stress distribution in the structure, variation in dimensional accuracy achieved in construction and the importance of the limit state being considered. For welded joint design, γ_m is taken as 1.1 and γ_{f3} as 1.1; k, which accounts for the fact that the strength of end fillet welds are stronger than side fillet welds of the same length, equals 0.9 for side fillets, 1.4 for end fillets in the end connectors and 1.0 for all the other types of welds.

According to a more refined method, the throat stresses are calculated for each type of load separately and then added vectorially to produce the combined stress, which is then compared with the allowable weld throat stress. The stresses are assumed to be uniformly distributed over the throat area[12,13,14].

Stresses are resolved across the weld throat, as shown in Fig. 2–1, into:

a) a normal stress $\sigma_\perp$, perpendicular to the throat
b) a shear stress $\tau_{//}$, acting in the throat parallel to the axis of the weld;
c) a shear stress $\tau_\perp$, acting in the throat transverse to the axis of the weld; and
d) a normal stress $\sigma_{//}$, along the axis of the weld, which has no effect on the strength of the weld and can thus be ignored.

Then the welded joints are checked using:

$$\sqrt{\sigma_{\perp}^{2} + K_w(\tau_{//}^{2} + \tau_{\perp}^{2})} \leq \sigma_{per} \tag{2-2}$$

The definition of K_w and σ_{per} is left to individual national codes. For example, BS 5400 uses $K_w = 3$ and

$$\sigma_{per} = \frac{k(\sigma_Y + 455)}{2\gamma_m \gamma_{f3}}, \tag{2-3}$$

where $\sigma_Y, k, \gamma_m, \gamma_{f3}$ are the same as in Eqn (2-1); BS 5950[5] lists values of the design strength of fillet welds according to the steel and electrode grades used in a table. For other types of electrode and/or other steel grades that are not listed in that table, the allowable strength is taken as half of the minimum tensile strength of the electrode but should be less than 55% of the specified minimum tensile strength of the parent metal. IIS/IIW[15] (International Institute of Welding) uses $K_w = 3$ and σ_{per} is taken as the permissible tensile strength in the base metal. For an ultimate strength analysis σ_{per} can be taken as the tensile strength of the weld metal. IIS/IIW also introduces another constant, which multiplies the left hand-side of Eqn (2-2). The value of this constant is taken as 0.7 for Fe 240 (Fe 360) steel and 0.85 for Fe E 350 (Fe 510) steel while for other steels, it is determined by means of linear interpolation proportional to the guaranteed yield strength of the steel. Eurocode 3[16] specifies that

$$\sigma_{per} = \frac{f_u}{\sqrt{3}\beta_w \gamma_{Mw}}, \tag{2-4}$$

where f_u is the nominal ultimate tensile strength of the weaker part joined, β_w an appropriate correlation factor varying from 0.8 – 0.9 based on the value of ultimate tensile strength of steel joined, and γ_{Mw} the partial factor for the resistance of welded connections and is taken as 1.25.

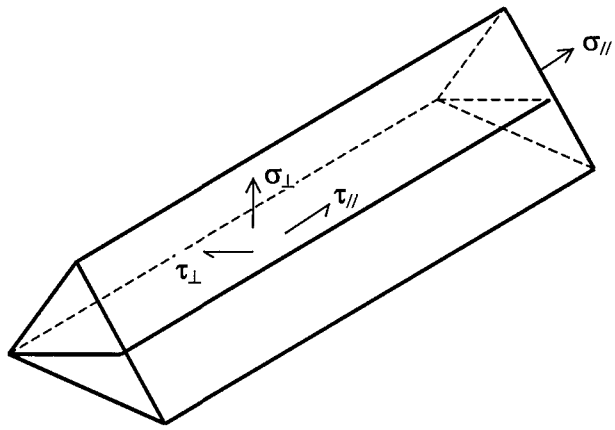

Fig. 2–1 Stresses resolved in the throat area

A less conservative directional method is provided by BS 5950 which makes some allowance for the dependence of the weld strength on the direction of loading[4].

The method discussed above assumes that the weld throat is the critical plane of failure. However, test results have shown that the actual plane of failure does not coincide with the throat plane[9,17,18,19] but is positioned at a certain angle α_1 relative to the base of the weld OB, as shown in Fig. 2–2. This angle depends on the form of the weld[7,20], and it increases with increasing angle α_2 at the tip of the fillet weld leg, and with increasing depth of penetration h_p. Thus the magnitude of the permissible load in the calculation of the strength of the end fillet weld should increase with increasing angle α_2 and depth of penetration[19]. In homogeneous components made of ductile materials failure usually starts at the position of greatest shear strains, which may not correspond to the weld throat[17]. Additionally, the stress distribution over the weld throat area is not uniform as this method assumed[6].

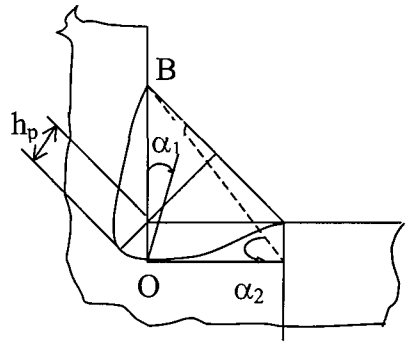

Fig. 2–2 Failure plane and penetration of a fillet weld

Design charts or tables are also available as a quick method of sizing a weld. For example, Tsai[8] obtained a set of design curves for fillet welded T-joints with various degrees of flange flexibility by finite element calculations and experiments. Dawe et al.[21] developed a theoretical method to predict the ultimate loads of eccentric welds based on an empirical load-deformation relationship. For the convenience of engineering application, they gave typical ultimate loads in a table for eccentric loaded beam-column welded connections of different weld lengths and eccentricity. But these tables or charts were derived from studies of specific types of welded joints and are not safe to apply generally to all welds.

A considerable amount of experimental and theoretical work has been carried out on the failure of transverse fillet welds. The failure load has been empirically related to the tensile strength of the weld metal according to the relation[22,23]:

$$R_u = K_w L w \sigma_c \tag{2-5}$$

or

$$R_u = K_a L a \sigma_c \tag{2-6}$$

where R_u is the failure load, K_w, K_a constants, L weld length, w the combined leg length, σ_c the tensile strength of the weld metal, and a the combined throat length.

The experimental values of K_w and K_a exhibit considerable variation. A detailed comparison of their values given by different researchers in the literature has been summarised by Mellor et al.[22]. The values listed indicate that the cruciform geometry

of weld is weaker than the cover plate geometry and that there appears to be a size effect. The scatter in experimental data suggests that minor differences in geometry, e.g. in fit up, which is the gap between the two plates joined, and microstructure of welds has a noticeable effect on the strength of the weld. From the literature reviewed, Mellor et al.[22] concluded that K_w and K_a should be considered dependent on the degree of throat penetration, h_p, and the weld leg length, w.

2.3 Failure mechanism of welds

In general, crack driving force and fracture resistance compete against each other at a crack tip of a welded joint and the result of this competition determines the failure criterion.

The crack driving force is a function of the geometrical nature of the joint and the crack while the fracture resistance is determined by the critical value of the maximum shear stress, the stress intensity factor and strain energy absorption in the cases of ductile failure, brittle fracture and impact failure, respectively. The fracture resistance is a material property. Residual stresses in the weldment are another contributor to the crack driving force in addition to the applied stresses. The fracture resistance is a material property that involves ultimate strength, toughness and ductility[24].

Although steel is a ductile material, brittle fracture can happen in a welded steel structure. Welding can introduce irregularities such as slag inclusions, lack of fusion and cracks. When the welded steel is stressed, these irregularities interrupt the stress field and, like all such features, have the effect of a notch, which locally increases the stress. Among various factors, the metallurgical structure discontinuity, weld defects and residual stresses are the most important ones to be blamed for causing brittle fracture. This thesis is not intended to address the brittle fracture of welded joints; for this reason only the ductile failure mode has been comprehensively reviewed.

2.3.1 Ductile failure

In a ductile failure, fracture usually starts at high stress concentration sites or physical discontinuity locations. Local yielding and rupture dominate the initial fracture mechanism. After necking of the joint the crack extends at a rather high speed in a ductile mode and causes complete fracture[24]. Failure of welded joints occurs when the weld cross-section yields to form a plastic hinge, and the load necessary to cause this being defined as the ultimate load[24].

Conventional design methods, as discussed in Section 2.2, are based on ductile failure of the welded joints, where the joint is assumed to be rather "perfect". Granstrom et al. [25] argued that strain hardening should be considered when calculating the design strength of a connection. In the tests conducted on welded cruciform joints, the ultimate strength of the welded joint in tension was found to be 1.7 times the yield strength of the steel and up to 2.6 times in bending. Obviously, the welded joints were failing in a ductile mode and plasticity developed in the joint material[25].

The factors affecting the ductile strength of welded joints are:

(i) Mechanical properties of parent metal, weld metal and HAZ

As indicated in the design formulae discussed in Section 2.2, the ultimate strength of welded connections increases with increase of the yield and ultimate strength of the weld metal and parent metal. In addition, the mechanical properties of the joint material will vary considerably from the central welded metal to the unaffected parent metal. The metallurgical structure is very complicated in the heat-affected zone. This non-uniformity in metallurgical structure will lead to nonuniformity in strength across the HAZ. The nonuniformity in strength and the inability to accommodate deformation between hard and soft substructures lead to a "metallurgical notch" in which stress or strain is concentrated in stronger or weaker parts of the weld zone, even in the absence of a geometrical notch[26], and this affects the strength of the welded joint. Strength mismatch including yield strength[27,28,29,30], elastic modulus and strain hardening exponent[29] mismatch between weld metal and

parent metal has also been found to have a noticeable effect on the strength of welded joints, of which yield strength mismatch has been the most studied.

(ii) Geometry of welded joints

In general, increasing the size of the weldment will increase the load carrying capacity of the welded joints. Other geometrical parameters such as fit up[22], size and shape of the HAZ[29], amount of penetration[23], mis-alignment, and shape of the weld cross section[9] affect the strength of welded joints as well.

(iii) Weld defects

Welds often contain various types of defects. In reality, it is very difficult, if not impossible, to eliminate all the defects from a weldment. The shape of a defect and its orientation relative to the direction of loading significantly affect the stress concentration around it. Appendix A, Table A-1 lists the types of weld defects while Fig. A-1 shows a sketch of a weld with multiple defects[31]. There are two reasons why weld defects reduce the strength of welded joints. First, the presence of the defects decreases the sectional areas. Second, stress becomes concentrated around the defects[32]. The extent to which weld defects affect structural strength depends upon many factors such as the nature and extent of defects; properties of the material; and type of loading.

A number of research programmes have been carried out to determine experimentally how defects affect the strength of weldments in various metals. Kahara et al.[33] summarised the experimental results obtained from a large number of specimens to show the general tendency of how weld defects affect the static tensile strength of a weld in steel. For example, Appendix A, Fig. A-2 shows how the size of a defect affects the static strength of a butt-welded joint in a low-carbon steel.

(iv)Residual stresses and distortion

Under static loading, the effect of residual stresses will decrease with increase of external loading, especially after the externally induced maximum von Mises stress

exceeds the yield point. Thus the residual stresses are not expected to have a significant influence on the static ductile strength of welded connections[32]. However, the yield load of welded joints may be affected by the presence of residual stresses[34]. Kamtekar[9] concluded from his analytical study that the presence of longitudinal residual stress actually increases the strength of end fillet welds by about 15 per cent while it has no effect on the strength of side fillet welds. In fracture analysis of welded joints, residual stresses do increase the crack driving force and result in a lower fracture load. More details on the effect of residual stress and distortion are given in section 2.4 of this chapter.

2.3.2 Finite element analysis on strength and failure of welded joints

Many experimental and numerical studies have been carried out on the static strength and fracture analysis of weldments[35]. Finite element analysis (FEA), in particular, has been widely used in studying the fracture behaviour of welded joints. However, few FE studies on the static strength of welds have been reported; many studies presented on the static strength of welds in the literature were experimental[13,17,36,37] and these date from the late 1920's to the late 1980's. Furthermore, the most common type of the joint tested was the lap joint and much less work has been done on the fillet welded T-joint. FE simulation of crack growth behaviour of welded joints under fatigue loadings has received much attention in recent years[38]. Destructive and non-destructive evaluations of weldments with cracks have been verified by finite element computation[39,40,41]. The effect of strength mis-match and defects[42] has also been studied using FE analysis. However, most of these studies are based on weldments with a particular and simple geometry, so that they cannot be used generally.

Rodrigues et al.[29] simulated a tensile test on a butt welded joint using a home-generated 3D finite element program to study the influence of the strength mis-match and size of HAZ of a weld in a high strength steel on the overall strength and ductility of the welded joint. They concluded that the tensile strength of a soft HAZ determines the overall strength of the joint and in the cases where the strength of the

HAZ was the same or smaller than that of the weld metal and base metal, the strength of the joint is strongly dependent on the HAZ dimensions.

Zhao et al.[43] conducted a series of tests on longitudinal fillet welds in high-strength cold formed rectangular hollow members that have a thickness less than 3 mm. Based on these experimental results and the FE analysis results performed on identical models, they proposed design rules for longitudinal fillet welds in thin-walled members, similar to Eqns (2-5) and (2-6), that is, based on the tensile strength of the base metal or weld metal and the size of the welds. The only change was the different values of the constants K_w and K_a used.

Raghavendran et al.[44] studied the effect of a single porosity defect of 3 mm diameter and the angle of weld toe overfill on the stress distributions of butt-welded joints with embedded porosity using two-dimensional FEM based on the general-purpose program SAPIV.

Nguyen et al.[45] generated a 2D FEM model based on ANSYS, a general-purpose package, to obtain the local stress distributions of butt-welded joints with an undercut and the results were used for the calculation of the effective stress intensity factor. However, no further details on the modelling process were given except for the mesh map.

Zhang and Dong[46] studied the effects of defects on the fracture behaviour of a beam-column weld connection by introducing a crack-like defect in the weld root. Without considering residual stresses, a large-size defect results in a greater crack driving force than a small defect. However, when the residual stress effects are included, a small defect size yields an even larger fracture driving force than the large defect without residual stress.

Tang and Shi[47] applied a 2-D elastic-plastic FEM program to study the effect of crack depth and strength matching properties of welds on the fracture resistance of weld specimens. Lin et al.[28] conducted a 2-D plane strain FE analysis to study the

effects of yield strength mis-match as well as thickness of the weld metal on the fracture resistance and load-deformation for both under- and overmatched welded joints. The effect of mis-match on the crack growth resistance was found to be much more significant than on the maximum load.

An elasto-plastic FEM analysis was used to evaluate the effect of local brittle zone (LBZ) size on the resistance to fracture and to simulate crack tip opening displacement (CTOD) tests for evaluating crack stability behaviour[48]. The FEM model was based on ABAQUS and involved the simulation of a three-point bend test of a heterogeneous specimen. The FEM CTOD calculations were validated by comparing them with those obtained by the BS 5762 procedure and extrapolation method and good agreement was observed.

It is also popular to use FEM to evaluate the J-integral of welded joints as a fracture criterion[49,50,51,52]. Huo et al.[51] carried out a plain strain 2-D elastic-plastic finite element analysis based upon the J-integral parameter to calculate the failure assessment curve (FAC) for welded joints. The influence of the strength mismatch of welded joints, the widths of welds and the crack sizes on the FAC was discussed.

2.4 Welding-induced residual stresses and distortion

2.4.1 Finite element analyses

As pointed out in the Introduction, experimental results on welding-induced residual stresses and distortion are limited to welds of a particular size and shape. Over the past two decades, the finite element method (FEM) has been applied in several attempts to predict such information for any weld geometry and material characteristics. Due to the influence of residual stresses on the fracture and fatigue strength of welded joints, this is still one of the most active topics in the welding research area today. The majority of these simulations focus on simple structural components in the area immediately adjacent to the weld. Due to the complexity of the welding process, different assumptions have been made in those simulations depending on the types of problems studied.

2-D versus 3-D analyses

It has been recognised that the thermal and mechanical response of a weldment is a three-dimensional (3-D) problem the solution of which is computationally expensive and very time-consuming. It has long been noticed that a quasi-steady state exists in certain long welds made under uniform welding speed[53,54]. Tsai et al.[55] found that, except within the regions near the ends of the plate, the majority of cross-sections are at a quasi-steady state so that a two-dimensional (2-D) model of any of the cross-sections should satisfactorily predict the thermal and mechanical behaviour of a three-dimensional joint. For example, two-dimensional models on the plane perpendicular to the welding direction produce good residual stress approximations for continuous welds made at relatively high welding speeds[56]. A ramp heat input function has been proposed to take into consideration the welding travel speed effect in 2-D simulations[55,57,58,59,60]. The ramp function considers the out-of-plane heat transfer effects on a specified 2-D cross section as the arc approaches, travels across and departs from it. Three-dimensional models of welding process have also been generated[46,53,55,61,62].

Temperature dependency of material properties

Since materials experience temperature cycles during welding from ambient to as high as above their melting point and this temperature gradient is one of the important causes of residual stresses, the temperature-dependence of some thermal and mechanical material properties has been considered by most researchers. However, most recent analyses are based on temperature-dependent data taken from earlier publications without paying particular attention to the realistic assessment of these values. The accuracy of temperature-dependent material properties input may play an important role in the accuracy of predicted residual stresses[63]. The actual material properties of WM and BM could be affected not only by the chemical composition of the metal but also by the cooling rate and the maximum temperature reached. In other words, the material properties are both temperature and

temperature-history dependent. In particular, the temperature history dependency of the thermal expansion coefficient and yield strength has been considered[54,59,64,2,65]. Small variations in the thermal dilatation diagram were found to have little influence on the residual stresses[54,65]. The assessment of properties of the HAZ is even more complex. Due to lack of information on the temperature-dependent mechanical material properties of the WM and HAZ, some researchers applied the same properties to the WM and HAZ as those of the BM, although some have attempted to assign different properties to the WM[54,65,66]. However, for temperature-dependent thermal properties, to the best of the author's knowledge, all the researchers cited in this area applied the same properties to both base metal and weld metal. Moreover, due to the difficulty of measuring these thermal properties at high temperatures, none of the researchers cited obtained data from their own experiments for the particular types of steels they used. However, despite the uncertainties in thermal material properties, it has been claimed by some researchers that the final residual stress results are insensitive to the thermal properties at high temperatures[55,58,67].

Phase transformation and transformation plasticity

In arc welding, WM is deposited onto the workpiece in a molten state and then solidifies and cools down to ambient temperature. During the liquid-solid phase change, a large amount of heat, named latent heat, is released without any temperature change. Depending on the cooling rate and the maximum temperature reached, a change in crystal structure occurs for the WM and HAZ, which is accompanied by a change in volume. In addition, these phase transformations occur under the compressive load applied by the surrounding material. This compressive load influences the solid state phase transformations in the way of additional plastic strains being formed. This phenomenon is referred to as transformation plasticity[59]. All these latent heat[2,56,66,68,69], volume change due to phase change[54,65] and transformation plasticity[1,2,68] effects have been modelled by various researchers. Transformation plasticity was found to have the effect of reducing the residual stresses.

Heat source model

For the solution of the transient heat transfer problem, various heat input models have been proposed. Surface heat flux[54,65,68], body heat generate rate[46,55], and the combined surface load and body load[57,58,60] were used. For surface heat flux, Gaussian[57,58,60,68,69], double elliptical[1,56, 70], and uniform distributions of heat input[54,64,65] were proposed. Free convection has been the common boundary condition but attempts have been made to take also into account radiation[56,66,68,69]. Other issues addressed in the literature include the effects of preheating on cooling rate, clamping mechanism as a heat sink and multi-pass welding on weldment temperatures[71]. Borjesson et al.[2] generated a fully coupled thermal, metallurgical and mechanical (TMM) FE model to calculate microstructure evolution, temperature development and residual stresses induced from welding in a multi-pass butt-welded plate. Ferrite, pearlite, bainite, and martensite phases were considered in their calculations. Mainly martensite and some bainite were found to be formed in the heat affected zone. Brown and Song[72] proposed a combination of rezoning and dynamic sub-structuring techniques that was believed to make the finite element welding simulation of large structures more tractable and dramatically reduce the computational time for the simulation of welding.

Simulation of welding process of T-joint

FEM simulations of the welding process of fillet welded T-joints have been presented in the literature. However, those models either assume simultaneous welding on the two sides[73,74], or showed only the results of a one-side welded joint[75,76]. No results have been found in the literature on simulating welding the two sides sequentially although this is what actually happens most commonly in real life. The complexity of the modelling process may have contributed to this apparent lack of analytical results.

Element rebirth and pass-lump techniques in multi-pass welding simulation

Multi-pass welding is very common in practice. In simulating multi-pass welding processes, element rebirth and pass-lump techniques have been used by some

researchers[57,55,58,66,60,77]. The former technique has been recognised as one of the few effective methods whereby the filler metal effect can be readily incorporated in existing commercial FE packages and has been adopted by most of the FE simulations of the multi-pass welding process. The latter technique is adopted to save CPU time. The results of the pass by pass stress development from the study by Hong et al.[57,58] show that there is no great variation of residual stresses in welded plates between successive passes and the first pass causes most of the residual stresses; this is consistent with the result obtained from the experimental investigation by Rao et al.[78].

FEM validation

FEM simulations of welding can be validated by comparing their predictions with experimental results. A number of experiments have been conducted by various researchers in this field. Test methods such as X-ray diffraction[68,77], sectioning[78,79], blind hole drilling[54,55,56,57,60,62,65,66], and neutron diffraction[59,80] have been applied. Table 2-1 lists some of the advantages and disadvantages of these residual stress measuring methods. Although the results are limited to some particular-sized welds and cannot be applied to welds other than those tested, they give some idea of how the residual stresses are distributed and affected by various factors.

The accuracy of residual stress measurements can be affected by many factors. In general, sectioning and hole drilling methods are viewed reliable and are the most widely used methods. The theory behind the sectioning and blind hole drilling methods is simple; according to these methods, a residual stress is determined by measuring the elastic-strain release that takes place when a specimen is cut into pieces (sectioning) or has a piece removed (hole drilling). However, in addition to human errors, extra strains introduced from the sectioning and drilling process is another source of errors. The strain release measured is for the surface which is, however, affected by strain release in the through-thickness direction. Moreover, strain is normally measured by strain gauges which cover a small area rather than a point. In positions with a steep residual stress gradient, this inevitably affects the accuracy of residual stress measurements. Tsai et al.[55] calibrated the blind hole

drilling technique by measuring the residual stresses in an annealed plate and claimed that the maximum measurement error in their measurement of residual stresses in a butt welded plate was within 34.5 MPa, that is, about 15% of the yield strength of the steel plate used in the experiment. Most of the other researchers did not give a clear indication of the accuracy of their measurements. The principle of X-ray and neutron diffraction techniques is the same. Elastic strain can be determined by measuring the lattice parameter (spacing between the atomic planes) in metals that have crystalline structures[32]. The X-ray method is not very accurate, especially in situations where high temperature has distorted the atomic structure of the material. X-ray measurement is also affected by the surface condition of the object to be measured[80]. Measurement scatter of 50% is not un-common in experiments of measuring residual stresses using this method[81].

Table 2-1 Comparison of residual stress measurement techniques

Method	Advantages	Disadvantages
Stress-relaxation techniques (Sectioning, Hole drilling etc.)	Simple principle; Reliable results; Relatively cheap; Relatively easy to apply;	Destructive; Only measure surface stress; Discrete measurement;
X-ray diffraction	Non-destructive;	Measure only surface stress; Time consuming; Discrete measurement; Relatively less accurate
Neutron diffraction	Non-destructive; Measure in-depth stress; Good for mapping stress;	Expensive; Time consuming; Limited equipment available

Appendix B lists the finite element simulations for residual stresses found in the literature reviewed. It can be seen from this table that different combinations of factors, which may affect the residual stress results, were considered by various researchers for various types of geometry and welding process. In none of these works have all the factors been taken into account systematically. Since all authors claimed that their FEM results showed good agreement with experimental or other numerical analysis results, some of the factors may have an insignificant effect on

the final residual stress results. It is important to generate a cost-efficient FEM model that simplifies the modelling procedure while preserving the necessary accuracy.

Appendix B also shows that most of the researchers either used the commercial package ABAQUS[46,55,56,57,60,61, 82] for their study or generated their own FEM program[1,59,65,83].

2.4.2 Effect on weld behaviour

It is now well known that welding residual stresses can play an important role in the fracture behaviour of welded structures. Residual stresses may cause initial distortion in welded structures. Residual stresses and distortion cause cracking and misalignment. The magnitudes of residual stresses possibly up to yield stress level, may greatly affect fatigue crack initiation and crack growth rate in the region where tensile residual stresses exist. Through thickness residual stresses may cause lamellar tearing in thick-section weldments. To take into account the effect of the residual stresses in assessing crack-like flaws at weld toes using fracture mechanics techniques, accurate predictions of the residual stress distribution across the plate thickness are required. With the presence of distortion, dimensional tolerances can be difficult to maintain during welding fabrication and misalignment in the welded joints may result in reaction stresses not considered at the design stage[84].

Zhang and Dong[46] conducted a series of finite element studies to determine the residual stress distribution in moment frame weld connections. The effects of residual stresses on the structural and fracture behaviour of welded joints were studied in detail. Zhang and Dong[46] concluded from their study that weld residual stresses could play a dominant role in the fracture process in the moment frame joints. Welding-induced residual stresses significantly increase the fracture driving force due to the presence of high tensile residual stresses. The high tri-axial residual stress states identified in these moment frame connections can greatly reduce the plastic deformation capability, consequently promoting brittle fracture.

Dong and Zhang[85] studied the combined effects of weld strength mismatch and welding residual stresses on the fracture of welded structures based on a series of comprehensive studies. They concluded that under-matched welds, due to the lower absolute values of residual stresses produced, can lead to a significantly lower fracture driving force if the residual stresses are a dominant loading mode. If large scale plastic deformation occurs prior to final failure under dominant external loading conditions, the residual stresses in under-matched welds can be sufficient to trigger an unfavourable cross-section yielding mode. Therefore, the combined effects of the strength mismatch and residual stresses on the fracture behaviour could be of critical importance in a fracture mechanics analysis of welded structures.

2.5 Summary

From the review presented in this chapter, it is clear that the behaviour of a welded joint is very complicated and not fully understood although considerable research has been performed on this subject. Various design methods and design codes are now available to calculate the strength of welded joints, however, these empirical calculations are based on assumptions such as that the stress is uniformly distributed in the "failure plane" which has been proved not to be the case in real practice. Therefore, even under static load and for the joint failing in a ductile mode, the design methods need to be improved. More uncertainties arise when the weld fails due to its inherent imperfections such as weld defects, residual stresses and distortion, and variable material properties in the HAZ. Although a large amount of research has been conducted, its application is limited to the particular cases studied. Furthermore, most of the experimental studies were on simple butt welds or fillet welds in lap joints. The fillet welded T-joint has received relatively much less attention.

FEM, as the most widely used numerical technique in engineering, has been successfully applied by many researchers to simulate the behaviour of welded joints. Many aspects, such as the welding process, fracture behaviour, fatigue crack growth, have been investigated through FE analysis. However, little has been done on the prediction of static strength of welded joints using FEM. Although it is a rather "classical" problem compared to, say, fatigue behaviour, the static strength of welded

joints should not be ignored as it is by no means accurately represented in the current design formulae. By using FEA, the detailed stress and strain distribution within the weld area and in the vicinity of the weld can be obtained which is believed to be beneficial to the determination of the strength of the welded joint and how various factors may affect it.

The above findings are consistent with the aims of the present research as described in Chapter 1. Material properties, especially strength mis-match, and the non-uniformity of material properties within the HAZ resulting from the complex metallurgical structures induced in the area from the welding process, have been found to affect the strength of welded joints. Emphasis should be given to the accurate representation of material properties of the weld metal, HAZ and base metal.

Conventionally, welding-induced residual stresses are regarded as secondary stresses and therefore not accounted for in structural analysis. But this has been proved not to be adequate in practice[46]. Their effect must therefore be taken into consideration in structural models of welded structures. However, the welding process itself is a very complex phenomenon, which has not been fully understood so that the distribution and magnitude of residual stresses is not readily available from the literature. Although there are various methods to measure residual stresses experimentally, they are either expensive, destructive or have limited application. Most experimental measurements of residual stresses are at discrete locations. It is, therefore, useful to develop models for simulating the welding process, which would produce not only qualitative but also quantitative information on more detailed mapping of residual stresses. The effect of weld defects also needs to be considered. Experimental work needs to be carried out for purposes of both studying the behaviour and assessing the FE models.

References

[1] Gu M., Goldak J., Knight A., Bibby M., Modelling the evolution of microstructure in the heat-affected zone of steady state welds, *Canadian Metallurgical Quarterly*, **32**(4), pp351-361, 1993

[2] Borjesson L., Lindgren L.E., Simulation of multipass welding with simultaneous computation of material properties, *Transaction of ASME Journal of Engineering Materials and Technology*, **123**(1), pp106-111, 2001

[3] Yu W.W., Cold-Formed Steel Design, 3rd edition, *John Wiley & Sons, Inc.*, 2000

[4] Trahair N. S., Bradford M. A., Nethercot D. A., The Behaviour and Design of Steel Structures to BS 5950, 3rd edition, *Spon Pres,* 2001

[5] BSI, BS 5950-1:2000, Structural use of steelwork in building – Part 1: code of practice for design – rolled and welded sections, 2000

[6] Solakian A.G, Claussen G.E., Stress distribution in fillet welds – A review of the literature to January 1, 1937, The Engineering Foundation Welding Research Committee, *Supplement to the Journal of the American Welding Society*, pp1-24, 1937

[7] Miazga G.S., Kennedy D.J.L., Behaviour of fillet welds as a function of the angle of loading, *Canadian Journal of Civil Engineering*, Vol.**16**, pp583-599, 1989

[8] Tsai, M-J, Tsai, C-L, New design curves for fillet welded T-joint, *Journal of the Chinese Institute of Engineers*, **12**(1), pp109-118, 1989

[9] Kamtekar A.G., A new analysis of the strength of some simple fillet welded connections, *Journal of Constructional Steel Research*, **2**(2), pp33-45, 1982

[10] American Welding Society, AWS D1.1-96, Structural Welding Code: Steel, 15th Edition, AWS, 1996

[11] BSI, BS 5400: 1982, Steel, concrete and composite bridges, Part 3: Code of practice for design of steel bridges, 1982

[12] Hicks J.G., Welded Joint Design, **2**nd edition, *Abington Publishing*, 1997

[13] Archer F.E., Fischer H.K., Kitchen E.M., Fillet welds subjected to bending and shear, *Civil Engineering and Public Works Review*, **54**(634), pp455-458, 1959

[14] Merriman H.B., Welding and the draughtsman, *British Welding Journal*, pp255-265, June, 1959

[15] Commission XV "Fundamentals of design and fabrication for welding" of the IIW, Doc. IIS/IIW 504-76, *Welding in the World*, **14**(5/6), pp132-149, 1976

[16] ENV 1993-1-1:1992, Eurocode 3: Design of steel structures, Part 1-1: General rules and rules for buildings, *European Committee for Standardization*, 1992

[17] Higgins T.R. & Preece F.R., Proposed working stress for fillet welds in building construction, *Welding Research Supplement*, **47**, pp429s-432s, 1968

[18] Fessler H. & Pappalettere C., Plastic-elastic strains in two-dimensional sections of partial-penetration fillet welds, *Journal of Strain Analysis*, **24**(1), pp15-21, 1989

[19] Barshi, O.A., Zaitsev, N.L., Increasing the load-carrying capacity of lap and T joints with fillet welds, *Welding Production*, **24**, pp1-4, 1977

[20] Biggs M.S., Crofts M.R., Higgs J.D., Martin L.H., Tozogius A., Failure of fillet weld connections subject to static load, Conference on Joints in Structural Steelwork, Teeside Polytechnic, *Pentech Press,* pp1.92-1.109, 1981

[21] Dawe J.L., Kulak G.L., Welded connections under combined shear and moment, *Journal of the Structural Division*, **100**(ST4), pp727-741, 1974

[22] Mellor B.G., Rainey R.C.T, & Kirk N.E., The static strength of end and T fillet weld connections, *Materials & Design*, **20**, pp193-205, 1999

[23] Kato B., Morita K., The strength of fillet welded joints, *Doc. XV-267-69, International Institute of Welding*, 1972

[24] Tsai C.L., Using computers for the design of welded joints, *Welding Journal*, **70**(1), pp47-56, 1991

[25] Granstrom A., Konstruktioner AG, Strength of connections in bending compared to ultimate behaviour rather than elasto-plastic theory, *Connections in Steel Structures: Behaviour, Strength & Design,* Edited by Bjorhovde R., Brozzetti J., and Colson A., E*lsevier Applied Science*, 1988

[26] Gray T.G.F., Spence J., North T.H., Rational Welding Design, *Newnes-Butterworths*, London, 1975

[27] Hao S., Schwalbe K.-H., Cornec A., The effect of yield strength mis-match on the fracture analysis of welded joints slip-line field solutions for pure bending, *International Journal of Solids and Structures*, Vol.**37**, pp5385-5411, 2000

[28] Lin G., Meng X.G., Cornec A., Schwalbe K.H., The effect of strength mis-match on mechanical performance of weld joints, *International Journal of Fracture*, **96**, pp37-54, 1999

[29] Rodrigues D.M., Menezes L.F., Loureiro A., Fernandes J.V., Numerical study of the plastic behaviour in tension of welds in high strength steels, *International Journal of Plasticity* Vol.**20**, pp1-18, 2004

[30] Rak I., Treiber A., Fracture behaviour of welded joints fabricated in HSLA steels of different strength level, *Engineering Fracture Mechanics*, Vol.**64**, pp401-415, 1999

[31] Lochhead J.C., Rodgers K.J., Weld defects: considering the big picture, *Welding Journal*, pp49-54, October 1999.

[32] Masubuchi K., Analysis of Welded Structures, MIT, *Pergamon Press*, 1980

[33] Kahara H., Tada Y., Watanabe M., Ishii Y., Nondestructive Testing of Welds and their Strength, 60th Anniversary Series, 7, *The Society of Naval Architects of Japan*, Tokyo, 1960

[34] Fessler H., Pappalettere G., Fillet welds under bending and shear, *5th International Conference on Pressure Vessel Technology*, pp47-61, Sept. 1984

[35] Tsai C.L., Using computers for the design of welded joints, *Welding Journal*, **70**(1), pp47-56, 1991

[36] Ligtenberg F.L., International test series. Final Report, IIW Document XV-242-68, *International Institute of Welding,* 1968

[37] Butler L.J., Kulak G.L., Strength of fillet welds as a function of direction of load. *Welding Journal Research Supplement*, **50**(5), pp231s-234s, 1971

[38] Mackerle J., Finite element analysis and simulation of welds: a bibliography (1976-1996), *Modelling Simulation of Materials Science and Engineering*, **4**, pp501-533, 1996

[39] Dufour L.B., Gortemaker P.C.M, Decision making with regard to the inspection desirability of stub tubes from a BWR pressure vessel ECF6, *Fracture. Contr. Eng. Str., (EMAS),* pp933-946, 1986

[40] Gifford L.N., Explosive testing of the full thickness precracked weldments, *Fracture Mechanics*, 21st Symp. Editor J. P. Guides, STP1074 (ASTM), pp157-177, 1990

[41] Lee M.M.K., Luxmoore A.R., Sumpter J.D.G., A numerical and experimental study on defect assessment of plain and welded bars with shallow crack geometries, *International Journal of Fracture*, **62(3)**, pp245-268, 1993

[42] Gensheimer DeGiorgi V., Matic P., Jolles M.I., Numerical prediction of welded joint performance – relative criticality of weld defect and remote deformation, *Journal of Pressure Vessel Technology*, **112**(2), pp175-181, 1990

[43] Zhao X.L., Al-Mahaidi R., Kiew K.P., Longitudinal fillet welds in thin-walled C450 RHS members, *Journal of Structural Engineering*, **125**(8), pp821-828, 1999

[44] Raghavendran, N.S., Fourney, M.E., Stress analysis of a welded joint, *Engineering Fracture Mechanics,* **48**(5), pp619-627, 1994

[45] Nguyen N.T., Wahab-MA, The effect of undercut and residual stresses on fatigue behaviour of misaligned butt joints, *Engineering Fracture Mechanics*. **55**(3), pp453-469, 1996

[46] Zhang J., Dong P., Residual stresses in welded moment frames and implications for structural performance, *Journal of Structural Engineering*, **126**(3), pp306-315, 2000

[47] Tang W., Shi Y.W., Influence of crack depth and strength matching on deformation and plastic zone for welded joint specimen, *International Journal of Fracture*, **74**(1), pp77-87, 1996

[48] Kim D.S., Tsai C.L. & Parritan, J., Evaluation of local brittle zone using the finite element method, *Welding Research Supplement*, **73**(11), pp257s-264s, 1994

[49] Xiao D., Dexter R.J., Finite element calculation of applied J-integral for cracked ship structural details, *Engineering Fracture Mechanics*, **60**(1), pp59-82, 1998

[50] Kang J.D., Huo L.X., Zhang Y.F., On the J-integral as fracture parameter in heterogeneous welded joints, *Key Engineering Materials*, Vol. **145-149**, pt.1, 1998

[51] Huo L.X., Yang X.Q., Zhang Y.F., Study on J-integral failure assessment curve of heterogeneous welded joints, Fracture and Strength of Solids, pts 1 and 2, *Key Engineering Materials*, **145**(9), pp13-18, 1998

[52] Shi Y., Sun S., Geometry effect of welded joints on failure assessment curves, *International Journal of Pressure Vessels & Piping*, Vol.**74**, pp71-76, 1997

[53] Gu M., Goldak J.A., Steady-state formulation for stress and distortion of welds, *Journal of Engineering for Industry*, Vol. **116**, pp467-474, November 1994

[54] Jonsson M., Karlsson L., Lindgren L-E, Deformations and stresses in butt-welding of large plates, Numerical Methods In Heat Transfer, Volume III, by *Lewis R.W., John Wiley & Sons Ltd*, pp35-58, 1985

[55] Tsai C.L., Lee S.G., Shim Y.L., Modelling techniques for welding-induced residual stress predictions, *International Conference Proceedings on Modelling and Control of Joining Processes,* ed. T. Zacharia, AWS, pp462-469, 1993

[56] Michaleris P. DeBiccari, A., Prediction of welding distortion, *Welding Journal Research Supplement,* **76**(4), pp172s-181s, 1997

[57] Hong J.K., Tsai C. –L, Dong P., Assessment of numerical procedures for residual stress analysis of multipass welds, *Welding Journal Research Supplement*, **77**(9), pp372s-381s, 1998

[58] Hong J.K., Dong P., Tsai C.L., Finite element simulation of residual stresses in multipass welds, *International Conference Proceedings on Modelling and Control of Joining Processes,* Edited by Zacharia T., AWS, pp470-476, 1993

[59] Wikander L., Karlsson L., Nasstrom M., Webster P., Finite Element simulation and measurement of welding residual stresses. *Modelling and Simulation of the Materials Science and Engineering*, **2**(4), pp845-864, 1994

[60] Shim Y., Feng Z., Lee S., Kim D, Jaeger J., Papritan J.C., Tsai C-L., Determination of residual stresses in thick-section weldments, *Welding Journal*, **71**(9), pp305s-312s, 1992

[61] Brown, S.B., Song, H., Implications of three-dimensional numerical simulations of welding of large structures, *Welding Journal Research Supplement*, **71**(2), pp55s-62s, 1992

[62] Dilthey D., Reishen U., Kretshmer M., Comparison of FEM simulations to measurements of residual stresses for the example of a welded plate: a state-of-art report, *Modelling and Simulation of the Materials Sciences and Engineering*, **8**, pp911-926, 2000

[63] Song J., Peters J., Noor A., Michaleris P., Sensitivity analysis of the thermomechanical response of welded joints, *International Journal of Solids and Structures*, Vol.**40**, pp4167-4180, 2003

[64] Andersson B.A.B., Thermal stresses in a submerged-arc welded joint considering phase transformations, *Transactions of the ASME Journal of Engineering Materials and Technology*, **100**(4), pp356-362, 1978

[65] Jonsson M., Karlsson L., Lindgren L-E, Deformations and stresses in butt-welding of large plates with special reference to the mechanical material properties, *Transactions of the ASME, Journal of Engineering Materials and Technology*, **107**(4), pp265-270, 1985

[66] Lindgren L-E, Runnemalm H., Nasstrom M.O., Simulation of multipass welding of a thick plate, *International Journal for Numerical Methods in Engineering*, **44**(9), pp1301-1316, 1999

[67] Laudau H. G., Weiner J. H., Zwicky E. E., Thermal stress in a viscoelastic-plastic plate with temperature-dependent yield stress, Journal of Applied Mechanics, **27**(2), pp297-302, 1960

[68] Argyris J.H., Szimmat J., Willam K.J. Finite element analysis of arc-welding processes, *Numerical Methods in Heat transfer*, Volume III, edited by Lewis R.W., John Wiley & Sons Ltd., pp1-34, 1985

[69] Bonifaz E.A., Finite element analysis of heat flow in single-pass arc welds, *Welding Journal Research Supplement*, **79**(5), pp121s-125s, 2000

[70] Goldak J., Chakravarti A., Bibby M., A double ellipsoid finite element model for welding heat sources, *IIW Doc.No.212-603-85*, 1985

[71] Glickstein S.S, Friedman E., Weld modelling applications, *Welding Journal*, **63**(9), pp38-42, 1984

[72] Brown. S.B., Song, H., Rezoning and dynamic substructuring techniques in FEM simulations of welding processes, *Journal of Engineering for Industry – Transactions of the ASME,* **115**(11), pp415-423, 1993

[73] Michaleris P. DeBiccari, A., Prediction of welding distortion, *Welding Journal Research Supplement,* **76**(4), pp172s-181s, 1997

[74] Teng T-L., Fung C-P., Chang P-H., Yang W-C., Analysis of residual stresses and distortions in T-joint fillet welds, *International Journal of Pressure Vessels and Piping*, Vol.**78**, pp523-538, 2001

[75] Brown, S.B., Song, H., Implications of three-dimensional numerical simulations of welding of large structures, *Welding Journal Research Supplement*, **71**(2), pp55s-62s, 1992

[76] Brown, S., Song, H., Finite element simulation of welding of large structures, *Journal of Engineering for Industry – Transactions of the ASME*, **114**(11), pp441-451, 1992

[77] Dong, P., Zhang, J., Residual stresses in strength-mismatched welds, *Engineering Fracture Mechanics,* Vol. **64**, pp485-505, 1999

[78] Rao N.R.N., Tall L., Residual stresses in welded plates, *Welding Journal Research Supplement*, **40**(10), pp468s-480s, 1961

[79] Rao N.R.N., Tall L., Residual stresses in welded shapes, *Welding Journal Research Supplement*, **43**(7), pp295s-306s, 1964

[80] Mochizuki M., Hayashi M., Hattori T., Numerical analysis of welding residual stress and its verification using Neutron diffraction measurement, *Transaction of ASME Journal of Engineering Materials and Technology*, **122**(1), pp98-103, 2000

[81] Sinclair I., Private communication, University of Southampton, 2004

[82] Tsai C.L., Finite element analysis of underwater welding repairs, *Welding Research Supplement*, **76**(8), pp283s - 288s, 1997

[83] Yuan M. G., Ueda Y., Prediction of residual stresses in welded T- and I- joints using inherent strains, *Journal of Engineering Materials and Technology*, **118**(4), pp229-234, 1996

[84] Hong J.K., Dong P., Tsai C.L., Finite element simulation of residual stresses in multi-pass welds, *International Conference Proceedings on Modelling and Control of Joining Processes,* ed. T. Zacharia, AWS, pp470-476, 1993

[85] Dong P., Zhang J., Residual stresses in strength-mismatched welds and implications on fracture behaviour, *Engineering Fracture Mechanics*, **64**, pp485-505, 1999

3. Finite Element Prediction of Residual Stresses

3.1 Overview

The experimental measurement of residual stresses is expensive and may be affected by many error sources. Furthermore, most of the available measurement methods are destructive and give only residual stress measurements at discrete locations. A reliable and efficient numerical analysis, validated through experimental measurements, can thus be considered as a desirable alternative method for obtaining the detailed mapping of residual stresses as a result of welding. As a first attempt, a finite element simulation of the welding process yielding the welding-induced residual stresses in a butt-welded plate was performed and is presented in this chapter. The reliability of the model was assessed through comparison of its predictions with published experimental[1] residual stress measurements and distortion results from empirical calculations. As discussed in Chapter 2, Section 2.4, the experimental measurement of residual stresses is affected by various factors and an experimental error of 15% is not uncommon. Thus an FE analysis which gives residual stresses within 15% of those derived from experiments is considered as providing acceptable precision. Thermal and mechanical properties as functions of temperature are not available for every steel used in the experimental study on residual stresses in welds. Thus data were obtained from the literature for similar structural steels. These data were compared and a set of data was then chosen to be used in the current study based on this comparison and the confidence claimed by various sources. The sensitivity of the temperature development and the final residual stress results on these properties was studied by varying their values between the extremes used by other researchers. Parametric studies, based on the model developed were then carried out to assess the effects of the amount of heat input, the yield strength of the material as well as external constraints on the final residual stress. Based on these studies, a simplified modelling procedure of acceptable accuracy was proposed.

3.2 Residual stress fundamentals

In fusion welding, a weldment is locally heated by the welding heat source. Due to the non-uniform temperature distribution developed, during the thermal cycle, incompatible strains lead to thermal stresses. When the weld is completed, incompatible strains due to dimensional changes associated with solidification of the weld metal, metallurgical transformations, and plastic deformation, remain in regions near the weld and are the sources of residual stresses and distortion. When welding processes and parameters are changed, the heat-flow patterns are also changed. The change in heat-flow pattern causes a change in the distribution of incompatible strains, and this causes changes in shrinkage and distortion.

The procedure for welding-induced residual stress analysis can be divided into two parts: thermal and mechanical analysis. For the welding problem the thermo-mechanical coupling remains negligible for the thermal analysis since the temperature field is dominated entirely by the heat input from the welding heat source[2, 3, 4].

The mathematical analysis of transient heat flow in a weldment is essentially based on the following partial differential equation[5]

$$\rho c \frac{\partial T}{\partial t} = q_G + \left[\frac{\partial}{\partial x}\left(k \frac{\partial}{\partial x} \right) + \frac{\partial}{\partial y}(k \frac{\partial}{\partial y}) + \frac{\partial}{\partial z}\left(k \frac{\partial}{\partial z} \right) \right] T \qquad (3\text{-}1)$$

where T is the temperature, ρ the density, c the specific heat, k the thermal conductivity and q_G the rate of heat generated per unit volume.

Eqn (3-1) is solved for a given set of initial conditions (initial temperature distribution) and boundary conditions (shape and intensity of the heat source, geometry of the weldment etc.). Solutions of Eqn (3-1) in some special cases can be found in Masubuchi[5]. Complex problems can be analysed using FEM which generates the following equation[6]

$$[C] \{\dot{T}\} + [K] \{T\} = \{Q\} \qquad (3\text{-}2)$$

where, [C] is the specific heat matrix, {T} the nodal temperature vector, $\{\dot{T}\}$ the time-derivative of {T}, [K] the effective thermal conductivity matrix, and {Q} the effective heat flow rate vector. Appendix C gives more details on how Eqn (3-2) is derived from Eqn (3-1).

Customarily the amount of heat supplied to the work piece, Q, is expressed as:

$$Q = \eta_a VI \,(\mathrm{W}) \tag{3-3}$$

where η_a is the arc efficiency, V the arc voltage and I the arc current. The heat generated by the welding process dissipates into the work piece by thermal conduction and into the surrounding atmosphere by radiation and convection from the work piece and directly from the arc.

Solution of the temperature-induced stress problem is derived from the temperature history obtained from the thermal analysis. Studies on transient thermal stresses during welding started in the 1930s[5]. However, due to the complexity of the problem, analyses of thermal stresses were limited to simple cases only, before the use of modern computers.

3.3 Finite element modelling procedure

In this study, a butt-welded steel plate was modelled using the general-purpose FEM package ANSYS[7] to predict the residual stresses introduced from the welding process. As pointed out in Chapter 1 Section 1.2, research in this project centred on a fillet welded T-joint, however, the butt welded joint was modelled first due to the availability in the literature of results from a considerable number of numerical and experimental studies. These results enabled an assessment of the accuracy of the modelling methodology adopted in the current study to be conducted. Furthermore, the modelling methodology adopted for a butt weld and a T-joint is essentially the same so that it is more cost effective to assess the reliability of the FEM modelling through a simpler example.

3.3.1 Description of the model

As discussed in Chapter 2, Section 2.4.1, although welding simulation is a 3-D problem, 2-D models on the plane perpendicular to the welding direction give a good approximation due to the presence of a quasi-steady state in relatively long welds. In this study, a 2-D model was developed to predict the residual stresses generated by the welding process. The weldment was assumed to be symmetric so that only one half of the model was analysed. For comparison purposes, the dimensions adopted were the same as those of the T-2-6 specimen tested by Rao and Tall[1]. This specimen was chosen because it is a simple single pass butt weld and some specific information on its material properties was given. Referring to Fig. 3-1, the dimensions of the model are L = 127 mm, T_1 = 12.7 mm, b = 2 mm, B =16.665 mm, and T_2 = 1 mm. The dimension b was assumed to be 2 mm, a value within the range (0-3.2 mm) specified by AWS[8] for pre-qualified butt welds with a production groove angle, $\theta = 60^o$ (see Fig. 3-1). The height of overfill, T_2 was assumed to be 1 mm. An overfill of less than 1/16 inch, i.e., 1.6 mm is recommended by Lincoln Electric[9]. The value of T_2 = 1 mm is not uncommon in practice.

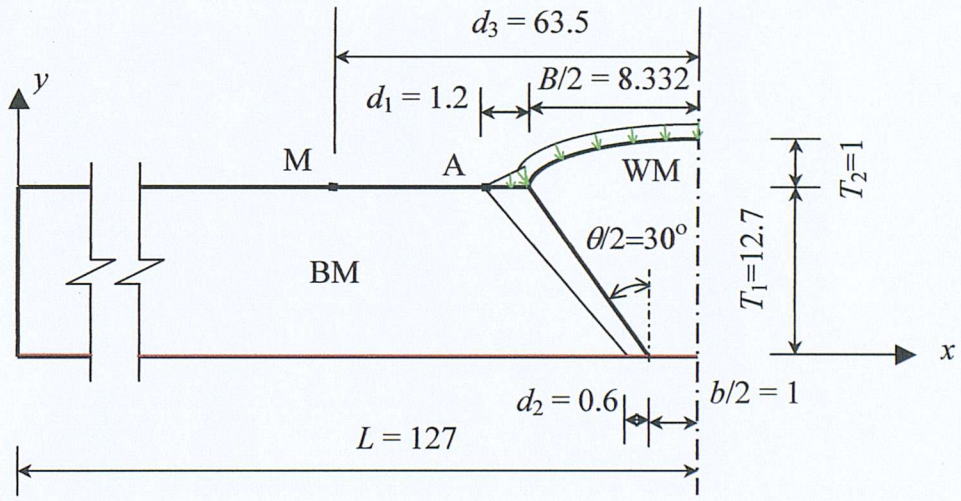

Fig. 3-1 Geometry of the butt-weld model, dimensions in mm, not to scale, BM = base metal, WM = weld metal

Four-node 2-D thermal solid elements were used for meshing both weld metal and base metal areas with the temperature as the only degree of freedom at each node.

Mesh3, as shown in Fig. 3-2, was first generated based on the element size used by Hong et al.[15] An element size of 5 mm was used for the base metal area far from the weld, with a refined element size of 0.5 mm in and near the weld area and HAZ. Another two coarser and two finer meshes were then generated according to Table 3-1 where number of divisions $n_1 - n_6$ are defined in Fig. 3-2.

Table 3-1 Number of line divisions and total number of element for Mesh1-Mesh5

	n_1	n_2	n_3	n_4	n_5	n_6	Total number of Elements
Mesh1	5	9	8	8	10	2	91
Mesh2	9	16	14	15	13	3	237
Mesh3	17	30	28	30	16	3	746
Mesh4	26	48	42	44	20	4	1624
Mesh5	34	64	55	59	26	5	2865

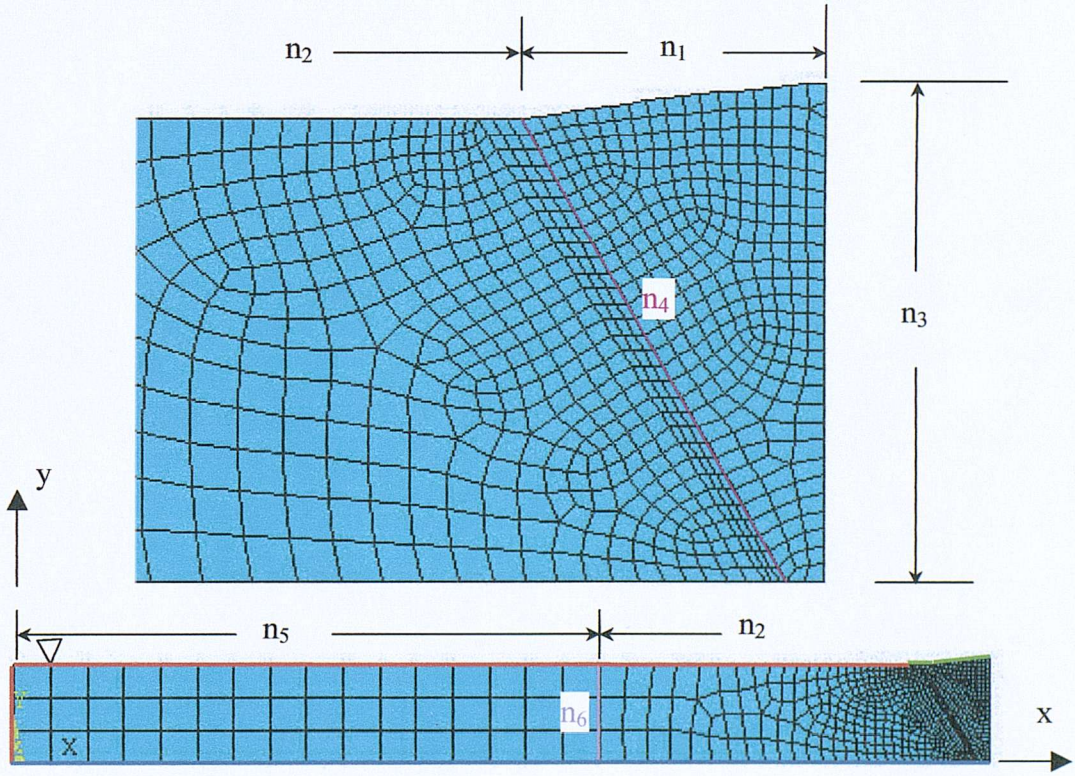

Fig. 3-2 Mesh map of the model, Mesh3

The FE analysis was carried out in two steps. A thermal analysis was conducted first to obtain the global temperature history generated during the welding process. A stress analysis was then developed with the temperatures obtained from the thermal analysis used as loading to the stress model. ANSYS [10] was utilised for both thermal and stress analysis performed sequentially using the appropriate combination of elements. Coupled thermal and stress analysis is also available in ANSYS, however, the decoupled method is recommended as element types that can be used for coupled analysis are limited while all possible thermal loads in the thermal analysis option and all possible structural loads in the stress analysis portion can be used in the decoupled analysis. In addition, when the thermal analysis is transient, only those temperature results at time points where temperature gradients are large need to be inputted into the stress analysis.

3.3.2 Thermal analysis

The non-linear transient heat flow analysis accommodated the temperature-dependent thermal properties and predicted the temperature development during the welding process.

Heat input

The amount of heat input is calculated using Eqn. (3-3). The arc efficiency η_a is used to account for the heat loss from the arc to the surrounding environment. Part of the net heat input calculated from Eqn. (3-3) is used to melt the electrode and this part might be as high as 40%[27].

Table 3-2 lists the heat source model and welding process simulated by various researchers in the literature. The value used for the arc efficiency is one of the uncertainties in this simulation area and the relevant published information is rather confusing. Most of the arc efficiency values used were assumed rather than measured without explanation on why these values were chosen. Only Karlsson and Josefson[11] stated that due to the absence of root gap and extraordinary good conditions in the experiment a high value of arc efficiency was assumed. Michaleris et al.[12] only give a heat input amount in their paper without mention of the arc efficiency or the initial

temperature for the weld metal. Arc efficiency values for various types of welding processes were suggested based on empirical studies[5], e.g., for gas metal arc welding, η_a varies from 0.66 to 0.7; for coated electrode shielded metal-arc welding it ranges between 0.66 and 0.85; and for submerged-arc welding, from 0.90 to 0.99. Jonsson et al.[13] used a higher value, because they adjusted this value in order to achieve good agreement with the experimentally measured temperature history.

Table 3-2 Heat input model and welding process simulated by various researchers

Reference number	η_a	Welding process①	Heat source model	Initial WM temperature	Applied heat Q^{app}②
4	0.85	GMAW	Uniform	Not clear	Q_a
11	0.90	MIG	Uniform	Not clear	Q_a
13	0.72	GMAW	Uniform	Not mention	Q_a
15	0.85	GMAW	Surface: Gaussian; body: uniform	21.1 °C	Q_a
16	0.90	SAW	Uniform	1800 °C	Q_a-Q_m^w
17	0.60	Not given	Gaussian	1600°C	Q_a-Q_m^w
19	0.80	Not given	Uniform	Not clear	Q_a

①: SAW: Submerged arc welding; GMAW: gas metal arc welding; MIG: metal inert gas;
②The applied heat Q^{app} in the table is defined as the heat applied as surface and/or body load to the model. Q_a is the amount of heat calculated from Eqn. (3-3); Q_m^w the amount of heat used to melt the deposited weld metal.

In this study, the values of V and I were taken equal to 40 V and 375 A, respectively, as given by Rao and Tall[1] for the specimen T-2-6 the welding of which was simulated in this study.

Rao and Tall[1] did not give the type of welding process used in their experiments but the values of current and voltage used, the picture of a typical welding plate set up, and the electrode type used, all indicate that the welding process is shielded metal-arc welding. From the results of the experimental study on arc efficiency carried out by Christensen et al.[14], the arc efficiency for this type of welding process on mild

steel falls in the middle of the range of 0.66-0.85. A value of 0.75 was assumed and used initially in this study. Different values of arc efficiency were used in Section 3.5.1 to assess the effect of heat input magnitude on the residual stresses results.

In practice, the weld metal is deposited into the weldment in a molten state. It is thus more reasonable to assign an initial temperature at above the melting point to the weld metal but the amount of heat used to achieve this temperature rise should be deducted from that supplied by the arc. In this study, the initial temperature of the weld metal was assumed to be 1803 K, the melting temperature. The amount of heat used for melting the weld metal Q_m^w was calculated and subtracted from the heat calculated from Eqn. (3-3) to obtain the heat input into the model. Table 3-2 shows that most of the researchers did not mention the initial temperature adopted in their models for the weld metal except Hong et al.[15], Andersson et al.[16], and Brown and Song[17], who clearly stated the relation between the heat input calculated from Eqn. (3-3) and the initial temperature of the weld metal.

Heat source model

In the literature, heat has been input into the model in the forms of surface heat, Q_s, and body heat, Q_b, applied to the weld metal and/or the part of the base metal close to the arc. As the arc supplying heat to the workpiece is normally spread over a small area above the weld metal and a small area of the base metal adjacent to the weld metal, it is reasonable to apply surface heat to both weld metal and base metal. Heat is also applied to the weld metal through conduction from the arc so that body heat input should also be applied to the weld metal.

For surface heat flux, Gaussian, double ellipsoid, and uniform distribution have been proposed and applied (see Table 3-2). For body heat input, a uniform distribution was used. Gaussian and ellipsoid distributions are preferable when the weld pool shape is to be modelled which itself is very complex involving plasma pressure from the arc and fluid motion in the pool. The double-ellipsoid model was proposed to examine the 3-D temperature field in welding process[25,26]. The 3-D effect can be

accounted for by the ramped heat input function proposed by Hong et al.[15] as discussed later.

Similar results were obtained by various researchers using different heat source models including uniformly distributed surface heat. For example, Andersson et al.[16] used a uniform distribution of surface heat in his model and the temperature history obtained had very good agreement with experimental measurements. In addition, the application of a Gaussian or ellipsoid model is more complex and the parameters to define these distributions should be obtained from experiment which is not the case in this study. The surface heat was then chosen to be uniformly distributed over the weld metal top surface and decrease to zero at Point A, as shown in Fig. 3-1 by the green arrows.

Hong et al.[15] suggested that the ratio of surface load, Q_s, to the body load, Q_b, can be adjusted to achieve a more accurate representation of the fusion zone. Since the fusion zone is not known from the experiment simulated by this study, a ratio of Q_s/Q_b equal to ¼ was adopted as recommended by Hong et al.[15]

Loading steps

As pointed out in Chapter 2 section 2.4, the welding process is a 3-D problem. In a 2-D simulation, the cross-section studied is in the middle region of the weldment transverse to the welding direction. Before the arc reaches that section, the base metal of the section has already started to heat up due to the heat conducted from the part under the arc. Upon the arc reaching the position of the section, a large amount of heat is transferred from the arc directly to the section. When the arc leaves a section, this section is still receiving heat from the part under the arc through conduction. To include the effect of out-of-plane heat input as well as to avoid numerical divergence problems which may be caused by a sudden increase in temperature, Hong et al.[15] applied a ramped heat input function. The heat was input in four load steps corresponding to t_1, t_2, t_3 and t_4 as shown in Fig. 3-3. A ratio of t_1 to the actual welding time, $t_1 + t_2$, equal to 0.2 was used which is believed to give the best correlation with gas metal arc welding (GMAW) experimental data[4,15]. In

this study, the actual welding time, $t_1 + t_2$, was taken to be 0.23 seconds corresponding to a welding speed of 4.32 mm/s as given by Rao and Tall[1].

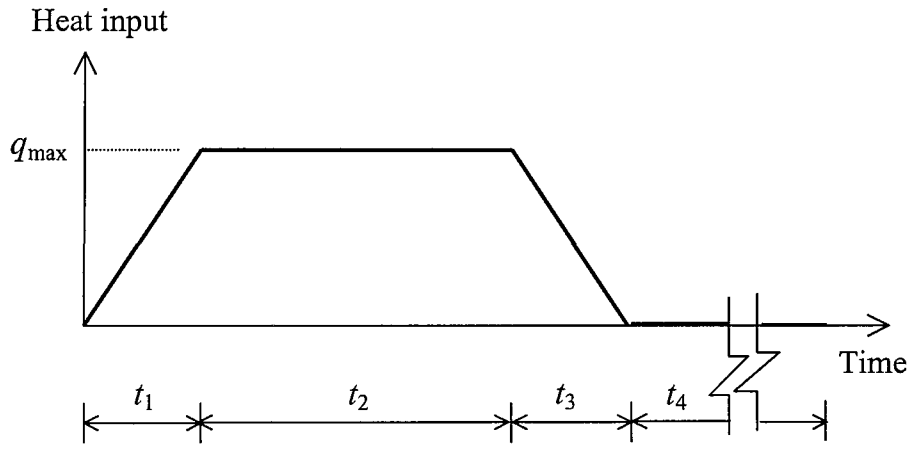

Fig. 3-3 Ramped heat input function for the butt welding simulation

Temperature-dependent thermal material properties

As discussed in Chapter 2, Section 2.4, the temperature-dependence of some thermal material properties has been considered by most researchers[2-4, 12,18,19,22-25] in this area since the material experiences temperature cycles from ambient to above the melting point. Temperature-dependent values of specific heat and conductivity are required.

As listed in Table 3-3, most researchers either assumed material properties taken from other researchers[11,13,15,19] or used values taken from handbooks for somewhat different steels without justifying their validity[12,18]. Some researchers[17,20] simply listed the material properties used with no mention of how these values were obtained or where from. Since they all concluded that their FE simulation gave reasonably reliable results, it is expected that variation of certain material properties has negligible effect on the final residual stress results if their claims are to be believed. Song et al.[21] studied the effect of thermal material properties on the temperature history results and the mechanical material properties on the resulting von Mises stress. The temperature history was seen to be influenced by thermal

properties and stress by mechanical properties, however, the effect of thermal property variation on the final residual stress results was not examined. As early as 1949, Weck[22] stated that the welding procedure was of little influence on the magnitude of residual stresses. Laudau et al.[23] argued that residual stress solutions are not sensitive to the details of temperature distribution. Hong et al.[15] drew the same conclusion from their study on the effect of the amount of heat input, and initial temperature for the weld metal.

It was not possible to obtain experimentally these material property variations with temperature in this study. The method used here to solve this problem involves two steps, i.e., firstly methodically select data available from the literature, examine their reliability and secondly perform a sensitivity study on the properties to which less confidence was attached. Material property values from eleven sources were compared and the confidence on these values was assessed. Table 3-3 shows the specification and chemical composition of the steels used by these researchers. These are all seen to be for structural steels which have similar compositions to those in the experiment simulated in this study. Based on this comparison, a set of data was chosen initially to be used for the current model, the sensitivity of the temperature and residual stress results was then assessed by changing these material properties to the extreme values for structural steels given in the literature by previous researchers.

Table 3-3 Steel, source (see Table 3-4) of material properties and assumptions used by various researchers for welding simulation

Reference number	Steel specification	Chemical composition (%)										Source (see Table 3-4)		Assumptions	
												Thermal properties	Mechanical properties	Phase change	Radiation
16	Fine grain steel	C	Mn	Si	Nb							Richter[a]; steel manufacturer[b]	Richter[a]; steel manufacturer[b]	yes	yes
		0.13	1.57	0.2	0.024										
17	Mild steel	Not given										Not mentioned	Iwamura et al.[c]	yes	yes
15	ASTM A36	C	Mn	P	S							Shim[d]	Shim[d]	no	no
		≤ 0.26	≤ 1.2	≤ 0.04	≤ 0.05										
13	Fine grain steel	C	Mn	Si	Al							Andresson et al.[16]	Andersson et al.[16]; Steel manufacturer[e]	yes	no
		0.13	1.11	0.18	0.046										
11	Swedish SIS 2172	C	Mn	Si	Cr	Cu						Hildenwall[f]; Sjostrom[g]; Andersson[16];	Hildenwall[f]; Sjostrom[g];	yes	yes
		0.18	1.3	0.3	0.3	0.4									
18	Swedish SIS 2134	C	Mn	Si	V	S	P					Metals Handbook[h] for AISI 1524	Richter[a]; Suzuki[i]	yes	yes
		0.2	1.6	0.5	0.15	0.035	0.035								
12	AH-36, but used those for SAE 1020	C	Mn	P	S							Brown and Song[17]; BISRA[j]	Goldak[k]; Mizukami[l]	no	yes
		0.18-0.23	0.3-0.6	≤ 0.04	≤ 0.05										
20	Mild steel	Not given										Not mentioned	Not mentioned	no	no
19	SS2132/ SS2172	C	Mn	P	N							Jonsson[13]	Jonsson[13]; Troive[m]	yes	no
		≤ 0.2	≤ 1.6	≤ 0.035	≤ 0.02										
1*	ASTM A7	P		S											
		≤ 0.06		≤ 0.05											

* Steel used in experimental determination of residual stresses in weld[1]

Table 3-4 Sources referred to in Table 3-3

Reference number in Table 3-1	Source
a	Richter F., Die wichtigsten physikalischen eigenschaften von 52 eisenwerkstoffen, Stahleisen Sonderberichte, Heft 8, 1973
b	Hannerz N.E., private communication reported in 16
c	Iwamura Y., Rybicki E. F., A transient elastic plastic thermal stress analysis of flame forming, *ASTM Journal of Engineering for Industry*, pp163-171, 1973
d	Shim Y. L., Feng Z., Lee S., Kim D., Jaeger J., Papritan J. C., Tsai C.-L., Determination of residual stresses in thick-section weldments, *Welding Journal* **71**(9), pp305s-312s, 1992
e	Svenskt Stal AB, Box 1000, 613 011 Oxelosund, Sweden (Mr Lars Hoglund)
f	Hildenwall B., Prediction of residual stresses created during quenching, Linkoping Studies in Science and Technology, Diss. No. 39, Linkoping, Sweden, 1979
g	Sjostrom S., The calculation of quench stress in steel, Linkoping Studies in Science and Technology, Diss. No. 84, Linkoping, Sweden, 1982
h	Metals Handbook, 1 Properties and selections: Iron and steels, ASM, *Cleveland*, 1978
i	Suzuki H., et al., Studies on the flow stress of metals and alloys, Report of the Institute of Industrial Sciences, *University of Tokyo*, **18**(3), 1968
j	The British Iron and Steel Research Association (eds.), Physical Constants of Some Commercial Steels at Elevated Temperatures, *Butterworths Scientific Publications*, London, 1964
k	Goldak J., A predictive method for computing distortion due to welding in ship structures, Report submitted to Edison Welding Institute, Columbus, Ohio, 1994
l	Mizukami H., Miyashita Y., Mechanical properties of continuously cast steel at high temperatures, Tetso-to-Hagane (Iron and Steel), 63:46 (in Japanese), 1977
m	Troive L., Karlsson L., Lindgren L. E., Deformation and stresses in butt-welding of large plates, Numerical Methods in Heat Transfer, Vol. III, ed Lewis R. W., and Morgan K., *Wiley*, London, 1985

A) Specific heat / enthalpy

Fig. 3-4 shows the temperature-dependent specific heat used by other researchers. Data from studies in Reference 12, 15, and 20 which did not consider the latent heat due to the phase change are not included in Fig. 3-4. The trend of the variation of specific heat with temperature, especially below approximately 970 K when the solid-solid phase transformation occurs, are similar and the magnitudes are also very close except those from Karlsson and Josefson[11]. As indicated in Table 3-3, none of these researchers obtained the property values through their own experiments.

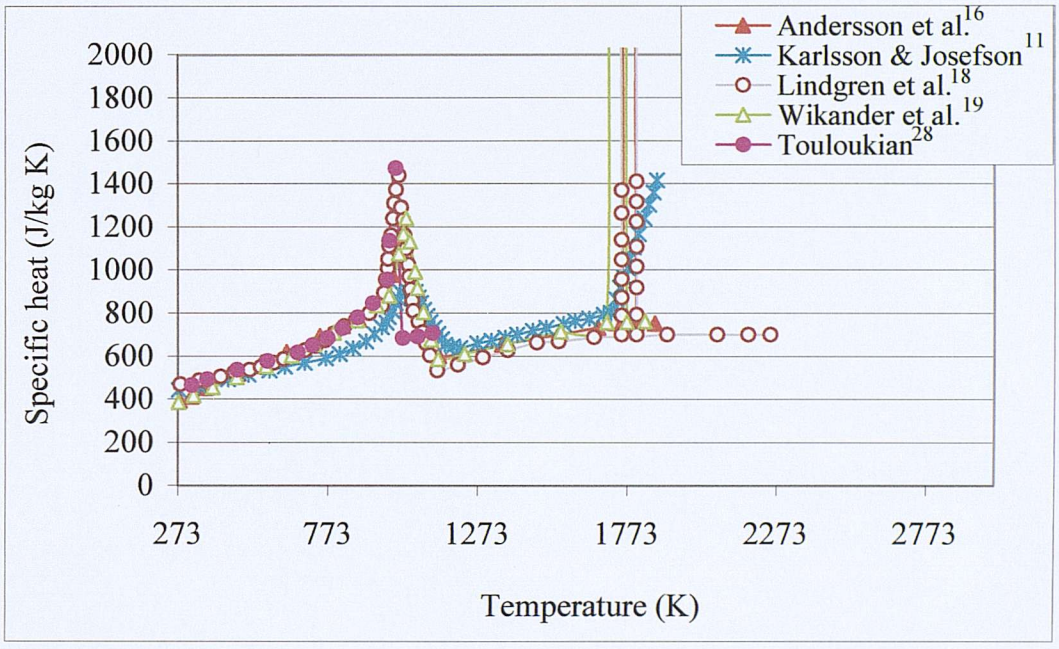

Fig. 3-4 Temperature-dependent specific heat considering latent heat from phase transformations from various sources

It is recommended by ANSYS[7] to use enthalpy rather than specific heat when phase transformation is taken into account as its distribution is much smoother. Enthalpy can be evaluated from

$$H = \int_{T_{ref}}^{T} \rho\, c\, dT \qquad (3\text{-}4)$$

where, H is the enthalpy with respect to a reference temperature T_{ref}, measured in J/m^3; ρ the density, which is taken as 7680 kg/m^3 for structural steel.

Despite the variation in specific heat values indicated by Fig. 3-4, the enthalpy distribution computed from the specific heat using Eqn. (3-4), shows less variation (see Fig. 3-5).

Fig. 3-5 allows the comparison of the enthalpy values calculated from the specific heat data given by various researchers. The enthalpy values are almost identical before the solid-solid phase transformation, and during the solid-solid phase change Karlsson and Josefson[11]'s value is less than 10% lower than the Lindgren et al.[18] value. The consistency of the data plotted in Fig. 3-5 is an indication of their reliability. The values provided by Andersson et al.[16], which have been tested by other authors[13,19] and found reliable, were adopted in this study.

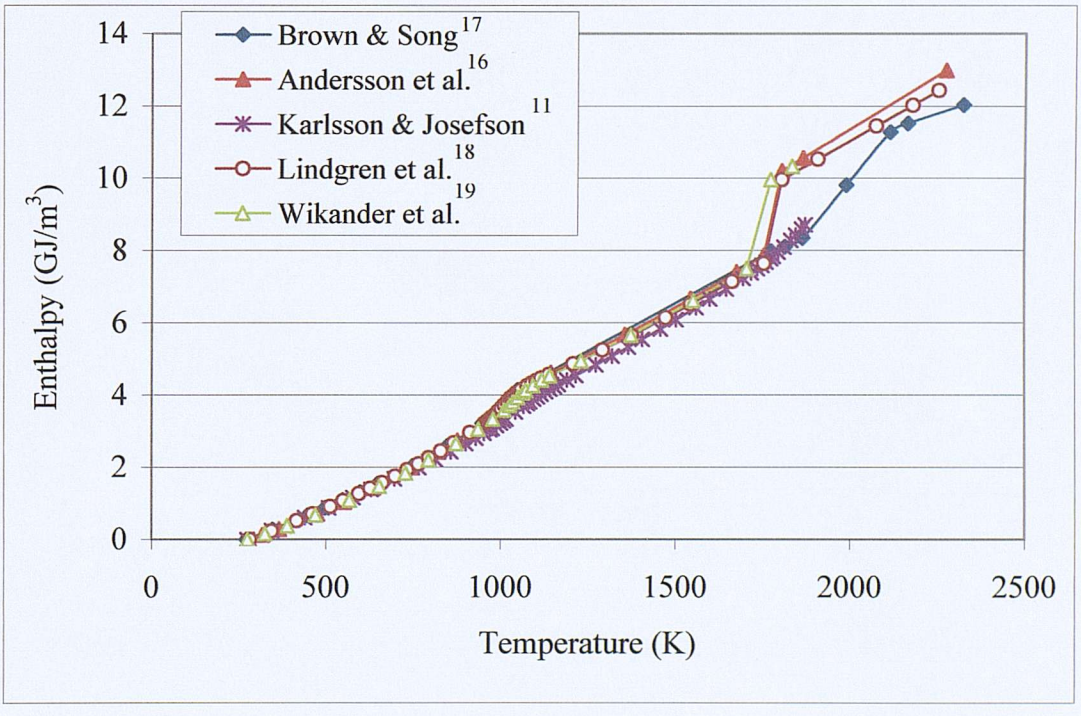

Fig. 3-5 Temperature-dependent enthalpy from various sources

B) Conductivity

Fig. 3-6 shows the variation of conductivity with temperature from various sources in the literature. These curves have the same trend, although the magnitude of conductivity varies, for example, from 40 to 51 W/m K, that is, by 27.5% of the maximum at room temperature. The high value of the conductivity above the melting temperature was used to model the stirrer effect in the molten metal[13,16,24]. In this study the values used by Michaleris et al.[12] were first adopted as their values were taken from the BISRA handbook and are very close to those given by Brown and Song[17], Hong et al.[15] and Lindgren et al.[18]. The values given by Andersson et al.[16], which are seen to have the most significant difference from the values of Michelaris et al.[12] at low temperatures were then used to study the effect of conductivity on the final residual stress results.

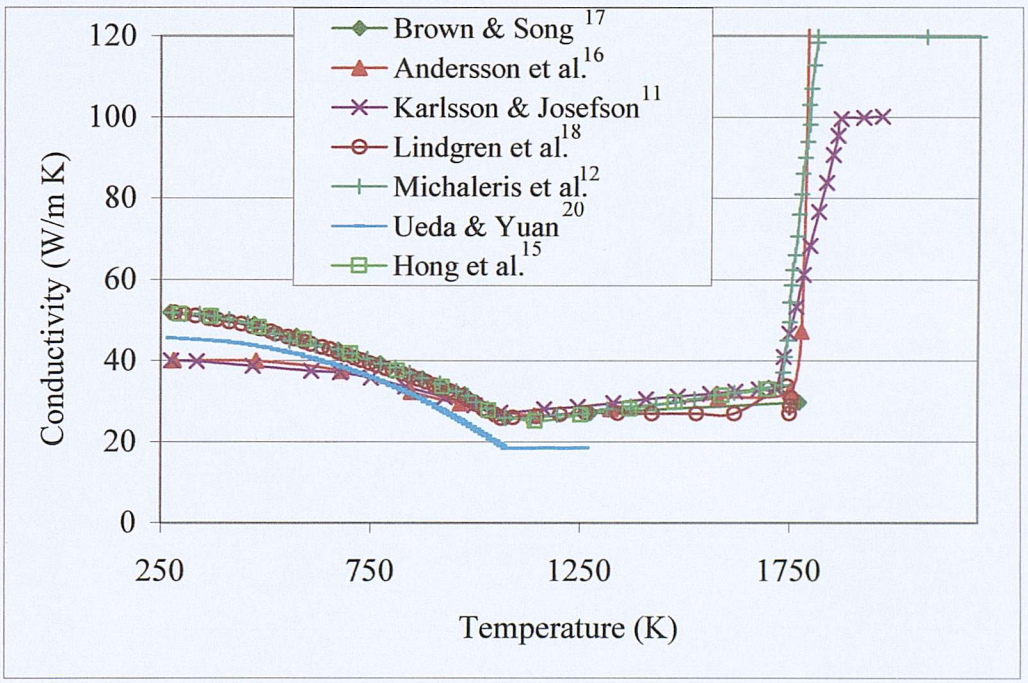

Fig. 3-6 Temperature-dependent conductivity from various sources

Boundary conditions

The centre line of the weld is assigned a plane of symmetry. Convection and radiation have been applied to all free surfaces, as shown by the red and green lines in Fig. 3-2. However, ANSYS does not allow convection and surface heat flux to be input to the same surface at the same time. Thus, during the heating load steps (t_1+t_2+t_3 in Fig. 3-3) surface heat flux was applied to surfaces represented by the green lines in Fig. 3-2. At the start of the cooling load steps (t_4 in Fig. 3-3), surface heat flux was removed and convection applied.

Not all cited researchers used a temperature-dependent convection coefficient. Some[13,16,18,19] used a constant value of 12 W/m^2 °C. Ueda and Yuan[20] used a lower value at room temperature and a more rapid increase with temperature. In this study, the distribution used by Brown and Song[17], which is very close to that used by Michaleris et al.[12] will be employed initially and the values given by Ueda and Yuan[20] will also be utilised to study its effect on both temperature and residual stress results.

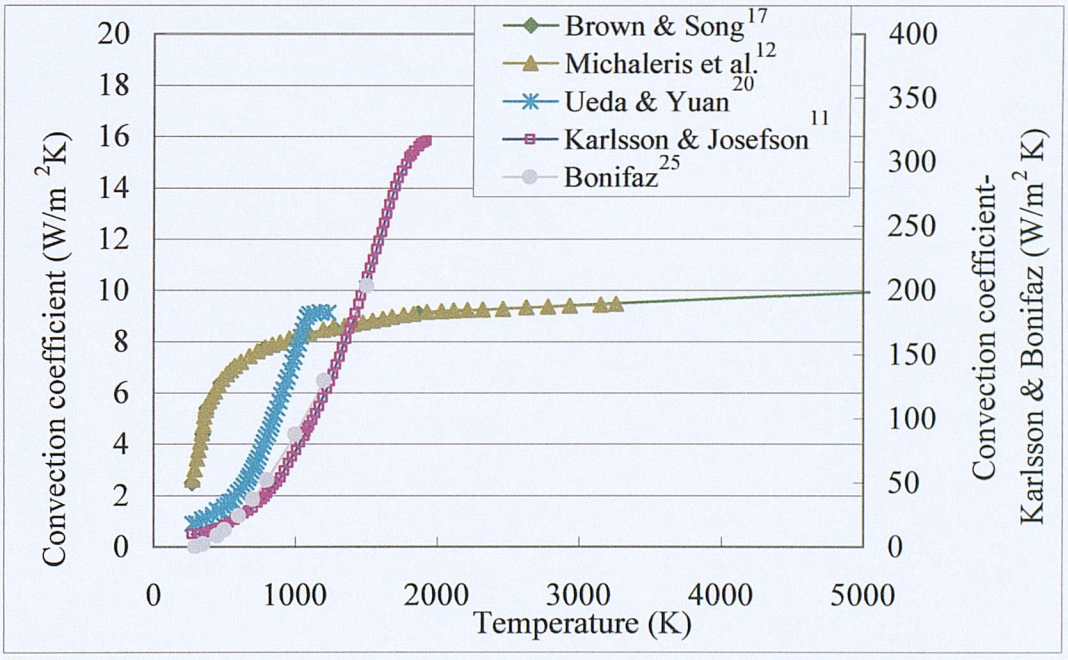

Fig. 3-7 Temperature dependent convection coefficient from various sources

Only Brown and Song[17] used a temperature-dependent emissivity for radiation, as shown in Fig. 3-8. Several authors[13,15,19,20] ignored the radiation effect. Andersson et al.[16] used a constant value of 0.28, Lindgren et al.[18] used 0.5 while Michaleris et al.[12] used 0.2. The difference in emissivity values used by different researchers is large and even those who ignored the radiation effect claimed that their residual stress results were good. Radiation could result in significant heat loss at high temperatures as the heat loss through radiation is proportional to T^4. As shown in Fig. 3-7, Karlsson and Josefson[11]'s convection coefficient values are the most different at high temperatures as they claimed that their values included the effect of radiation as well. Bonifaz[25] used

$$h = 24.1 * 10^{-4}\, \varepsilon\, T^{1.61} \tag{3-5}$$

where h is the effective convection coefficient, ε is taken to be 0.9 following recommendation by Goldak et al.[26] for hot-rolled steel, to calculate a combined convection and radiation boundary condition and the values from this equation are very similar to those given by Karlsson et al.[11], as can be seen in Fig. 3-7.

In this study, models not taking into account and taking into account radiation were generated to study the effect of radiation on both the temperature and residual stress results.

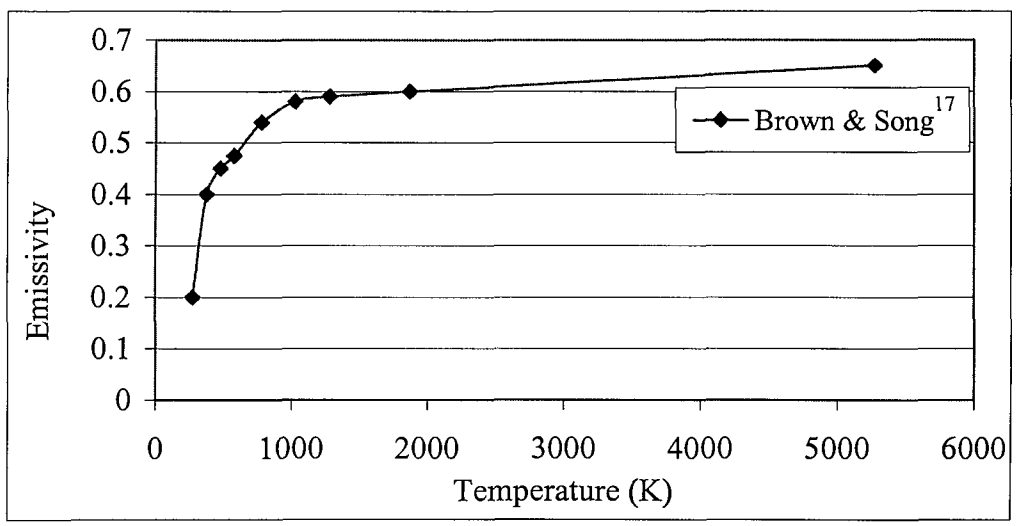

Fig. 3-8 Temperature-dependent emissivity

Particular attention needs to be given to the bottom surface of the weldment (surface represented by the blue line in Fig. 3-2) which is resting during welding on a steel column block, details of which were not given, in the experimental paper by Rao and Tall[1]. The heat loss through this surface is thus expected to be more significant than the other free surfaces with normal conditions. Two ways can be used to model this effect. One is to use a higher convection coefficient for this bottom surface. Wikander et al.[19], for instance, used a convection coefficient, as high as 300 W/m^2 °C, compared to the value of 12 W/m^2 °C for other free surfaces, to simulate the heat transfer between the model and an external fixture used to clamp the model. The other way is to use an additional gap conducting element the modelling of which is more complex. In this study, an effective convection coefficient was calculated based on the assumption that the heat loss per unit time through convection was equivalent to the heat loss through conduction.

Under steady-state conditions, the heat flow per unit time, Q^k, through conductivity from surface A_1 to surface A_2 of thickness l, as shown in Fig. 3-9, is calculated as:

$$Q^k = k A (T_1 - T_2) / l \tag{3-6}$$

Heat loss through surface convection of surface A_1, Q^h, is:

$$Q^h = h A (T_1 - T_{am}) \tag{3-7}$$

From $Q^k = Q^h$, and noting that $T_2 = T_{am} = 293$ K,

$$h = k / l \tag{3-8}$$

where, k is the conductivity; h convection coefficient; A, the area of A_1; T_1, T_2, and T_{am} the temperature at surface A_1, A_2 and ambient, respectively.

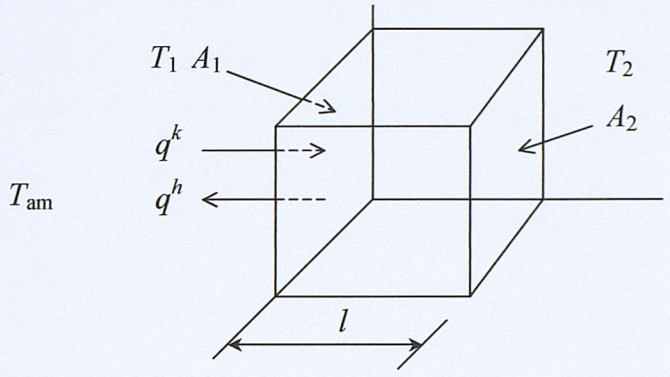

Fig. 3-9 Heat transfer of a volume $A * l$

Under transient conditions, Q^k depends also on time and the validity of approximation (Eqn. (3-6)) depends on the duration of the transient effect. The latter increases with l, for this reason a support plate of certain minimum thickness must be assumed. Fig. 3-10 shows the equivalent convection coefficient adopted initially (h^e_1) for the bottom plate surface in the FE model derived from Eqn. (3-5) based on conductivity variation (as shown in Fig. 3-6) with the support plate thickness assumed to be 100 mm. These values were changed to h^e_2 and h^e_3 to study its effect on the temperature and residual stress results, as detailed in Section 3.5.3.

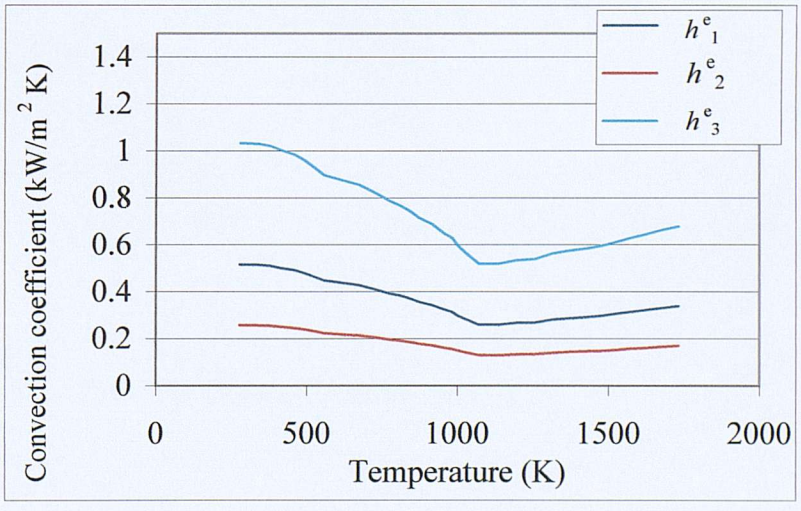

Fig. 3-10 Equivalent convection coefficient adopted in the FE model for the bottom surface of the weldment

As a summary, the FE model initially adopted enthalpy taken from Andersson et al.[16], conductivity and convection coefficient from Michaleris et al.[12], and emissivity from Brown and Song[17]. Values that are most different from those initially chosen within the range given in he literature for structural steels were used as well to study the sensitivity of temperature and residual stresses on these properties, as described in more detail in Section 3.5.

3.3.3 Stress analysis

A 2-D non-linear quasi-static stress analysis was subsequently conducted to calculate the welding-induced residual stresses. The thermal element (PLANE55) was converted to a plane strain element (PLANE42); this is easily achieved in ANSYS through a single element type change command. Thus, the mesh used in stress analysis was identical to that in the thermal analysis.

Temperature loading

The nodal temperature solutions obtained from the thermal analysis were read as loading into the stress analysis. In order to capture the residual stresses induced due to the heating and cooling cycle, the temperature history needed to be read at a sufficiently large number of time points, especially where the temperature gradient is large. The temperatures were read in load steps. However, the greater the number of the thermal solution steps used, the more the computational time and the larger the store space required. One way to improve efficiency is to identify the time points when the temperature gradient is low and remove some of the corresponding solution steps.

Temperature-dependent mechanical properties

As with thermal material properties, temperature-dependent mechanical properties have also been considered by researchers in this area. Some researchers[11,16,18] have also attempted to include the temperature history dependency by using different thermal expansion coefficient curves for heating and cooling. The Young's modulus and the stress-strain curve at room temperature are easy to obtain. Unfortunately,

uncertainties arise for these properties at high temperatures. In general, none of the researchers[2,4,11-21] working on FEM simulation of welding obtained experimentally temperature-dependent mechanical properties, especially at high temperatures.

A) Young's modulus

The Young's modulus at room temperature varies little with the composition of structural steel. It is expected that its value decreases with temperature and it becomes very small, almost zero when the steel is in its molten state. Fig. 3-11 shows the Young's modulus variation with temperature from various researchers. As expected, the value at room temperature varies from 200 to 210 MPa, and becomes close to zero at high temperatures. However, the rate of decrease adopted varies from one researcher to another. The rate of decrease is slow at relatively low temperatures in all cases. From about 600 K, the rate starts to increase. The main discrepancy is the temperature at which the Young's modulus decreases to a small value.

Several authors[12,15,17,18,27] obtained their data from some other sources, others[20] did not mention how and where their data were obtained. Andersson et al.[16] obtained his data from another source and a steel manufacturer. Efforts were made by him to obtain reliable material property data. In general, he is viewed as a reliable source. Karlsson and Josefson's[11] data were taken from another two sources which were based on several experimental investigations. Karlsson and Josefson[11] is another source that appears to be reliable and his values are close to those given by Andersson et al.[16]. Thus the values used by Andersson et al.[16] were adopted in this study.

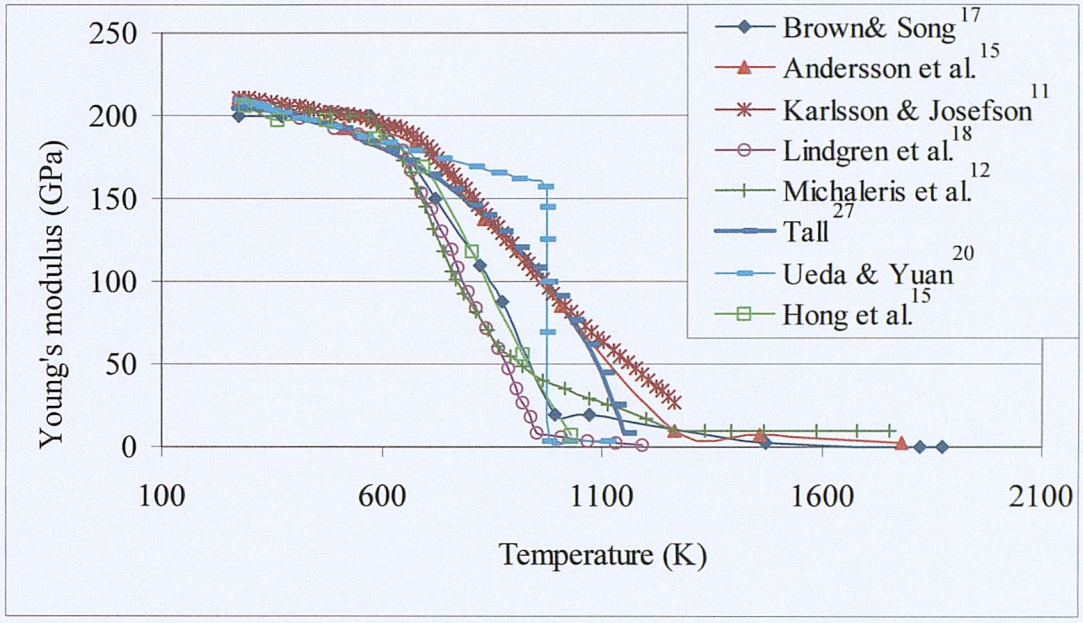

Fig. 3-11 Temperature-dependent Young's modulus from various sources

B) Thermal expansion coefficient/thermal dilatation

In the literature, some researchers[12,15,17] gave temperature dependent values of the thermal expansion coefficient, which normally do not account for the volume change due to phase change. Others[11,16,18,19,28] used temperature dependent thermal dilatation, ε^T, which normally includes the volume change due to phase change, and sometimes the temperature history dependency was included as well. The second group of researchers were mainly from Sweden. Touloukian[28] gave thermal dilatation data for steels with different carbon contents together with the reference temperature from experiments he reviewed. Fig. 3-12 shows the variation of thermal dilatation with temperature from various sources. The three sources which gave thermal expansion coefficient, α, directly are shown in Fig. 3-13. Thermal dilatation, ε^T, and thermal expansion coefficient, α, are related by

$$\alpha(T) = \varepsilon^T(T) / (T - T_{ref}) \qquad (3\text{-}9)$$

It is obvious that Lindgren et al.[18]'s thermal dilatation curve starts from 0 at 273 K, it was then converted to a coefficient based on a reference temperature of 293 K, $\alpha^{T_{ref}}(T)$, using

$$\alpha^{T_{ref}}(T) = \alpha^{T_0}(T) + \left(\frac{T_{ref} - T_0}{T - T_{ref}}\right)\left(\alpha^{T_0}(T) - \alpha^{T_0}(T_{ref})\right) \qquad (3\text{-}10)$$

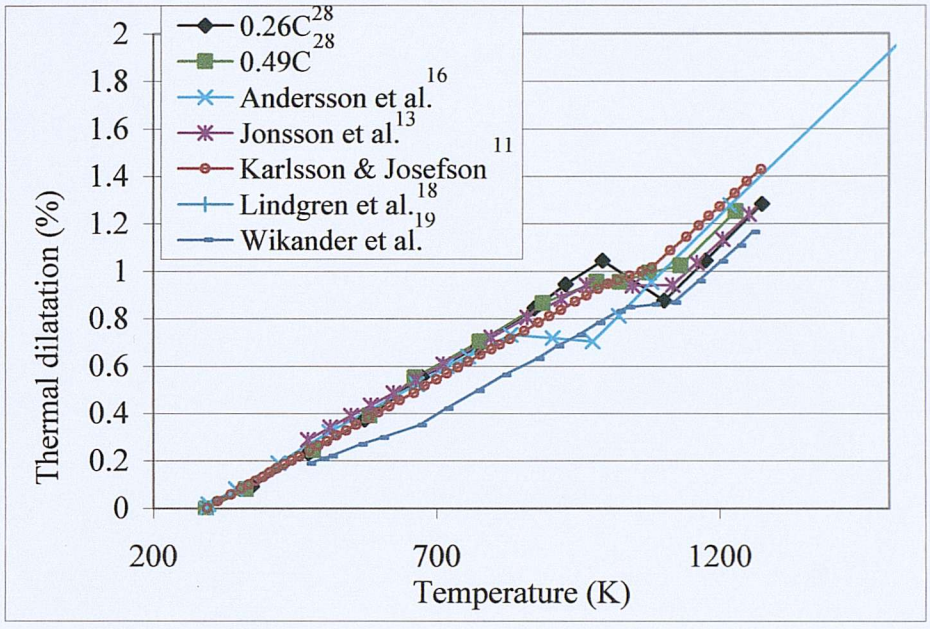

Fig. 3-12 Temperature-dependent thermal dilatation from various sources

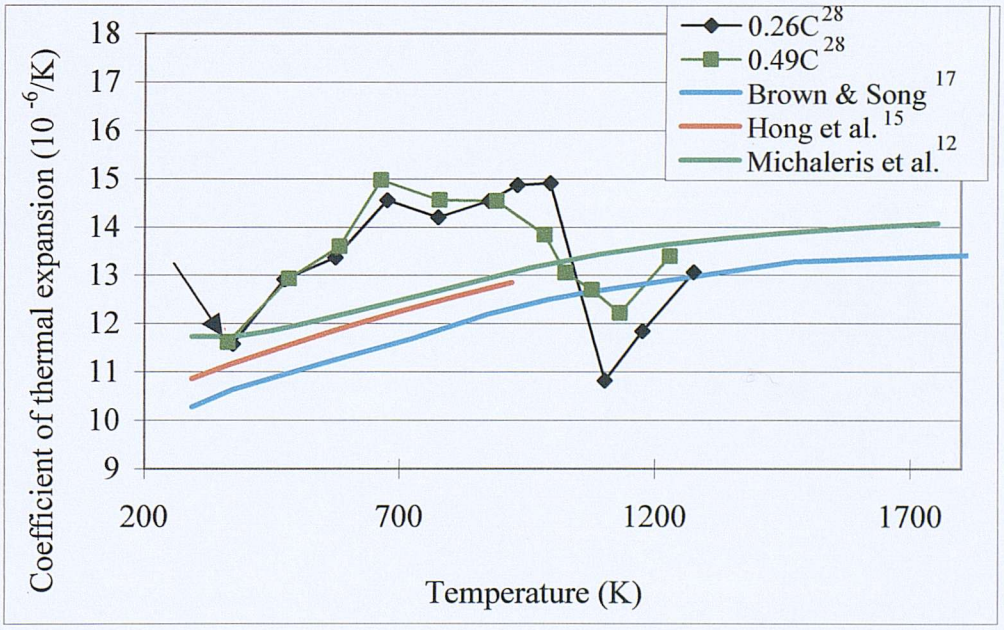

Fig. 3-13 Temperature-dependent coefficient of thermal expansion from various sources

Significant discrepancies are seen in Fig. 3-13. Certain authors[12,15,17] did not include the volume change due to phase change, and the thermal expansion coefficient show a similar increasing trend except that Michaleris et al.[12] used a constant value below 362 K (arrowed in Fig. 3-13). For comparison purpose, thermal expansion coefficient converted from the thermal dilatations given by Touloukian[28] for steels of 0.26 and 0.49 carbon content as labelled 0.26C and 0.49C are also plotted in Fig. 3-13. These two curves show a similar trend until a volume change occurs when the thermal expansion coefficient starts to decrease. They also show that chemical composition affects only slightly the magnitude of thermal expansion coefficient. Since the steel plate used in Rao and Tall[1]'s test is a structural steel which normally contains ≤ 0.26% carbon, the 0.26C curve is the closest one and was used for this study. Values from Andersson et al.[16] and Wikander et al.[19] which form the two boundaries of the ranges, as shown in Fig. 3-12, were used as well to study the effect of thermal expansion coefficient variation on residual stress results.

C) Yield strength

Yield strength is considered as the most important material property that affects the final residual stress results. Fig. 3-14 shows the yield strength variation with temperature used by various researchers. As expected the yield strength values at room temperature show significant differences as different types of steel have been used in these studies. Several researchers[15,17,19,27] used the same properties for both weld metal and base metal. A different yield strength was assigned to weld metal and base metal by the rest of those cited. As expected, the magnitude of yield strength decreases with increasing temperature. Most researchers used three different rates of decrease i.e., a relatively slow decrease from room temperature up to about 670 K, the strength then decreases faster to a small value at around 1000 K, and finally the strength decreases slowly again to a near zero value above the melting temperature. Although the yield strengths at room temperature differ from 248 to 461 MPa, the majority of values at a temperature around 1000 K vary within 10 to 40 MPa, and then decrease to a near zero value at the melting temperature. There is thus a clear consistent trend of how the yield strength varies with temperature, as can be seen in Fig. 3-15, where the normalised yield strength [$\sigma_Y(T)/\sigma_Y(T_{ref})$, where T_{ref} = 293 K]

variation with temperature has been plotted. Efforts have been made by Andersson et al.[16] to predict the yield strength variation from the CCT diagram. Karlsson and Josefson[11] and Wikander et al.[19] have also made an attempt to account for the temperature history-dependency by using different curves for heating and cooling.

Rao and Tall[1] conducted tensile tests on the base plate and weld metal at room temperature in order to obtain their yield strength. The average value from the test specimens listed for base plate was 244 MPa and 342.4 MPa for weld metal. It should be noted however, that the value for the weld metal was obtained from specimens consisting not entirely of the weld metal. The base plate steel used was ASTM A7, with a specified minimum yield strength of 228 MPa. The value obtained from the tensile tests conforms to this specification. The normalised Andersson et al.[16] and Jonsson et al.[13]'s curves were used as a basis for generating a variation with temperature for the base metal and weld metal yield strengths, as shown in Fig. 3-16. The effect of different yield strength-temperature relations on residual stress will be considered in Section 3.5.5.

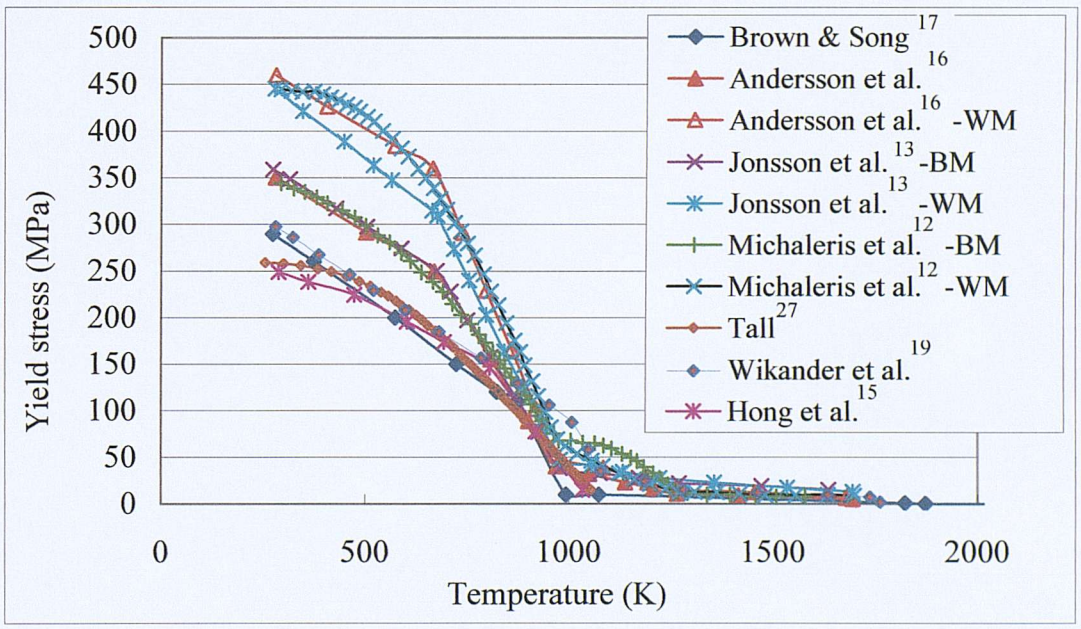

Fig. 3-14 Temperature-dependent yield strength from various sources

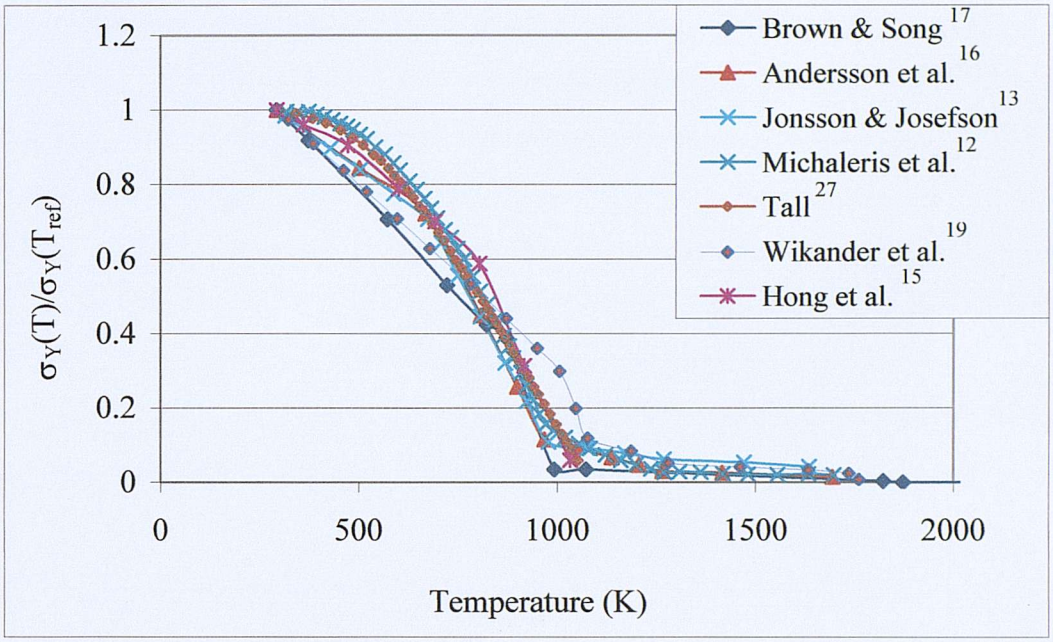

Fig. 3-15 Normalised yield strength variation with temperature

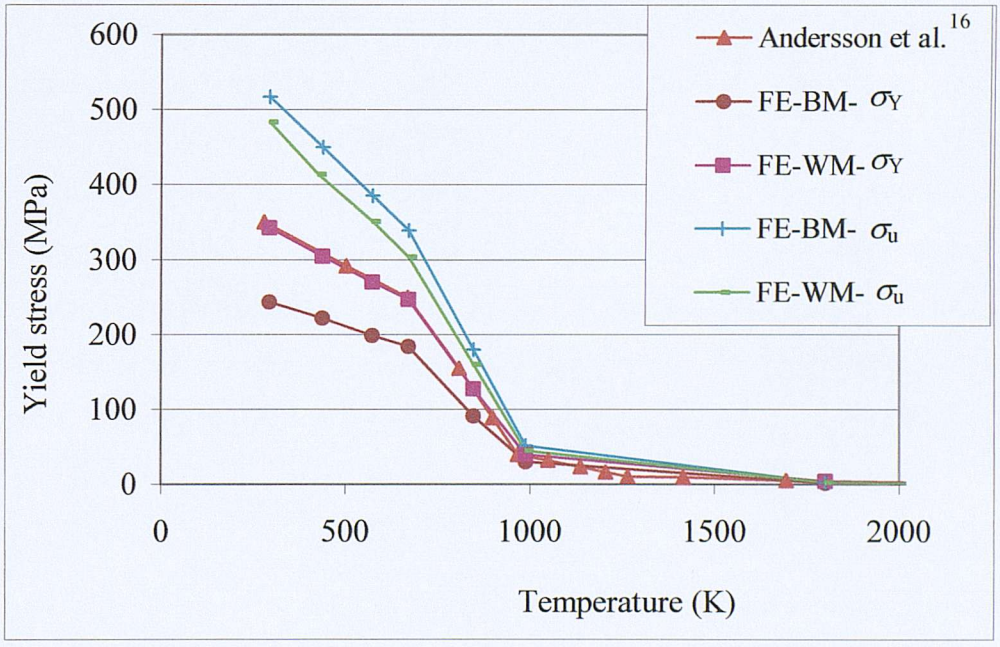

Fig. 3-16 Temperature-dependent yield strength used in the FE model

D) Strain hardening/Hardening modulus

Most researchers assumed isotropic strain hardening in their models except from Michaleris et al.[12] who adopted kinematic strain hardening. The material in and near the fusion zone experiences a cycle of compressive plastic strain and then tensile, it is thus more realistic to use kinematic strain hardening. Andersson et al.[16] actually believed that the discrepancies between his FE and experiment results was mainly due to this Bauschinger effect not accounted for. In this study, kinematic strain hardening was adopted. To avoid numerical difficulties as well as to model the stress-strain curves more closely, multi-linear strain hardening was applied to both base metal and weld metal.

The ultimate strength of base metal and weld metal was not given by Rao and Tall[1]. Through literature search, the ultimate strength of the base metal was found to be within 410-500 MPa for ASTM A7 steel[29]. A value of 450 MPa, which is somewhere in the middle of the given range was initially assumed in this study and the corresponding strain at this value was assumed to be 15%. Test results from Lincoln Electric[30] show that the ultimate strength of the same electrode used by Rao and Tall[1] varies in the range 414-538 MPa. The ultimate strength of the weld metal was thus first assumed to be 440 MPa at a strain value of 12%. The variation of ultimate strength with temperature was assumed to have a similar trend to that of yield strength, accounting for the effect of a decreasing hardening modulus suggested by other researchers. Fig. 3-17 and Fig. 3-18 show the true stress-logarithmic strain curves with reference to temperature for the base metal and weld metal, respectively. Models with different values of ultimate strength for both the base metal and weld metal were also analysed to study its effect on the final residual stress results.

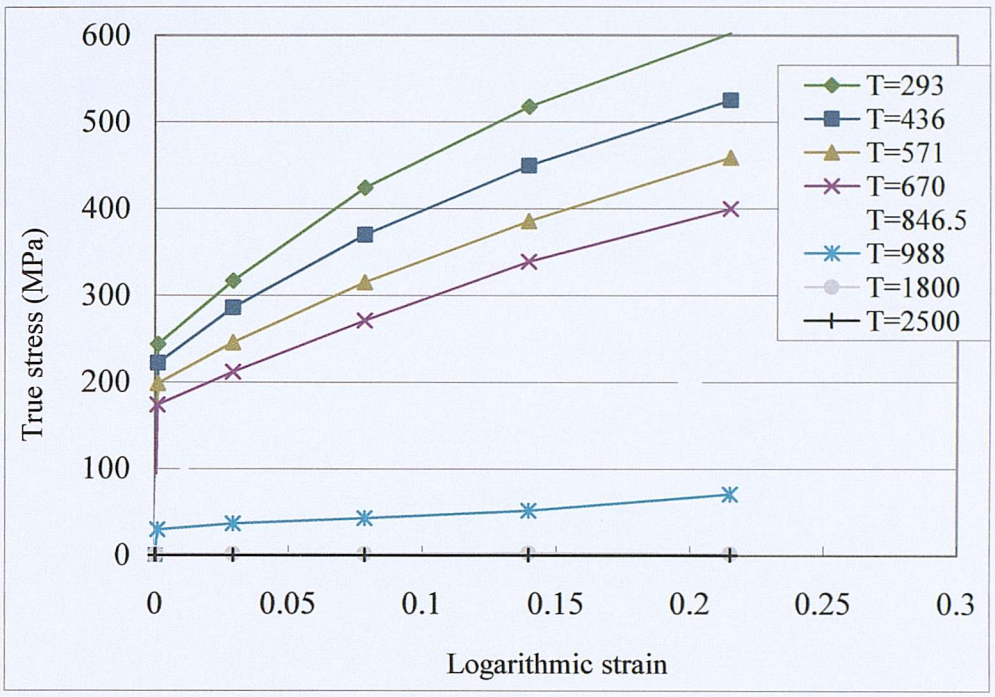

Fig. 3-17 The adopted true stress – logarithmic strain curves for the base metal at various temperatures

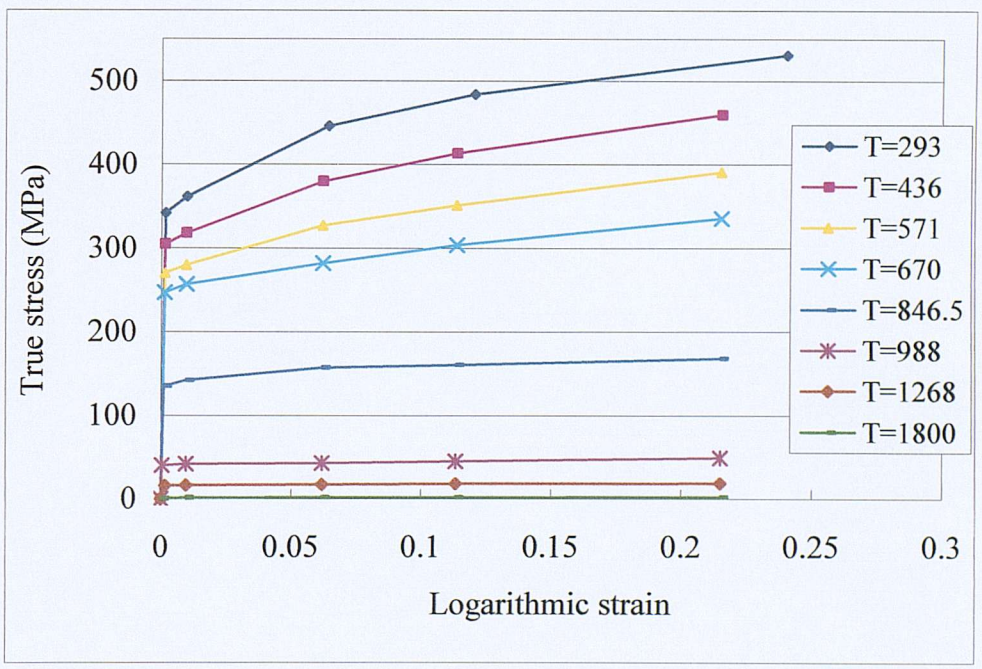

Fig. 3-18 The adopted true stress – logarithmic strain curves for the weld metal at various temperatures

Boundary conditions

Symmetry constraint was applied to the symmetric line (shown by the dotted line in Fig. 3-1). The middle point on the bottom surface of the weld area was vertically fixed to prevent rigid body movement. The plates were actually clamped during welding but this constraint was applied at a later stage.

3.4 Results and discussion

3.4.1 Temperature development

The temperature history at Point A on the top surface of the plate, 1.2 mm to the left of the weld toe (Fig. 3-1), is shown in Fig. 3-19.

It can be seen that temperature increased rapidly during heating and cooled down relatively slowly at lower temperatures.

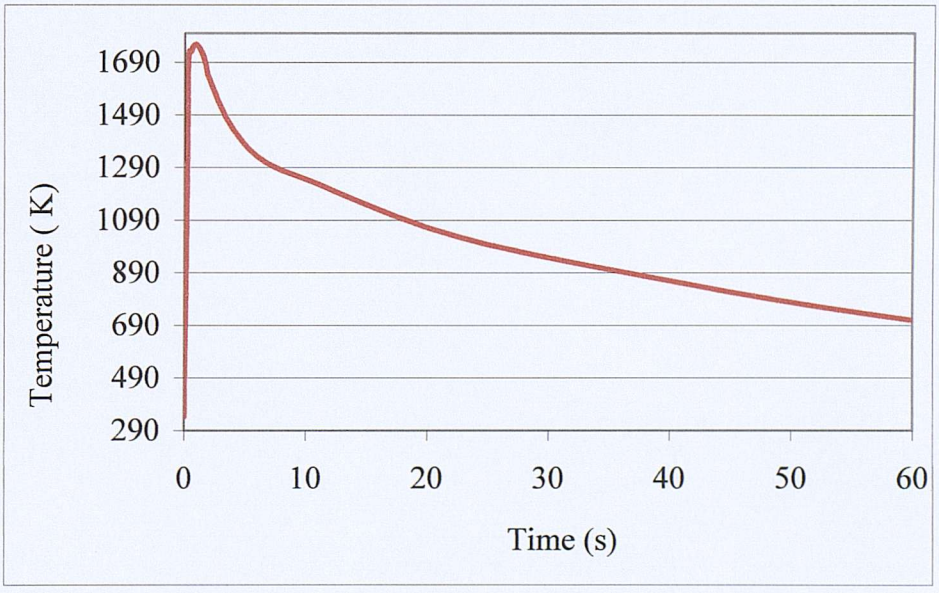

Fig. 3-19 Temperature history at Point A (see Fig. 3-1)

Mesh sensitivity study

Fig. 3-20 shows the sensitivity of the temperature result at the weld centre on the top surface at time $t_1 + t_2$ (see Fig. 3-3) to element sizes in terms of the number of line

divisions, n_3. The results start to converge from Mesh3 with the temperature difference between Mesh3 and Mesh5 being only 0.14%. The size used in Mesh3 for elements in and around the weld area is thus considered to be satisfactory.

The resulting temperature history at Point M on the top surface in the base metal (see Fig. 3-1), 63.5 mm away from the weld centre, which is five times the plate thickness, is shown in Fig. 3-21 for Mesh1 to Mesh5. The temperature histories obtained from the five meshes are very close so that the larger element size in the left end is considered to be sufficient.

Mesh3 can also be seen to be satisfactory from Fig. 3-22, the contour plot of the temperature distribution at the end of heat input step (t_1 + t_2+ t_3, see Fig. 3-3) obtained from Mesh3 and Mesh5.

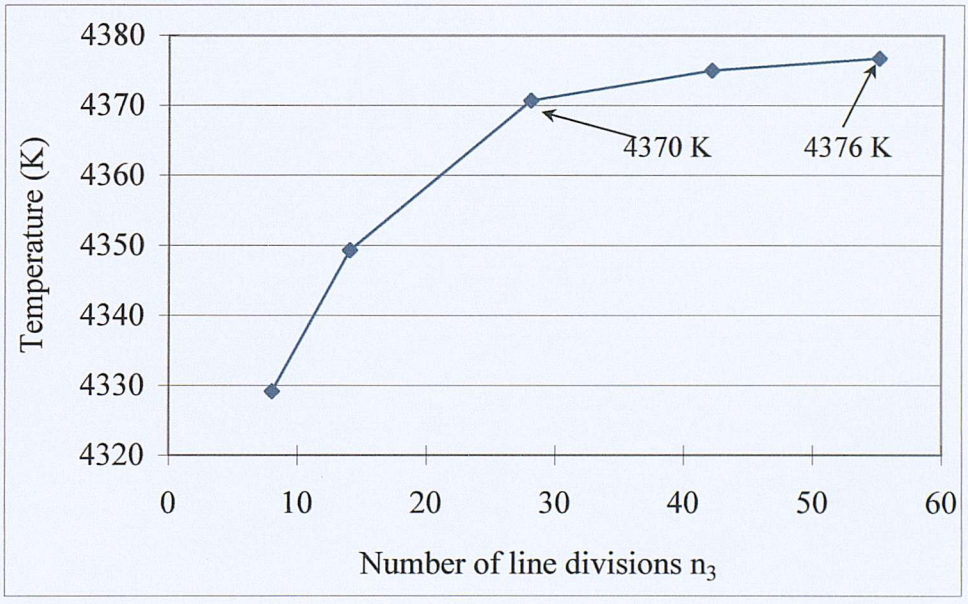

Fig. 3-20 Temperature at the weld centre on the top surface at time (t_1 + t_2) for Mesh 1 - Mesh 5

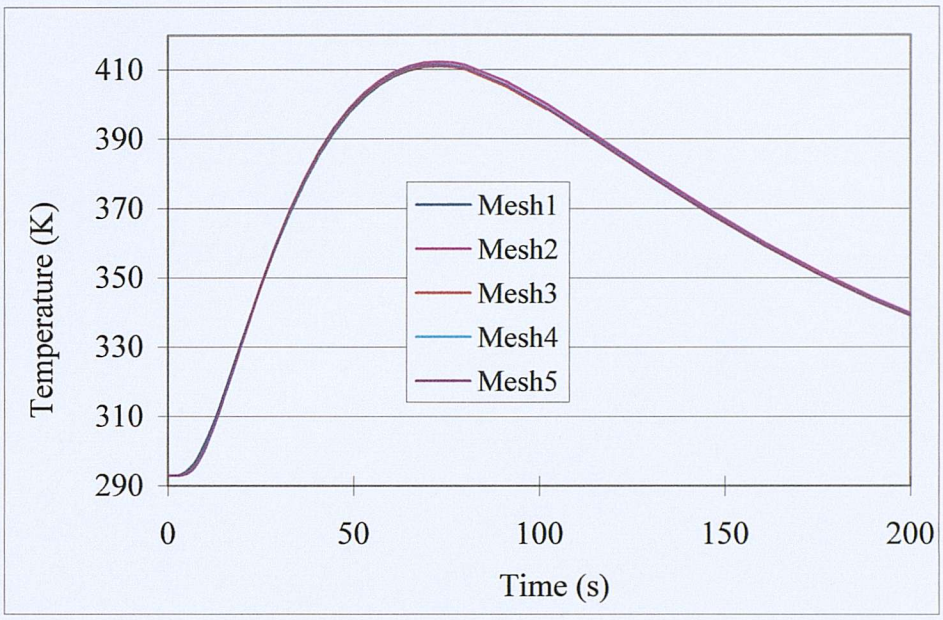

Fig. 3-21 Temperature history at Point M (see Fig. 3-1) on the top surface

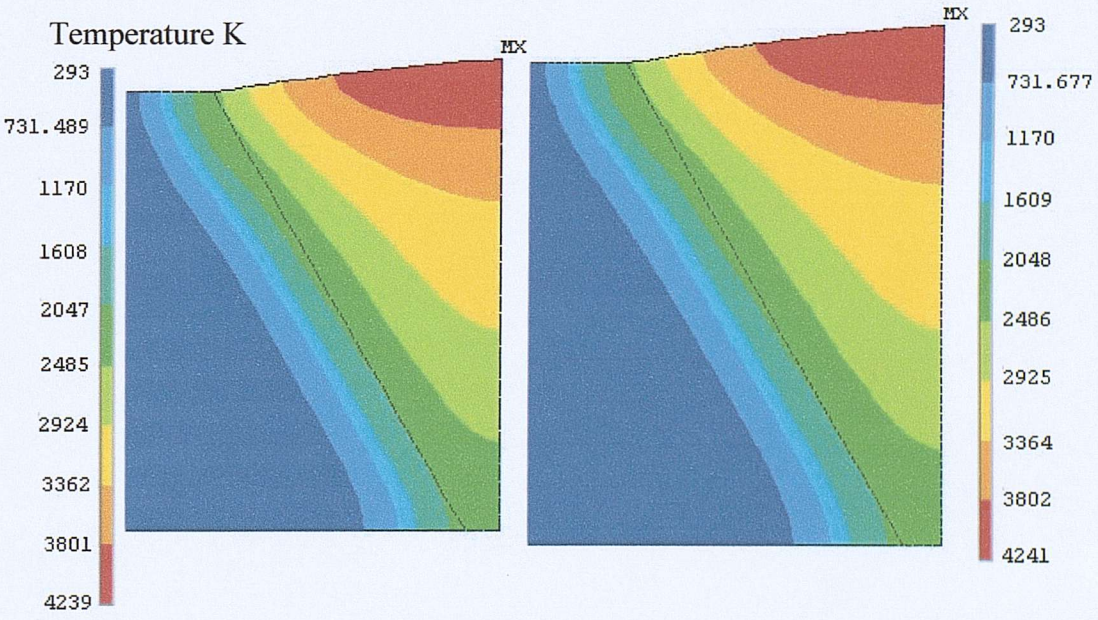

(a) Mesh3 (b) Mesh5

Fig. 3-22 Temperature distribution at time $t_1 + t_2 + t_3$ (see Fig. 3-3)

3.4.2 Longitudinal residual stress distribution

Welding induced residual stresses are in self-equilibrium. To take into account the over-constraint imposed by the plane strain condition assumed in the FEM analysis, the mean stress σ_z^m over the cross section normal to z-axis is calculated from

$$\sigma_z{}^{m} = \frac{\sum_{n=1}^{N^e} \sigma_z^n A^n}{\sum_{n=1}^{N^e} A^n} \tag{3-11}$$

where N^e is the total number of elements; σ_z^n the longitudinal stress of element n; A^n the area of element n. Then, the mean stress was deducted from the longitudinal residual stresses obtained directly from the FE model. In reality the plane studied moves in the longitudinal direction and non-uniform out-of-plane deformation may also occur. Generalised plain strain allows this out-of-plane rigid body motion to be accounted for, which unfortunately was not available in the current ANSYS version. A 3-D model is able to account for the full deformation of the plane, however, the complexity of the modelling process and computational time will increase significantly.

Fig. 3-23 and Fig. 3-24 show the variation of the longitudinal residual stress, σ_z, i.e. the stress in the direction of welding, as a function of the x-coordinate over the top and bottom surfaces, predicted by the FE analysis as well as the values obtained from experiment by Rao and Tall[1]. The pink curve labelled FEM-modified was obtained by deducting the mean stress $\sigma_z{}^{m}$ over the cross section area calculated from Eqn. (3-11)

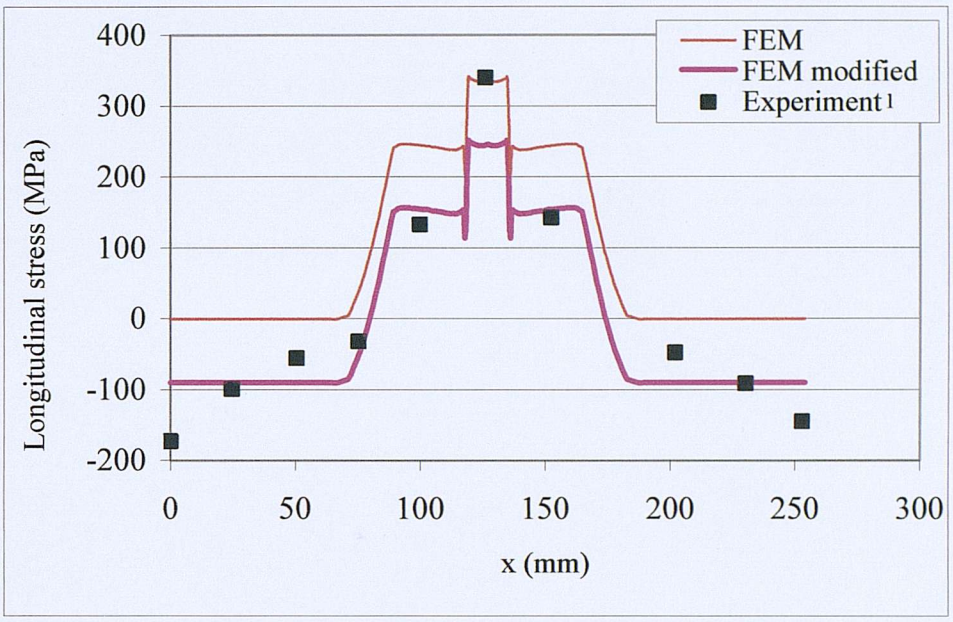

Fig. 3-23 Longitudinal residual stress (σ_Z) distribution along the top surface

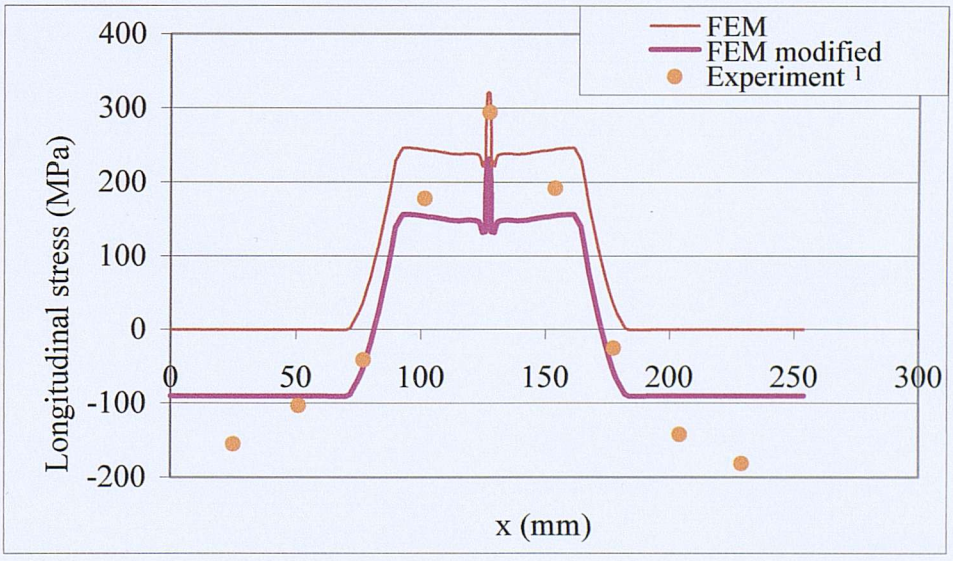

Fig. 3-24 Longitudinal residual stress (σ_Z) distribution along the bottom surface

Sensitivity to mesh refinement

As stress analysis is very time consuming, it was performed for Mesh3 and Mesh4 only using the initially chosen material property parameters and the resulting longitudinal residual stress (σ_z) distribution along the top and bottom surfaces was compared to study the efficiency of Mesh3. As shown in Fig. 3-25, the difference between these two meshes is negligible. Mesh3 thus proved to be adequate for this analysis.

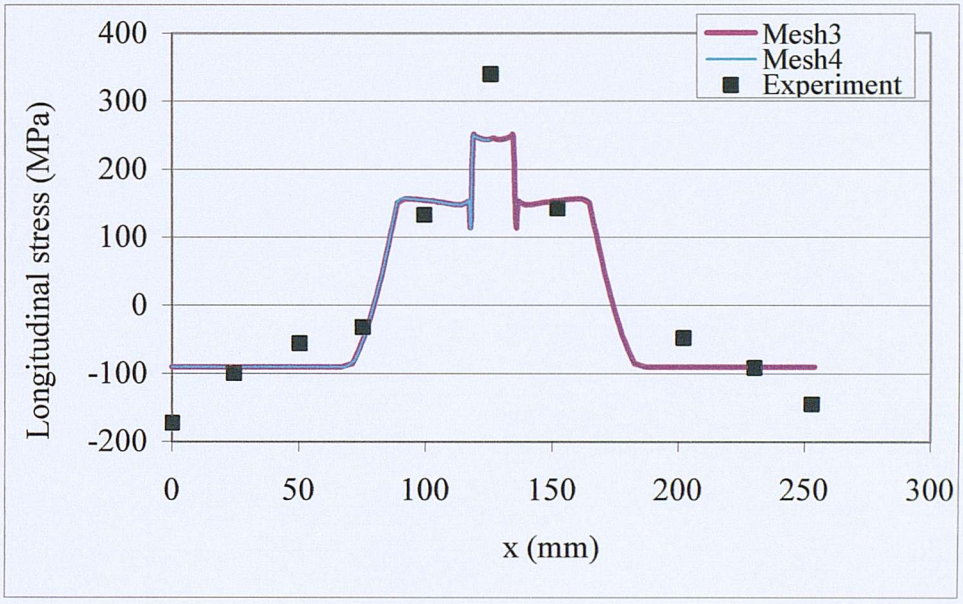

Fig. 3-25 Longitudinal residual stress (σ_z) distribution obtained for Mesh3 and Mesh4

Fig. 3-23 and Fig. 3-25 show that there is qualitative agreement between analytical and experimental results. The longitudinal residual stress is seen to be tensile in and near the weld metal and compressive away from it. The discontinuity at the weld metal and base metal boundary can be attributed to the sudden change of material properties assigned to the two areas. In a real specimen however, this change is expected to be gradual, hence the stress variation would be smooth. The FE model with the initially assumed material properties and amount of heat input predicted a lower value of the maximum tensile stress in the weld and the compressive stress

near the end of the plate. As discussed in Chapter 2, Section 2.4.1, additional plastic strain may be produced at the edge of the hole or section in the sectioning or hole drilling methods, which results in higher residual stress measured. Another possible reason is that the plate before welding was not totally stress free from manufacturing, as suggested by Rao and Tall[1]. This part of residual stress from manufacturing cannot be simply subtracted though, as the heating and cooling cycles applied by the welding process may release some of the residual stress in certain positions while in some other positions increase it. It should also be noted that in the experiment the plates to be welded were constrained rather than the free-to-deform condition assumed in the FEM simulation. Uncertainties from the assumed material properties could also have a significant effect on the accuracy of the predicted residual stress results. A parametric study was then carried out to study the effect of variation of material properties, heat input, and boundary conditions on the temperature and longitudinal residual stress results.

3.5 Parametric studies

A very useful feature of ANSYS is the provision of a tool called ANSYS Parametric Design Language (APDL) that enables users to change selected input values very easily and then run their program with the new values. In this study, the input file was written using APDL to represent certain parameters, in order to assess their effect on the final residual stress results. Appendix I lists certain important parts of the input file written using APDL for this model.

3.5.1 Heat input variation

Effect on temperature development

Variable heat input was used to study the effect of its magnitude on temperature development. This was achieved by changing the value of the arc efficiency, η_a, to the two limit values for metal-arc welding, i.e., 0.66 and 0.85, as suggested in the literature[5,14]. Fig. 3-26 and Fig. 3-27 show the temperature histories at the weld centre and at Point M, respectively. The maximum temperature at the weld centre increased by about 16% when the arc efficiency changed by 13% and decreased by

about 14.5% when η_a decreased by 12%. For the maximum temperature at Point M, the corresponding changes are 3% in both cases. Therefore, variation in the amount of heat input within the given empirical range has a significant effect on temperature development in the weld area.

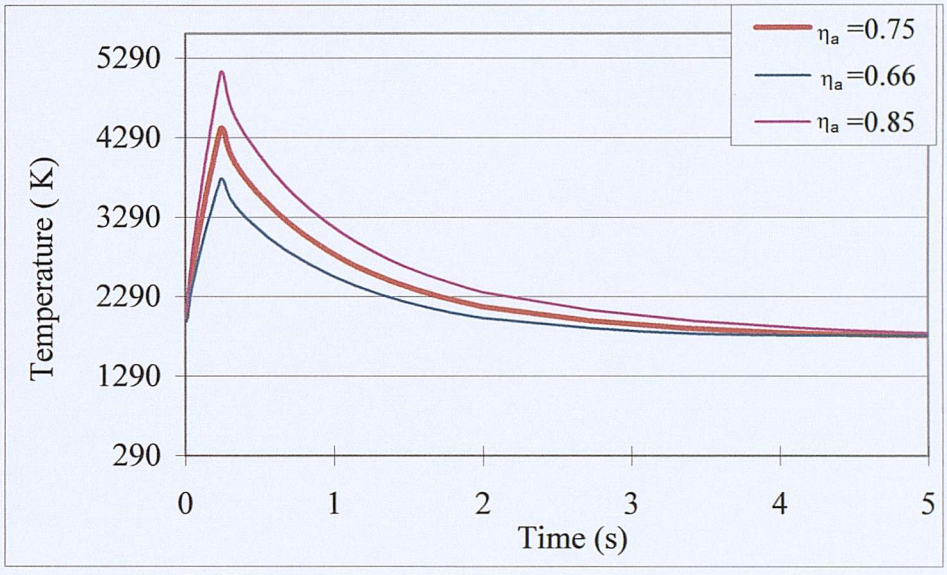

Fig. 3-26 Effect of heat input amount on the temperature history at weld centre

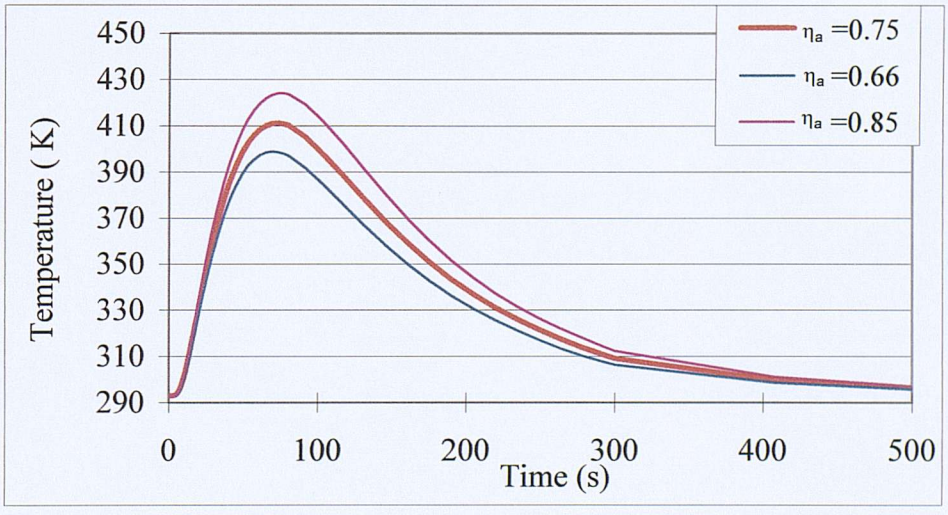

Fig. 3-27 Effect of heat input amount on the temperature history at Point M (see Fig. 3-1)

Effect on longitudinal residual stress distribution

Fig. 3-28 shows the longitudinal residual stress distribution along the top surface for different amounts of heat input. Reducing the heat input amount by 12% increased slightly the magnitude of the tensile residual stress by 1.1% and at the same time reduced the extent of the tensile region slightly.

It can be seen from this study that although the amount of heat input affects significantly the temperature development in the weld area, the resulting longitudinal residual stress is not affected significantly. The reason may be that the formation of residual stress is more affected by the temperature gradient between adjacent areas. This agrees with the conclusion draw by Hong et al.[15]. They studied the effect of heat input on the final residual stress results of a butt welded pipe by varying the arc efficiency from 0.62 to as high as an unrealistic value of 1.08 and found that the predicted residual stress results were not sensitive to the amount of heat input. Based on the parametric study on arc efficiency presented above, as long as the type of welding process is specified, the value of arc efficiency can be selected almost arbitrarily from within the range given for that type of welding process without concern about any significant inaccuracy in the results.

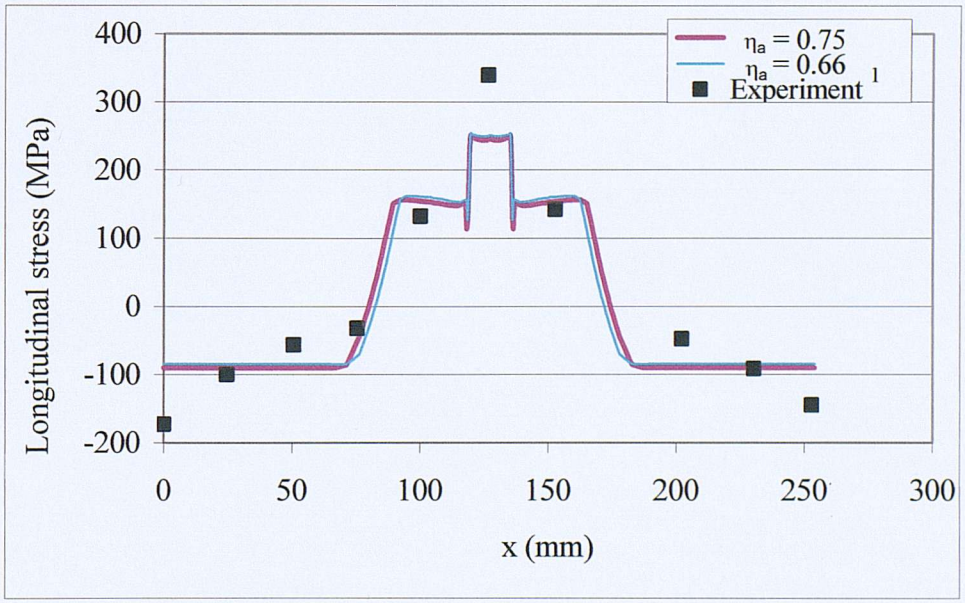

Fig. 3-28 Effect of heat input amount on longitudinal residual stress (σ_Z) distribution along the top surface

3.5.2 Thermal properties variation

A) Conductivity

Effect on temperature history

As discussed in Section 3.3.2, the conductivity values given by Andersson et al.[16] were also used to study its effect on the temperature development. As shown in Fig. 3-6, the maximum difference between the conductivity values used by Andersson et al.[16] and those given by Michaleris et al.[16] was 27.5% at room temperature. Fig. 3-29 and Fig. 3-30 show the temperature histories at Point A and Point M (see Fig. 3-1) obtained from models using conductivity values from Michaleris et al.[12] (k_1) and Andersson et al.[16] (k_2), respectively.

The maximum temperature at Point A increased by about 10% as a result of the higher conductivity at high temperature used by Andersson et al.[16]. However, at Point M (Fig. 3-30) the maximum temperature was 1.4% lower when using Andersson et al.[16]'s data (k_2) and the cooling rate was slightly greater. This is expected as the conductivity k_2 is smaller than k_1 at low temperatures.

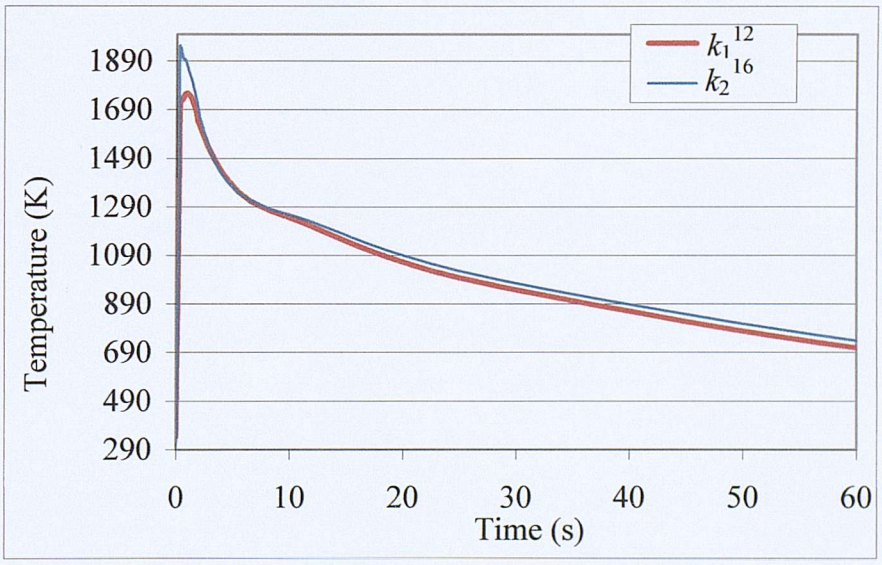

Fig. 3-29 Effect of conductivity variation on temperature history at Point A (see Fig. 3-1)

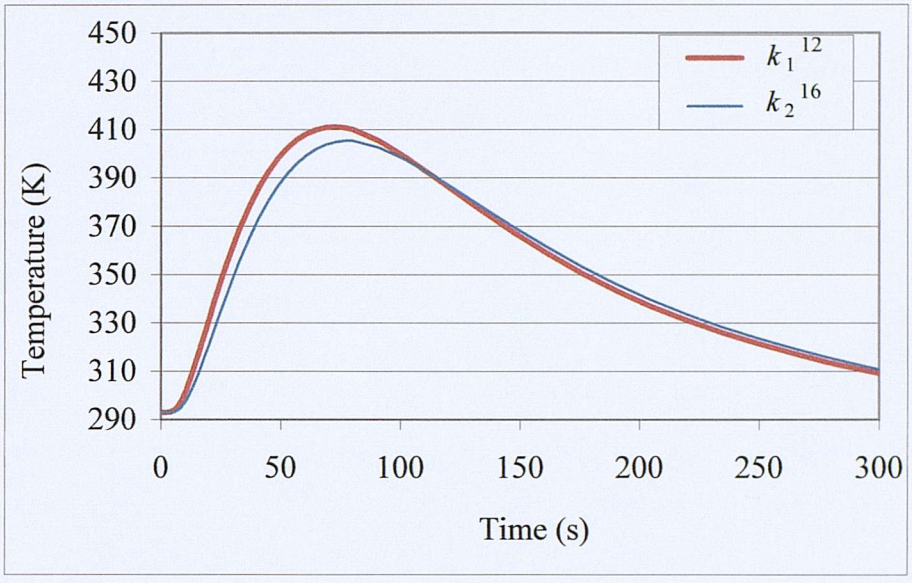

Fig. 3-30 Effect of conductivity variation on temperature history at Point M (see Fig. 3-1)

Effect on longitudinal residual stress distribution

The stress analysis results for the two conductivity inputs, k_1 and k_2, were compared and little effect on the magnitude and distribution of the longitudinal residual stress was found. Comparing Fig. 3-29 and Fig. 3-30 to Fig. 3-26 and Fig. 3-27, the effect of conductivity variation is seen to have no more significant effect on the temperature development than the amount of heat input. It is thus expected that the effect of conductivity would not affect the longitudinal residual stress significantly.

3.5.3 Variation of boundary conditions

A) Convection coefficient

The temperature-dependent convection coefficient used by Ueda and Yuan[20] (h_2) was adopted and results compared with those obtained by using the convection coefficient given by Michaleris et al.[12] (h_1). As shown in Fig. 3-7, the maximum difference between h_2 and h_1, below temperature 1050 K, is around 70% and h_2 is greater than h_1 by around 10% above this temperature. There is no noticeable

difference in the corresponding temperature histories at the weld centre and Point A. It can thus be concluded that the choice of convection coefficient within the range given in the works cited excluding those combined with radiation, as shown in Fig. 3-7, has little effect on temperature development. In this study, the effect of radiation on the temperature development was studied separately and presented in more detail in the following section.

B) Radiation

Radiation was considered using the temperature-dependent emissivity given by Brown and Song[17] as shown in Fig. 3-8. Fig. 3-31 and Fig. 3-32 show the effect of radiation on the temperature history at Point A and Point M, respectively.

Including the radiation heat loss decreases the magnitude of temperature by about 2% at Point A and about 1.2% at Point M and increases the cooling rate slightly as well.

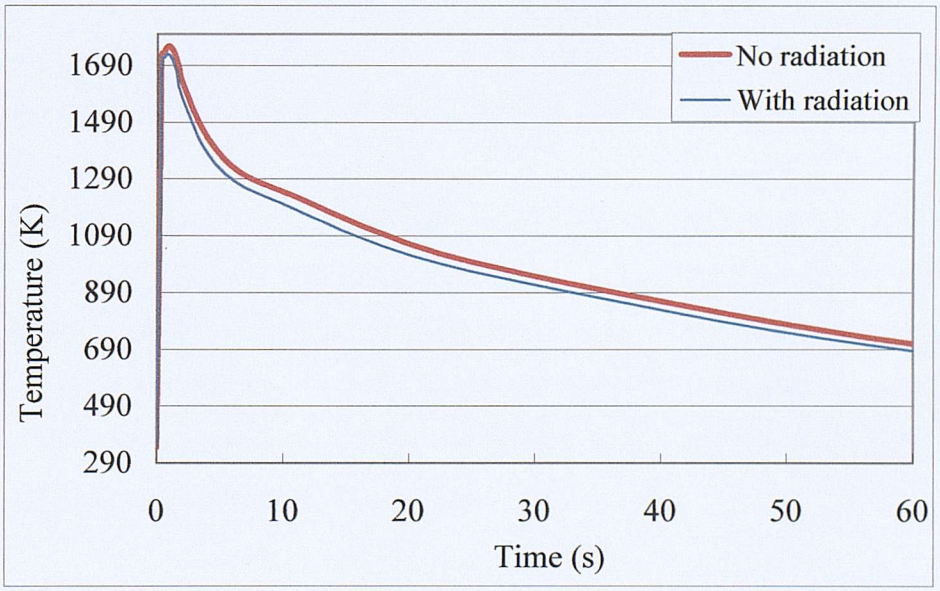

Fig. 3-31 Effect of radiation on the temperature history at Point A (see Fig. 3-1)

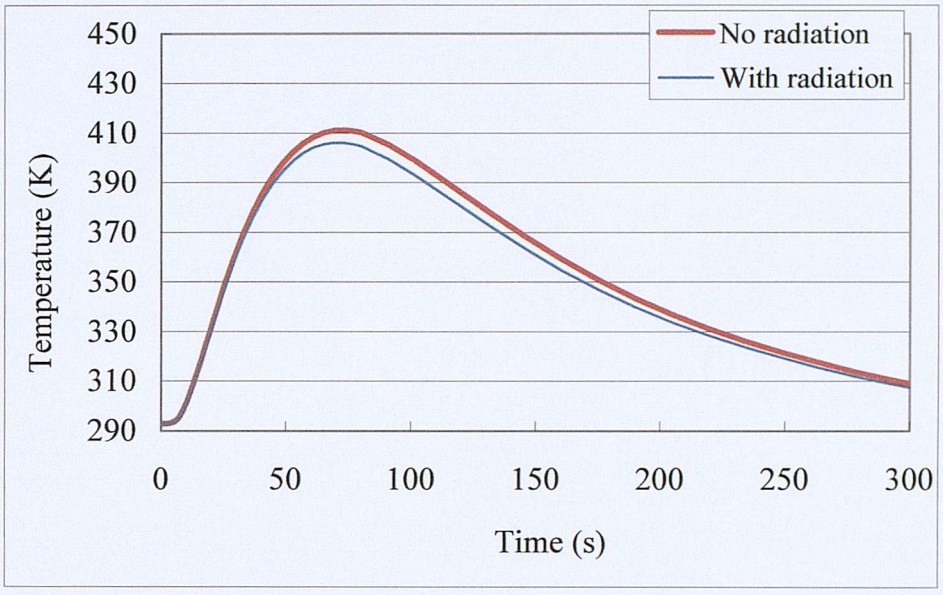

Fig. 3-32 Effect of radiation on the temperature history at Point M (see Fig. 3-1)

Comparing Fig. 3-29 to Fig. 3-32, the effect of convection and radiation are seen to have no more significant effect on the temperature development than the conductivity. It is thus expected that the effect of convection and radiation would not affect the longitudinal residual stress significantly.

It can be concluded from the above discussion that variations in the temperature-dependent thermal material properties and boundary conditions affect the temperature development, however, their effect on the final residual stress results is not significant for the range of values considered. To simplify the modelling process and to save computational time, radiation can be ignored as its effect on the final residual stress results is insignificant.

C) Variation of heat loss from the plate bottom surface

Effect on temperature development

As discussed in Section 3.3.2, the heat loss from the bottom surface was initially represented by assuming a convection coefficient causing equivalent heat loss as that

through conduction through an underneath steel column of effective thickness 100 mm. As no clear details are available on the support geometry of the steel column used in the experiment, two alternative convection curves h^e_2 and h^e_3, as shown in Fig. 3-10, were also used to study the effect of such variation on both the temperature and residual stress results. Fig. 3-33 and Fig. 3-34 show the effect of changing the heat loss from the bottom surface on the temperature history at Point A and M, respectively.

The magnitude of the bottom surface convection coefficient showed little effect on the maximum temperature near and within the weld area. However, the cooling rate was affected. A more significant difference was seen further away from the weld area. As shown in Fig. 3-34, the maximum temperature at Point M increased by about 9% when the equivalent convection coefficient decreased by 50% from h^e_1 to h^e_2.

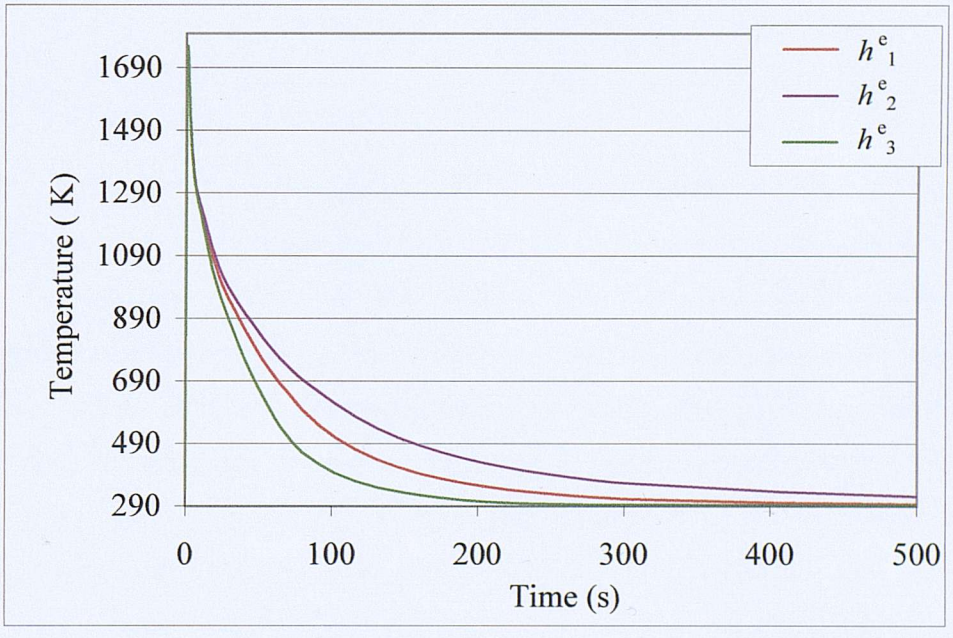

Fig. 3-33 Effect of bottom surface convection coefficient on temperature history at Point A (see Fig. 3-1)

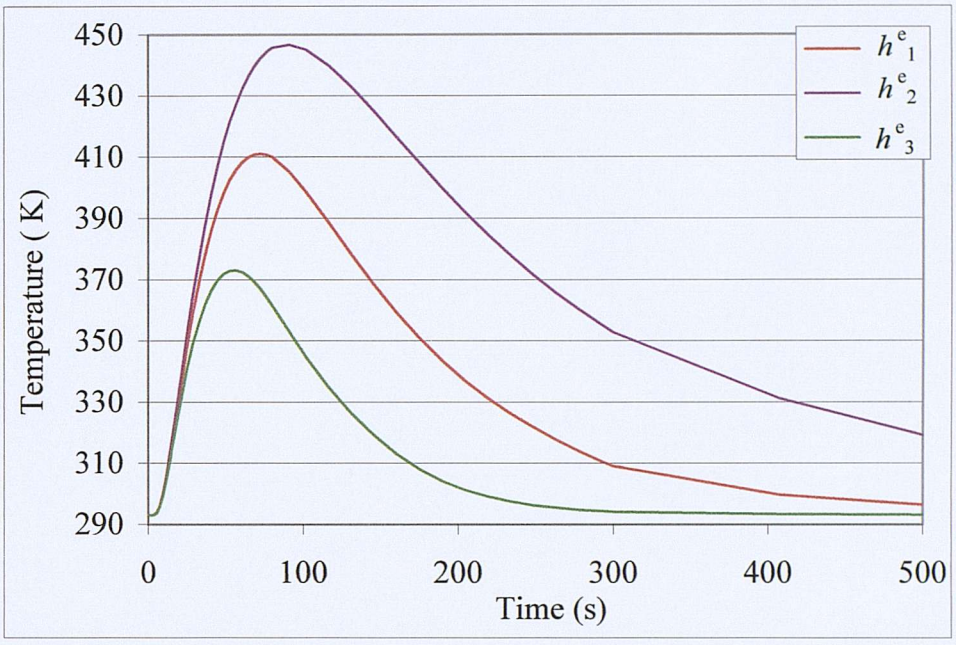

Fig. 3-34 Effect of bottom surface convection coefficient on temperature history at Point M (see Fig. 3-1)

On longitudinal residual stress distribution

Fig. 3-35 shows the longitudinal residual stress distribution along the top surface. It can be seen that the magnitude of maximum tensile stress increases with increasing cooling rate. The width of the tensile range was decreased. The longitudinal residual stress results obtained from the model with free surface convection (h_1) applied to the plate bottom surface is also plotted in Fig. 3-35. The maximum tensile residual stress in the weld area obtained from the model applying convection coefficient h_1 to the plate bottom surface is 54% lower than that from the model using h^e_1 while the maximum compressive stress away from the weld decreased by 61.5%. It is therefore important to model the boundary conditions as close to reality as possible.

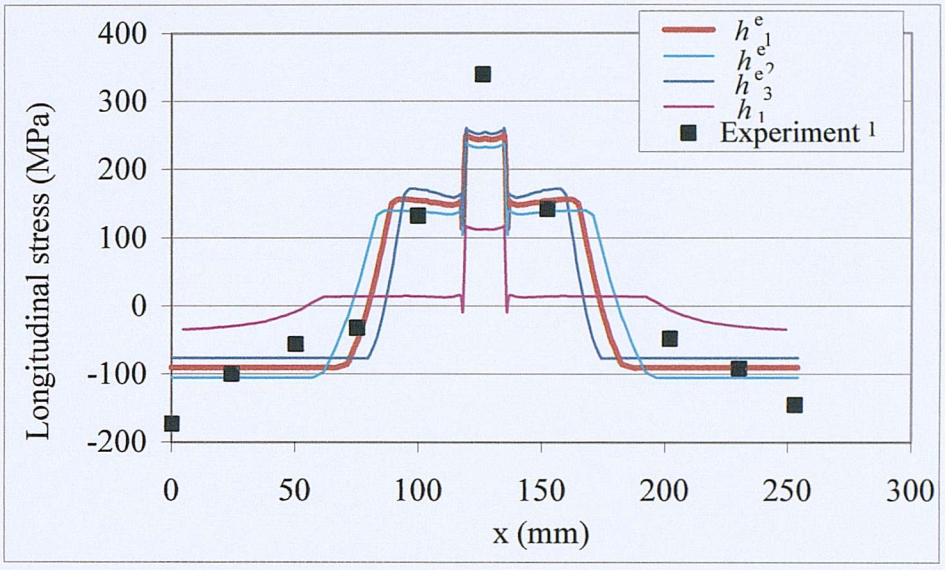

Fig. 3-35 Effect of heat loss through the bottom surface on longitudinal residual stress (σ_Z) distribution along the top surface

3.5.4 Variation of thermal expansion coefficient

As discussed in Section 3.3.3, in addition to the data obtained from Touloukian[28] labelled α_1, the thermal expansion coefficient values given by Andersson et al.[16] (α_2) and Wikander et al.[19] (α_3) were also used to study the effect of its variation on the residual stress results. As shown in Fig. 3-12, the maximum difference between α_2 and α_1 is about 33% below temperature 1100 K and α_2 is greater than α_1 by 9% above this temperature. The maximum difference between α_3 and α_1 is 26%. Fig. 3-36 shows the longitudinal residual stress distribution from the three curves of thermal dilatation used, which are shown in Fig. 3-12. The maximum tensile stress decreased by about 3.1% and the tensile region increased when the thermal dilatation values α_2 were used. The residual stress predictions obtained using the thermal expansion coefficients α_1 and α_3 were very similar.

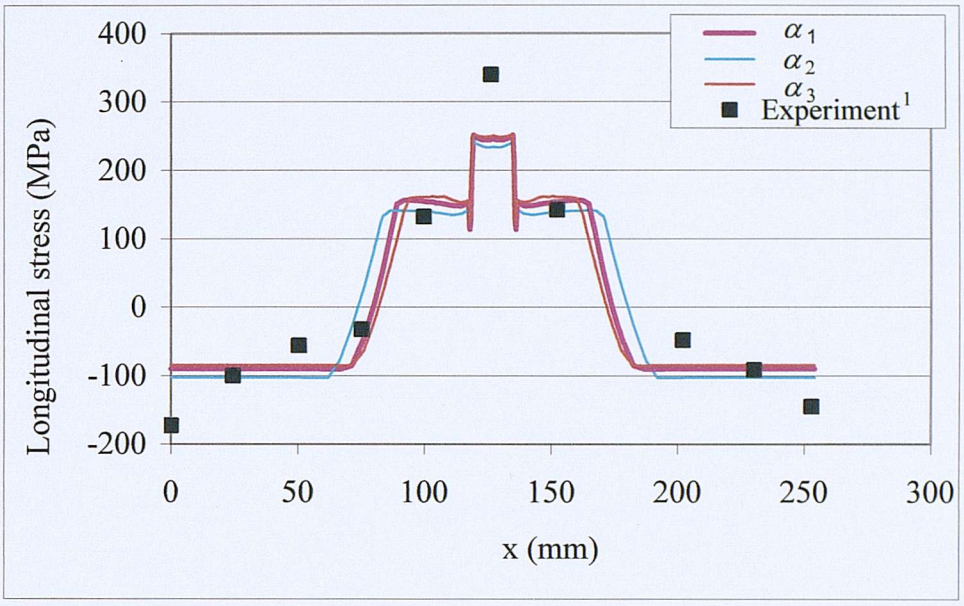

Fig. 3-36 Effect of thermal expansion coefficient on longitudinal residual stress (σ_Z) distribution along the top surface

3.5.5 Effect of yield strength

Fig. 3-37 shows the different base metal yield stress versus temperature relationships used as input to the FE model. The yield stress of the weld metal was varied in a similar way. The room temperature yield stress in data σ_Y(T)-2, 3, and 4 was 30% greater than that in model σ_Y(T)-1. It should be noted that this amount of increase in yield strength is only intended for the purpose of studying the quantitative effect of yield strength on residual stresses.

Fig. 3-38 illustrates the residual stress results from the FE models with the yield-temperature relationships shown in Fig. 3-37.

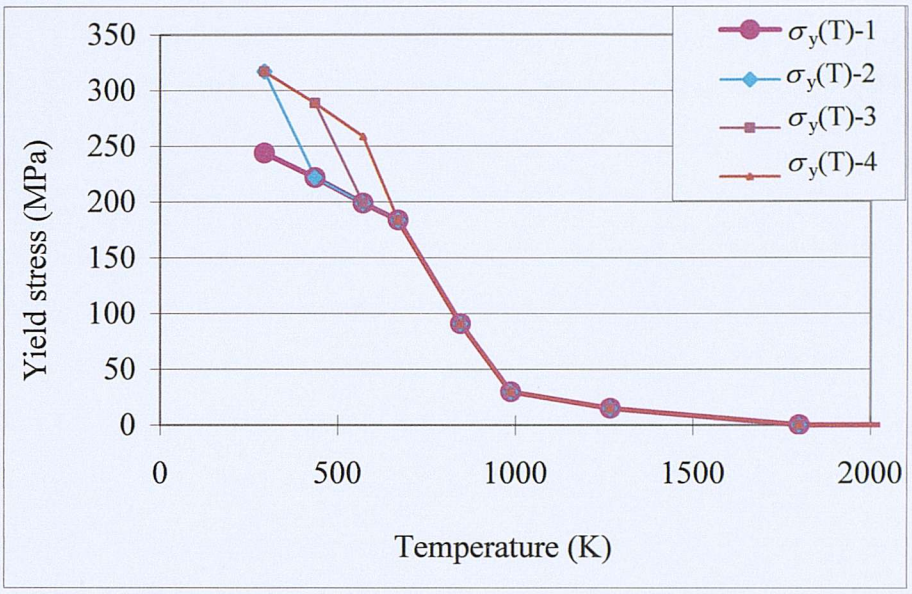

Fig. 3-37 BM yield strength-temperature variations studied

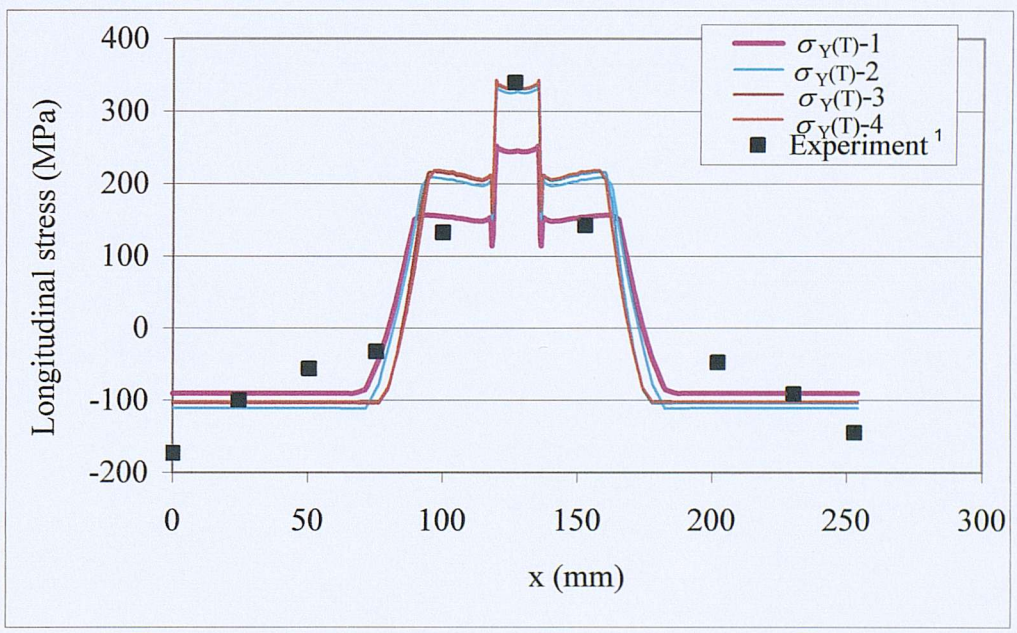

Fig. 3-38 Effect of yield strength on longitudinal residual stress (σ_Z) distribution

Fig. 3-38 clearly shows that changing the yield stress at room temperature has the most significant effect on the magnitude of tensile longitudinal residual stress among all parameters studied previously. Increasing the yield strength at room temperature by 30% results in an approximate 33% increase in the maximum longitudinal residual stress in the weld area. However, the increase in the compressive stress away from the weld area is somewhat less (23%). In general, the residual stresses increase with increasing yield strength at various temperatures, but yield strength variation at higher temperatures has much less effect.

3.5.6 Effect of ultimate strength

The ultimate strength of the base metal and weld metal is another uncertainty in this study as no values were quoted for the steel whose residual stresses were experimentally determined. The ultimate strength was assumed to be 20% higher than the initially assumed values while keeping the yield strength unchanged. The value of 20% was chosen because at the specified room temperature, the ultimate strength for the structural steel used varies within 20% from 410 to 500 MPa.

Fig. 3-39 shows the longitudinal residual stress distribution along the top surface obtained from the model using the initially assumed ultimate strength (σ_u-1) and the 20% higher values (σ_u-2). The maximum tensile residual stress in the weld area is seen to increase by 12%.

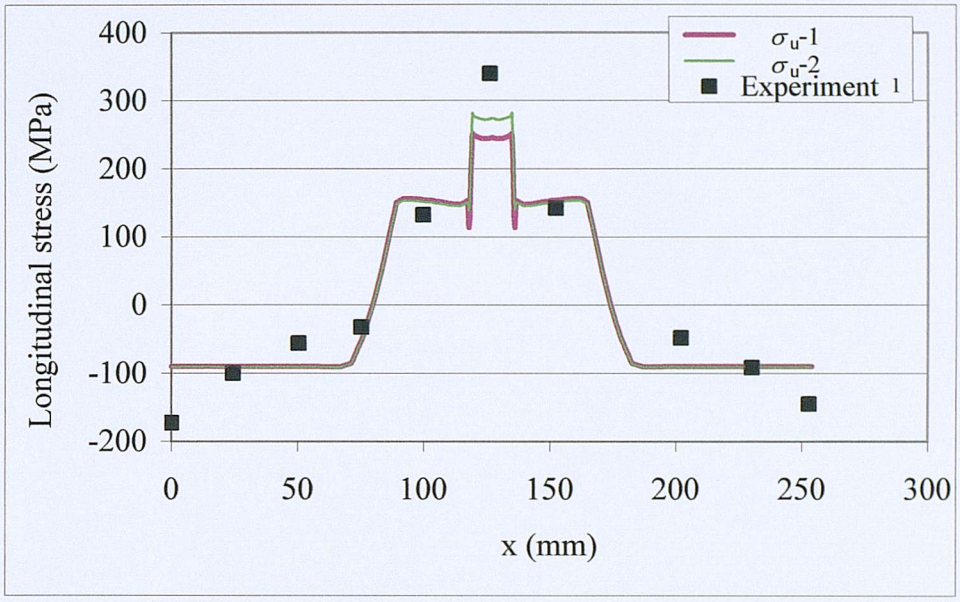

Fig. 3-39 Effect of ultimate strength on longitudinal residual stress (σ_Z) distribution along the top surface

From the above parametric study, the yield strength and ultimate strength are the two most important factors that affect the magnitude and distribution of the longitudinal residual stress. As pointed out in section 3.3.3, the yield strength for the weld metal quoted by Rao and Tall[1] was obtained from specimens containing some portion of the base plate. It is thus reasonable to adjust the yield strength of the weld metal to a higher value. A yield strength of between 331 – 480 MPa was obtained from tests conducted by Lincoln Electric[30] and a typical value of 430 MPa was obtained by ESAB Group[31]. If a value of 420 MPa is used as the yield strength of the weld metal and 500 MPa as the ultimate strength, the resulting longitudinal residual stress distribution along the top surface is shown in Fig. 3-40 together with experimental results for comparison.

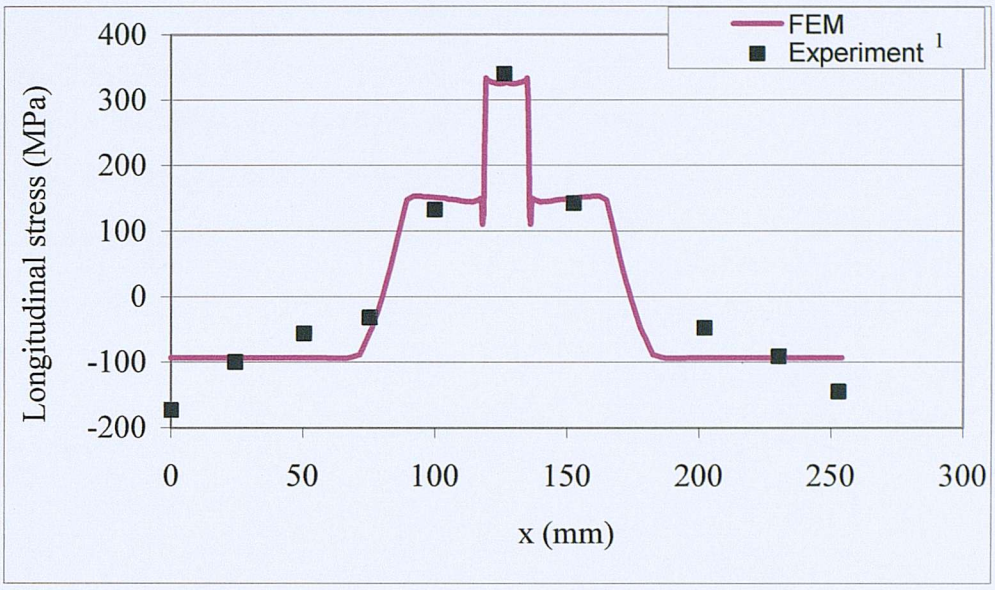

Fig. 3-40 Longitudinal residual stress (σ_Z) distribution along the top surface with adjusted strength of the weld metal

The FEM is seen to underestimate the compressive residual stress towards the ends of the plate. The extra constraint applied by the clamps at the two ends of the plate in the experiment, which was not modelled in the current model, is the possible reason. This was studied in more detail in Section 3.5.7.

3.5.7 Effect of constraint

An attempt was made to model the constraint applied by the clamps at the ends of the plate and the support of the steel column to the bottom surface of the plate in the experiment in order to study its effect on longitudinal residual stress results. Node-node contact elements (CONTAC12) were generated. One node of each contact element was connected to the bottom surface of the plate, as shown by the red line in Fig. 3-1. The other node was constrained in the x and y direction. These contact elements do not allow the plate to move downwards but it is free to move upwards. The node at about 5 mm away from the end of the plate was assumed to be constrained in both x and y direction to simulate the clamps applied. This position is only approximate as no more detail was given.

The program was run with the same input as that generating the result shown in Fig. 3-40. Fig. 3-41 shows the longitudinal residual stress distribution along the top surface obtained from the constrained model compared with the experiment. While the tensile stress in the weld was not affected, the compressive stress at the ends of the plate was seen to have better agreement with the experimental results.

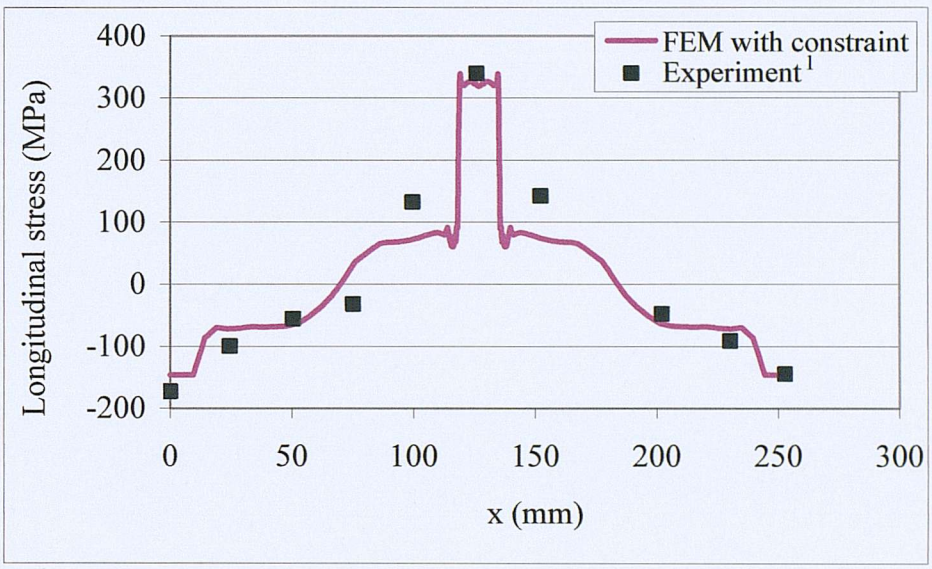

Fig. 3-41 Longitudinal residual stress (σ_Z) distribution along the top surface with constraint

3.6 Transverse residual stress

The parametric study presented in Section 3.5 focused on longitudinal residual stress as this result is available from experimental measurement by Rao and Tall[1] for comparison. Although the transverse residual stress (σ_x) is usually smaller in magnitude than the longitudinal stress (σ_z), it may have significant effect on fracture which occurs at low-applied cyclic load, that is, fatigue failure when cracks normal to the transverse direction are often present.

Fig. 3-42 shows the contour plot of the transverse residual stress distribution obtained from the model with the original choice of input parameters. Comparing

this with the longitudinal residual stress, the magnitude of the transverse residual stress in the un-constrained butt weld is much lower.

Fig. 3-43 shows the transverse residual stress distribution along the top surface of the weldment. As no transverse residual stress results were obtained from the experiment by Rao and Tall[1], a direct comparison is not possible. However, the distribution shown in Fig. 3-42 agrees qualitatively with those obtained from FE simulations on butt welds by various researchers[15,16, 32 , 33] . Experimental measurements on a butt welded plate by Dilthey et al.[33] show a similar distribution. It is worth noting that in the study carried out by Tsai et al.[32], utilisation of generalised plane strain elements reduces the predicted compressive stress in the weld area compared with plane strain elements.

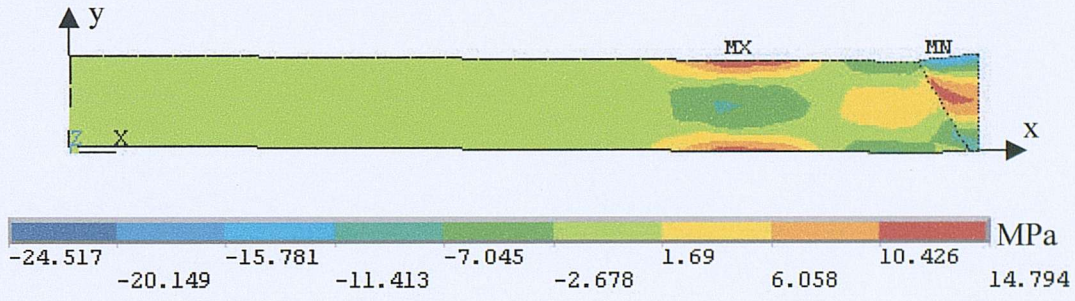

Fig. 3-42 Contour plot of transverse residual stress σ_x

As for the longitudinal residual stress, the amount of heat input and variation of thermal material properties within the range given in the literature for structural steels have insignificant effect on the resulting transverse residual stress. The maximum tensile transverse residual stress along the top surface increased by 0.34 MPa (2.3%) when the arc efficiency increased by 12%; 0.43 MPa (3%) when conductivity k_2 (see Sections 3.3.2 and 3.5.2 for values of k_1 and k_2) was used.

The yield strength of the material has a more significant effect on the transverse residual stress. The magnitude of the maximum transverse residual stress increased by 25.9% with an increase of 30% of the yield strength of the material. The heat loss from the plate bottom surface also affects the transverse residual stress. By using h^c_2

(50% lower than h^e_1, see Sections 3.3.2 and 3.5.3 for values and comparison of h^e_1 – h^e_2), the maximum transverse residual stress along the top surface of the joint increased by 48.5%.

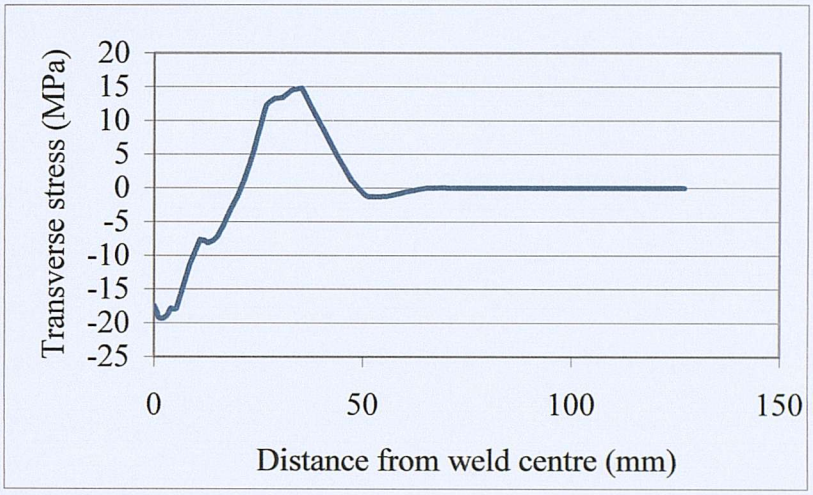

Fig. 3-43 Transverse residual stress (σ_x) distribution along the top surface

Fig. 3-44 shows the contour plot of the transverse residual stress distribution obtained from the constrained model. As expected, the transverse residual stress was affected most significantly by the application of constraints in the x and y-direction.

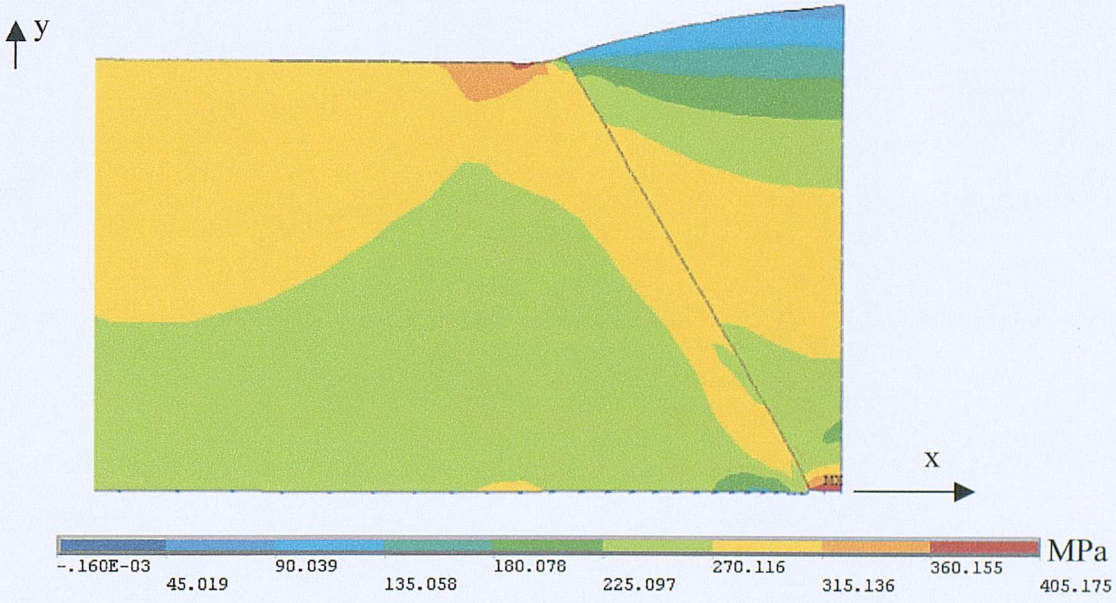

Fig. 3-44 Contour plot of the transverse stress (σ_x) distribution from the constrained model

The transverse residual stress was also found to be sensitive to the yield strain at high temperature, the values of which are dependent on the relative decreasing rate of the yield strength and the Young's modulus. The yield strain decreases with temperature below melting temperature[34]. As discussed in Section 3.5.5, the variation of yield strength at high temperatures has insignificant effect on the final longitudinal residual stress results. A small variation of yield strength at high temperature thus will not affect the longitudinal residual stress results. However, the resulting yield strain will change and this was found to have some effect on the transverse residual stress results. Fig. 3-45 shows the contour plot of the transverse residual stress obtained from a model with yield strain variation ε_Y-2 (see Fig. 3-46). As shown in Fig. 3-46, for curve ε_Y-2, the yield strains at temperatures above 1000 K are greater than those for ε_Y-1, which will result in less plastic strains from the same amount of thermal strains. As the material was assumed to be kinematic, for the same amount of thermal strains developed during the heating and cooling period, the final stress developed in the model with yield strain curve ε_Y-2 is higher than that with ε_Y-1, as illustrated in Fig. 3-47. This is consistent with the results shown in Fig. 3-43 and Fig. 3-45.

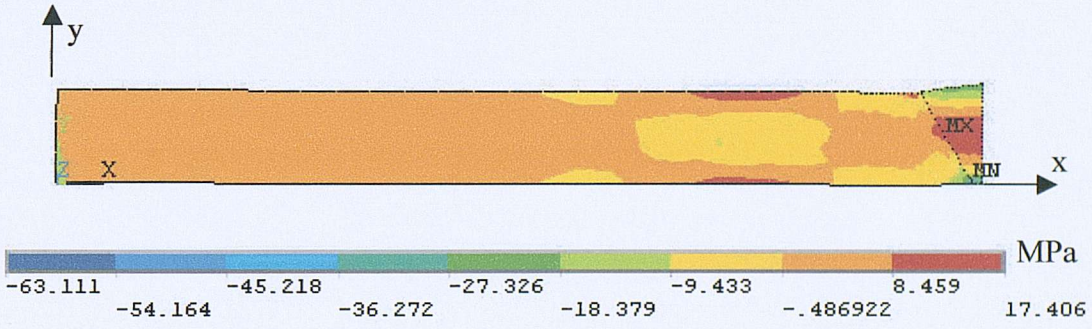

Fig. 3-45 Contour plot of the transverse residual stress (σ_x) distribution from the model with yield strain variation ε_Y-2

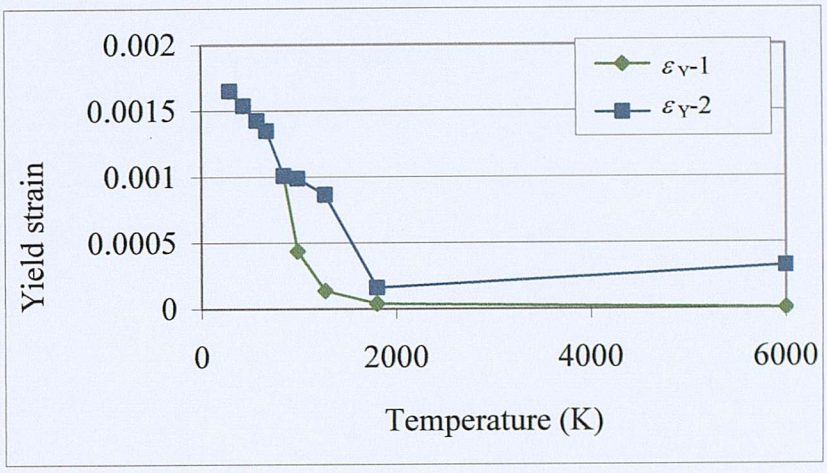

Fig. 3-46 Variation of yield strain with temperature

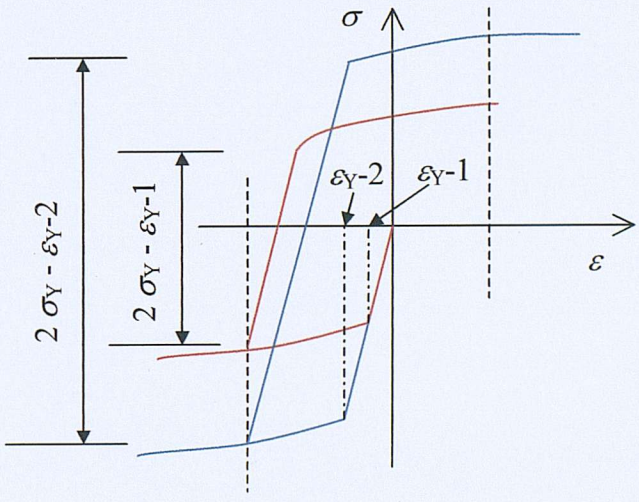

Fig. 3-47 Stress development in the weld area with yield strain variation of ε_Y-1 (red) and ε_Y-2 (blue)

3.7 Distortion

The final deformed shape of the model after welding was found similar to that described in the literature. The angular distortion of the butt weld, β (see Fig. 3-48), obtained from the FE model with initial input parameters is listed in Table 3-5 (under 'original').

A considerable amount of empirical work has been reported in the literature on predicting weld distortion[5,35]. However, most of the proposed prediction models were obtained from analytical or empirical analyses based on experiments of a particular weld and geometrical conditions with various simplifications. There is no model applicable universally because of the wide range of factors that may affect the distortion. Verhaeghe[36] reviewed a number of models predicting welding distortion and formulae predicting distortion were recommended. It should be noted, as pointed out by Verhaeghe[36], that these models only provide an indication of the magnitude of distortion that can be expected rather than the exact value. None of the FEM studies on residual stress prediction cited in this thesis addressed distortion and no comparison with any analytical or empirical results was attempted. Attempts were made in this section to compare the angular distortion, β, predicted from the current FEM with those calculated from some of the predictive formulae reviewed by Verhaeghe[36].

Based on experiments carried out, Oherblom[36] concluded a series of curves for which the angular distortion can be predicted based on the ratio of p/t and B/t, where p is the penetration depth (= t for a full-penetration case), t the plate thickness; B the width of the weld top surface (see Fig. 3-1). For the weld studied here, $p/t = 1$, $B/t = 1.31$, the angular distortion is approximately 0.0125 in radians. Gray, Spence and North[36] proposed angular distortion to be calculated by

$$\beta = \alpha \Delta T \tan(\theta/2) \qquad (3\text{-}12)$$

where α is the thermal expansion coefficient, which equals to 12×10^{-6} / K for structural steel; ΔT the temperature interval (taken as the temperature interval between the melting and room temperature, 1510 K); θ the angle as shown in Fig. 3-1.

The angular distortion predicted by these predictive formulae for the current case were listed in Table 3-5. The FE models with the initially selected input parameters (original) and a 30% higher yield strength at low temperatures (σ_Y-2) predict a similar magnitude of angular distortion to those calculated.

Table 3-5 Angular distortion results obtained from various models

Model	FEM				Empirical	
	Original	σ_Y-2	h^e_2	ε_Y-2	Okerblom[36]	Gray et al.[36]
β (radians)	0.0159	0.0128	0.0211	0.0033	0.0125	0.0105

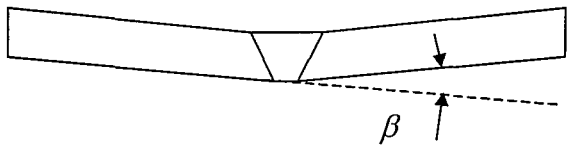

Fig. 3-48 Angular distortion

Angular distortion was found to be affected by the heat loss from the bottom surface, strength of the material and the yield strains at high temperatures as well. Table 3-5 also lists the angular distortion obtained from the models with the initial input parameters (original) and those with different yield strength (σ_Y-2), effective convection coefficient of the bottom surface (h^e_2) and yield strain variation with temperatures (ε_Y-2). Increasing the yield strength at low temperature by 30% decreases the angular distortion by 20% as more constraint is applied from the

material at the lower part of the plate. Greater heat loss from the bottom surface results a higher magnitude of distortion as more heat propagated to the lower part of the plate the temperature of which becomes higher. The softer lower part of the plate thus provides less constraint to the upper part and results in more free distortion. Higher yield strain at high temperatures (ε_Y-2) decreases the distortion significantly.

Most of the predictive formulae for angular distortion were based on the heat input and/or weld size. The FE analysis indicated that the distortion may be affected by other factors such as the strength of the material, the heat loss rate, as well as the yield strain variation of the material at high temperatures. These, however, were not taken into account by the empirical formulae.

3.8 Summary

In this chapter, a finite element simulation of the welding process has been carried out in order to predict the welding-induced residual stresses in a butt-welded plate. The reliability of the model was assessed by comparison of its predictions with published experimental residual stress measurements and distortion result from empirical calculations. Temperature-dependent material properties, especially those at high temperature, were not available so that values used by other researchers in this area were collected and compared. Based on this comparison those appearing to be more reliable were initially chosen for the current study. The sensitivity of the temperature and longitudinal residual stress results to the temperature-dependent material properties was then studied. Several parametric studies were conducted from which a number of conclusions can be drawn.

Heat input

Residual stress results are not sensitive to variation of the amount of heat input studied for a value of arc efficiency within the range given in literature for a specified welding process. A value chosen within this range is sufficient to give acceptably accurate residual stress results.

When the melting temperature is employed as the initial temperature for the weld metal, the amount of heat used to melt the electrode should be deducted from the total heat input into the model.

Thermal and mechanical material properties

Temperature-dependent thermal properties affect the temperature development in the weld, however, their effect on the final residual stress results is not significant. The material data obtained from the literature for structural steel thus can be used with confidence.

Yield strength is the most important factor that affects the residual stress results developed due to welding. Ultimate strength is the other factor that affects the longitudinal residual stress results significantly. Yield strain at high temperatures was also found to affect the transverse residual stress and distortion results. Care should be taken to define these values as accurately as possible.

The thermal expansion coefficient affects the longitudinal residual stress results by less than 3.1% compared with results obtained from the two extremes given in the literature for structural steel.

Boundary conditions

The variation of radiation and convection parameters within practical limits has no significant effect on the final longitudinal residual stress distribution. It is not, therefore, necessary to take into account the radiation effect if the residual stresses are mainly of interest while convection coefficient values within the range of those given in the literature can be used without causing significant inaccuracy to the residual stress results. Residual stresses are however affected significantly by external constraints which should be modelled as accurately as possible.

Based on the results from the parametric studies, a simplified modelling process for simulating welding-induced residual stresses using the commercial FE package ANSYS appears to be acceptable. The main features of such a simulation are:

A) A 2-D plain strain model. Kinematic strain hardening should be used. Material properties obtained from the literature can be used but plastic properties must be accurately specified especially at room temperature for the particular type of steels used.

B) Simulation of the 3-D effect of arc travelling by applying a ramped heat input function.

C) An uncoupled thermal and stress analyses technique is adopted with the temperature history results read from the thermal analysis as loading to the stress analysis. The thermal analysis should be transient to trace the rapid change of temperature with time while a quasi-static analysis can be adopted for the stress analysis. However, a significant number of time points, at which the temperature results are read into the stress analysis, should be defined to capture the temperature gradient and give accurate residual stress results using the load steps option.

Limitations of the FE model

The FE model simulated a welding process carried out by other researchers. Information needed for the FE model was not given fully by the published work so that certain parameters had to be assumed although great care was taken in choosing those parameters such as arc efficiency, size of overfill, etc. The variation of both thermal and mechanical material properties with temperature were not given and no relevant values are available for the type of steel used from literature due to the difficulties in measuring these material properties at high temperatures. For most properties, temperature-dependent values used by other researchers had to be taken for this study. The sensitivity to these material properties and some other input parameters of residual stress results was examined to gain more confidence in these input values. In addition, the accuracy of the measurements must have been affected by experimental error which may result in some doubts regarding the assessment of

the FE model based on comparison with these results. However, Rao and Tall[1] show their confidence on their test results by checking the self-equilibrium of the residual stresses. In addition, they were well experienced since they have carried out measurements on a large number of butt welds and welded shapes.

The ratio of surface heat flux to body heat input was taken from Hong et al.[15] for a GMAW welding process. It is difficult to know exactly the value of this ratio in the actual welding. However, a best-fit value can be found by comparing the predicted fusion zone profile after welding with that obtained from experiment, as proposed by Hong et al.[15]. Due to lack of information on the actual fusion zone in the experimental specimen simulated in this study, this ratio was not calibrated. Different values (3/7 and 1/9) of this ratio has also been adopted and no significant effect was found on the maximum values and distribution of the residual stress results.

Transformation plasticity, temperature-history dependency were not modelled in this study. Plasma pressure, and the fluid movement in the weld pool were not included either. These inevitably will influence the residual stress development during welding, especially in the weld area. However, welding itself is such a complex process and it is very difficult, if not impossible, to take into account everything in one FE model using the current available computer and software. From the final results obtained, which are within an acceptable range, i.e. within the uncertainty of experimental measurements, it is believed that this FE modelling method has considered the most important factors and provides information sufficient for engineering use.

The 3-D effect of the welding process may be represented more accurately by using the generalised plane strain element, which however, is not available in the current version of ANSYS.

References:

[1] Rao N.R.N., Tall L., Residual stresses in welded plates, *Welding Journal Research Supplement*, **40**(10), pp468s-480s, 1961

[2] Argyris J. H., Szimmat J., Willam K. J., Finite element analysis of arc-welding processes, Numerical Methods in Heat Transfer, Vol. III, Edited by Lewis R. W., *John Wiley & Sons Ltd*, pp 1-35, 1985

[3] Argyris J. H., Szimmat J., Willam K. J., Computational aspects of welding stress analysis, Computer Methods in Applied Mechanics and Engineering, **33**, pp635-666, 1982

[4] Shim Y., Feng Z., Lee S., Kim D, Jaeger J., Papritan C., Tsai C. L., Determination of residual stresses in thick-section weldments, *Welding Journal*, **71**(9), pp305s-312s, 1992

[5] Masubuchi K, Analysis of Welded Structures, MIT, *Pergamon Press*, 1980

[6] ANSYS Theory Manual, *SAS, Inc.*, 1999

[7] ANSYS, *SAS, Inc.*, 1999

[8] American Welding Society, AWS D1.1/D1.1M: 2004: Structural welding code – steel, 19th Edition, AWS

[9] Lincoln Electric Company, The Procedure Handbook of Arc Welding, 3rd edition, The Lincoln Electric Company, Cleveland, Ohio, 1995

[10] Thermal Analysis, a revision 5.0 tutorial, *Swanson Analysis Systems, Inc.*, 1992

[11] Karlsson R. I., Josefson B. L., Three-dimensional finite element analysis of temperatures and stresses in a single-pass butt-welded pipe, *Journal of Pressure Vessel Technology, Transactions of the ASME*, **112**(2), pp76-84, 1990

[12] Michaleris P., DeBiccari A., Prediction of welding distortion, *Welding Journal Research Supplement*, pp172s-181s, 1997

[13] Jonsson M., Karlsson L., Lindgren L.-E., Deformation and stresses in butt-welding of large plates, Numerical Methods in Heat Transfer, Vol. III, Edited by Lewis R. W., *John Wiley & Sons Ltd*, pp35-58, 1985

[14] Christensen N., Davies V. de L., Gjermundsen K., Distribution of temperatures in arc welding, *British Welding Journal*, **12**(2), pp54-75, 1965

[15] Hong J.K., Tsai C. –L., Dong P., Assessment of numerical procedures for residual stress analysis of multipass welds, *Welding Journal Research Supplement*, 77(9), pp372s-381s, 1998

[16] Andersson B. A. B., Thermal stresses in a submerged-arc welded joint considering phase transformations, *Journal of Engineering Materials and Technology, Transactions of the ASME*, **100**, pp356-362, 1978

[17] Brown S., Song H., Finite element simulation of welding of large structures, *Journal of Engineering for Industry*, **14**(11), pp441-451, 1992

[18] Lindgren L-E., Runnemalm H., Nasstrom M. O., Simulation of multipass welding of a thick plate, *International Journal for Numerical Methods in Engineering*, **44**, pp1301-1316, 1999

[19] Wikander L., Karlsson L., Nasstrom M., Webster P., Finite element simulation and measurement of welding residual stresses, *Modelling Simulation of the Materials Science and Engineering*, **2**, pp845-864, 1994

[20] Ueda Y., Yuan M. G., Prediction of residual stresses in butt welded plates using inherent strains, *Journal of Engineering Materials and Technology*, **115**, pp417-423, 1993

[21] Song J., Peter J., Noor A., Michaleris P., Sensitivity analysis of the thermomechanical response of welded joints, *International Journal of Solids and Structures*, **40**, pp4167-4180, 2003

[22] Weck R., Residual stresses due to welding, *Welding Journal Research Supplement* **28**(1), 9s-14s, 1949

[23] Laudau H. G., Weiner J. H., Zwicky E. E., Thermal stress in a viscoelastic-plastic plate with temperature-dependent yield stress, *Journal of Applied Mechanics*, **27**(2), pp297-302, 1960

[24] Smith D. J., George D., Bouchard P. J., Watson C., Measurement and prediction of residual stresses in a thick section steel welds, Recent Advances in Welding Simulation, *IMECHE Seminar Publication*, 2000

[25] Bonifaz E.A., Finite element analysis of heat flow in single-pass arc welds, *Welding Journal Research Supplement*, **79**(5), pp121s-125s, 2000

[26] Goldak J. A., Chakravarti A. P., Bibby M., A new finite element model for welding heat sources, *Metallurgical Transactions* 15B, pp299-305, 1984

[27] Tall L., Residual stresses in welded plates – a theoretical study, *Welding Journal Research Supplement*, **43**(1), pp10s-23s, 1965

[28] Touloukian Y. S., Thermophysical properties of high temperature solid materials, Volume 3: Ferrous alloys, *The Macmillan Company*, 1966

[29] ASTM Specifications, Historical listing of selected structural steels, http://www.cisc-icca.ca/historical_steels.html

[30] Lincoln Electric, Fleetweld 7, AWS: E6012, http://www.lincolnelectric.com

[31] The ESAB Group, Inc., Lesson 3 – covered electrode for welding mild steels, http://esabna.com

[32] Tsai C. L., Lee S. G., shim Y. L., Modelling techniques for welding-induced residual stress predictions, pp462-469, 1992

[33] Dilthey U., Reisgen U., Kretschmer M., Comparison of FEM simulations to measurements of residual stresses for the example of a welded plate: a state-of-the art report, *Modelling Simulations for Material Sciences and Engineering*, vol. 8, pp911-926, 2000

[34] Harokopos T., Geaz T. H., The collapsing of the Towers of New York, *Journal of TEE*, (in Greek), pp106-107, April, 2002

[35] Watanabe M., Satoh K., Effect of welding condition on the shrinkage and distortion in welded structures, *Welding Journal Research Supplement,* **40**(8), 377s-384s, 1961

[36] Verhaeghe G., Predictive Formulae for Weld Distortion – a Critical Review, *Abington Publishing*, 1999

4. Static analysis of a cruciform joint

The behaviour of a welded cruciform joint under quasi-static loads was simulated using the finite element method (FEM). The purpose of this analysis was threefold. First, a cruciform joint geometry is very similar to that of a T-joint, therefore, the respective modelling process would also be similar. Secondly, the geometry, material properties and loading conditions of the joint were similar to those of a specimen for which experimental results were available[1] so that the performance of the FEM model could be assessed. Finally, this analysis provided the opportunity of modelling and studying the effect of variable material properties over the weld region, for which data were available from the original experimental study. Particular attention was given to the accurate representation of material property variations from the base metal (BM), across the heat-affected zone (HAZ) to the weld metal (WM). The limited material information from the earlier experimental work was supplemented with data on strain hardening and maximum elongation for all three material zones. Material parameters were selected within the ranges specified for the grades of steel used. Attempts have been made to validate the model by comparing the resulting principal strain difference distribution along the tensile edge of the side plate under pure bending with that of theoretical calculations assuming elastic-perfectly plastic material behaviour. Based on hardness data, a property gradient approach was also attempted and shown to produce more realistic results. The effect of varying weld geometry on the strain and stress distributions was studied using the generated model.

4.1 Joint specimen

The geometry of the specimens used by Fessler and Pappalettere[1] is shown in Fig. 4-1. Two strips of equal length l = 50 mm, are attached to a plate of length $2L = 100$ mm to form a cross weldment. The strips and the plate have the same nominal thickness $d = T$ = 12.5 mm (0.5 in.) and a width of 150 mm. No weld edge preparation was made for the four fillet welds. Crosses of 10 mm thick were cut from the weldment and loaded under pure bending. The photo-elastic coating technique was used by Fessler and Pappalettere[1] to measure the strain on one lateral surface.

The material used in the experiment was BS 4360: 50D, a typical structural steel. BS 639 E51, 33B electrode was used for the weld. Some information on the properties of these materials was given by Fessler and Pappalettere[1].

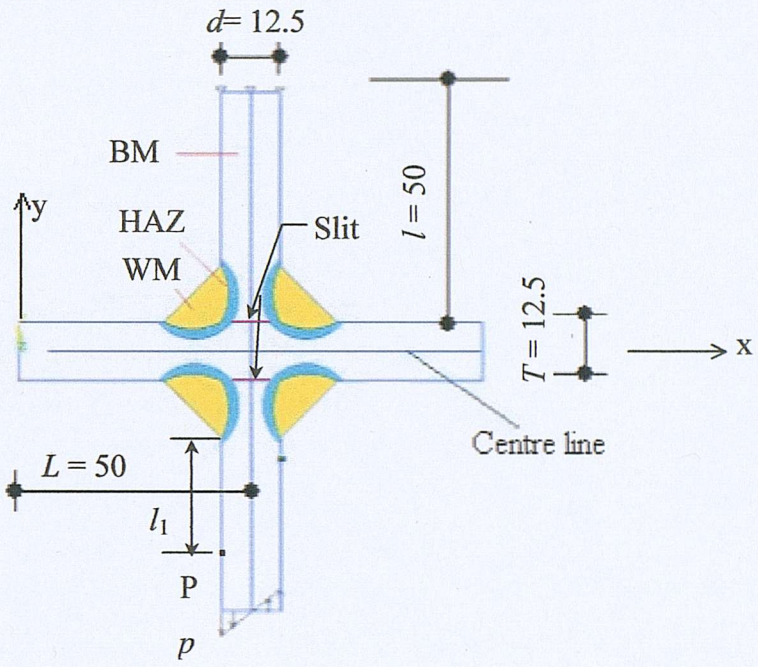

Fig. 4-1 Typical section through the welded cruciform joint tested by Fessler and Pappalettere[1], dimensions in mm

4.2 FEM model

4.2.1 Geometry

The solid model of the section shown in Fig. 4-1 was generated using the pre-processor of the general-purpose finite element package ANSYS[2]. The extent of the HAZ modelled in the FEM model was determined from a micrograph taken after etching a number of prepared surfaces given by Fessler and Pappalettere[1]. The boundary of the weld area and HAZ was simplified and idealised as smooth arc curves. The geometry of the model is assumed to be symmetric about the centre lines of the attachment plates and the main plate. However, under the bending moment

shown in Fig. 4-1, unsymmetrical contact is expected to occur between the attachment plates and the main plate (along the slit, see Fig. 4-1). It is for this reason that the whole model was generated. The upper half of the model was generated first and the "mirror copy" function provided by ANSYS was used to generate the whole model.

4.2.2 Boundary conditions and loading

To simulate the loading conditions applied in the experiment, the edge of the upper attachment was constrained in both x and y-directions, and the bending moment was simulated by applying a linearly-varying pressure to the end of the lower attachment plate, as shown in Fig. 4-1.

4.2.3 Elements and Mesh

The element types used to mesh this model are a 2-D 4-node quadrilateral element under plane stress (PLANE42) for BM, WM and HAZ and a point-to-point contact element (CONTAC12) over the contact areas between the main plate and the attachments (the slit, as shown in Fig. 4-1). Since the loaded specimen was cut from the weldment, plane stress with a thickness of 10 mm was used. The final mesh of the model adopted is shown in Fig. 4-2. It consists of 6294 elements and 6302 nodes. The fine mesh used next to the weld toe in the attachment plates is for the purpose of assigning a gradual change of material properties to elements from the WM across the HAZ to the BM. This is discussed in more detail in Section 4.5.

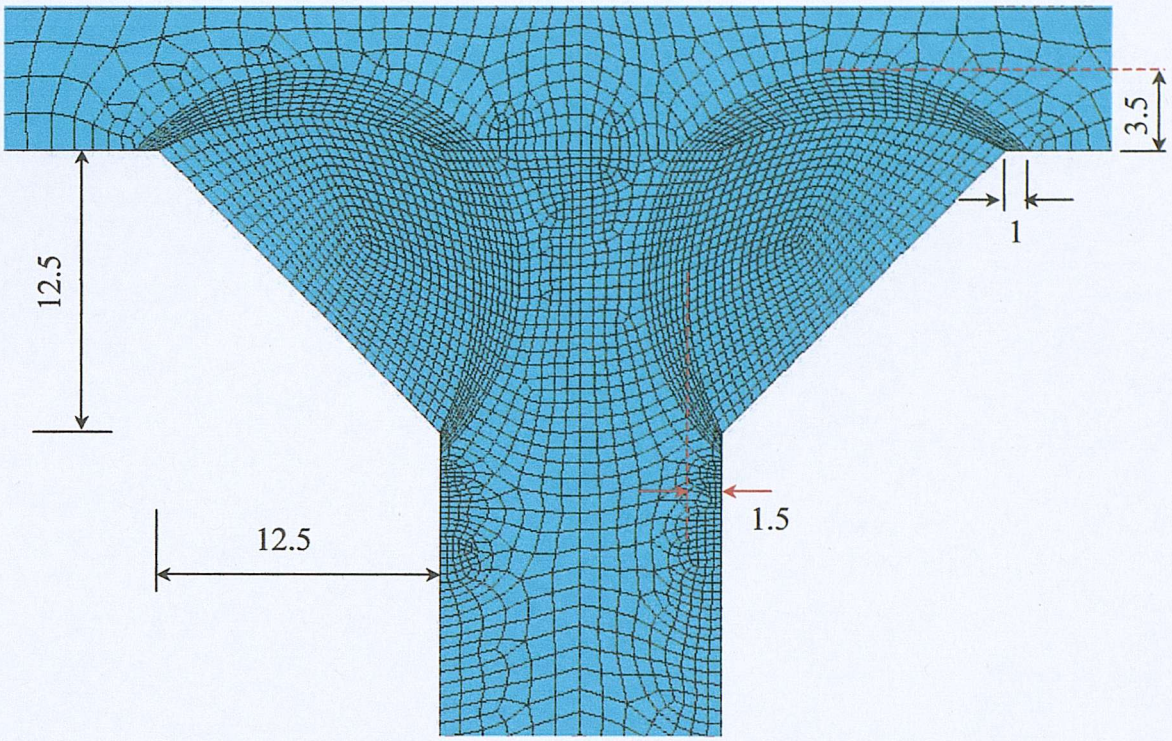

Fig. 4-2 Mesh map used in the FEM, dimensions in mm

4.2.4 Material model

Different material properties were assigned to the three areas, BM, WM and HAZ. Multi-linear kinematic-hardening stress-strain relationships, as shown in Fig. 4-3, were adopted based on the limited material information given by Fessler and Pappalettere[1]. Such relationships were built using the true stress-strain relation, $\sigma = K\varepsilon^n$, to represent the post-yield elasto-plastic behaviour of these materials. The initial choice of the various parameters describing the material model for the three areas are given in Table 4-1. The values of the yield stress are those given by Fessler and Pappalettere[1]. However, in Fessler and Pappalettere[1]'s paper only yield strength, tensile strength and reduction of area are given. Thus in order to calculate K and n the strain at the tensile strength, ε_u, had to be estimated from available information on similar materials. The determination of appropriate values for K and n is given in detail in Appendix D. A Young's modulus of 2.07×10^5 N/mm^2 and a Poisson's ratio

of 0.3, typical values for structural steel, were used for all areas. Appendix I section I.2 lists part of the input file for this model.

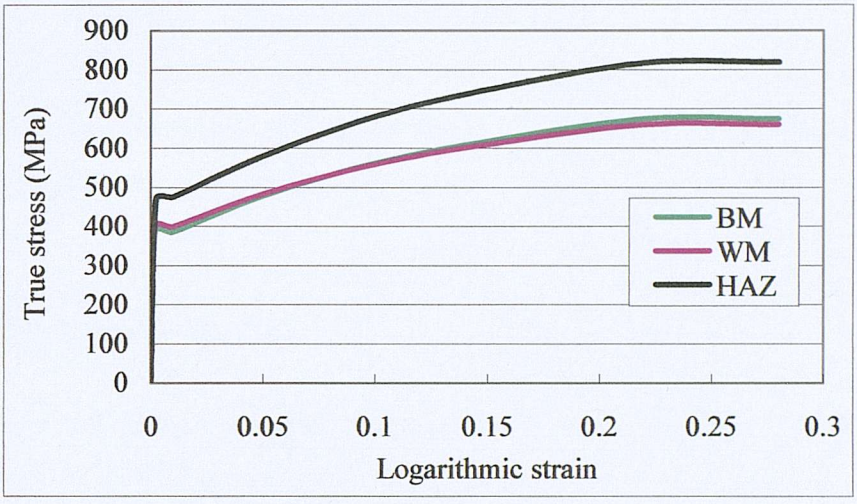

Fig. 4-3 True stress-strain curves used in the FEM

Table 4-1 Stress and strain properties for the three areas in the FEM model

	σ_Y (MPa)	K (MPa)	n	ε_u
BM	387	959	0.232	0.18
WM	398	911	0.212	0.18
HAZ	468	1165	0.233	0.18

In Table 4-1, the yield strength value for base plate was obtained from the steel maker and the Welding Institute for the strips from which the parts of the components of the specimens were cut. The yield strength for the weld metal and HAZ was obtained by another researcher[1] for the same grades of steel and electrode when used for joining one inch to two-inch plates. It is thus possible that the yield strength of the three areas in the actual experimental specimens were different from those given in Table 4-1. In the test conducted by the same authors on the main strip under tension after the side plates and the welds were removed, the plate was found to yield at a load of 78% the nominal yield strength of the plate. The presence of

tensile residual stresses was thought to be one of the reasons. A smaller actual yield strength of the material was also possible. The presence of the tensile residual stress has the equivalent effect of decreased yield strength of the plate.

It should also be noted that in the actual specimens, material properties vary gradually from the weld metal across the HAZ to the base metal. This inevitably will affect the strain results in these areas.

4.2.5 Mesh sensitivity study

Using the same initial material input parameters given in Section 4.2.4, another finer mesh, Mesh2 (10780 elements, 11164 nodes), where the element sizes were reduced uniformly by 30% of the initial mesh Mesh1 (see Fig. 4-2) was generated. The von Mises stress distributions obtained from the two models are shown in Fig. 4-4. The stresses from the two meshes show a very similar distribution and the magnitude of the maximum stress resulting from Mesh2 was only 0.1% greater than that from Mesh1. Mesh1 is thus considered to be satisfactory.

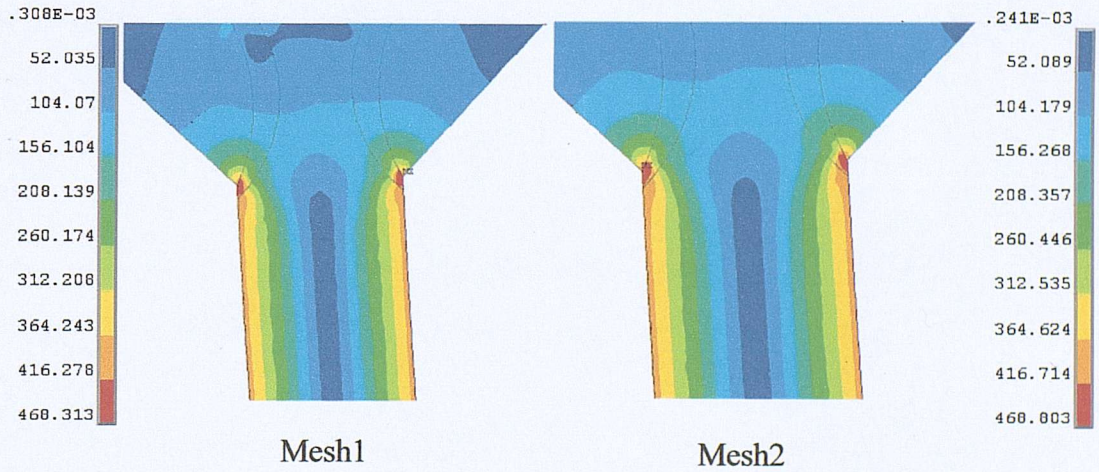

Fig. 4-4 Comparison of von Mises stress obtained from Mesh1 and Mesh2, stress units in MPa

A 2-D 6-node plane stress triangle element (PLANE2) was also adopted using the same mesh density as Mesh1. The von Mises stress distribution obtained is very similar to that of Mesh1 and Mesh2. The maximum von Mises stress increased by only 0.4% when the number of elements and nodes increased to 12362 and 25204, respectively. Thus a higher order element type is not necessary for this model.

4.3 Validation of the FEM assuming simplified material behaviour

Elastic-perfectly plastic material behaviour is assumed with the yield stress in compression equal to that in tension. Then from simple beam theory with assumptions that plane cross sections remain plane, the principal strain difference at the side of the beam cross section when the specimen behaves elastically can be calculated by

$$\varepsilon_1 - \varepsilon_2 = \frac{(1+\nu)}{E}\frac{6M}{bd^2} \tag{4-1}$$

where ε_1 and ε_2 are the first and second principal strains; ν the Poisson's ratio; E the Young's modulus; M the applied bending moment; b and d the width and height of the cross sectional area. When the yield stress is exceeded the same difference is given by

$$\varepsilon_1 - \varepsilon_2 = \frac{(1+\nu)\sigma_Y}{E} \Big/ \sqrt{3 - \frac{2M}{M_Y}} \tag{4-2}$$

where ε_1, ε_2, ν, E, M, b and d are the same as those in Eqn. (4-1) and M_Y the bending moment initiating yielding of the cross section.

For validation purposes, the FE model was assumed to have the same elastic-perfectly plastic material behaviour and the predicted strain difference results obtained from the FE model were thus compared with those calculated from Eqns. (4-1) and (4-2). Fig. 4-5 shows the plot of the principal strain difference, ε_1-ε_2, versus applied bending moment obtained from both the FE model and the theoretical calculation at the side plate position Point P (see Fig. 4-1, l_1 = 10.7 mm between the

weld toe and Point P). This principal strain difference result was chosen for comparison because it is also measured and given from the experimental work[1]. Since the joint is under pure bending, except at the stress concentration positions, i.e., at and near the weld toe and the end of the side plate where the load was applied, the strain is uniformly distributed along the edge of the plate. The position of Point P can thus be chosen to be anywhere within this uniform strain region. Results at positions where l_1 = 5.6 and 18.7 mm were also checked and found to be identical with that shown in Fig. 4-5. The results obtained from the FEM are seen to have very close agreement with the theoretical calculation. Other results, such as principal stresses and strains obtained from the FEM show also close agreement with those calculated theoretically.

For models with kinematic strain hardening, the theoretical calculation is more complex. Fig. 4-5 also plots the results obtained from the FE model with the multi-linear kinematic strain hardening parameters given in Table 4-1. As expected, a moment greater than 1.5 M_Y (M_Y is 100.8 kN mm with nominal yield strength of 387 MPa and cross section $b \times d$ = 10 × 12.5 mm) was sustained in the model with strain hardening while for the model with elastic-perfectly plastic material behaviour, the applied moment is limited by 1.5 M_Y (see Eqn. (4-2)), as shown by the dotted green line in Fig. 4-5.

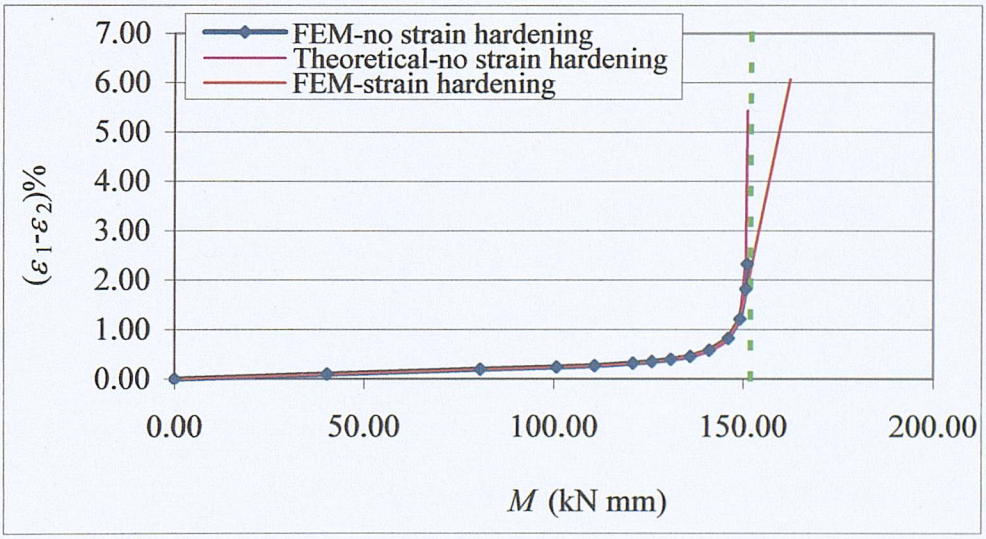

Fig. 4-5 Comparison of strain-moment relation at Point P (Fig. 4-1) obtained from FEM and theoretical calculation

4.4 Comparison with experimental results

The model was subjected to an end-moment simulated as a linearly varying pressure, p, as shown in Fig. 4-1. The maximum magnitude of the applied moment in the experiment was 1.45 M_Y. M_Y was defined as the bending moment initiating yielding of the BM section based on the yield strength of the base metal given in the paper. A value of 100.8 kN mm was calculated based on a nominal yield strength of 387 MPa with a cross section area of $b \times d = 10 \times 12.5$ mm.

The difference of the principal strains from both the experimental measurement through a photo-elastic film and the FEM model at position P (Fig. 4-1) is plotted versus the applied bending moment in Fig. 4-6. Results from the theoretical calculation, by assuming elastic-perfectly plastic material behaviour, as discussed in Section 4.3, are also plotted to provide comparison within the elastic range. It is expected that in the elastic range the current model with multi-linear kinematic strain hardening will be the same as that for the elastic-perfectly plastic model as the same Young's modulus and cross section area were adopted.

4.4.1 Results in elastic region

Fig. 4-6 indicates that in the elastic region the experimental values of $(\varepsilon_1 - \varepsilon_2)$ are lower than those predicted by about 25%. When the plate is still in its elastic region, the position of Point P has no influence on the strain results as the Young's modulus variation across the areas is negligible and the variation of the yield strength has no effect on the strain results, as can be seen from Eqn. (4-1). Possible reasons for the discrepancies in the elastic region could be (a) a higher Young's modulus in the tests than the assumed value, but this effect is only 1.4% if a value of 210 GPa is used instead of 207 GPa; (b) a smaller value of Poisson's ratio which could account for 1% if a value of 0.29 is used; (c) larger size of the cross section (b and d in Eqn. (4-1)) in the actual specimen than those used for calculation, for example, a cross section dimension of 10.5 × 13 mm will result in a 11% decrease; and (d) experimental errors.

4.4.2 Behaviour in plastic region

The principal strain differences in the plate are proportional to the applied load until M exceeds a value about 1.25 M_Y in both cases. Strain then increases rapidly with little increase of moment. The magnitude of the strain difference obtained in the experiment is much higher than those predicted by the FEM at bending moments greater than M_Y. These principal strain difference values are very sensitive to the applied moment variation at a bending moment M greater than 1.25 M_Y.

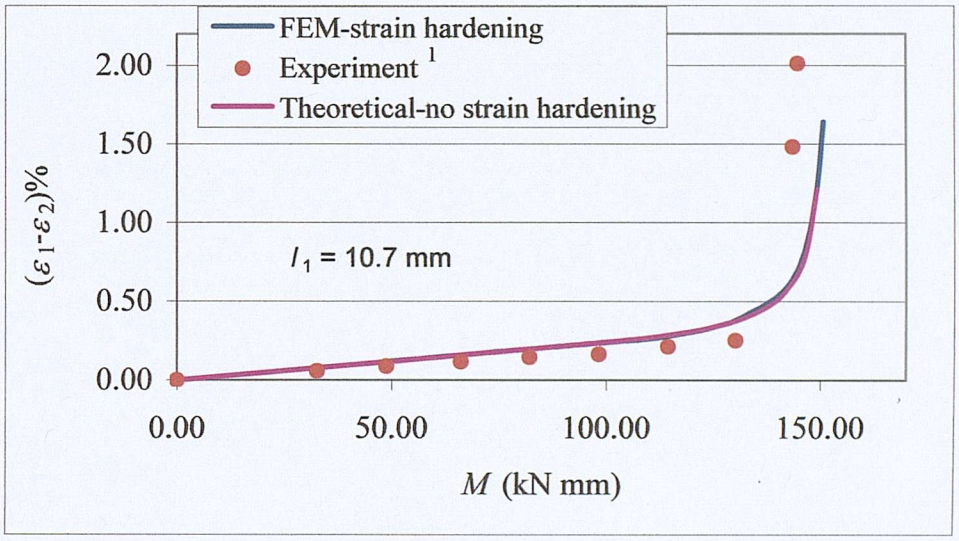

Fig. 4-6 (ε_1-ε_2) as a function of M at Point P (see Fig. 4-1)

The distribution of the same strain difference along the tensioned edge of the side plate for M = 1.25 M_Y and 1.45 M_Y obtained from both the experimental measurements and FEM prediction is plotted in Fig. 4-7 and Fig. 4-8, respectively.

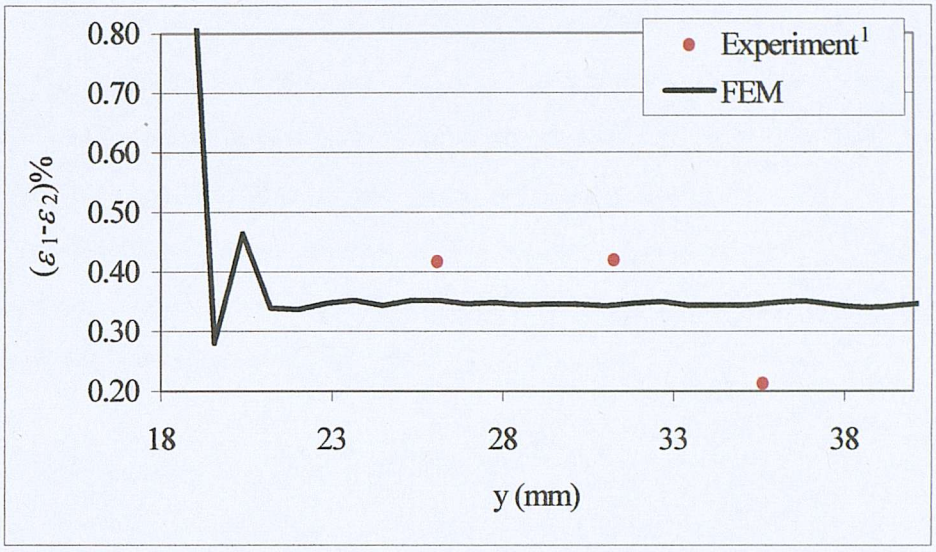

Fig. 4-7 Distribution of (ε_1-ε_2) along tensile edge of the side plate for M=1.25 M_Y

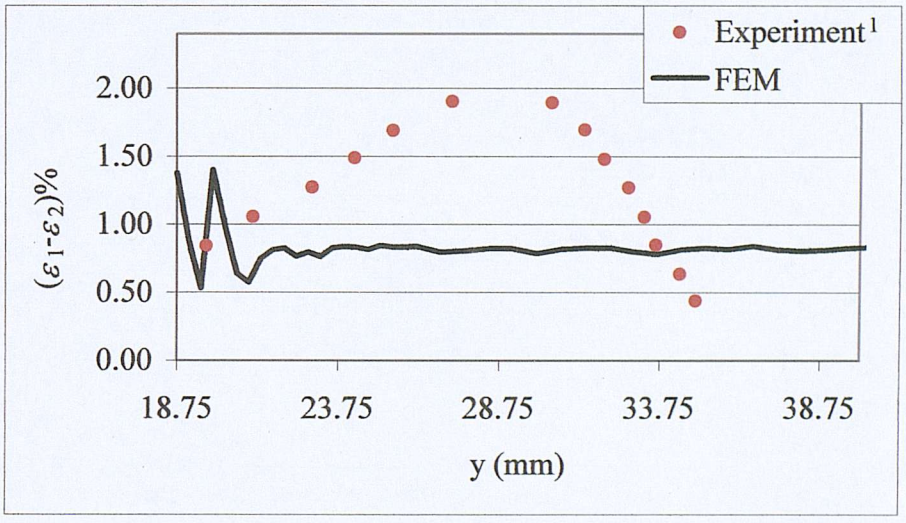

Fig. 4-8 Distribution of (ε_1-ε_2) along tensile edge of the side plate for M=1.45 M_Y

Significant discrepancies of the principal strain difference distribution results between the FE prediction and experimental measurement are seen in Fig. 4-7 and Fig. 4-8. Possible reasons for the discrepancies in the strain magnitude away from the HAZ as shown in Fig. 4-7, Fig. 4-8, and in the plastic region as shown in Fig. 4-6 could be

(a): The value of σ_Y = 387 MPa adopted could be slightly different from the real value in the actual specimen. A small change of σ_Y will have a significant effect on the strain results at bending moments higher than 1.25 M_Y. Different values of yield strength for the base metal were used and strain results compared with the experiment, as shown in Fig. 4-9 for the strain versus bending moment relationship at Point P and in Fig. 4-10 for the strain distribution along the tensile edge of the side plate at bending moment $M = 1.45\ M_Y$.

A better agreement between the FE and the experimental strain results at Point P was obtained for bending moments greater than 1.3 M_Y, as shown in Fig. 4-9, when the yield strength of the base plate was taken as 374.2 MPa, a 3.3% decrease from the original 387 MPa. Fig. 4-10 shows that the maximum principal strain difference results further away from the HAZ increase dramatically with the same slight decrease of the base metal yield strength, i.e., the strain increased by more than 50%. A yield strength of 374.2 MPa for the base metal is thus seen to result in better agreement between the FE prediction and the experiment.

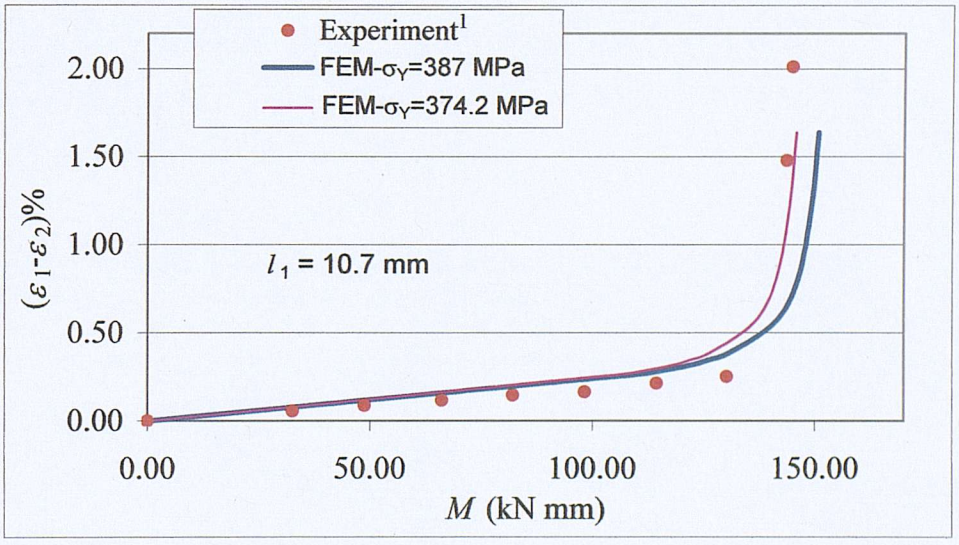

Fig. 4-9 Effect of yield strength on the (ε_1-ε_2)-bending moment relation at Point P (see Fig. 4-1)

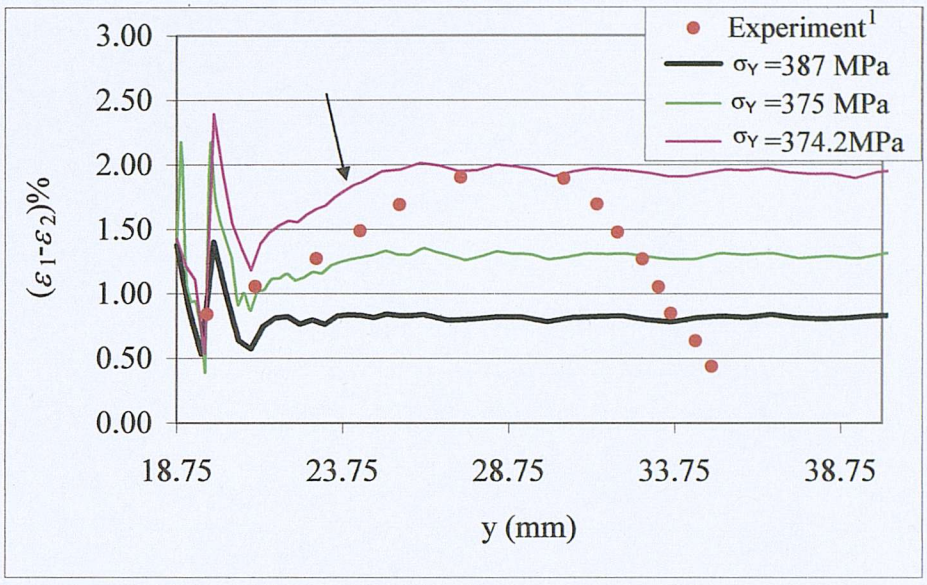

Fig. 4-10 Effect of yield strength on the distribution of (ε_1-ε_2) along the tensile edge of the side plate, M = 146.16 kNmm

(b) The strain hardening behaviour is not given and that used in the FE model may be different from the strain hardening of the actual specimens; Different values for the post-yield strain hardening parameters K and n, as listed in Table 4-2 were used to study its effect on the strain distribution. Fig. 4-11 shows the true stress-strain relations corresponding to these cases.

Table 4-2 Values of K and n defining different post-yield behaviour

Case		σ_Y (MPa)	K	n	ε_u
SH1	BM	374.2	988.0	0.248	0.18
	HAZ	468.0	1165.0	0.233	0.18
SH2	BM	374.2	1086.6	0.273	0.12
	HAZ	468.0	1165.0	0.233	0.18
SH3	BM	374.2	1086.6	0.273	0.12
	HAZ	468.0	1339.8	0.265	0.12

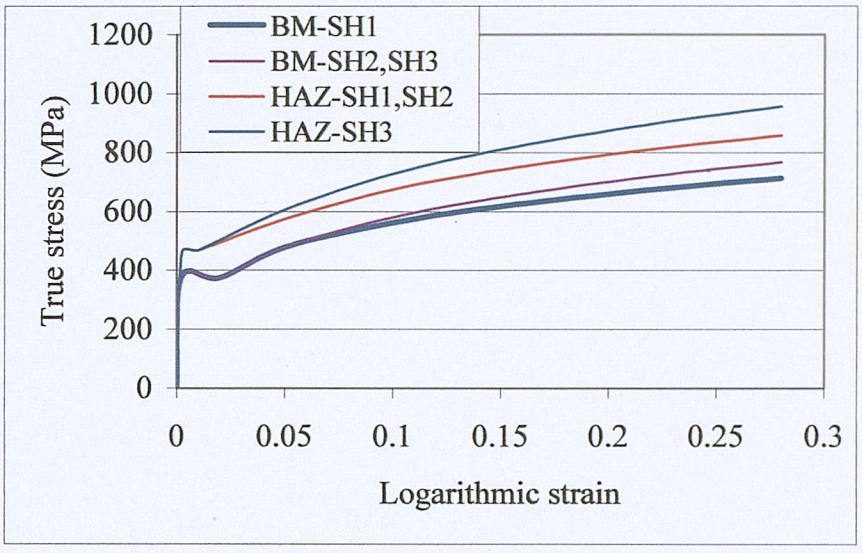

Fig. 4-11 Stress-strain curves corresponding to strain-hardening cases listed in Table 4-2

Fig. 4-12 shows the effect of different strain hardening models on the principal strain difference distribution along the tensile edge of the side plate. Comparing curve SH1 with SH2, the magnitude of the strain difference away from the HAZ decreases with a higher strain hardening exponent of the BM by about 4%. But this effect is much less than that of the yield strength, as can be seen by reference to Fig. 4-10 and Fig. 4-12. Since the material model for HAZ remains unchanged, the strain distribution at and near the HAZ was not noticeably affected.

For cases SH2 and SH3, the BM material model used was the same while the strain hardening properties for the HAZ were changed, as shown in both Fig. 4-11 and Table 4-2. The strain distribution and magnitude away from the HAZ was not affected due to the same BM properties used, but in and near the HAZ the magnitude of the minimum principal strain difference value decreased by about 40% for an 8.5% decrease of true stress value at the logarithmic strain of 15%.

This study demonstrates that the strain hardening behaviour has some effect on the strain difference results for the cruciform joint under bending, but this effect is much less than that of the yield strength of the material.

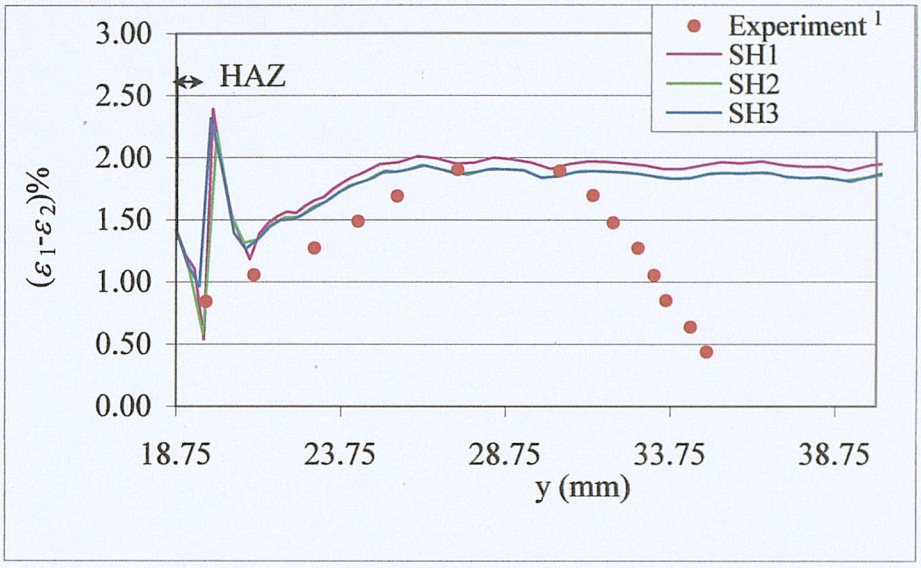

Fig. 4-12 Effect of strain hardening properties on principal strain difference distribution along the tensile edge of the side plate at M=1.45 M_Y

(c) dimensions of the cross section $b \times d$.

There was considerable ambiguity regarding the value of the steel plate thickness in Fessler and Pappalettere[1]'s paper. The nominal thickness of the cross joint in the z-direction was quoted as 10 mm. It is possible that the true dimensions of the tested specimens were slightly different from 10 ×12.5 mm which were used for calculating the yield moment M_Y. A slightly smaller dimension of the true specimen cross section than the nominal value is equivalent to having applied a greater bending moment to the specimens. To study the sensitivity of strain results to the variation of the plate thickness, models with different value of plate thickness, d = 12.3 mm and 12.4 mm, were generated and the models analysed with all the other parameters unchanged. Fig. 4-13 shows the results of the principal strain difference versus bending moment at Point P obtained from models with different plate thickness and the experimental measurements. A decrease of plate thickness by 1.6% in the real test specimen from the nominal value results in a better agreement between the FE results and the experimental measurements in the plastic region.

Fig. 4-14 shows the principal strain difference distribution along the tensile edge of the side plate obtained from models with different plate thickness under bending moment M = 1.45 M_Y = 146.16 kN mm. The maximum principal strain difference away from the HAZ increased by 159% if the plate thickness in the real specimen decreases by 1.6%. The variation of the plate thickness is seen to have significant effect on the strain results at applied bending moments higher than 1.25 M_Y.

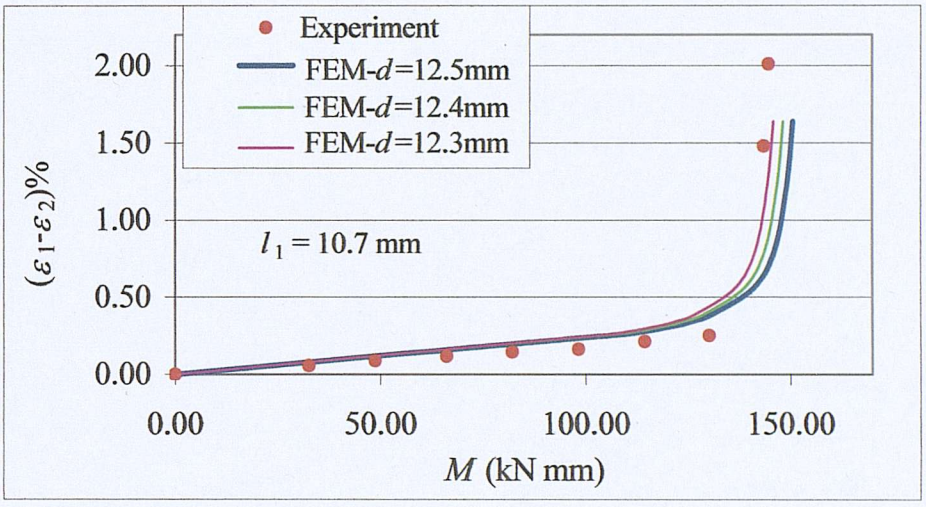

Fig. 4-13 Effect of plate thickness d on the (ε_1-ε_2)-bending moment relation at Point P (see Fig. 4-1)

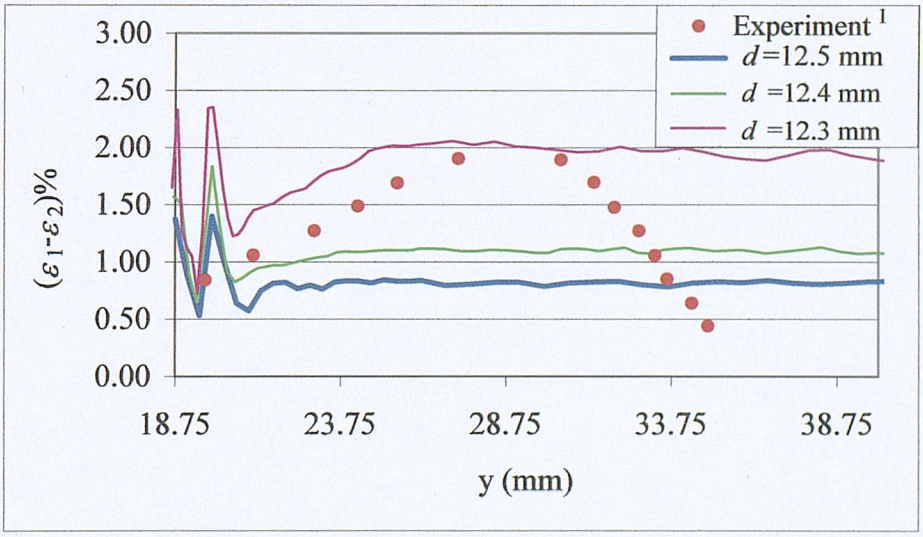

Fig. 4-14 Effect of plate thickness d on the distribution of (ε_1-ε_2) along the tensile edge of the side plate at bending moment M = 1.45 M_Y

(d) errors in photo-elastic measurement; and

(f) the presence of tensile residual stress in the y-direction which was not released by cutting the weldment in the longitudinal (z) direction. In the test conducted by the same authors on the main strip under tension after the side plates and the welds were removed, the plate was found to yield at a load of 78% the nominal yield strength of the plate. The presence of tensile residual stresses was thought to be one of the reasons. Tensile residual stress at the tensile edge of the side plate under bending has the equivalent effect of decreasing the yield strength of the material.

As shown in Fig. 4-10, the experimental strain measurements increase with distance from the weld toe and reach their maximum value at a position about mid-way between the edge of HAZ and the edge of the photoelastic coating. The strain difference then decreases until the edge of the coating is reached. Disregarding the peaks in and near the weld and HAZ areas, the FE prediction shows a similar trend between the weld toe and the location of the maximum value, at about 6 mm from the weld toe. From the results obtained from the Vickers microhardness test, it is clear that the mean hardness of the weld metal is greater than that of the parent plate and that the hardness of the HAZ is greater than that of the weld metal. This is consistent with the variation of the yield strength in these three materials, as listed in Table 4-1. These are the reasons for the increase of the strain in the strain distribution curves obtained both from the FE analysis and the experiment. In the tested specimen, the material properties vary gradually from the weld metal across the HAZ to the base metal until a certain distance from the edge of HAZ defined from an etched specimen. Thus the base metal close to the HAZ has actually a higher yield strength than the un-affected base plate. This gradual change of material properties was not accounted for in the current model and is the reason for the discrepancies in the strain values between the FE model and experimental measurements in the part of the curve to the left to the maximum strain value away from the weld toe (arrowed in Fig. 4-10).

The photo-elastic measurements decrease after the maximum value was reached. However, under pure bending and at a certain distance from the HAZ where the material properties of the unaffected base metal are uniform, the strain should be uniform. The FE model predicted this uniformly distributed strain. The reason why the experimentally measured principal strain differences decrease was not given by Fessler and Pappalettere[1]. The edge effect of the photoelastic layer used in the experiment may contribute to this drop.

The appearance of the local peak in the FE curve near the weld toe may be due to the combined effect of sudden material property change and the stress raising effect at the weld toe. One possible reason why the experiment did not detect this peak may be that the maximum strain that can be sustained is limited by the bonding between the photo-elastic coating and the specimen surface. High local deformation could cause premature bond failure[1]. The photoelastic method may not be sensitive to highly localised strain. Careful examination of the fringe patterns presented in Fessler and Pappalettere[1]'s paper reveals that there were fringes at the weld toe, which could be too intense, due to the high stress concentration, to be used to determine the strain difference. The other peaks in that part of the FE curve are due to the sudden-change of properties across the HAZ and base metal areas. In reality, as indicated from the hardness distribution obtained by Fessler and Pappalettere[1], the material properties change gradually from the base plate, across the HAZ to the weld metal. A property gradient method, as discussed in detail in Section 4.5, was used in an attempt to simulate the real situation and to remove these artificial peaks.

4.5 Effect of gradual change of material properties

Microhardness test results reported by Fessler and Pappalettere[1] show clearly that there is, in reality, a smooth gradual change of material properties across the BM, WM and HAZ. The hardness of the base plate continues to change from the boundary of the base metal and HAZ identified from an etched specimen. An average distance of about 4 mm from the weld toe to the unaffected base plate is commonly seen in the hardness distributions obtained from hardness tests presented

in Chapter 5 (for example, Fig. 5-15). In this FE study, a gradual change of material properties across the three areas was adopted, as shown in Fig. 4-15, by assigning linearly varying material properties to different layers of elements across the three areas. The true stress-strain curves for Mat1 – Mat17 are shown in Fig. 4-16. Mat1 – Mat17 were linearly extrapolated from that of the base metal (σ_Y = 374.2 MPa) and HAZ properties.

Principal strain distributions along the tensile edge of the side plate at a bending moment $M = 1.45\ M_Y$, from FEM models with sudden and gradual property changes across the three areas are shown in Fig. 4-17 as curves FE1 and FE2, respectively. The high peak at the edge of the HAZ is removed by applying a gradual change of material properties. In addition the experimental and FE results are now very similar at distances between 18.75 and 27 mm. This is evidence of the sensitivity of the FEM predictions to the assigned material properties. This may have a great effect on fatigue analysis of a welded joint because a fatigue crack is most likely to initiate from the weld toe and the stress state near the toe affects greatly crack propagation. A few small peaks are seen to be present near the HAZ. A finer mesh, e.g. smaller element size may produce a smoother strain distribution.

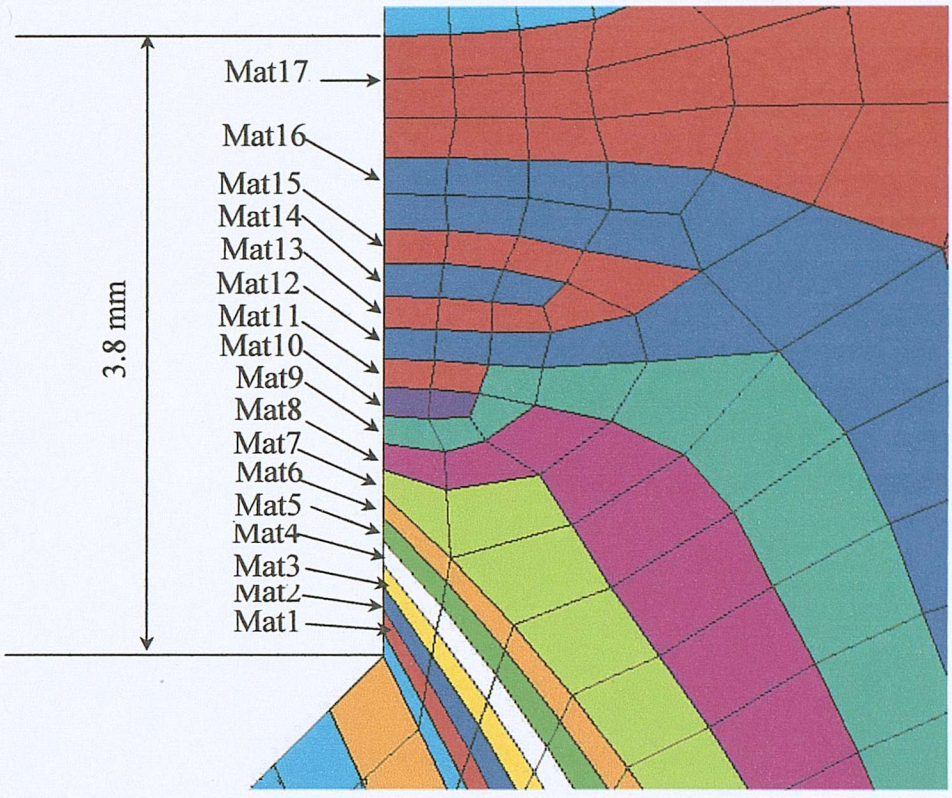

Fig. 4-15 Gradual change of material properties

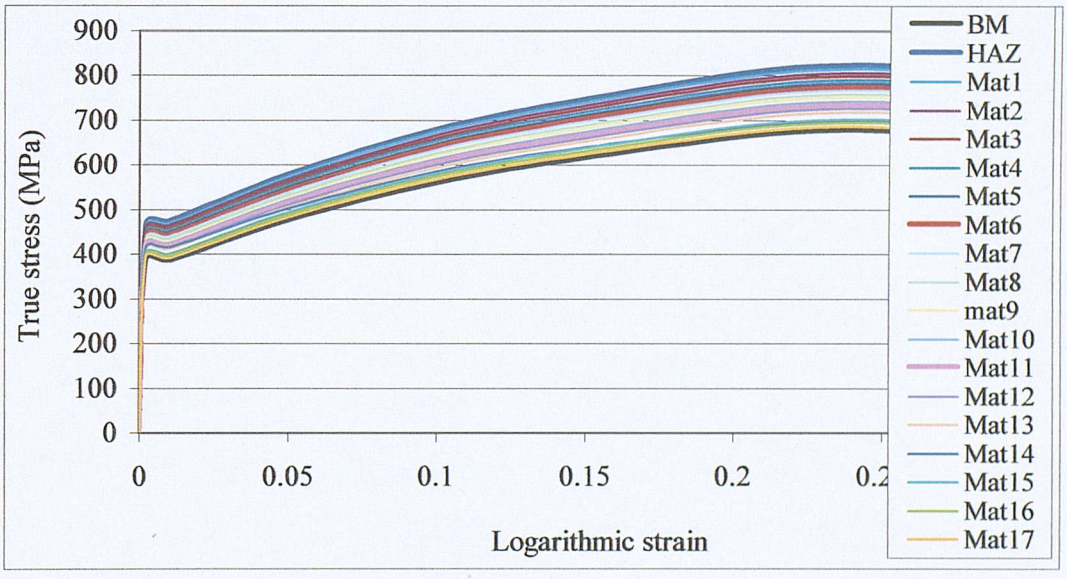

Fig. 4-16 Stress-strain curves for Mat1-Mat17

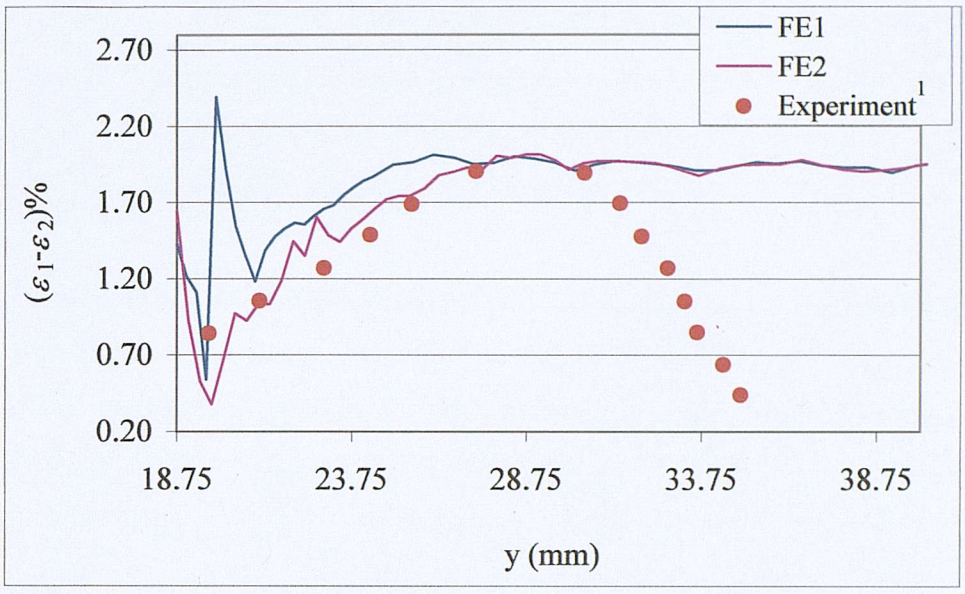

Fig. 4-17 Effect of gradual change of material properties on principal strain difference distribution

A satisfactory degree of confidence in the developed FEM model was achieved. Then, it was used for parametric studies on the effect of varying geometry of the weld on the joint behaviour. These studies were facilitated by the use of ANSYS Parametric Design Language. The results of the parametric studies gave some idea of how significant an effect different parameters have on the behaviour of a welded joint.

4.6 Effect of geometry

4.6.1 Weld size

The weld leg length in the original FE model was reduced by 36% to 8 mm. The combined weld throat is then less than the width of the side plate. The joint was then analysed under load. The stress concentration under bending is less significant and the stress developed in the weld area under bending is smaller. For this reason tension was applied to the joint. Fig. 4-18 shows the contour plot of the von Mises stress in the model with the side plates under tension applied as a uniform pressure of 350 N/mm to the edge of the lower side plate. While the original specimen was

expected to fail in the base metal, in the reduced weld size model, a strain significantly exceeding the yield strain of the weld metal was predicted in the weld metal area, as shown in Fig. 4-18. It may be deduced from Fig. 4-18 that failure will occur in the weld with a failure plane at around 10^{o} to the vertical plane.

The size of the weld was increased by 12.5% and 25% to 9 and 10 mm, respectively and the same tensile load was applied. Fig. 4-19 and Fig. 4-20 show the von Mises strain distribution predicted from the models with 9 and 10 mm leg length, respectively. The resulting strain decreased by 44% and 72.5% with an increase of weld leg length by 12.5% and 25%, respectively. The size of the weld is seen to have a significant effect on the strain developed in the welded joint. Under a lower load, when the majority of the joint is still in the elastic region except at the weld toe and root due to stress concentration, the effect of weld size on the maximum von Mises strain developed is less significant. For example, under a tensile stress of 100 N/mm^2, the strain decreased by 7.8% and 13.9% with an increase of weld leg length by 12.5% and 25%, respectively.

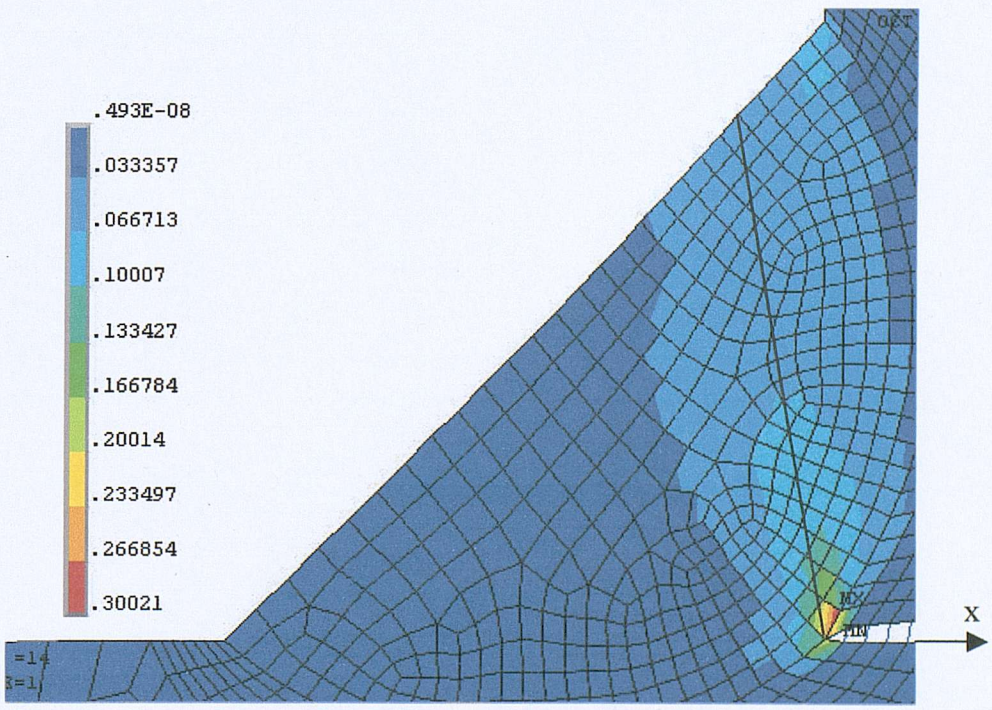

Fig. 4-18 Total von Mises equivalent strain in the model with an 8 mm leg length and no penetration subject to tension

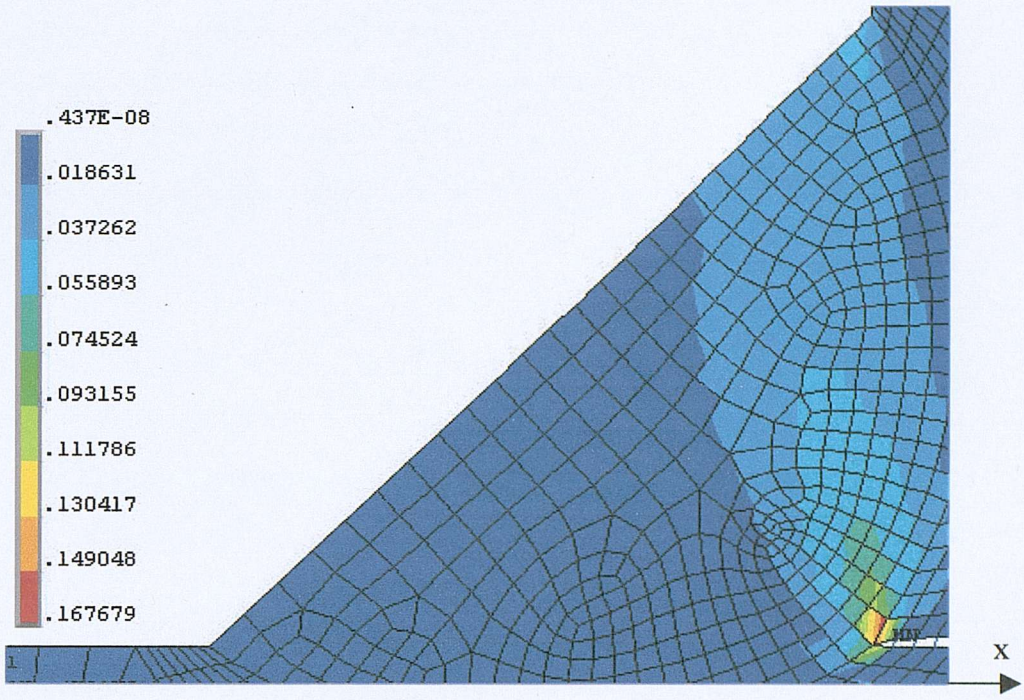

Fig. 4-19 Total von Mises equivalent strain with a 9 mm leg length and no penetration subject to tension

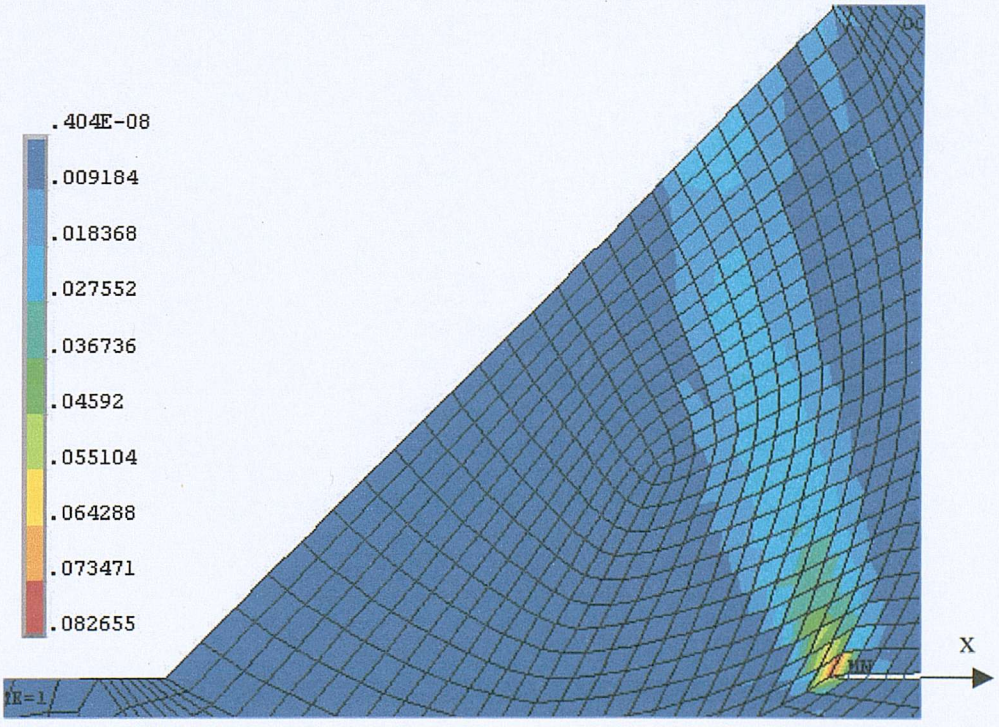

Fig. 4-20 Total von Mises equivalent strain with a 10 mm leg length and no penetration subject to tension

The stress concentration factor (SCF) at the weld toe under tension in this FE study was found equal to 1.7 for a weld leg length of 8 mm and this value decreased by about 18.2% and 27.1% when the weld leg length was increased by 12.5% and 25%, respectively, under the applied uniform stress of 350 N/mm^2. The SCF increased by 123.5% to 3.8 for the 8 mm leg length joint when the tension load decreased by 71%.

Conventional weld design assumes that the weld throat is the failure plane and that the stresses are uniformly distributed over the weld throat. However, test results have shown that the actual plane of failure does not coincide with the throat plane[3,4,5,6] and is positioned at a certain angle relative to the base of the weld. Furthermore, Solakian *et al.*[7] concluded that the stress distribution over the weld throat area is not uniform as the conventional design method assumes. The present FE study produced results that support the above arguments.

4.6.2 Penetration depth

Fig. 4-21 shows the result of the equivalent strain distribution in the joint with the leg length of 8 mm and 1-mm penetration under the same tensile loading as that applied to the model without penetration as discussed in Section 4.6.1. Comparing these von Mises strain results with those shown in Fig. 4-18, the maximum strain is found to decreased by 50.4%. It is thus clear that the introduction of penetration increased the load carrying capability significantly.

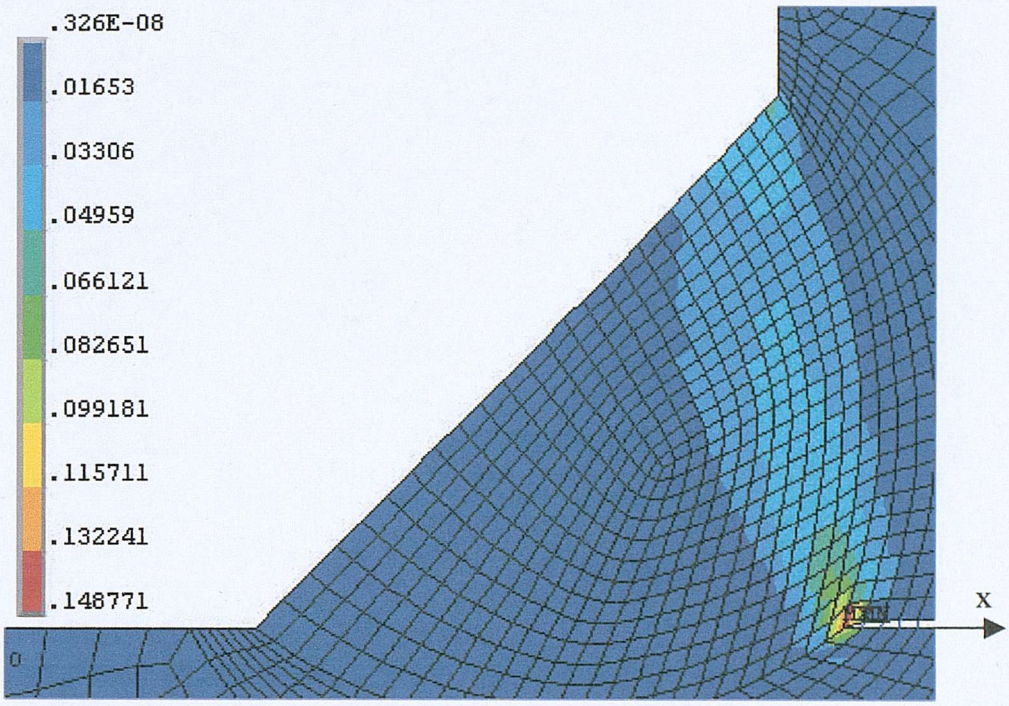

Fig. 4-21 Total von Mises equivalent strain in the model with 8 mm leg length and 1mm penetration under tension

4.6.3 HAZ size

The length parameters w, d_1 and d_2 were introduced, as shown in Fig. 4-22, in order to vary the size of the HAZ within the ANSYS program. These were changed to study the effect of the HAZ size on the behaviour of the welded joint under bending and tension. The original values of these parameters were w = 1 mm, d_1 = 1.5 mm, and d_2 = 3.5 mm (see Fig. 4-2)

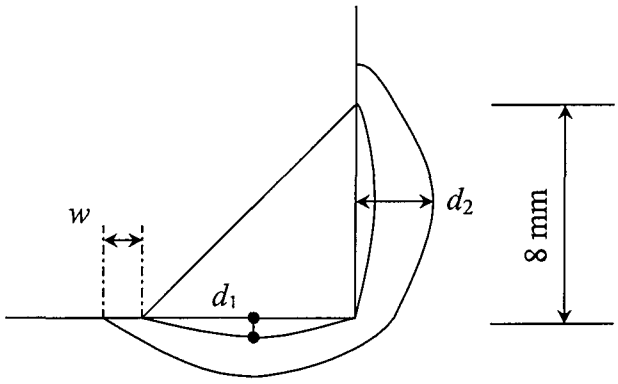

Fig. 4-22 Dimensions of HAZ

(a) Variation of w

Fig. 4-23 and Fig. 4-24 show, respectively, the predicted von Mises stress and equivalent strain distribution along the tensile edge of the side plate under a bending moment of $M = 1.49\ M_Y$ ($M_Y = 100.8$ kN mm) for a range of w values. From the von Mises stress distribution shown in Fig. 4-23, it can be seen that the distance between the position where the stress begins to rise and the weld toe is affected by the width of the HAZ. The wider the HAZ, the larger the region over which the stress rises, and the lower the stress concentration factor. The maximum strain away from the weld toe is not affected by the magnitude of w and the distance of the maximum value from the outer edge of the HAZ remains very similar for different w values. In the vicinity of the HAZ, however, both the peak magnitude and the distribution were affected. A contour plot of the von Mises equivalent strain for the joint under tension is shown in Fig. 4-25. It may be noted that due to reduced size of the weld leg length (8 mm) and of w (0.5 mm), while the number of line divisions used to mesh the model was kept the same, smaller size elements were generated in the weld and HAZ area. Path A is predicted to define the critical plane and the stress and strain distributions along this critical path were examined for various w sizes and were found to have very little variation. Comparing Fig. 4-25 with Fig. 4-18, the variation of w has no significant effect on the strain developed in the weld area.

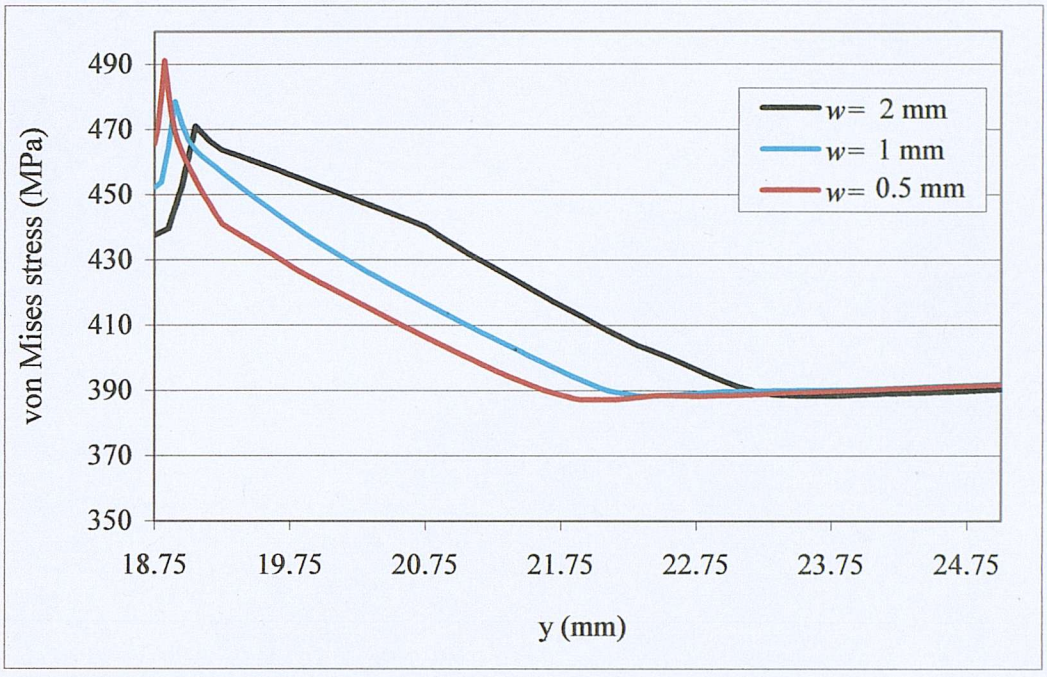

Fig. 4-23 Stress distribution along the tensile edge of the side plate for various *w* (Fig. 4-22)

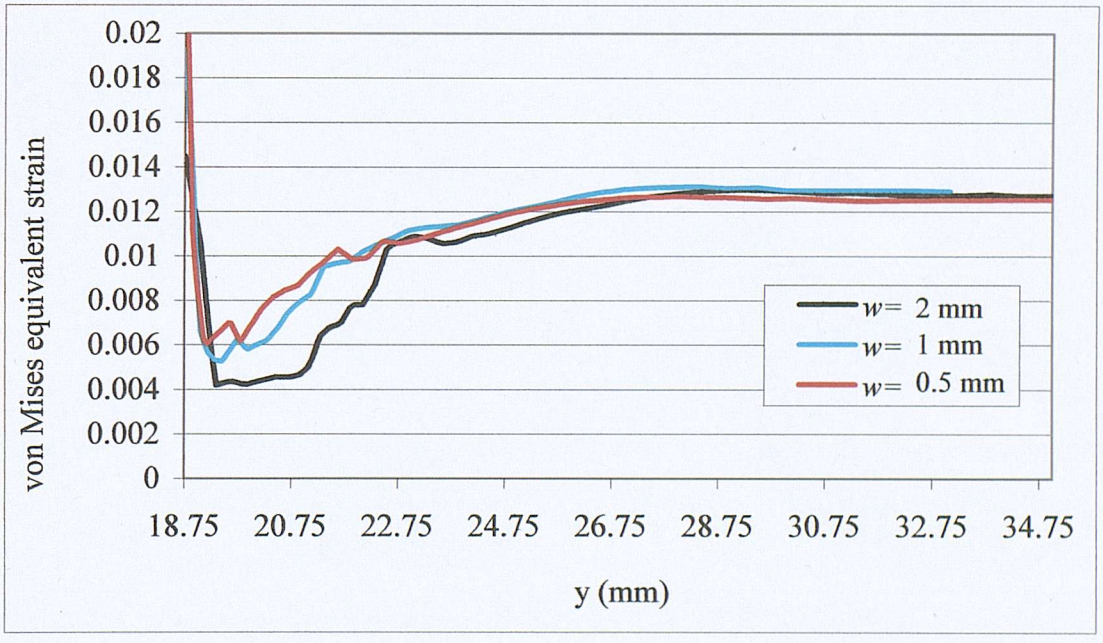

Fig. 4-24 Strain distribution along the tensile edge of the side plate for various *w* (Fig. 4-22)

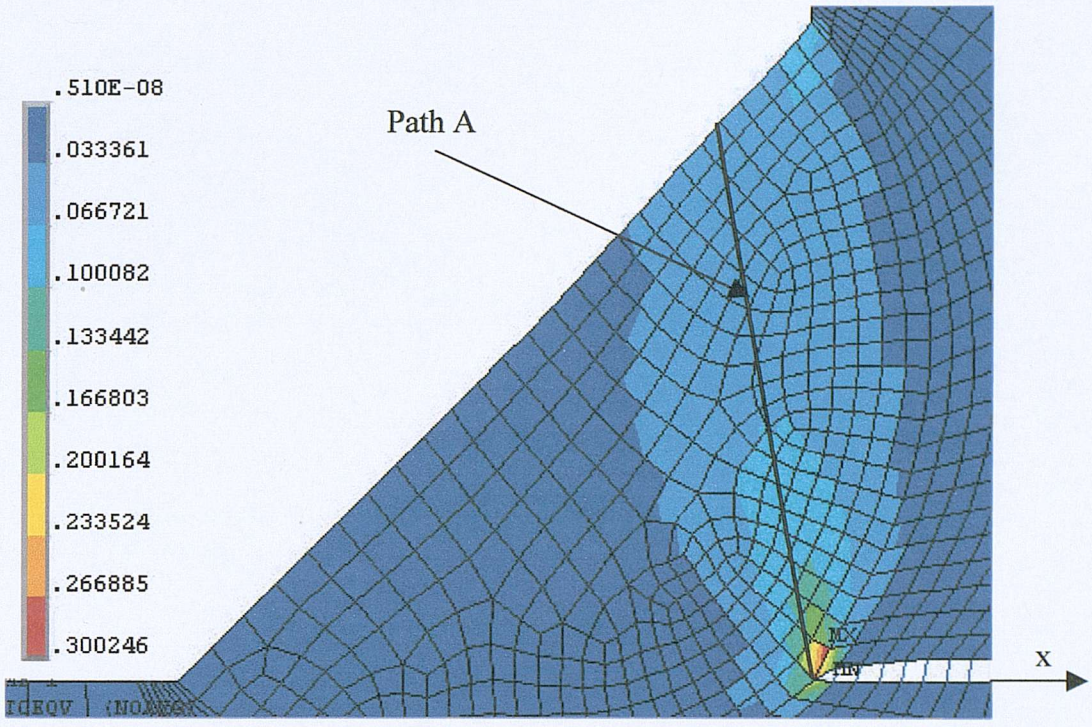

Fig. 4-25 Contour plot of equivalent strain under tension (w=0.5)

(b) Variation of d_1

The curves shown in Fig. 4-26 allow a comparison of von Mises stress distributions under bending for different d_1 values. There is very little variation in these distributions for positions away from the HAZ. However, a wider d_1 produces a slightly higher stress at the weld toe and a lower value within the HAZ, but the difference is only less than 3.5%, which is not very significant.

The effect of the magnitude of d_1 on the behaviour of the joint under tension was also studied. Fig. 4-27 shows the overall von Mises strain distribution from which the possible failure path (Path A) can be identified. Fig. 4-28 shows the von Mises stress and strain distributions along the path A. Increasing d_1 by 100%, from 1 mm to 2 mm, decreases the stress and strain at the weld root by 11% and 8.6% respectively. The effect of d_1 value on the orientation of the critical path is not significant.

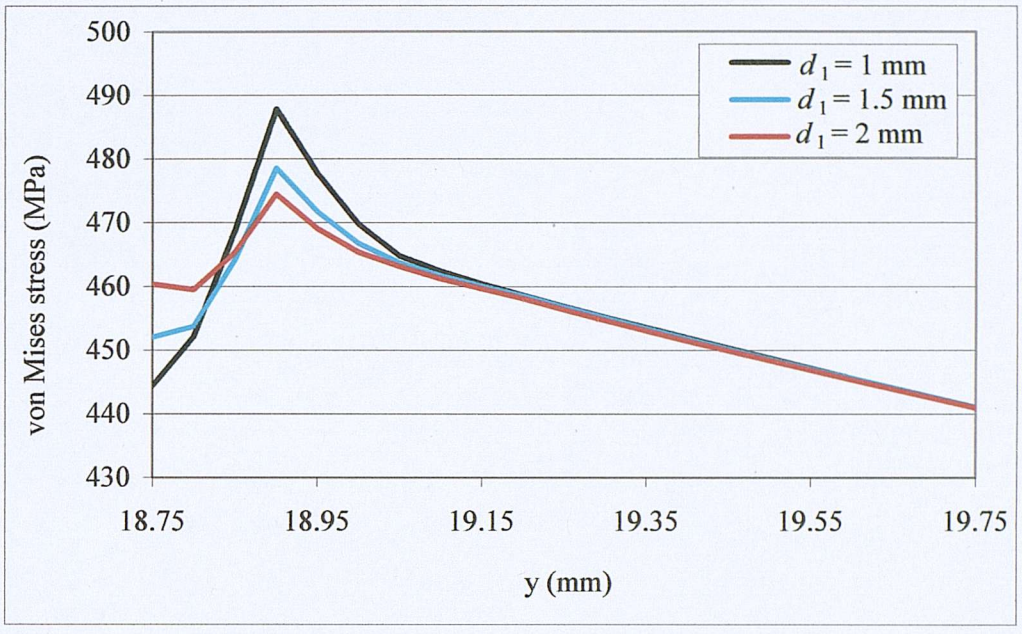

Fig. 4-26 Dependence of von Mises stress along the tension edge on d_1 (see Fig. 4-22) – joint under bending

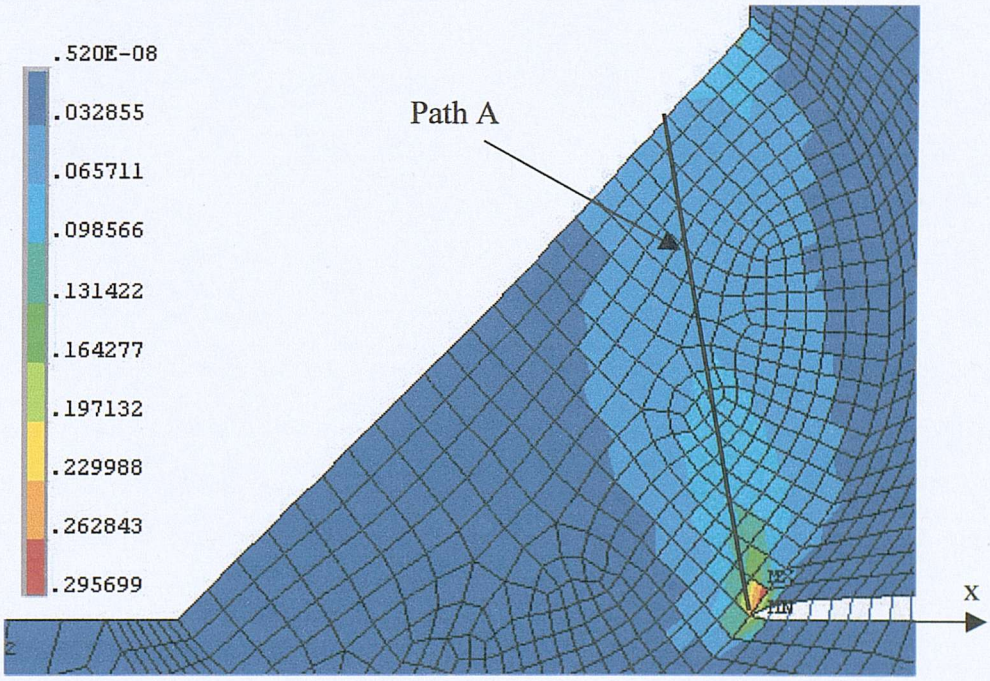

Fig. 4-27 Contour plot of von Mises equivalent strain with side plates under tension (d_1 = 2mm)

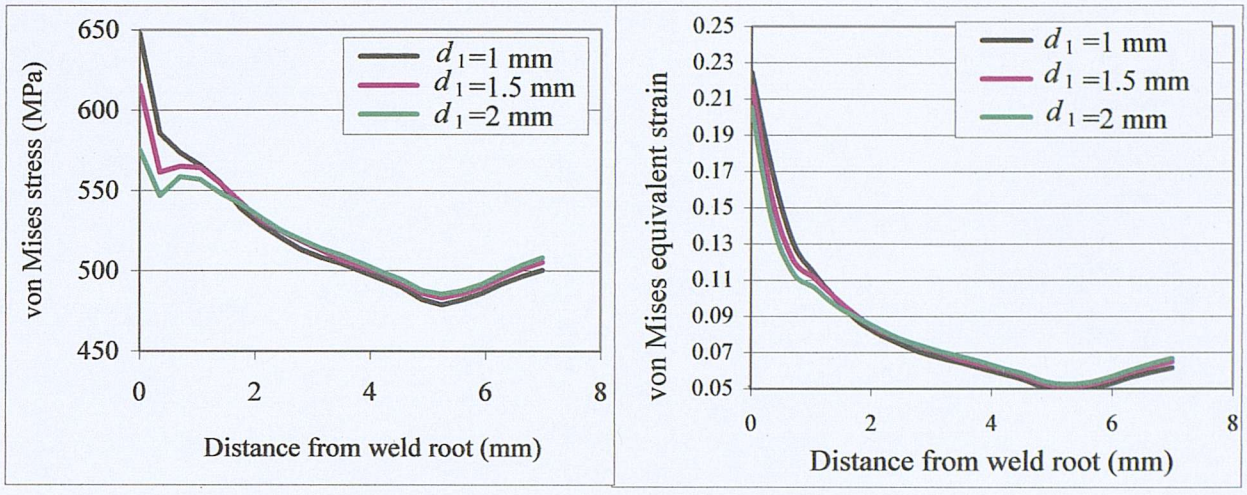

Fig. 4-28 Dependence of von Mises stress and strain distributions along path A (see Fig. 4-27) on d_1

(c) Variation of d_2

The effect of dimension d_2 on the stress and strain distribution has also been studied by varying its magnitude. No significant effect has been found when the cruciform joint is under bending. Fig. 4-29(a) shows the von Mises strain distribution for different d_2 values. In the region beyond 6 mm from the weld toe, the value of d_2 has no effect on the strain distribution, but in the region near the weld toe, the magnitude and distribution of the strain varies slightly with the d_2 values. The depth of the HAZ does not affect the stress concentration factor at the weld toe, as indicated by Fig. 4-29(b). It has also been found that the magnitude of d_2 has very little effect on the stress and strain distribution along the critical path in the weld area when the joint is subjected to tension.

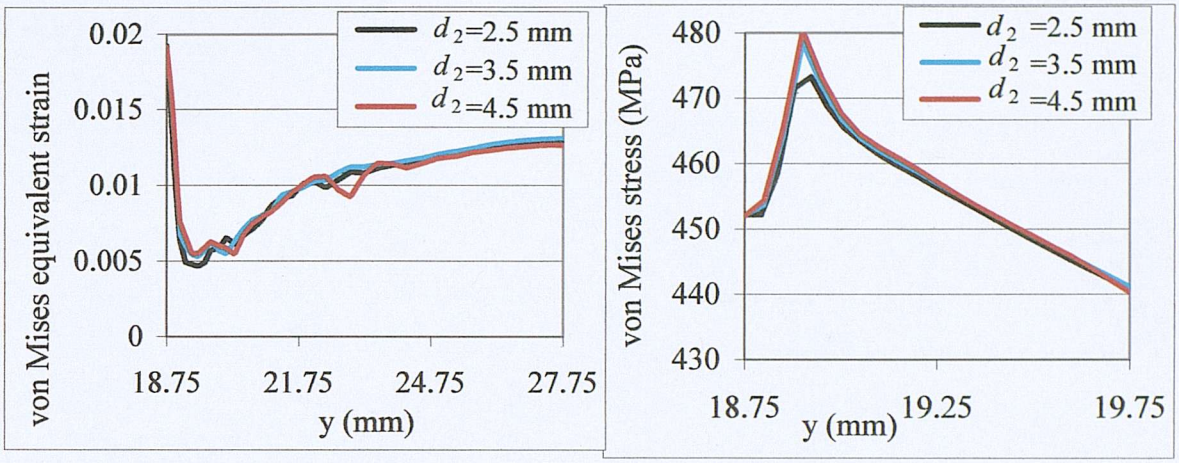

(a) von Mises equivalent strain distribution (b) von Mises stress distribution

Fig. 4-29 Dependence of stress and strain along the tension edge on d_2

4.6.4 Effect of plate length

The effect of changing the whole joint dimensions was examined as well by increasing L and l (see Fig. 4-1) by 100%. As expected, the length of the main plate does not affect the strain distribution since this plate is not load bearing. The length of the side plate, under either pure bending or tension, has also very little effect on the stress and strain distribution.

4.7 Summary and discussion

A cruciform welded joint, which has been tested by other investigators, has been analysed here using FEM. The reliability of the FEM model was examined by solving a benchmark problem, carrying out a mesh sensitivity study and comparing the principal strain difference-moment relation with experimental measurements. A 3.3% lower yield strength, a 1.6% thinner plate thickness, the presence of tensile residual stresses, and applying a gradual change of material properties cross the HAZ to the base metal were found to produce a closer agreement with the experimental

measurements. The sensitivity of the FEM prediction of strain distribution to material property variations was studied. Parametric studies were carried out on this model to study the effect of weld size and loading condition on the behaviour of the welded joint.

Comparison with the experimental results obtained by Fessler and Pappalettere[1] is hampered by the limited information provided. Because the principal strain difference results in the plastic region are very sensitive to the magnitude of the bending moment applied, information on accurate values of load applied, the stress-strain behaviour of the material as well as the cross sectional dimensions is vital. Uncertainty on the accuracy of the experimental results is another problem which makes the comparison difficult.

The geometry of the weld area simulated is not exactly the same as that of the experimental model. Geometric symmetry was assumed in the FE model, which is unlikely to be true in the real specimen.

Welding induced residual stresses were not included in this model. Such stresses may have some effect on the yielding behaviour of the joint depending on the directions of residual stresses as well as loading.

Failure of the joint under static load in this study is predicted from the von Mises equivalent stress/strain developed. In reality, small defects in the form of cracks may occur which modify the stress and strain magnitudes and distributions thus leading to fatigue and fracture at much lower loads.

It has been found from the modelling process that the strain distribution within and in the vicinity of the HAZ is very sensitive to the accurate representation of the gradual change of material properties in this area. Care should be taken when the detailed strain distribution is vital, for example, when assessing fatigue crack initiation, which normally start at the weld toe, and crack propagation behaviour. This model was intended only to demonstrate the importance of adopting a gradual change of material properties on the strain distribution. This gradual change would be

represented more precisely if the distance from the weld toe to the unchanged base metal is known. A finer and more regular mesh would also give more accurate results. However, to represent this gradual change in the FE modelling process is time-consuming. The mesh should then be decided depending on the accuracy requirement of the problem studied.

For welded joints with a combined weld throat larger than the thickness of the plates they join, failure is likely to occur in the plates. For smaller welds, failure is likely to occur in the weld with the failure plane located at an angle less than that of the throat to the weld edge. This is because the stress concentration at the weld toe is increased as the weld size decreases. The strength capability of the welded joint is increased by the introduction of weld penetration. The size of HAZ has some effect on the stress and strain distributions over and around the weld and HAZ areas. However, within the ranges studied here, these effects are generally too small to have a significant influence on the static strength of the joint.

References

[1] Fessler H., Pappalettere G., Fillet welds under bending and shear, *5th International Conference on Pressure Vessel Technology*, pp47-61, Sept. 1984
[2] ANSYS, *SAS, Inc.*, 1999
[3] Higgins T.R., Preece F.R, Proposed working stress for fillet welds in building, *Welding Journal Research Supplement*, **47**(10), pp429s-432s, 1968
[4] Fessler H., Pappalettere C., Plastic-elastic strains in two-dimensional section, *Journal of Strain Analysis*, **24**(1), 1989
[5] Barshi, O.A., Zaitsev, N.L., Increasing the load-carrying capacity of lap and T, *Welding Production*, **24**, pp1-4, 1977
[6] Kamtekar A.G., A new analysis of the strength of some simple fillet welded connections, *Journal of Constructional Steel Research,* **2**(2), pp33-45, 1982
[7] Solakian A.G, Claussen G.E., Stress distribution in fillet welds – *A Review of The Engineering Foundation Welding Research Committee*, pp1-24, 1937

5 Experimental study on welded T joints

5.1 Introduction

Finite element analysis is a cost-efficient method of studying the behaviour of welded joints and structures, but its reliability depends upon the accuracy of the input. Confidence in the generated FE models will be low unless they have been validated through experimental measurements and/or other analytical calculations. For this purpose, a series of experiments has been performed on fillet welded T joints with similar geometry to those analysed using FEM as described in the subsequent Chapters 6 and 7 of this thesis. Fig. 5-1 illustrates the flow chart of the whole testing procedure. The T joint was chosen because it is very common in engineering applications and has a more complex load transfer behaviour than a butt weld. One example is the wide application of fillet welded T stiffeners in ship building. Two types of T-joints have been produced, one welded in the Engineering Design and Manufacture Centre (EDMC) of the University of Southampton, which is referred to as WT1 in this thesis, and one commercially welded by Cussons Technology Limited[1], which is referred to as WT2. As the strength of the weld is the primary interest of this project, for the WT1 weldment, the fillet welds were sized so that failure will occur in the weld prior to the base metal under load. In addition, this type of smaller than full strength fillet welds are widely used in practice in rigidity or stiffener design where a full strength weld is not necessary. For example, 50% or 33% of full strength weld may be used in rigidity design[2]. Appendix E gives more detail on the WT1 weldment sizing.

From the flow chart of Fig. 5-1 it can be seen that the experimental study can be split into three areas; the welding process for a T-joint, material property tests, and load-carrying behaviour tests. The results obtained from the FE modelling of the T-joint specimen suggested critical measurement positions for the experiments. On the other hand, the material properties and welding parameters obtained from these tests can be incorporated into the FE model using APDL in order to improve the accuracy of the analysis.

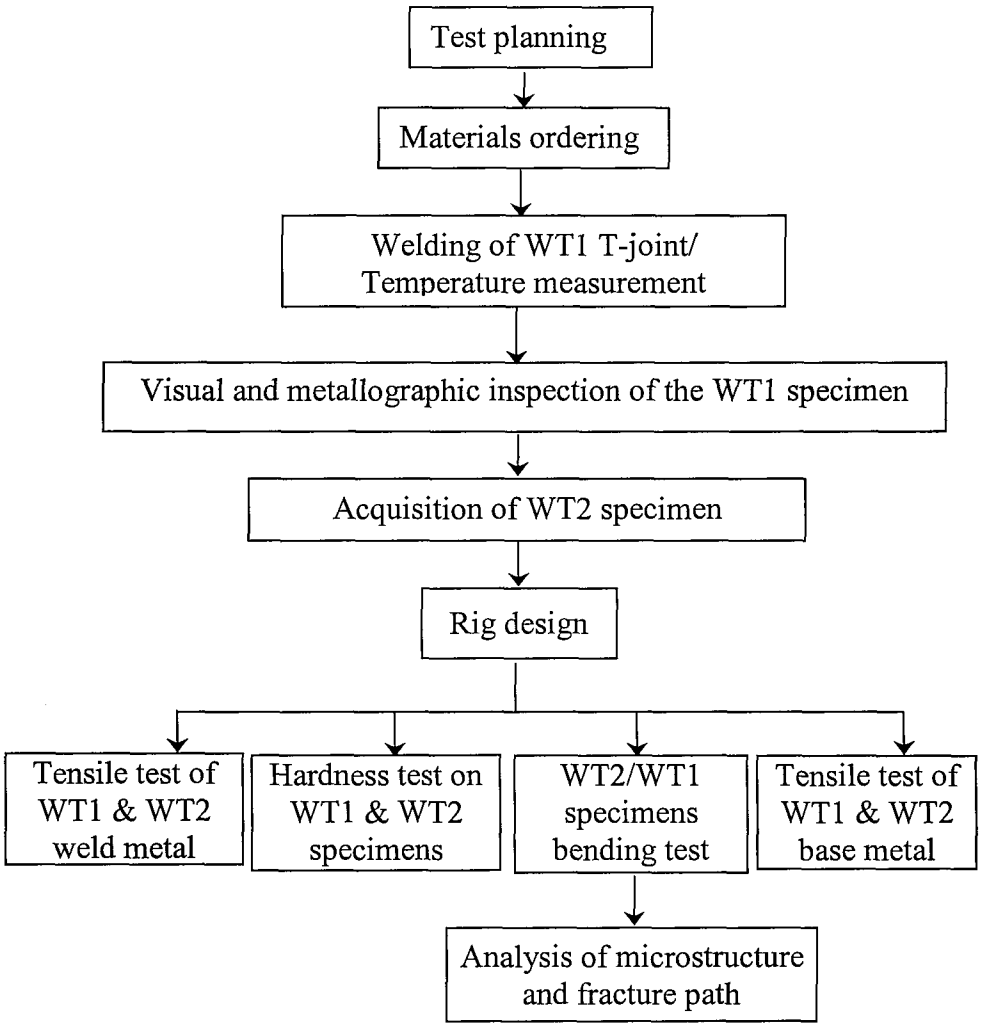

Fig. 5-1 Flow chart of the test procedure

5.2 Welding of the WT1 T-joint

5.2.1 Welding process

An attachment of nominal dimensions 120 × 500 × 12 mm was joined to a main plate of dimensions 260 × 500 × 12 mm by two single-pass fillet welds, the leg length of which was designed as 7 mm. There was no weld preparation of the WT1 weldment. A MIG Star 330C welding machine was used with BS 290 Pt1:A18 solid mild steel MIG welding wire of diameter of 1 mm. K-type thermocouples[3] were used to measure the temperature development during the weld heating and cooling processes. The positions where the thermocouples were attached are shown in Fig. 5-2.

Thermocouples TC8, TC11 and TC12 are Type K MI (125)[3] with Pot 1.0 mm and they were placed into pre-drilled holes from the side of the plate so that the temperature inside the plate could be measured. All the other thermocouples are Type K welded Tip Fibreglass thermocouples, which were spot-welded onto the surface of the plates using a J28M Instrument Welder. The temperature resulting from welding at the measuring positions are expected to be well within the measuring range of the thermocouples, i.e. 0-1100 °C. The main purpose of the temperature measurement is to provide temperature development data for residual stress analysis where the temperature gradient is more important. Very accurate absolute temperature is thus not vital, as also demonstrated by the residual stress modelling presented in Chapter 3 which indicated that a few degrees of temperature difference has negligible effect on the final residual stress results. The measurement of the thermocouple type used vary within ±1.5 °C for temperature under 375 °C or ± 0.004 T for temperature higher than that[3]. An accurate calibration of the thermocouple is thus considered not necessary. A HP Agilent 34970A data logger was used to collect the temperature results digitally. Although the instrument is capable of scanning 250 channels per second, due to the limitation of the storage capacity, for a recording period of more than three hours, the time interval of scanning was set to 0.4 second. During the welding process, the welding arc voltage and current were measured using an ISO-Tech ICM37 clamp multi-meter; and welding time for the two passes and the duration between the two passes was also recorded using a stop watch.

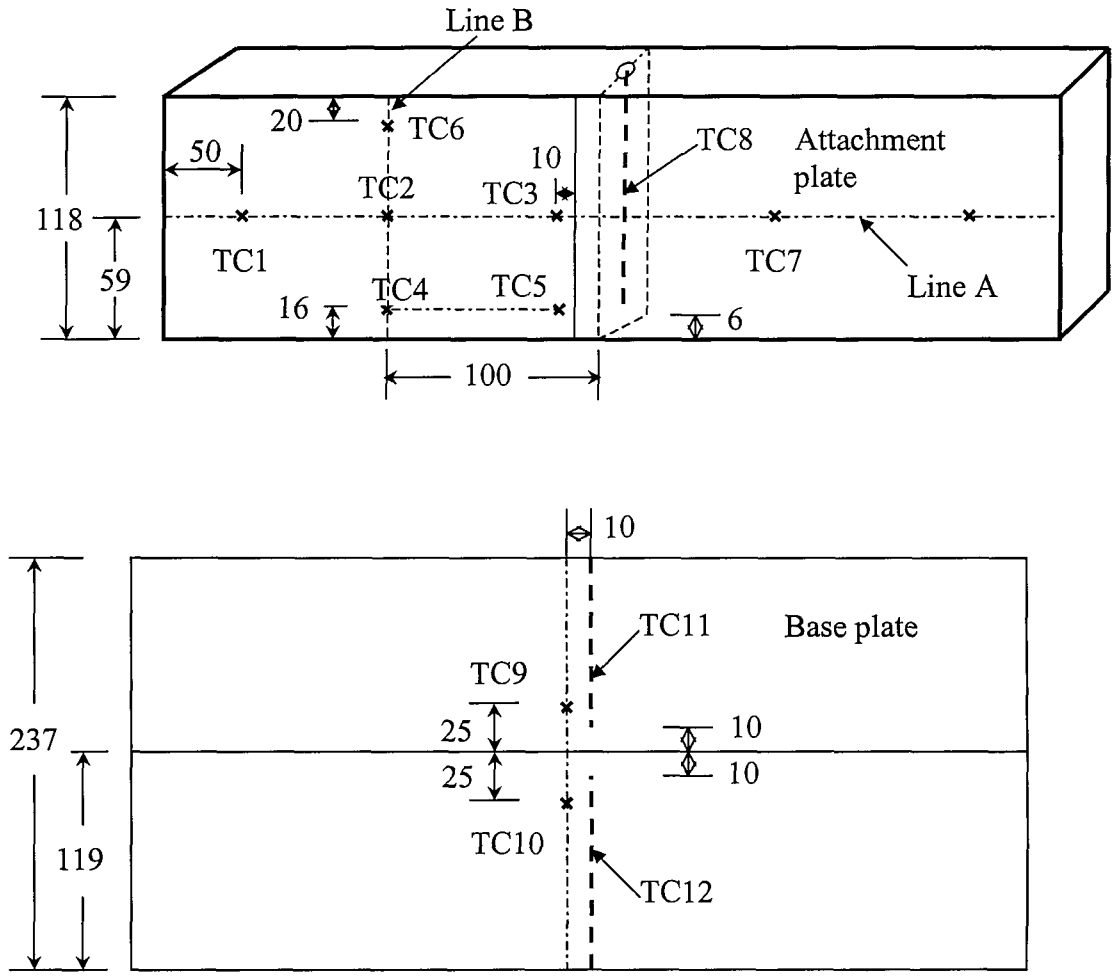

Fig. 5-2 Positions of the thermocouples attached to the WT1 weldment, dimensions in mm

5.2.2 Results and discussion

Table 5-1 shows the welding process set up parameters including welding voltage, current and durations of the welding process for both the first and second pass. The cooling time between the two passes was about 7 minutes. All these recorded parameters will be used in the welding process simulation presented in Chapter 6 of this thesis to obtain the welding induced residual stresses.

Table 5-1 Welding parameters

Weld pass	Voltage, V	Current, A	Duration, s
First pass	26.6	200	248
Second pass	24.4	200	241

The temperature development results for all the thermocouples are shown in Fig. 5-3. Temperature results recorded from the thermocouples along Line A (see Fig. 5-2) are shown in Fig. 5-4. It is evident that the temperature at the four positions along this line A develops during welding in the same way and the peak temperatures reached are also very close. The small difference in peak temperatures may be caused by possible variation in actual measurement positions from the hand-operated spot-welding of the thermocouples, as well as variation in arc heat input during welding as it is difficult to maintain a uniform welding speed and hence arc heat input during welding by a hand operation. This proves that except from the regions near the ends of the plate, the majority of the cross-sections are at a quasi-steady state, as observed by other researchers[4,5,6]. Fig. 5-5 shows the results from thermocouples along Line B (see Fig. 5-2). The peak temperature in the plate drops rapidly from position 4 to position 2, however, the rate of decrease is much slower from position 2 to position 6, although the distance between these three positions is very similar. This indicates that the high-amplitude, high-temperature heating and cooling cycle is very localised around the weld.

Table 5-2 lists the measured weld leg length and throat dimensions at different positions along the longitudinal length of the weldment for the two weld passes. The weld size, measured every 10 mm, is listed in Appendix F. Table 5-3 shows the measured distortion of the weldment, again, along the longitudinal direction in terms of the angle for the first weld, α, as shown in Fig. 5-6. Fig. 5-7 shows the dimensions of weldment after welding. Although the attachment plate had been aligned to the centre line of the base plate, due to welding distortion and no constraints applied, the far end of the plate moved 20 mm from the centre line during welding.

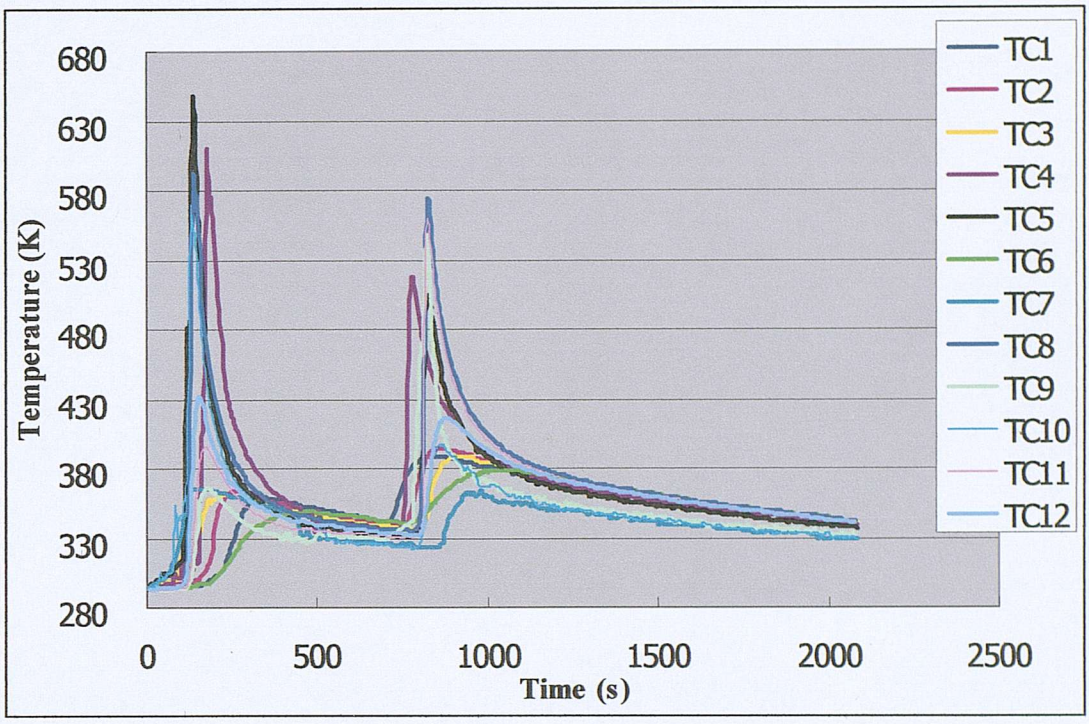

Fig. 5-3 Temperature development results during the welding process

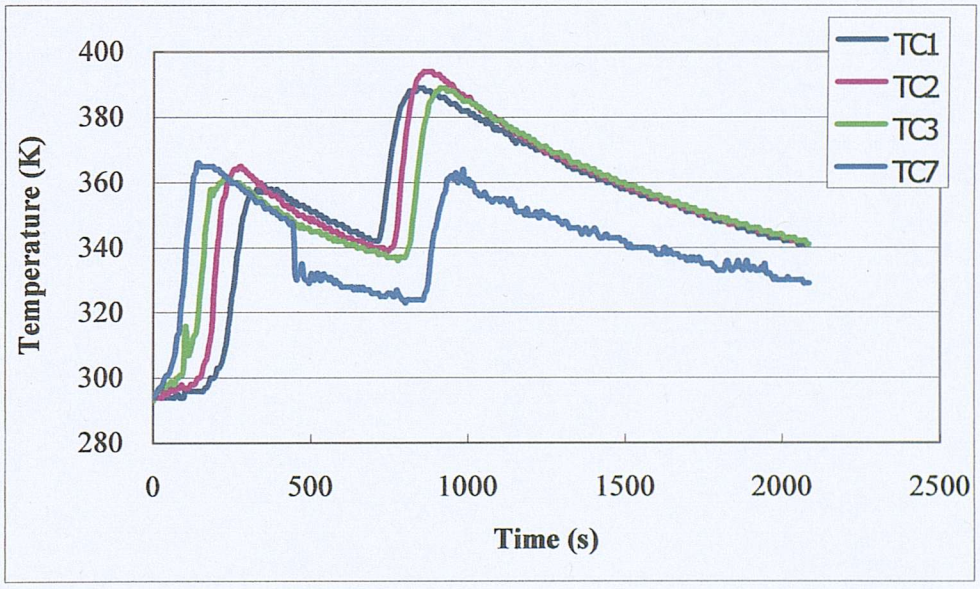

Fig. 5-4 Temperature results along Line A (see Fig. 5-2) during the welding process

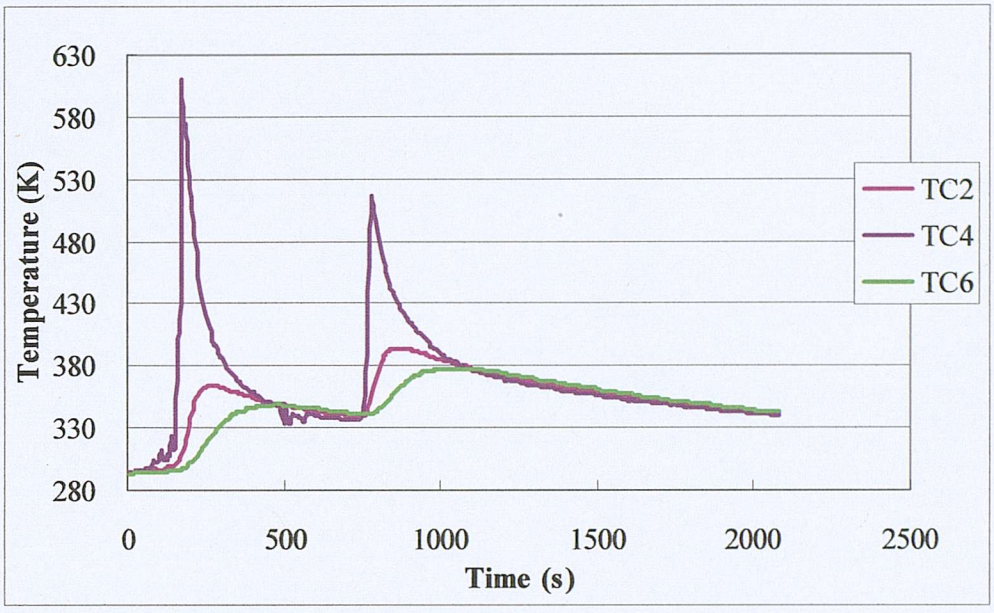

Fig. 5-5 Temperature results for positions along Line B (see Fig. 5-2) during the welding process

Table 5-2 Measured weld leg length and throat of the WT1 weldment

Distance from start of weld run (mm)	First weld pass		Second weld pass	
	Leg, mm	Throat, mm	Leg, mm	Throat, mm
10	6.8	3.0	7.0	6.0
100	6.8	3.0	6.0	6.0
200	6.0	2.3	5.5	6.0
300	6.0	3.0	5.8	6.2
400	6.5	3.0	5.9	6.0
490	6.0	3.0	6.4	6.5

Table 5-3 Distortion of the weldment

Distance from start of weld run (mm)	10	100	200	300	400	490	Average
Angle, α (°)	86.0	86.0	86.0	86.5	86.6	86.8	86.3

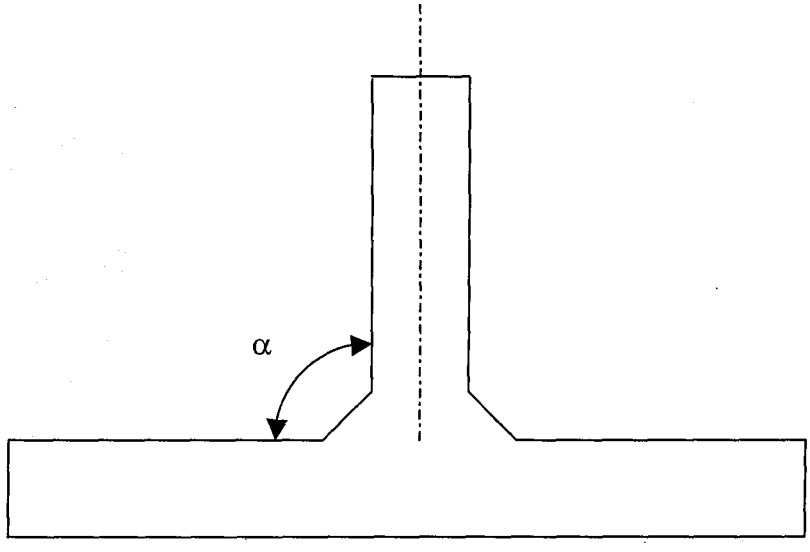

Fig. 5-6 Distortion of weldment WT1

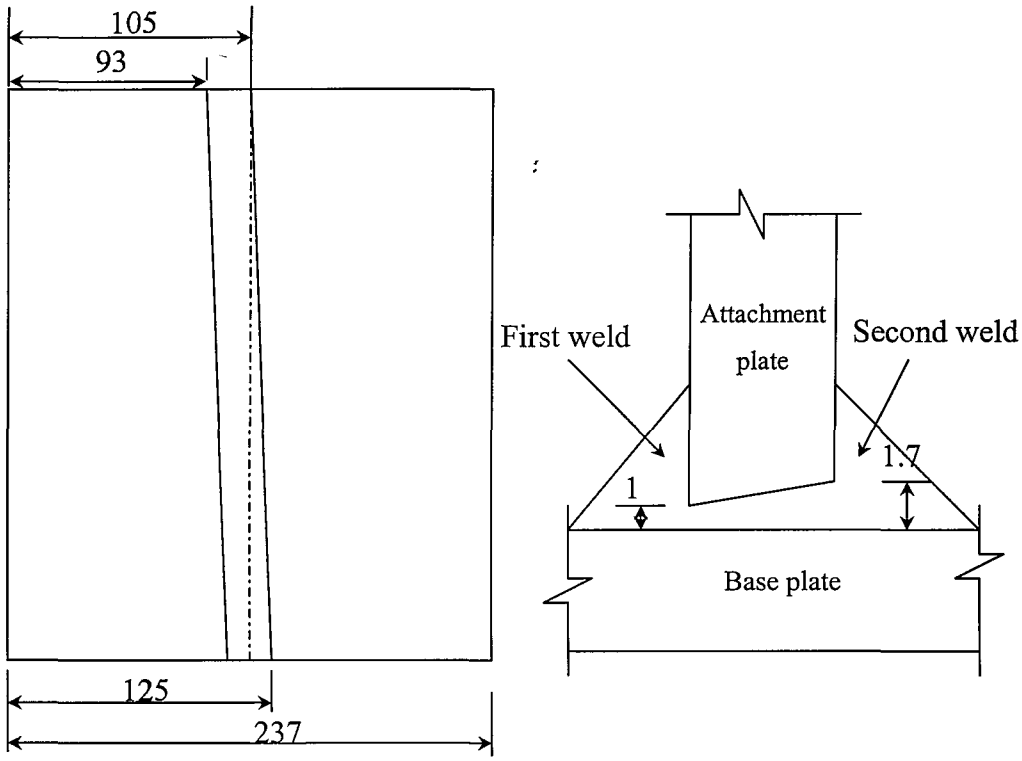

Fig. 5-7 Dimensions of the WT1 weldment after welding

5.2.3 Inspection of the WT1 weldment

As shown in Table 5-2 and Table F-1, relatively big variations in weld size were found along the weldment. Visually inspection also clearly revealed that the weld profile varied along the weld length. A cross section of the welded joint is illustrated in Fig. 5-8. Lack of penetration at the right side weld root is clearly seen. In addition, referring to the etched specimen shown in Fig. 5-19, more defects including lack of penetration in the side and root of the left-hand side weld, and porosity is present in the WT1 weldment. The profiles of the two sides are also very different. Though the presence of such defects was not intended, the WT1 weldment still provided useful temperature data for accessing the thermal part of residual stress analysis. In addition, the effect of defects can be studied using this weldment. However, a better quality weld is desired to study the behaviour of welded joints with acceptable quality. A commercially welded T-joint was thus obtained from Cussons Technology Limited[1].

that weldment was visually inspected and found satisfactory. Details on its manufacture are given in Section 5.3.1 (B).

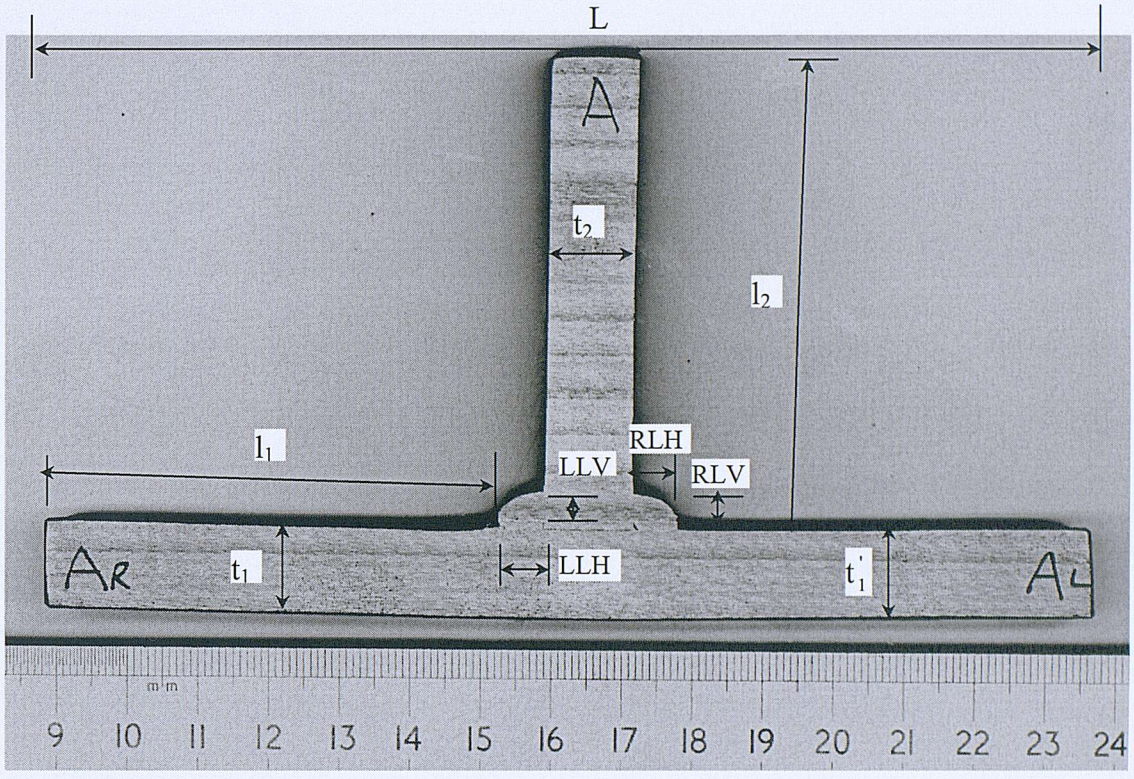

Fig. 5-8 A typical cross section of the WT1 weldment

5.3 Material properties tests

5.3.1 Tensile test on base metal

Accuracy in material property data is one of the most important factors in predicting reliably the behaviour of structures. A standard tensile test was carried out for the base metal to obtain its elasto-plastic stress-strain relation and basic mechanical properties such as the yield strength/0.2% proof strength, ultimate strength, Young's modulus as well as elongation to failure.

A) WT1 weldment

Specimen

The base metal used is BS 4360 – 43A grade steel that has a specified yield strength of not less than 275 MPa and a tensile strength of between 430 and 580 MPa[7].

ASTM[8] standard rectangular tensile test specimens with a gauge length of 50 mm were manufactured from the steel plate and tested. Details of the specimen dimensions, and apparatus used in the tensile test are given in Appendix G.

Results

The yield strength, tensile strength, elongation to failure and Young's modulus obtained from the three specimens are listed in Table 5-4. It can be seen that these results are within the required bounds according to the corresponding British standard (BS 4360 - 43A). The engineering stress-strain curves from which they were extracted are shown in Fig. 5-9. The true stress, σ, and the logarithmic strain, ε, which are the required input to an elasto-plastic, large deformation analysis are calculated from

$$\sigma = \sigma_0(1+\varepsilon_0) \tag{5-1}$$

$$\varepsilon = \ln(1+\varepsilon_0) \tag{5-2}$$

where, σ_0 is the engineering stress and ε_0 the engineering strain. It is assumed that the stress-strain behaviour is the same in compression as in tension. Both Table 5-4 and Fig. 5-9 show that the measurements from the three specimens were remarkably consistent.

Table 5-4 Base metal tensile test results for the WT1 specimens

Specimen	σ_Y (MPa)	σ_u (MPa)	E (GPa)	El (%)
A	289.4	449.8	207.2	26.9
B	290.2	451.5	201.1	23.9
C	290.8	445.8	205.1	25.9
Average	290.1	449.0	204.5	25.6

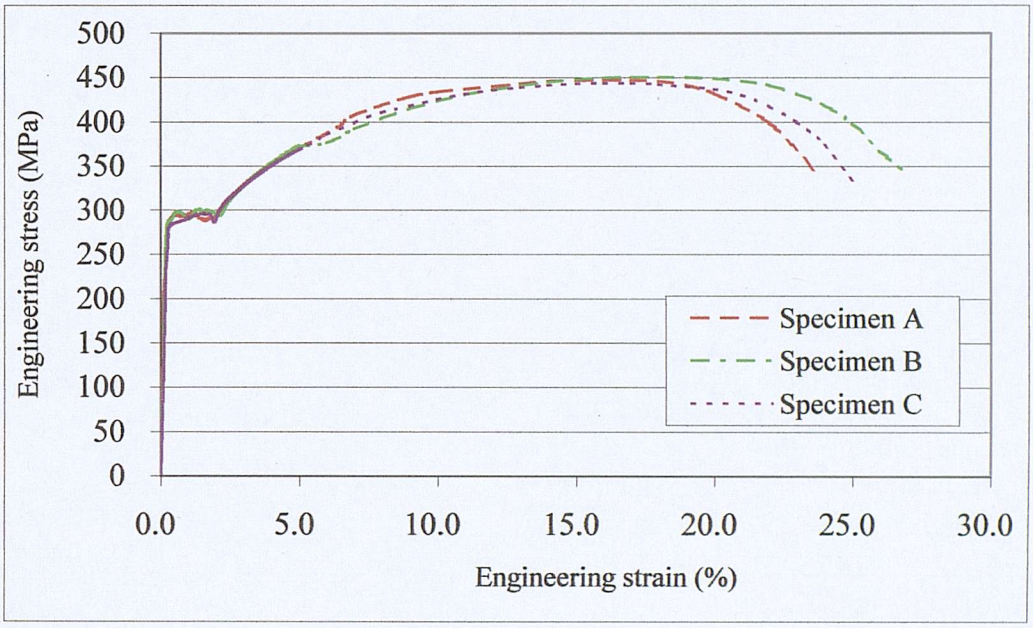

Fig. 5-9 Stress-strain curves of the base metal of the WT1 specimen

B) WT2 weldment

For the WT2 weldment obtained from Cussons Technology Limited, the grade of the steel was said to be BS 070 M20[1] (En 3A) mild steel that has a specified yield strength of not less than 215 MPa and a tensile strength of greater than 430 MPa[9]. Its elongation to failure is specified as 21% minimum. Its Brinell hardness would be expected to be in the 126-179 range.

The weld electrode used was 5 mm diameter Murex Zodian Universal (BS 639: 1986 E4322R; AWS:E6013)[1], with a specified yield strength of not less than 380 MPa and a tensile strength of greater than 470 MPa.

Specimen

ASTM standard round bar tensile test specimens were used, the details of which are listed in Appendix G. This type of specimen was chosen because an extensometer of 25 mm gauge length with 12.5 mm travel distance is available in the Materials Group which makes it possible to record the whole stress-strain curve from the test.

Results

The 0.2% proof strength, tensile strength, elongation to failure and Young's modulus obtained from the tests are listed in Table 5-5. The engineering stress-strain curves recorded from the tests are shown in Fig. 5-10. Unlike the base metal used for the WT1 weldment, there is no clear plateau in the stress-strain curves for WT2 base metal. Comparing the results obtained from the tensile tests to those given in the standard for the stated grade of the steel plate, it can be seen that the test strength results are much higher and the elongation much lower. Table 5-6 gives the results of chemical analysis on the WT2 steel. This satisfies the chemical composition requirement of 070 M20. The WT2 steel contains more carbon than WT1 and metallographic examination (see Fig. 5-22) indicates that it has a finer grain size. Finer grain sizes and higher carbon contents give improvements in strength. The reasons for the low elongation values to failure are not clear. It is possible that recrystallisation has not proceeded to completion after working, giving rise to a lower than expected elongation to failure.

Table 5-5 Base metal tensile test results for the WT2 specimens

Specimen	$\sigma_{0.2\%}$ (MPa)	σ_u (MPa)	*E* (GPa)	*El* (%)	*RoA (%)*
A	664.8	707.4	207.0	5.2	31.5
B	644.8	704.9	207.0	5.2	31.5
C	666.0	722.0		10.6	
Average	658.5	711.4	207.0	7.0	31.5

Table 5-6 Chemical composition of the WT2 weldment base metal

Ele.	C	Si	Mn	P	S	Cr	Ni	Mo	Nb
%	0.161	0.257	0.781	0.014	0.020	0.141	0.086	0.020	<0.01

Ele.	Cu	Ti	Al	V	As	W	Pb	Sn
%	0.155	0.011	0.028	0.003	0.011	< 0.01	< 0.01	0.004

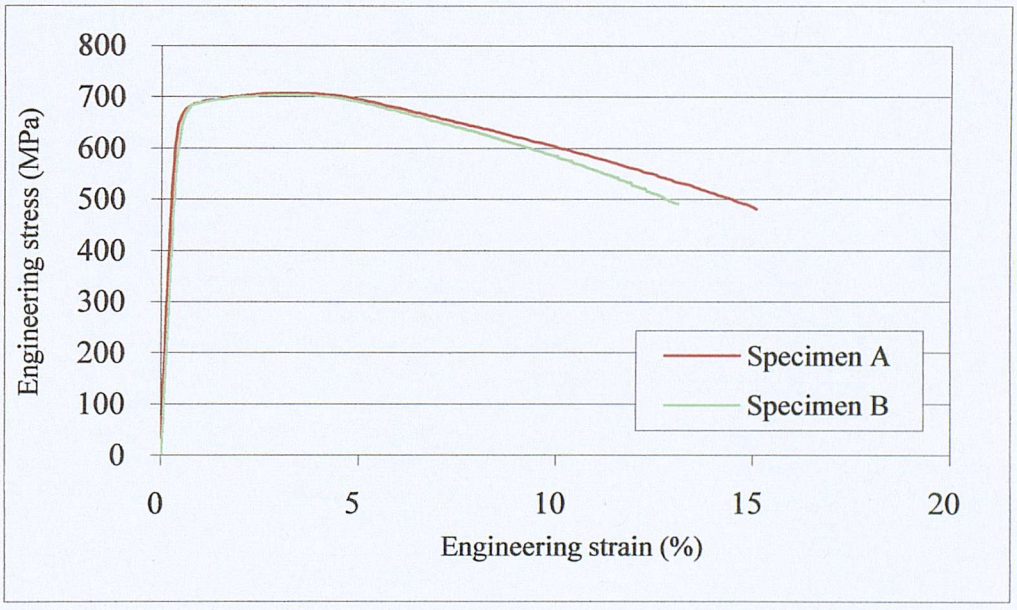

Fig. 5-10 Engineering stress-strain curves of the WT2 base metal

5.3.2 Tensile test on weld metal

Tensile tests on the weld metal have also been conducted in order to obtain its elasto-plastic properties as any difference between them and those of the base metal affects significantly the behaviour of the weldment. Standard round bar tensile specimens were extracted from the weld area and tested using the same procedure as for the base metal of the WT2 weldment. The dimensions of the specimen for both WT1 and WT2 are listed in Appendix G. The test results for the WT1 specimens are listed in Table 5-7; and for the WT2 specimens in Table 5-8. Fig. 5-11 and Fig. 5-12 show the stress-strain curves obtained from the tests on the weld metal of the WT1 and WT2 specimens, respectively. Big variations have been found in the elongation to failure values for the WT1 specimens. The reason for this is thought to be the randomness of weld defects present in the specimens. Due to manufacturing and size limitation, it is very difficult to extract a round tensile bar entirely from the weld metal, therefore defects such as those due to lack of fusion were included in the tensile specimens, as shown in Fig. 5-13. This inevitably affected the test results.

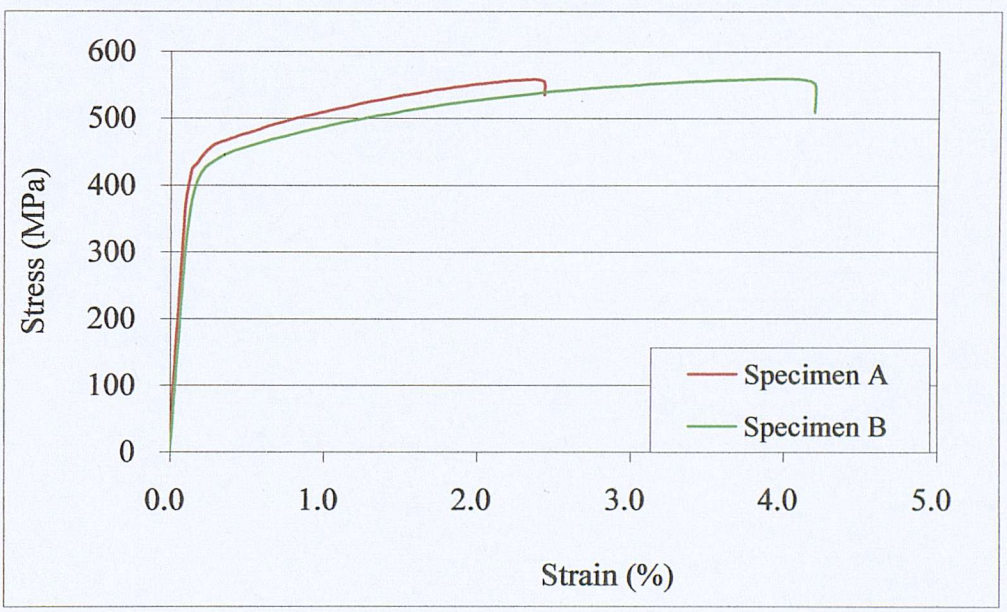

Fig. 5-11 Engineering stress-strain curves of the WT1 weld metal

Table 5-7 Weld metal tensile test results for the WT1 specimens

Specimen	$\sigma_{0.2\%}$ (MPa)	σ_u (MPa)	E (GPa)	El (%)
A	468.7	558.3	209.7	15.4
B	450.5	559.5	215.4	6.5
Average	459.6	558.9	212.5	10.9

Table 5-8 Weld metal tensile test results for the WT2 specimens

Specimen	$\sigma_{0.2\%}$ (MPa)	σ_u (MPa)	E (GPa)	El (%)
A	412.4	529.9	208.7	8.2
B	454.6	547.1	206.8	5.8
Average	433.5	538.5	207.8	7.0

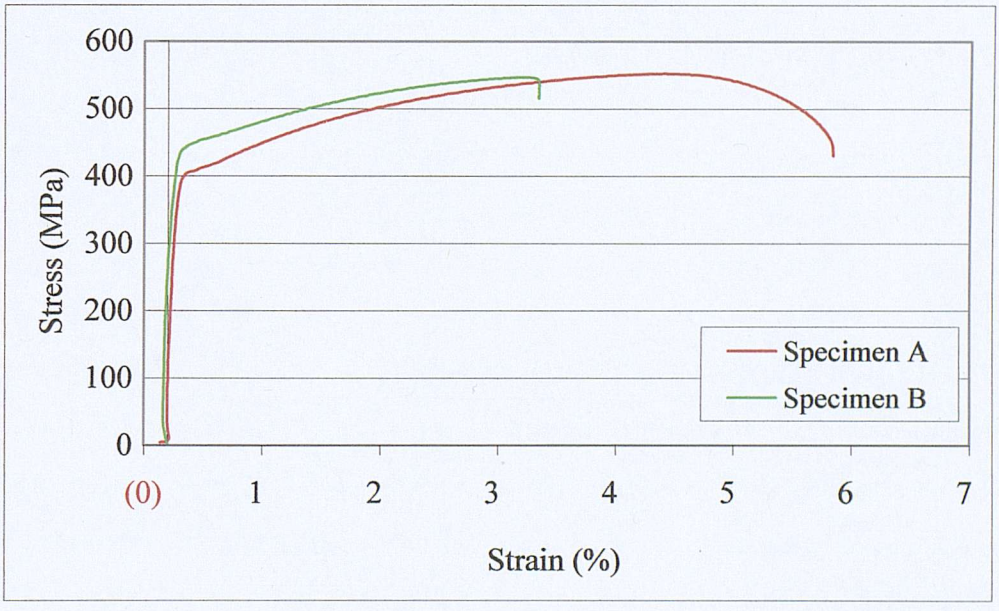

Fig. 5-12 Engineering stress-strain curves of the WT2 weld metal

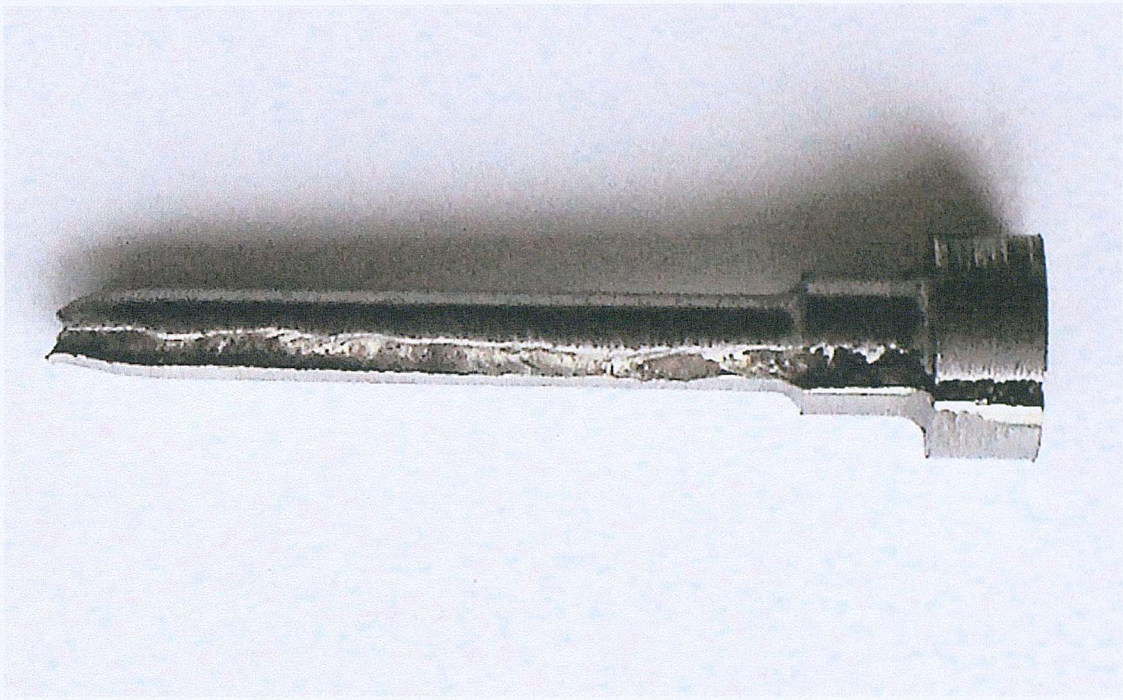

Fig. 5-13 Defects in tensile specimens for WT1

5.3.3 Hardness tests

Hardness is a measure of the resistance of a material to localized plastic deformation. From the hardness value, other mechanical properties of metals, such as ultimate tensile strength and 0.2% proof strength could be derived. Hence, the hardness test is an attractive indirect means for obtaining material properties, as these tests are easy and non-destructive. In addition, the result obtained from a tensile test is the strength for the whole specimen cross section, while from the hardness test, the hardness results are from a small indented area of material so that the variation of material properties over an area can be tracked. Another important reason why hardness tests were carried out in this study is because it is very difficult to perform a tensile test on the heat-affected zone of the weldment as this zone is too small to extract a tensile test specimen from it while in a hardness test, a number of indentations can be made over the HAZ. From the hardness number obtained, other properties of the HAZ can then be derived.

Hardness and strength are related to bonding forces on the atomic level. Therefore, it should be expected that hardness and strength are somehow related. A theoretical

relationship between hardness and strength, based on the complex mechanisms involved when a hardness indentation is made, is not practical. However, various relationships have been experimentally observed and empirically defined[10]. Tabor[11] has given the following relationship between hardness and ultimate strength of a material.

$$\sigma_u = \frac{H}{2.9}\left[1-(m-2)\right]\left[\frac{12.5(m-2)}{1-(m-2)}\right]^{(m-2)} \qquad (5\text{-}3)$$

where, σ_u is the ultimate strength of a material, kg/mm^2, H the Vickers hardness, kg/mm^2, and m the Meyer index. Cahoon et al.[12] derived a general expression which correlates the 0.2% proof strength with hardness for various material as follows:

$$\sigma_y = \frac{H}{3}(0.1)^{(m-2)} \qquad (5\text{-}4)$$

where σ_Y is the yield strength of a material, kg/mm^2; and H and m the same as in Eqn. (5-3). They also included the strain-hardening strength coefficient (defined in Appendix D) as this value would affect the yield strength versus hardness correlation.

In this study, Vickers micro-hardness tests have been carried out on sections of both WT1 and WT2 weldments. Specimens of 10 mm thickness were cut from the weldment, the surfaces of each specimen were polished and etched lightly to show the areas. To find the Meyer's index, a 2 mm ball Brinell indenter was used with the Vickers Hardness Tester to make indentations at loads, W, ranging from 20 to 120 kg. Since Meyer's index is defined through equation $W = kd^m$, it can be determined from the slope of the log W versus log d curve, where d is the diameter of indentation[13]. The corresponding ultimate and yield strengths were then calculated using equations Eqns. (5-3) and (5-4), respectively.

A) WT1 weldment

In total, 10 lines of indentations from the base metal across the HAZ as far as the edge of the weld fusion zone have been made with a distance between the indents of 1 mm. As the specimen has been etched, the type of weld area, i.e. base metal, HAZ or weld metal, within which the indentations were made was also recorded. Hardness values for base metal, weld metal and HAZ were then summarised and the yield strengths of these three areas were calculated from the averaged hardness values using Eqn. (5-4), as well as their ultimate strengths using Eqn. (5-3). Fig. 5-14 shows a contour plot of the hardness distribution over the specimen surface. Fig. 5-15 shows the hardness variation across the three areas at different positions along lines L1-L4 shown in Fig. 5-19. Some scatter in the values of hardness in the weld areas is seen. However the hardness of the weld metal and HAZ is consistently higher than that of the base metal and the hardness of the weld metal is always higher than that of the HAZ. Fig. 5-16 shows a typical plot of load W versus diameter of indentations d in logarithmic scales for the determination of Meyer index for the three areas. The average Vickers hardness and Meyer's index for base metal, weld metal and HAZ as well as the 0.2% proof and ultimate strength calculated from these values are listed in Table 5-9. Comparing these strength values for base metal with those obtained from the tensile test listed in Table 5-4, the yield strength is found higher by only 6.4%. It indicates that hardness tests provide a reasonably good approximation for yield strength for the base metal. The strength of WM obtained from the tensile test (Table 5-7) is about 34.6% lower than that from the hardness test, which can be explained from the defects in the tensile test specimens, as shown in Fig. 5-13.

Table 5-9 Hardness and strength obtained for the WT1 specimen

Area	Base metal	Weld metal	HAZ
Vickers Hardness	159.8	227.5	220.4
Meyers index	2.228	2.014	2.230
Calculated 0.2% Proof strength, MPa	308.8	719.4	423.6
Calculated Ultimate strength, MPa	561.4	739.8	776.7

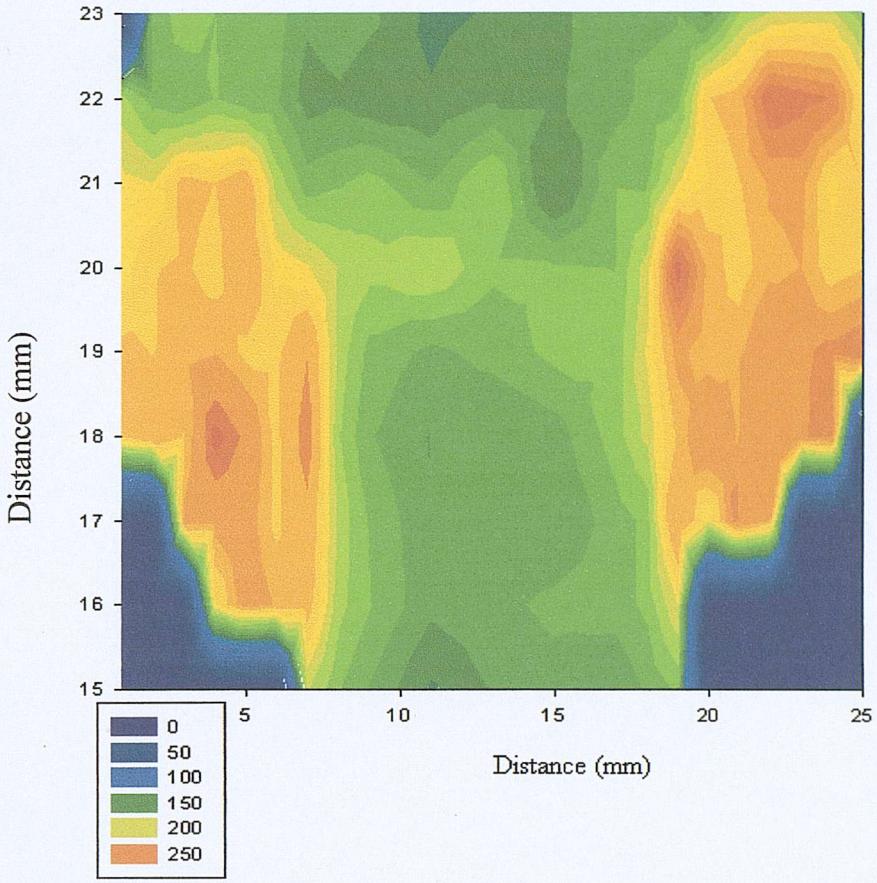

Fig. 5-14 Contour plot of the hardness distribution for WT1 specimen

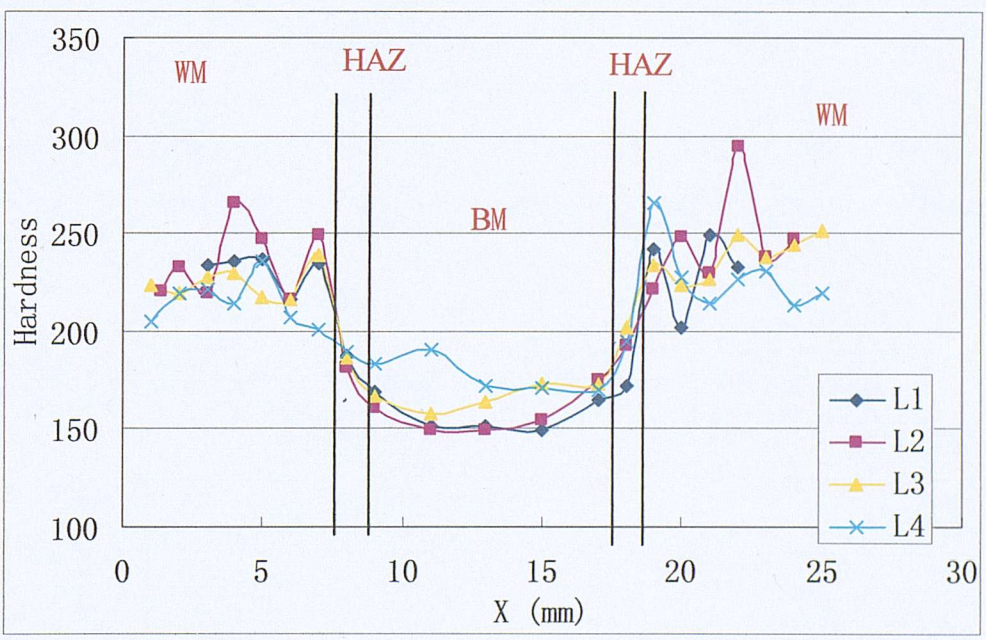

Fig. 5-15 Hardness distribution across the three areas at various positions

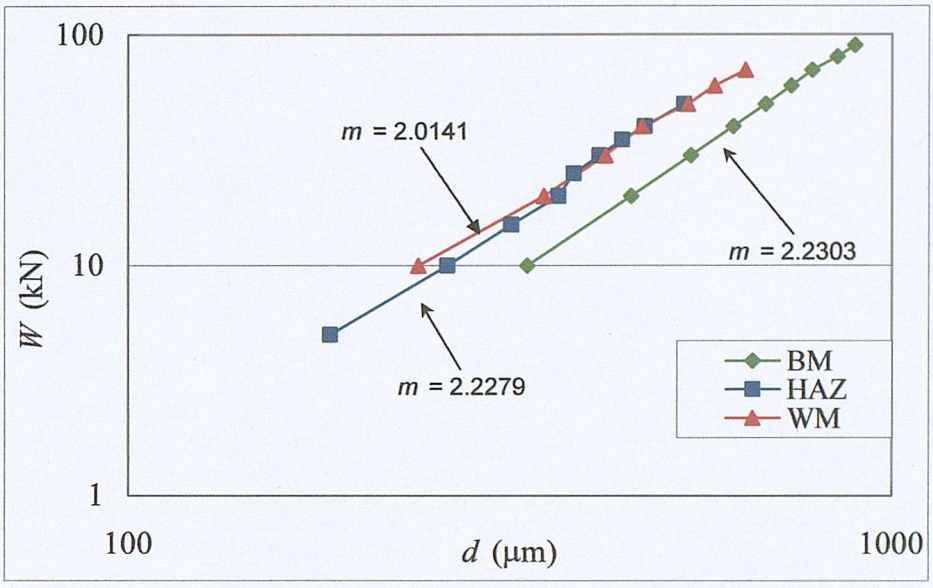

Fig. 5-16 Plot of load *W* versus diameter of indentation for WT1 specimen

B) WT2 specimens

Fig. 5-17 shows a contour plot of the hardness distribution over the surface of a slightly etched WT2 specimen. Table 5-10 lists the average hardness values for the three areas and the calculated strengths using the same method as for the WT1 specimens with the corresponding Meyer's index obtained from Fig. 5-18. The yield strength of the base metal obtained from the hardness test is about 3% lower than that from tensile tests (see Table 5-5) and the ultimate strength is about 5% lower. This also gives confidence in using the strength results for the HAZ predicted from the hardness test.

Table 5-10 Hardness and strength obtained for the WT2 specimens

Area	Base metal	Weld metal	HAZ
Vickers Hardness	205.7	176.1	165.3
Meyer index	2.010	2.013	2.217
Calculated 0.2% Proof strength, MPa	656.4	558.2	328.6
Calculated Ultimate strength, MPa	673.8	573.7	580.6

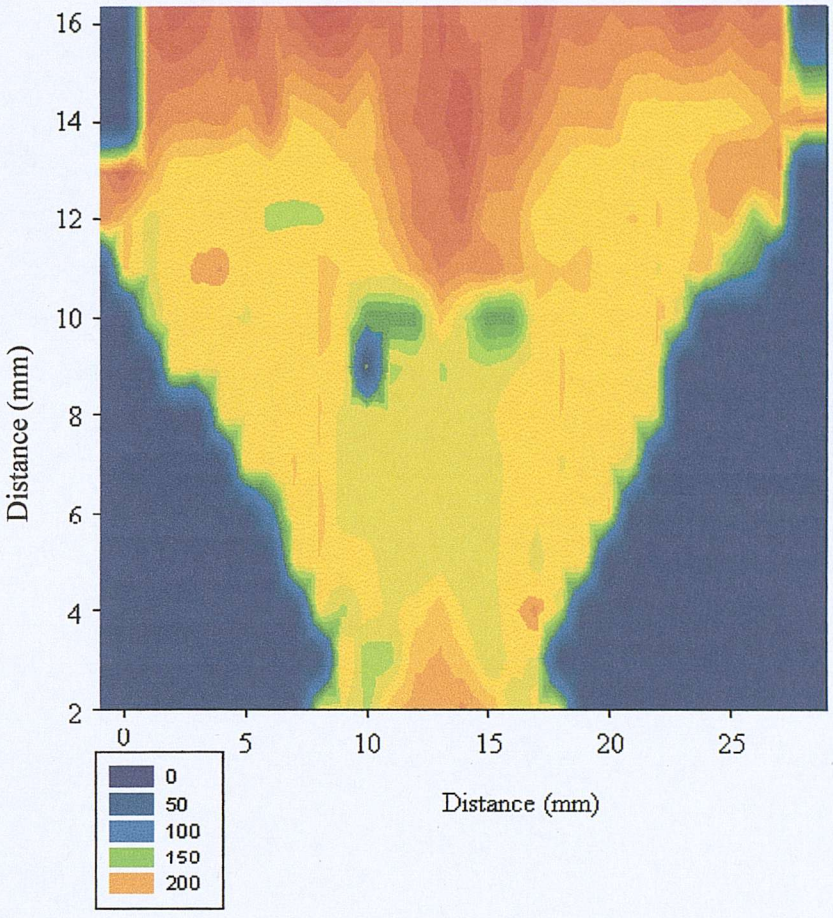

Fig. 5-17 Contour plot of the hardness distribution for the WT2 weldment

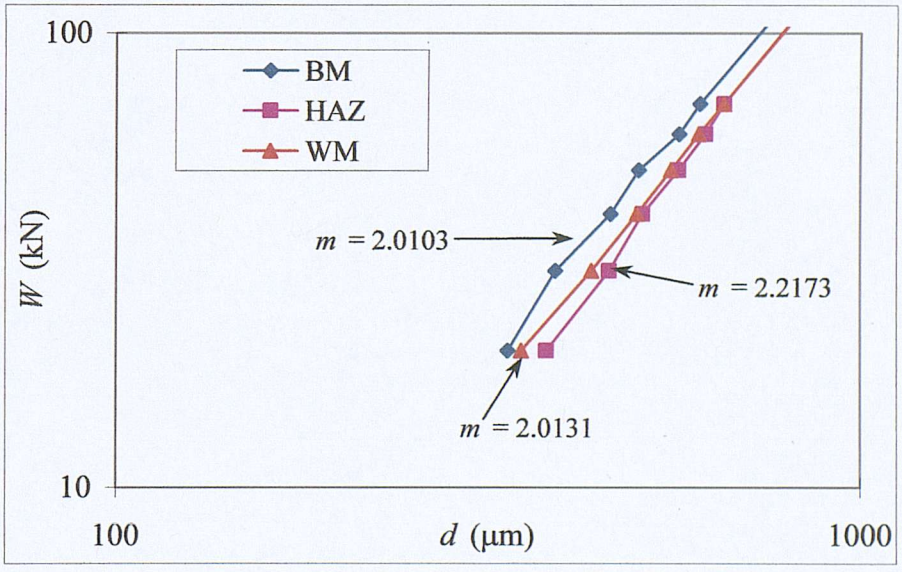

Fig. 5-18 Plot of load *W* versus diameter of indentation *d* for WT2 specimen

5.3.4 Weldment microstructures

In order to study their microstructure, specimens of 20 mm thickness were cut perpendicular to the welding direction from both the WT1 and WT2 weldments. The specimens were then polished using standard metallographic procedures finishing on 1 μm diamond paste. Samples were etched using the mixture of 100 ml methanol and 2 ml Nitric acid (nital). Micrographs taken after etching (Fig. 5-19 and Fig. 5-20), clearly show the weld area and HAZ for the WT1 and the WT2 specimen, respectively. These were then studied at higher magnification to reveal the microstructure of these etched specimens. Fig. 5-21 (a) shows the microstructure of the area around one of the weld roots in WT1, as indicated in Fig. 5-19. The structures shown in Fig. 5-21 (b)-(f) are in the areas b-f indicated in Fig. 5-21 (a), from base metal to HAZ and then to weld metal. Lack of penetration at the weld root is clearly seen in both welds. In addition, there is little penetration in the vertical side wall of the left side weld. The microstructure of the three areas in the WT2 specimen is shown in Fig. 5-22. Primary (grain boundary and polygonal) ferrite and Widmanstatten ferrite in the form of side plates and fine acicular ferrite are seen to form in the weld metal. The unaffected base metal contains ferrite and pearlite. The fusion line between the weld metal and HAZ is clearly seen in both weldments. In the HAZ, the base metal was heated up and then cooled down. Austenite was formed during the heating process. On cooling, a grain growth zone, grain refined zone and partial transformed zone have formed in the HAZ[14,15,16], as shown in (e), (d), and (c), respectively.

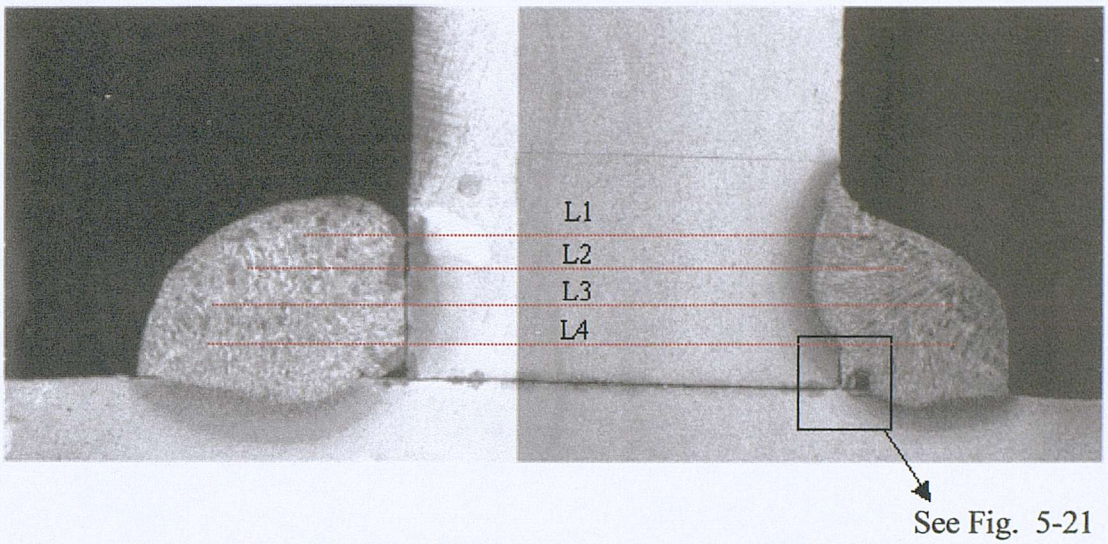

Fig. 5-19 A typical etched specimen from the WT1 weldment

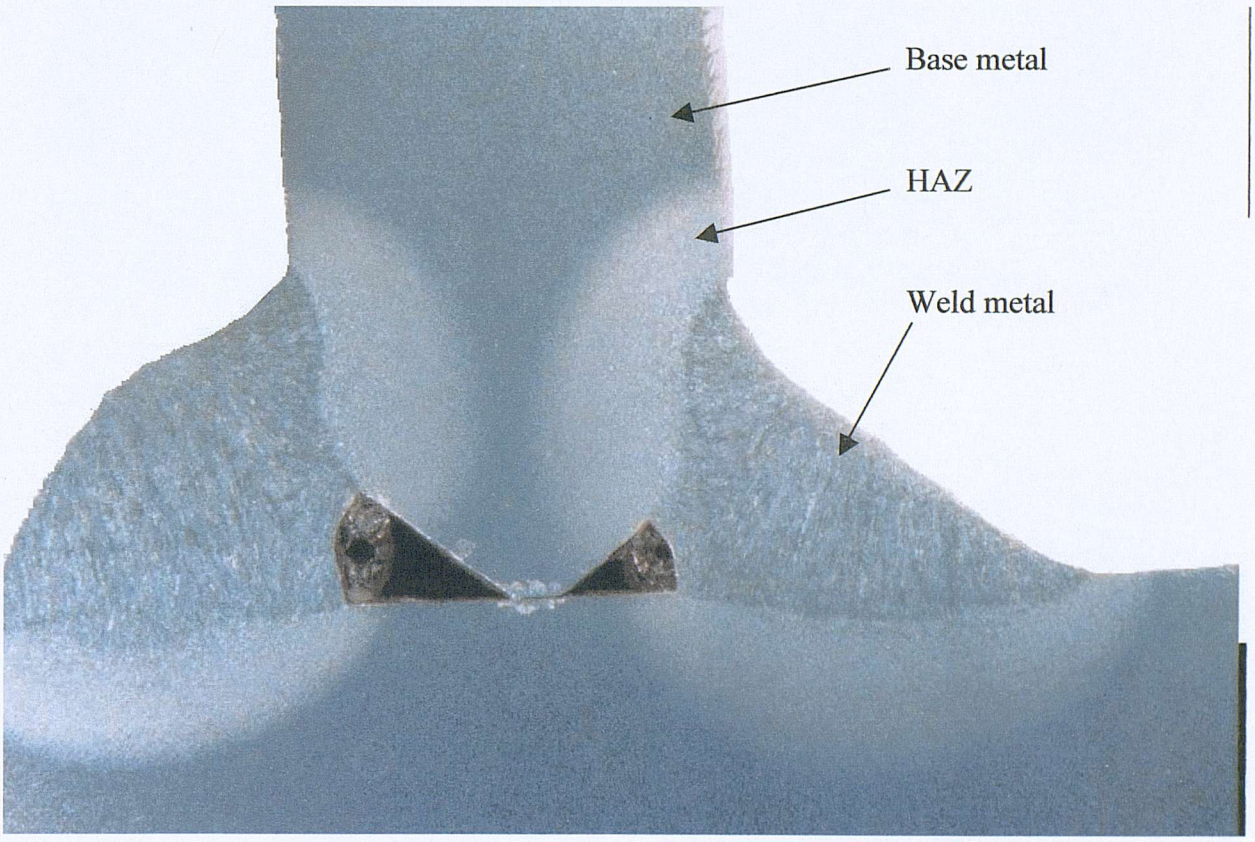

Fig. 5-20 A typical etched specimen from the WT2 weldment

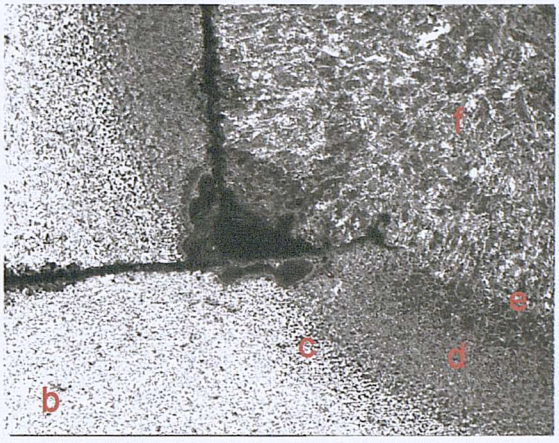

(a) Base metal, weld metal and HAZ, × 100

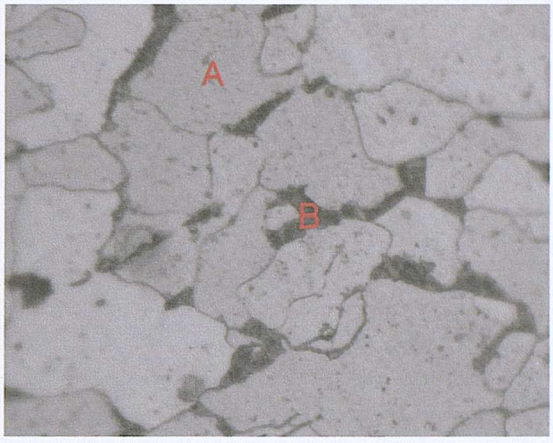

(b) Microstructure of WT1 base metal, showing pearlite (B) and ferrite (A) ×500

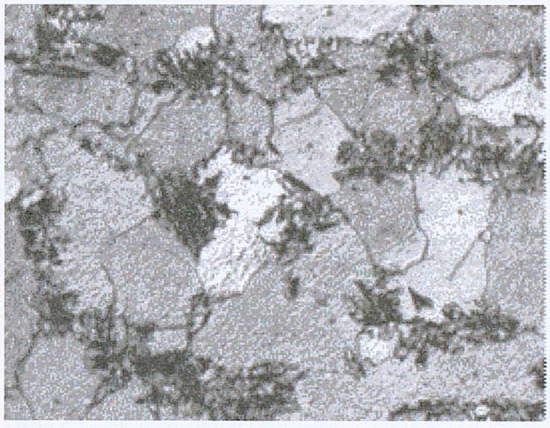

(c) Microstructure in the transition area from base metal to HAZ, where pearlite starts to decompose × 500

(d) Microstructure of HAZ, × 500

(e) Microstructure in the transition area from HAZ to weld metal, × 500

(f) Microstructure of weld metal, × 500

Fig. 5-21 Microstructure of the three areas in the right side weld of the WT1 weldment

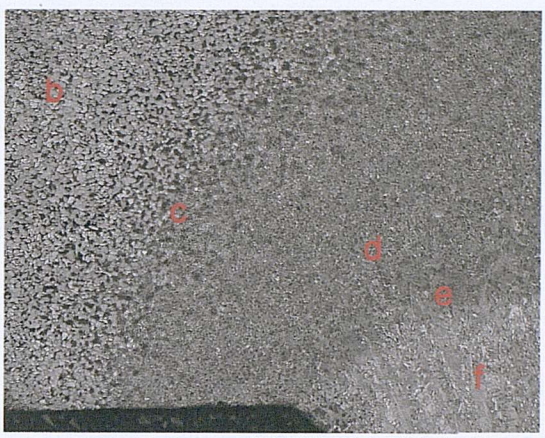

(a) Microstructure of base metal, HAZ and weld metal, ×100

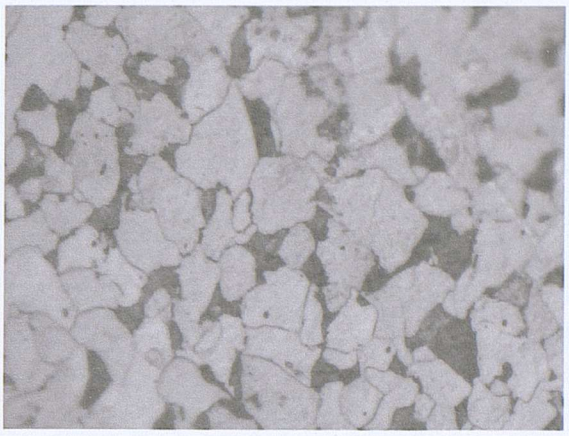

(b) Microstructure of base metal, × 500

(c) Microstructure in the transition area from base metal to HAZ, ×500

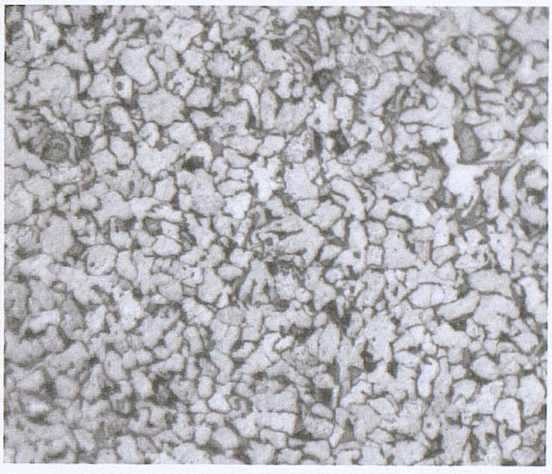

(d) Microstructure of HAZ, × 500

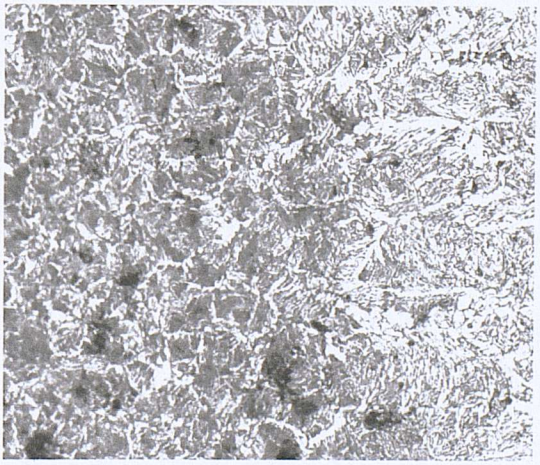

(e) Microstructure in the transition area from HAZ to weld metal, × 100

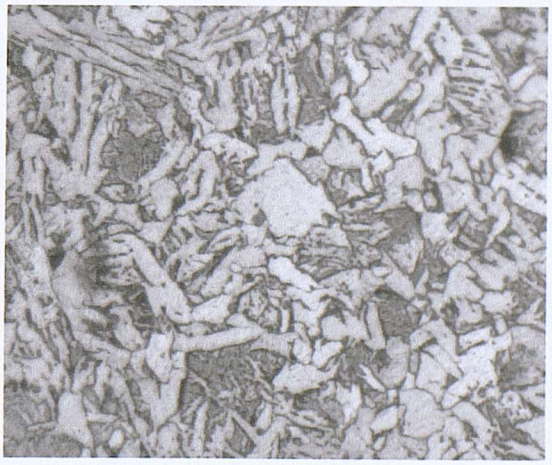

(f) Microstructure of weld metal, × 500

Fig. 5-22 Microstructure of the three areas in the WT2 weldment

5.4 Bending tests of T-joints

Bending tests were carried out on specimens cut from both the WT1 and WT2 weldments to study the behaviour of a welded T-joint under bending. The test results were also used to assess the FE model, which was based on similar geometry and loading conditions.

5.4.1 Testing procedure

First, specimens with thickness of approximately 12 mm were cut from the weldment and the dimensions were measured. Strain gauges were then attached to the surfaces of the specimens. This procedure strictly followed the bonding method[17] applicable to the type of strain gauges and gauge cement used, which includes surface preparation, gauge location, gauge installation etc. The specimens were tested under bending in an INSTRON 2511-320. The load data was recorded by both a HP Agilent 34970A data logger with a scanning speed of 0.4 seconds per reading and the INSTRON chart. During loading, photographs were taken from time to time in an attempt to record crack initiation and growth. The load value at which each photograph was taken was recorded on the load-displacement curve on the chart. After the test had finished, photographs of the failed specimen were taken and then the samples were broken after being cooled down by immersing them in liquid Nitrogen. After taking photographs of the fracture surfaces from which the failure mode could be found, the specimens were then cut to fit in the 30-mm-diameter Auto-polisher mount and polished. The polished specimen were then etched and studied under optical microscopy to determine the crack initiation point and the failure path.

5.4.2 Test set up

Fig. 5-23 illustrates the test set up. As the loading beam of the INSTRON can only travel in a vertical direction, and the bottom base of the INSTRON is the only place where specimens can be gripped or fixed, other supporting parts had to be designed so that the base plate of the T specimen can be fixed vertically and a vertical load can then be applied to its attached plate from the INSTRON loading beam in order to

apply a bending moment to the T specimen. This was achieved by means of a 38 mm thick L-shaped steel block. One leg of the L-shaped steel block was bolted to the test base of the INSTRON machine. One side of the base plate of the T-specimen was then fastened to the other leg of the L-shaped steel block by two 12 mm diameter bolts. The loading beam of the testing machine applied a compression load to the attachment plate of the specimen until the specimen fractured or the end of the attachment plate reached the base plate of the machine, as Fig. 5-24 shows. To fix the steel support to the base plate of the machine using the already existing holes in the test base plate, as well as to enable the crosshead beam to load the attachment plate of the specimen when the end of the attachment plate reach the test base plate, another steel plate with a thickness of 25 mm was inserted between the specimen and the L-shaped steel block support.

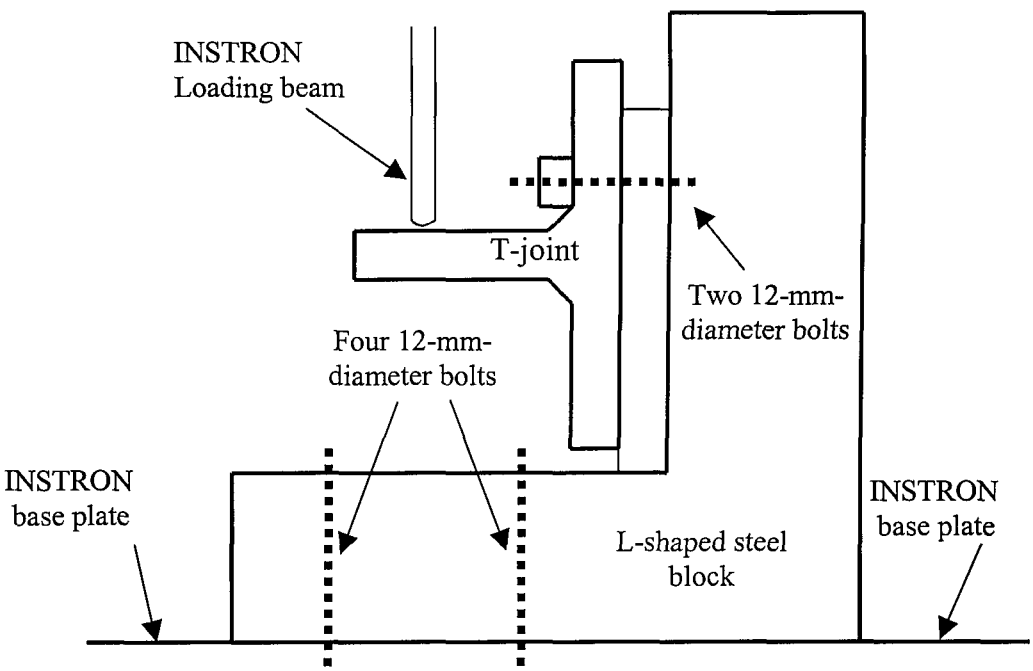

Fig. 5-23 Loading set-up for the WT2 bending tests

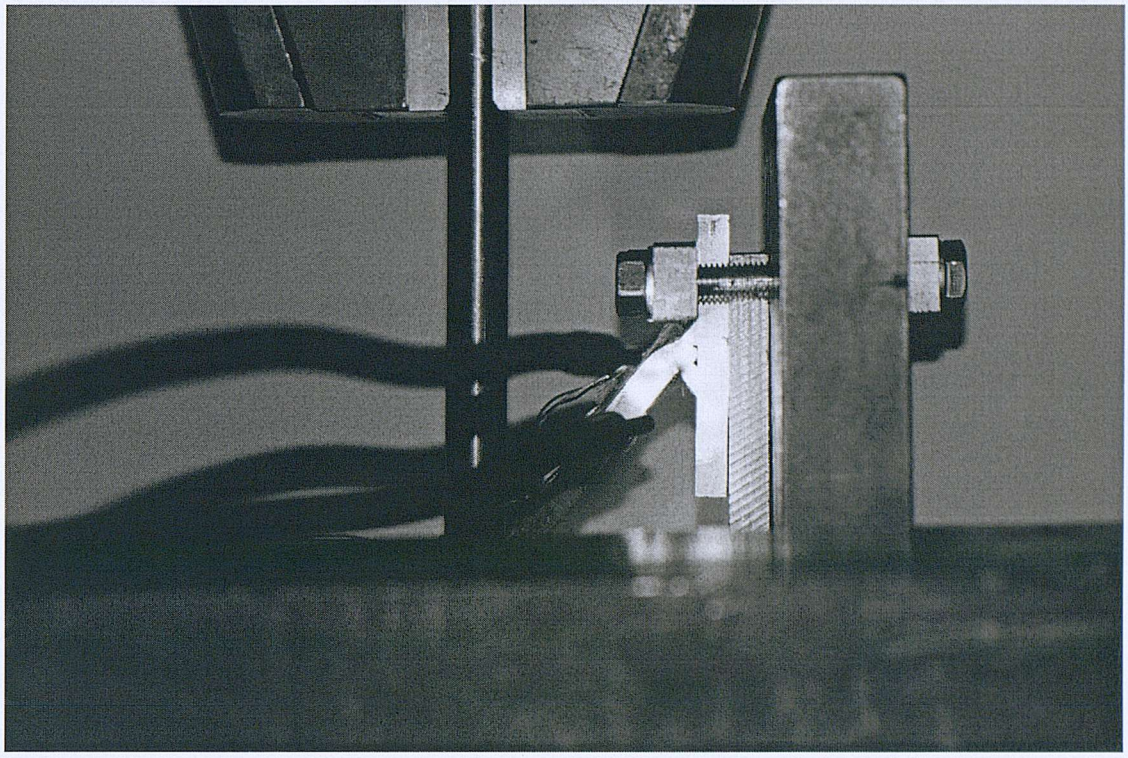

Fig. 5-24 Final loading position when specimen failed, attachment plate reached base plate of INSTRON

5.4.3 Apparatus specifications

An INSTRON 2511-320 was used as the loading machine. The strain gauges used were of the type KFG-2-120-C1-11[18], a unidirectional gauge with a grid dimensions of 2×1.2 mm and gauge resistance of 120 Ω; type KFG-1-120-D17-11, a stacked rosette strain gauge with a grid dimension of 1×1.1 mm, base diameter of 5 mm, for measuring stresses in three directions; and type KFG-1-120-D9-11 N10C2, a five-element uni-axial strain gauge with a grid dimensions of 1 ×1.4 mm, a base dimensions of 6× 4 mm, and a gauge resistance of 120 Ω, for measuring stresses distributed in a small area. The 2100 system Strain Gauge Conditioner and Amplifier System was used to generate conditioned high-level signals from strain gauges in the form of voltages and the program HP VEE was utilised to record the voltages which can then be used to calculate the strain generated in the strain gauges. The gauge cement used was CC-33A, and M-LINE[17] strain gauge application kit GAK-2-AE-10/15 was used to attach the strain gauges.

5.4.4 Specimens

A) WT2 weldment

Dimensions

In total six specimens were made and tested under bending. Fig. 5-25 shows a typical cross section of the specimens. The attachment plate had been given the edge preparation before welding as shown in Fig. 5-26. The edge of the chamfer was identified from the welded joint by drawing straight lines along the unwelded edge of the chamfer on a photograph taken from a real sample. The dimensions of both the left and right chamfer were then measured using the software DigXY. The profile of the two welds is obviously not the same. This is more clearly detected from Fig. 5-20 showing the etched specimen and the amount of weld metal deposited. This means that the heat input to the two welds were different as well. The attachment plate was closely aligned to the base plate leaving a small gap in between. The dimensions of these specimens are listed in Appendix H, Table H-1, where the symbols used are defined in Fig. 5-25 and h is the thickness of the specimens. In general, WT2 is a good quality weldment, although the dimensions of the weld vary slightly along the welding direction, which is very difficult to avoid in manual welding.

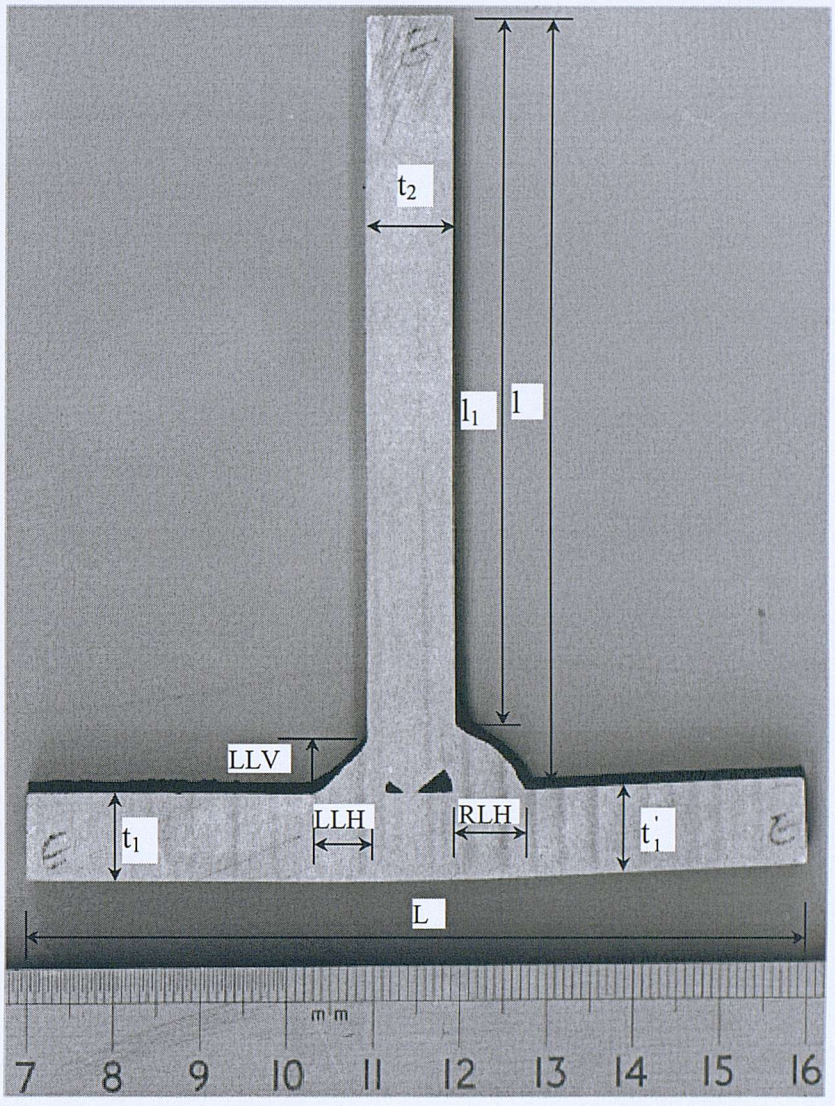

Fig. 5-25 A typical cross section of the WT2 bending specimen

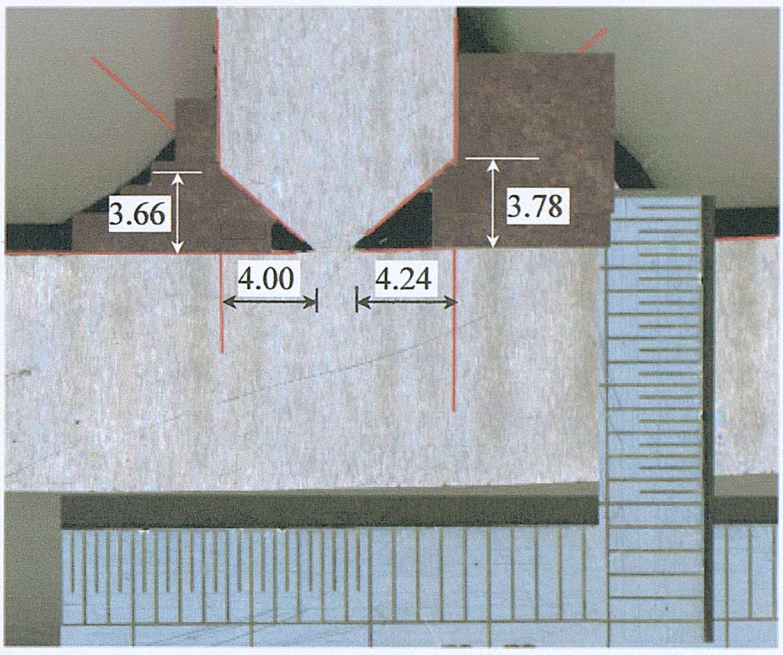

Fig. 5-26 Chamfered shape of the weldment base plate, dimensions in mm

Bending direction

To study the effect of welding sequence, specimens A, B and C were loaded in such a way that one pass of the weld was in tension while for specimens D, E, F, and G the other pass of the weld was in tension. Since the weldment was manufactured externally in Cussons Technology Limited[1], it was not known which of the two passes was the first one to be welded. However, after the welding of the first pass, the weldment was distorted, although the subsequent welding pass on the opposite side would counter some of this distortion, but not fully. The distortion of the weldment is largely determined by the first weld pass. From this observation, it was assumed that the first passes of specimens A, B, and C were loaded in tension.

Strain gauges

Strain gauges were attached to one surface of the specimen. Fig. 5-27 (a) – (f) show the specimens after strain gauges were attached. Strain distribution and development in the weld area and HAZ are of interest in this study, however, due to size limitation, only one strain gauge can be fitted in the weld area. Moreover, there were only five channels in the available strain acquisition system, while one rosette requires three

channels so that strain only on one side of the T-joint was measured with a rosette providing strains in three directions. On other specimens, a unidirectional gauge was attached perpendicular to the expected failure direction and another unidirectional gauge was attached on the attachment plate of the T-joint perpendicular to the direction of loading. As a rosette strain gauge only measures the average strain around a point while the strain distribution is also of interest, in some specimens, i.e. Specimen A and E, a type KFG-1-120-D9-11 N10C2 strain gauge which contains five unidirectional gauges was used in order to obtain the strain distribution within the weld area.

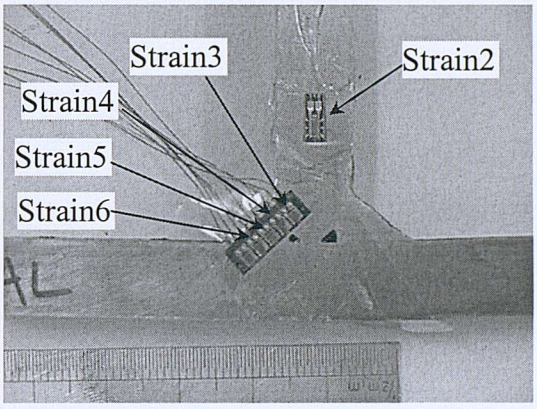

(a) Specimen A

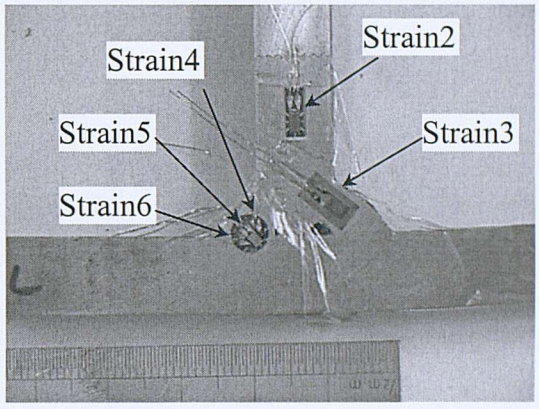

(b) Specimen B

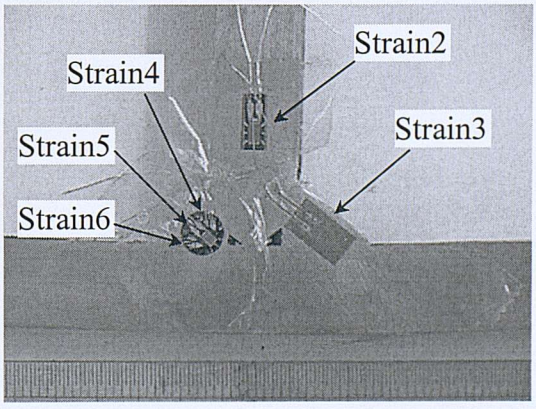

(c) Specimen C

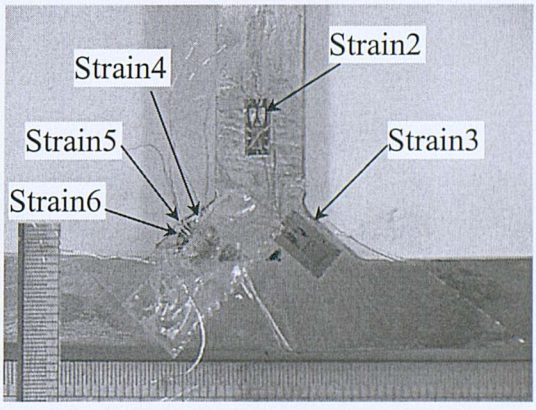

(d) Specimen F

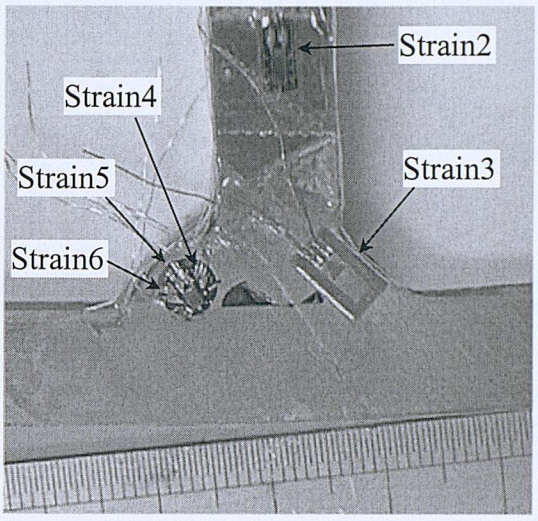

(e) Specimen D

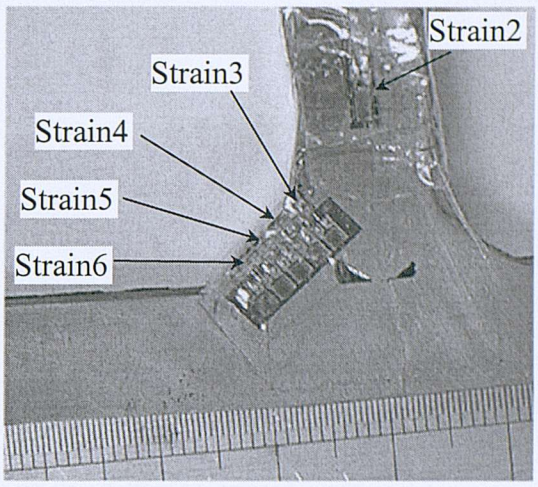

(f) Specimen E

Fig. 5-27 Strain measurement positions for WT2 specimens

B) WT1 specimens

Dimensions

Six specimens were prepared from the WT1 weldment. However, after two of them were tested, the results showed that defects which would not be accepted in practice were the predominant factor that affected the strength of the specimens. Since the significant effect of defects has been clearly demonstrated by these two specimens, the others were not tested. The dimensions of the two tested specimens are listed in Appendix H, Table H-2. Reference to Fig. 5-8 may be made for the definition of the symbols used while h is the thickness of the specimen.

Loading direction and Strain gauges

Specimen A was loaded in such a way that the second pass weld was in tension while for Specimen B the first pass weld was in tension. The same strain gauge selection considerations as those for the WT2 specimens were applied to WT1 specimens. Specimens with the strain gauges attached are shown in Fig. 5-28.

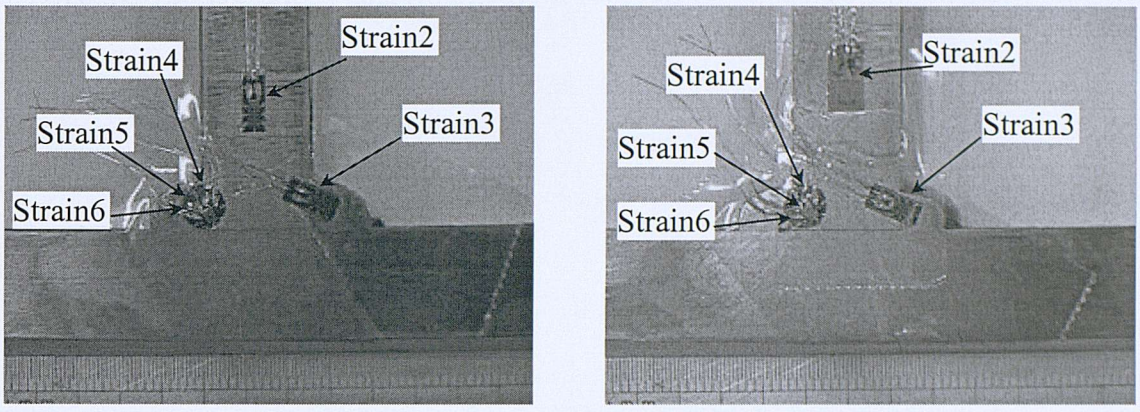

(a) Specimen A (b) Specimen B

Fig. 5-28 WT1 bending specimens with strain gauges attached

5.4.5 Results and discussion

A) WT2 specimens

Failure load

From both the chart recorded by the INSTRON machine and the digital data recorded by the data logger, the maximum loads which the specimens take can be found. The failure modes corresponding to these loads are described later in this section. The failure loads for all specimens are listed in Table 5-11. The variation between different specimens is reasonably small, irrespective of the differences in their failure path and the small variations in sizes and loading positions.

Table 5-11 Failure loads of the WT2 bending specimens

Specimen	A	B	C	D	E	F	Average	Standard deviation
Failure load (kN)	3.39	3.19	3.00	3.25	3.68	3.35	3.30	0.24

As discussed in Chapter 2 of this thesis, there are formulae for calculating the strength of a welded T-joint provided by various codes. For the geometry and

loading conditions of the specimens used in this test, Table 5-12 lists the calculated design loads based on BS 5400 and IIS/IIW codes. Comparison between Table 5-11 and Table 5-12 shows that BS 5400 underestimates the strength of fillet welded joints under static loading by around 30-40%. IIS/IIW specification gives higher permissible loading as the permissible stress used is taken as the tensile strength of the weld metal for an ultimate strength analysis.

Table 5-12 Design strength of the WT2 specimens by various codes

Specimen / Design load according to (kN)	A	B	C	D	E	F	Ave.
BS 5400	2.00	2.15	1.86	2.33	2.70	2.21	2.21
IIS/IIW	2.70	2.90	2.51	3.15	3.64	2.98	2.98

Load – strain curve

The data recorded by the system is due to changes in the resistance of the strain gauge and is in the form of a voltage which has been magnified by a 1/4 Wheatstone bridge. It should be converted into strain, ε, by the formula below:

$$\varepsilon = \frac{V_0}{V_{ex}} \times \frac{2}{GF} \times \frac{1}{\frac{1}{2} + \frac{V_0}{V_{ex}}} \qquad (5\text{-}5)$$

where V_0 is the initial voltage, which is the output voltage divided by the gain factor, 2000 in this study; V_{ex} is the excitation voltage, which is 5 V in this test and GF the gauge factor, which is given by the manufacturer.

The generated load-strain curves for each specimen are shown in Fig. 5-29 (a) – (e), for specimens A-D and F, respectively. In these figures, 'Strain 2-Strain 6' are strain data recorded from the corresponding strain gauges as labelled in Fig. 5-27. The kinks present in the load-strain curves for Specimen B were due to stopping of

loading for the purpose of taking a replica from the polished specimen surface. It was thought that a replica would enable crack initiation and propagation to be studied in more detail. However, distortion of the surface of the sample on loading made this impractical. For specimen D, strain data for Strain 6 was not recorded correctly and therefore has not been included in the figure. The non-smooth Strain 3 curve for Specimen F was thought to be due to faulty connection of the strain gauge to the data acquisition system. Measurements from all other strain gauges show that, upon loading, the load increases linearly with strain at all positions indicating elastic behaviour. The joint starts to yield when the load is about 2 - 2.5 kN, after that the strain increases much faster than the load.

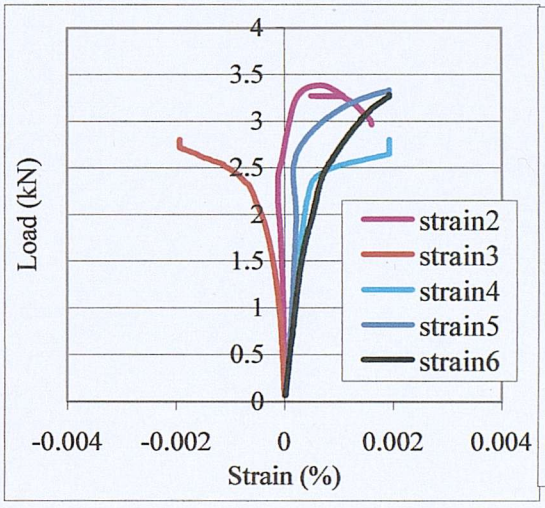

(a) Specimen A

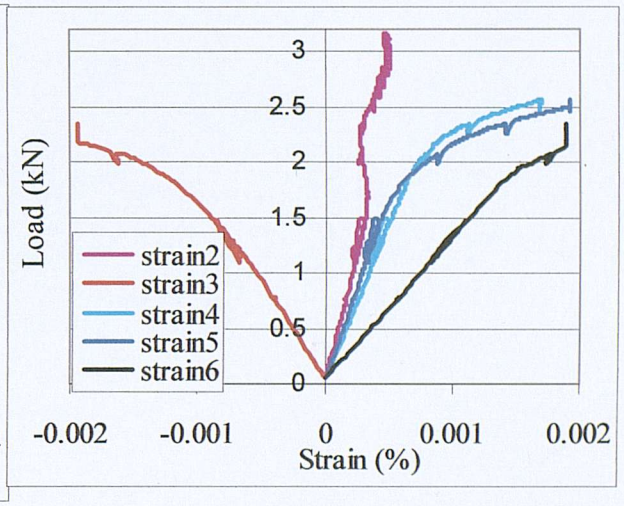

(b) Specimen B

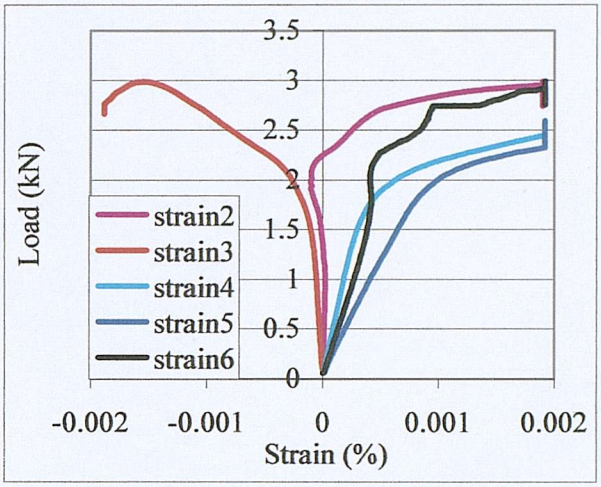

(c) Specimen C

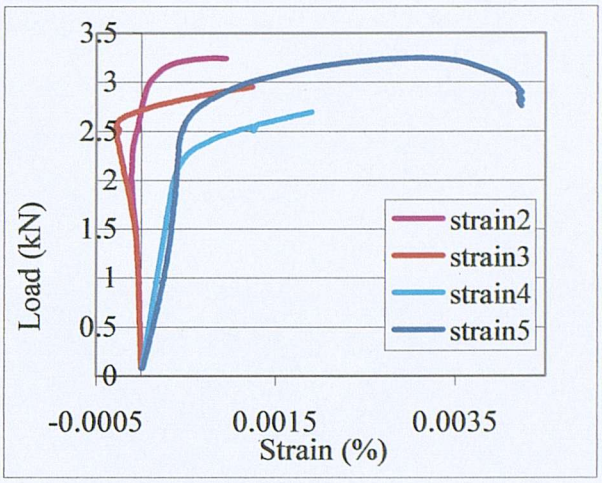

(d) Specimen D

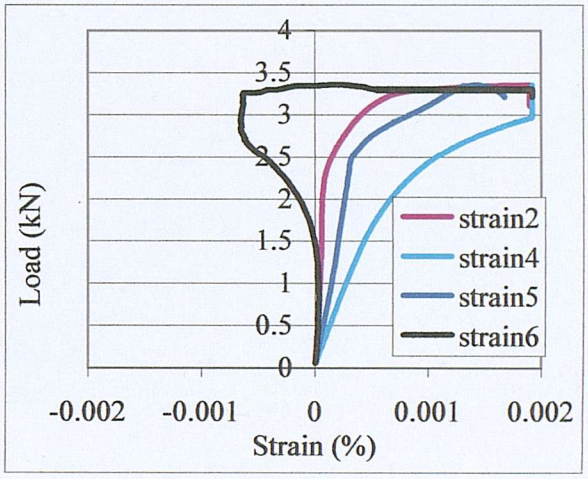

(e) Specimen F

Fig. 5-29 Load-strain curves for WT2 specimens under bending

Failure mode

Ductile failure: All the specimens initially failed in a ductile manner. Upon increasing the load, yielding starts to appear at the weld toe and/or root. The yield area grows bigger as the load increases and cracks start to initiate. A main crack then forms and propagates. The load-carrying area was then reduced and the load the specimen can carry starts to decrease.

Failure surface: The samples after bending testing were broken completely apart after cooling in liquid Nitrogen. The fractured samples were then placed in methanol

and allowed to warm to room temperature. Immersion in methanol prevented water condensing on the cold samples which causes corrosion. Fig. 5-30 shows a typical fracture surface taken from these broken specimens. The shining part at one edge represents brittle failure, which occurred at liquid nitrogen temperature.

Fig. 5-30 A typical failure surface of the WT2 bending specimens

Failure path: Specimen D and F all failed in the weld while Specimen A, E and a trial specimen failed through the T-joint attachment plate, as shown in Fig. 5-31. Specimen C did not break fully apart before the loading beam reached its final position, but the fracture path was predicted to be through the weld as a large crack had formed near the weld toe and weld root. The failed specimens were broken apart and the two parts mated and cut to fit in the 30-mm-diameter mount. After hot mounting the samples were polished using the auto-polisher until 1 μm and then etched. Fig. 5-32 shows these etched specimens, from which the failure path can be clearly seen. The red arrows in the figures show the bending direction.

(a) Specimen failed through the weld (Specimen F)

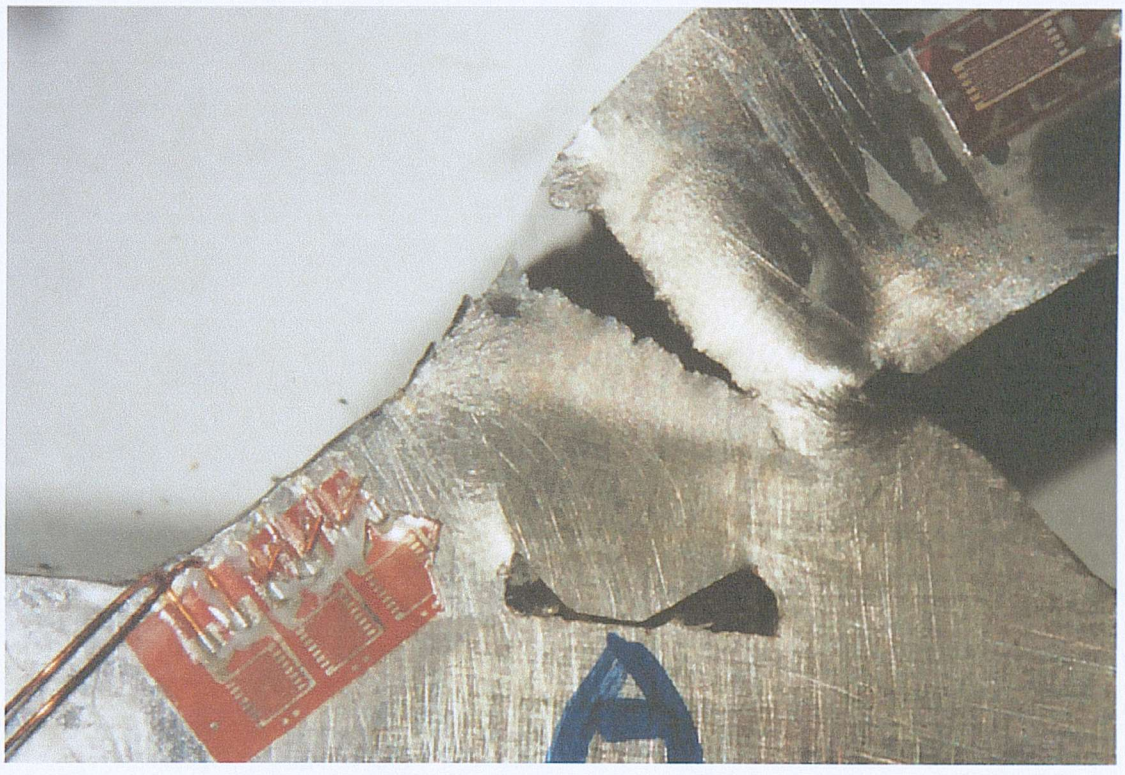

(b) Specimen failed through the plate (Specimen A)

Fig. 5-31 Two typical different failure paths of the WT2 bending specimens

(a) Specimen E (b) Specimen F

Fig. 5-32 Etched failed WT2 bending specimens

Failure initiation and crack propagation: the failed specimens were polished until 1 μm and etched with 2% nitric acid in methanol (nital) and then studied in more detail by optical microscopy. The cracks first initiated from the weld toe in the weld area for all the specimens except Specimen E, where the crack initiated from the HAZ in the attachment plate. For specimen A, the crack propagated along the weld-HAZ boundary for about 0.7 mm and then it changed direction and grew into the T-joint attachment plate and continued to grow in the steel plate until failure, as shown in Fig. 5-33. The photographs in Fig. 5-34, taken for Specimen E, show that yield first occurred at the weld toe of the weld in tension, but as the yield area continued to grow, a big crack emerged in the attachment plate near the yield area and this crack propagated quickly causing the joint to fail finally in the attachment plate. In the case of Specimen D, although a crack was seen to initiate at the weld toe and had the tendency to propagate in the attachment plate, as shown in Fig. 5-35, another crack started at the weld root as the load increased; this made the toe-root line the critical plane and failure occurred as the crack from the weld root met the crack from the weld toe. A crack also started at the weld root where a small undercut was present in Specimen F (see Fig. 5-36) along with yielding around the weld toe at the position where there is a small undercut as well. These two cracks propagated continuously and failure finally occurred when they met.

Although the specimens were cut from the same weldment, they failed in two different ways, one in the weld and the other across the attachment plate. The failure loads for the specimens, which failed in the weld, are generally lower than those for the specimens, which failed in the attachment plate, but the difference is very small. As the weldment was manually made, variations in the details of the weld such as size of the weld, width of the HAZ, defects, difference in microstructures, are inevitable. The reason for Specimens D and F failing in the weld is most likely a small defect present at the weld root and a shorter dimension between the weld toe and weld root, which caused a major crack to initiate and propagate quickly.

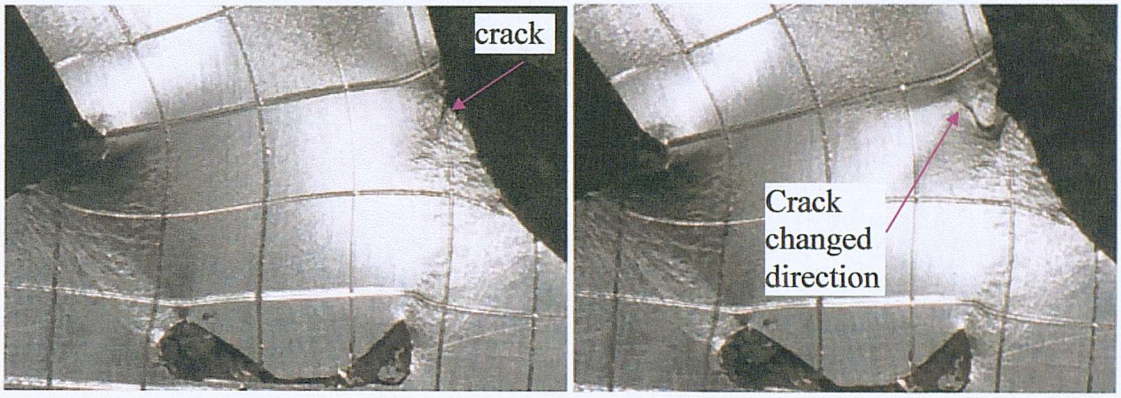

(a) Crack started at the weld toe (b) crack changed propagating direction

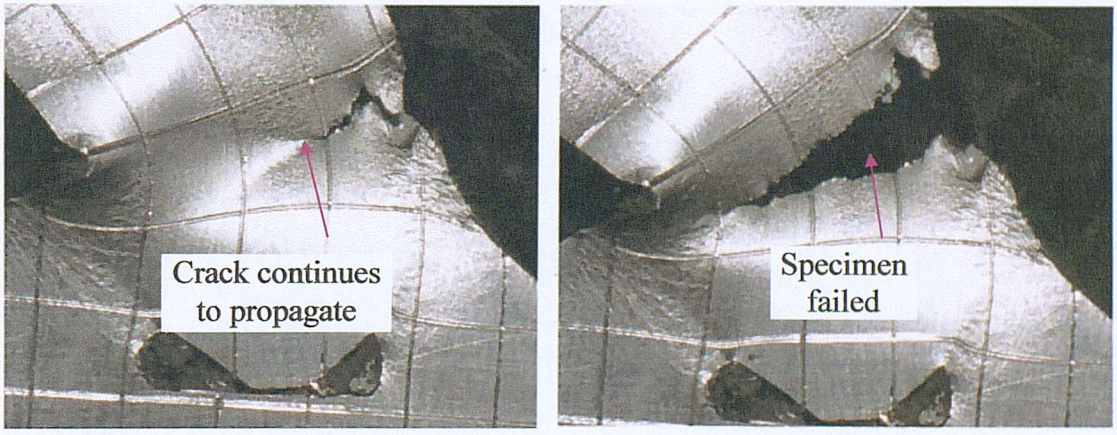

(c) Crack propagates in the attachment plate (d) Specimen failed

Fig. 5-33 Crack development in Specimen A during bending test

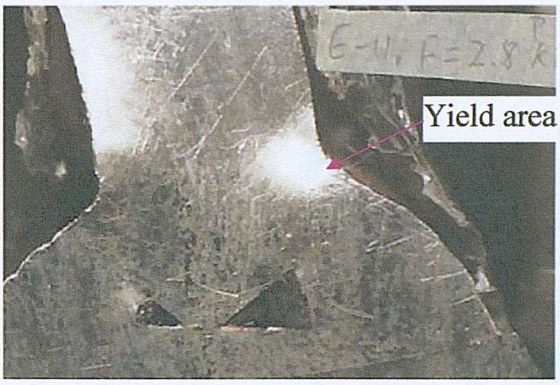

(a) Yield occurred at the weld toe

(b) Crack emerged and propagates at the attachment plate

(c) Crack continues to propagate at the plate

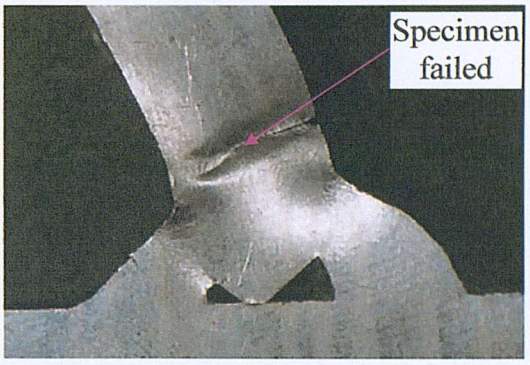

(d) Specimen failed

Fig. 5-34 Crack development in Specimen E during bending test

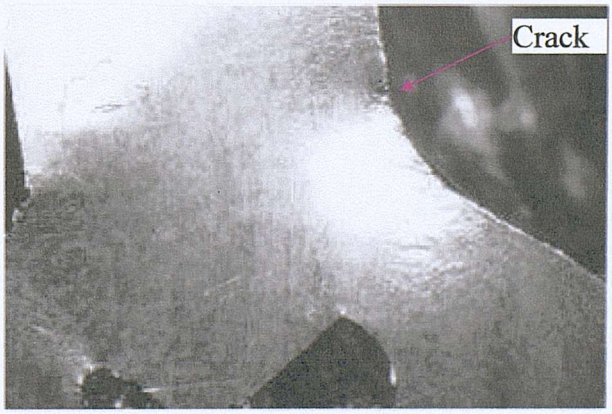

(a) Crack started at the weld toe and propagates through the plate

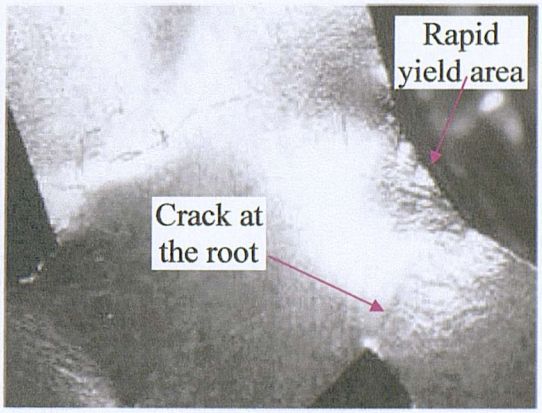

(b) Crack developed at weld root

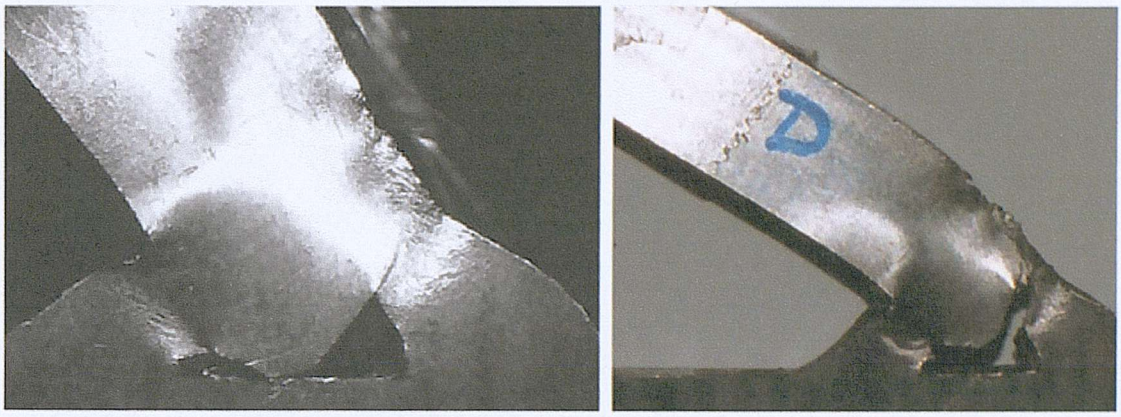

(c) Root crack propagates further (d) cracks met and specimen failed

Fig. 5-35 Crack development in Specimen D during bending test

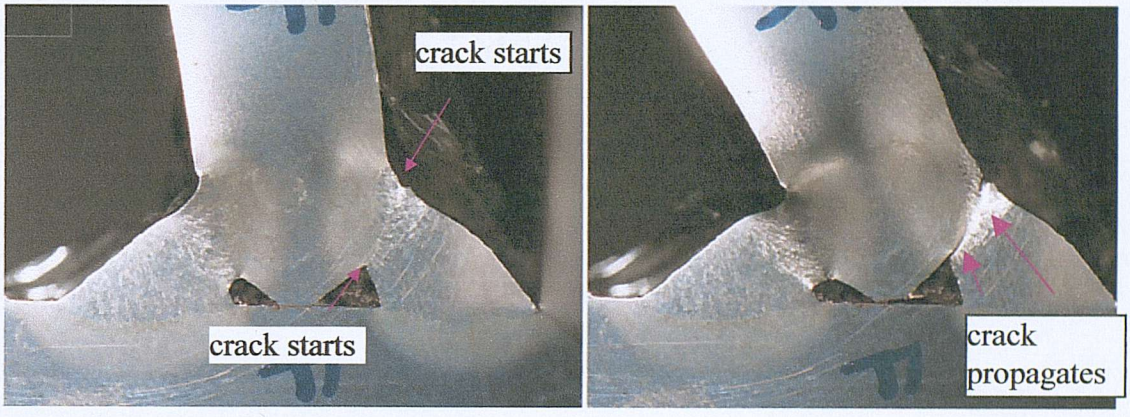

(a) Yield starts at weld toe and root (b) Cracks propagate in the weld

Fig. 5-36 Crack development in Specimen F during bending test

B) WT1 specimen

Failure load

The failure loads obtained from the bending test for WT1 specimens are given in Table 5-13. There is a larger difference in the behaviour of the two specimens than the corresponding variation among the WT2 specimens. This is reasonable since visible defects exist in the weldment. The respective design loads permitted by various codes are listed in Table 5-14. It is not surprising to see that the test results are much lower than those predicted by the codes, as the low quality of the weld tested is not permitted by the codes.

Table 5-13 Failure loads for the WT1 specimens

Specimen	A	B	Average	Standard deviation
Failure load (kN)	6.40	5.98	6.19	0.30

Table 5-14 Failure loads predicted by codes for WT1 specimens

Specimen / Design load according to, (kN)	A	B	Average
BS 5400	15.05	9.92	12.48
IIS/IIW	17.96	12.56	15.26

Load – strain curves

Fig. 5-37 shows the load-strain curves obtained from the bending test for the WT1 specimens. In the Figures, 'Strain 2 - Strain 6' are strain data recorded from the corresponding strain gauges as labelled in Fig. 5-28.

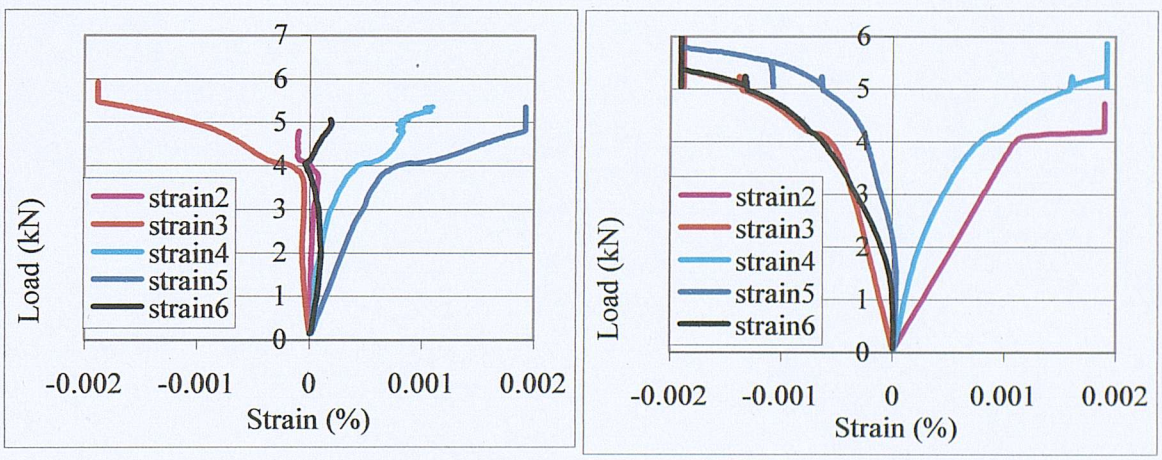

(a) Load-strain curves for Specimen A (b) Load-strain curves for Specimen B

Fig. 5-37 Load-strain curves for WT1 weldment

Failure modes

WT1 had several welding defects present. The behaviour of WT1 under bending is dominated by the presence of these welding defects which lead to early crack propagation, eventually linking up defects. Plastic deformation was observed to be limited to defect free areas of the weld.

For Specimen A, yield first started at the weld toe and at the tip of an existing crack due to lack of fusion at the weld root, as shown in Fig. 5-38. Upon increasing the load, cracks propagated in three directions, that is, along the weld-base plate interface, the weld-attachment interface at the weld root and along the weld-attachment plate interface at the weld toe. The gap between the attachment and base plate became wider on the tension side. Failure finally occurred when the weld broke off the base plate as less than half of the weld base plate interface was properly fused and connected. Lack of fusion defects are also present in the weld under compression in the bending test.

Specimen B was loaded in such a way that the first pass weld was in tension rather than the second as for Specimen A. However, there is also lack of fusion at the root of the first pass weld so that cracks started from both the weld toe and weld root, as shown in Fig. 5-39 (a). However, on this side of the weld, the lack of fusion is more severe in the weld attachment plate than at the weld base plate interface. Failure finally occurred when the attachment plate peeled off from the weld, as shown in Fig. 5-39 (b).

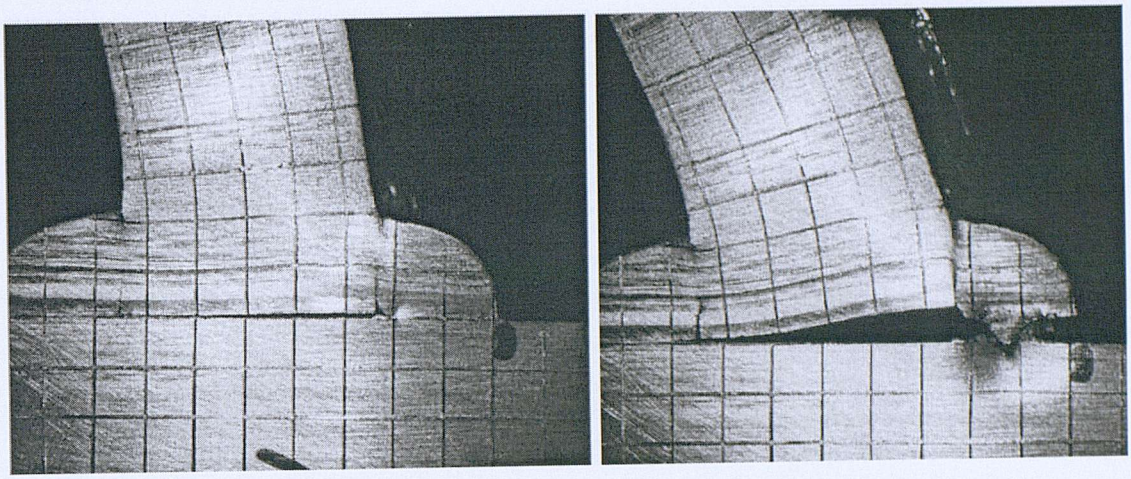

(a) Yielding started at the weld toe and root

(b) Specimen failed at the weld base plate interface

Fig. 5-38 Failure process of WT1 Specimen A

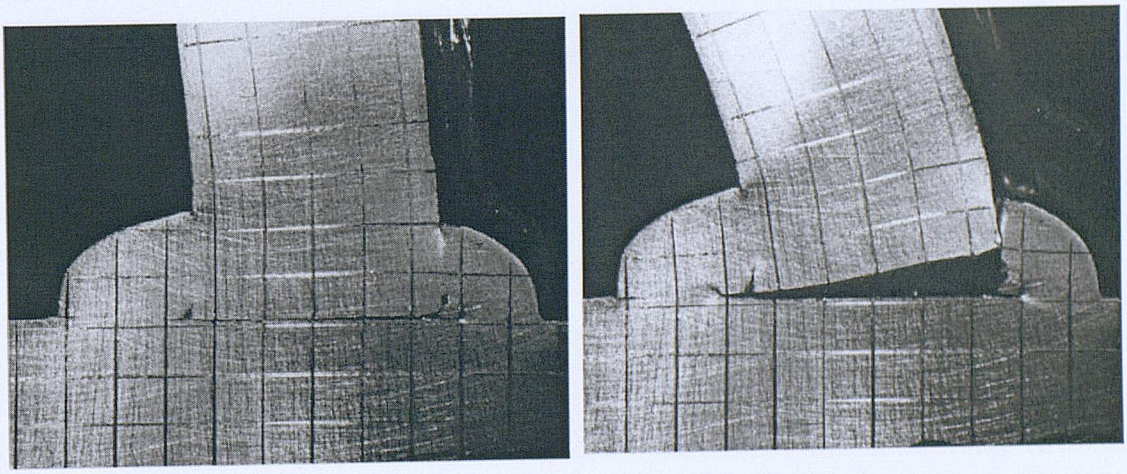

(a) Yielding started at the weld toe and root

(b) Specimen failed at the weld-attachment plate interface

Fig. 5-39 Failure process of WT1 Specimen B

C) Comparison between WT2 and WT1 specimens – effect of defects

It is obvious that defects, mainly due to lack of fusion played a vital part in the failure of the WT1 bending specimens. If these defects were not present, the load-carrying capacity of the WT1 weldment would be much higher. In the much better quality weldment, WT2, yield starts first at the geometric stress concentration points and ductile fracture occurred along the shortest path.

5.5 Summary

In this chapter, tests carried out on two different weldments were presented. Tensile and hardness tests were conducted in addition to metallographic study of the microstructure for characterising the material in the various weld zones. Fillet welded T-joints were tested under bending and their failure analysed. It is worth pointing out that the welding quality in the WT1 weldment is not acceptable in practice but is useful for studying the effect of defects in the current research. Tensile tests indicated that the parent material for the commercially welded WT2 weldment had a high yield strength than that of the weld metal. This, combined with the size of the fillet welds meant that the welded joint itself was approximately matched, rather than undermatched as designed.

It can be concluded from the test results that:

1. The hardness tests give a reasonable estimation of yield and ultimate strength of steel. It is therefore a useful method for estimating the strength of the HAZ since it is difficult to extract a tensile test specimen from such a small area.
2. In welded T-joints under bending, cracks most likely initiate from the weld toe and/or weld root where there is stress concentration. The fracture path can be either through the weld or through the attachment plate depending upon the strength and dimensions of the weld.
3. Failure in a good quality welded T-joint is ductile under bending. The joint undergoes large deformation before final failure. This is desirable in practice as it gives early warning of failure.

4. The presence of defects greatly reduces the load-carrying capacity of weldments.
5. Codes can underestimate or overestimate the strength of welded T-joint under static loading. Moreover, the actual failure plane does not appear to be the throat area as assumed by the codes.
6. The monitoring of temperature variation of the WT1 weldment shows that except from the regions near the ends of the plate, the majority of the cross-sections are at a quasi-steady thermal state. During welding, the part of the steel plate adjacent to the weld was subjected to a rapid heating and cooling process; however, this high-temperature heating and cooling cycle is very localised around the weld.
7. Weld preparation and welding parameters are important to ensure enough fusion has been achieved, thus to improve the quality of weldment.

The important purpose for these tests was to provide data for assessing respective FE models presented in Chapter 6 and Chapter 7 of this thesis. Parametric studies based on these models can then be carried out to investigate the effect of various factors on the strength of fillet welded T-joints.

It is recognised that the range of T-joints and the number of specimens tested is limited in this study as it was intended to provide model information and results for assessing respective FE models. Specimens manufactured under high-quality control welding conditions and covering a wider range of geometric configurations and material properties should be carried out, given more time and resources, for any reliable and general conclusions to be drawn. Experimental measurements of residual stresses in the WT1 weldment would help the assessment of the FE models simulating the welding process, as presented in Chapter 6. However, this could not be carried out due to limitation of apparatus available.

References:

[1] Burgess P., An investigation into crack propagation in fillet welds under collision loading conditions, BENG Dissertation, *University of Southampton*, 2000
[2] The Lincoln Electric Company, The Procedure Handbook of Arc Welding, 30th Edition, 1995
[3] TC Ltd., A Guide to Thermocouple and Resistance Thermometry, 1999
[4] Gu M., Goldak J.A., Steady-state formulation for stress and distortion of welds, *Journal of Engineering for Industry,* Vol. **116**, pp467-474, November 1994
[5] Jonsson M., Karlsson L., Lindgren L-E, Deformations and stresses in butt-welding of large plates, *Numerical Methods in Heat Transfer*, Volume III, by *Lewis R.W., John Wiley & Sons Ltd*, pp35-58, 1985
[6] Tsai C.L., Lee S.G., Shim Y.L., Modelling techniques for welding-induced residual stress predictions, *International Conference Proceedings on Modelling and Control of Joining Processes,* ed. T. Zacharia, AWS, Fla., pp462-469, 1993
[7] BS 4360 : 1990, British standard specification for weldable structural steels, *BSI*, 1990
[8] ASTM Designation E 8M – 98: Standard test methods for tension testing of metallic materials, 1998
[9] BS 970: Part 1: 1983: Wrought steels for mechanical and allied engineering purposes through hardening steels including steels capable of surface hardening by nitriding.
[10] Hardness test, EM327, Mechanics of materials laboratory, http://www.public.iastate.edu/~em327/experiments/instructions/hardness.pdf
[11] D. Tabor, *Journal of Inst. Metals*, Vol.**79**, pp 1-18, 1951
[12] Cahoon J. R., Broughton W. H., Kutzak A. R., The determination of yield strength from hardness measurements, *Metallurgical Transactions*, **2**(7), pp 1979-1983, 1971
[13] D. Tabor, The Hardness of Metals, *Oxford At The Clarendon Press*, 1951
[14] Lancaster J.F., Metallurgy of Welding, 6th edition, *Abington Publishing*, 1999
[15] Easterling K., Introduction to the Physical Metallurgy of Welding, 2nd Edition, *Butterworth-Heinmann*, 1993
[16] Vishnu R., Solid-state transformations in weldments, ASM Handbook, Vol. **6**, Welding, Brazing and Soldering, *ASM International*, pp70-87, 1993
[17] Measurement Group, Inc., Surface preparation for strain gauge bonding, M-Line Accessories, Instruction Bulletin B-129-7, 1999
[18] KYOWA, Strain gauges, a complete lineup of high performance strain gauges and accessories, KYOWA Electronic Instruments Co., Ltd.

6 Finite Element Prediction of Residual Stresses in a Fillet Welded T-joint

6.1 Introduction

It has been already pointed out that the welded T-joint is one of the most commonly used in engineering practice and how important is it to consider the residual stresses and distortion induced by the welding process in order to assess reliably its behaviour. FEM simulations of the fillet welding process for T-joints have been presented in the literature. However, these models are either representative of only single-fillet weld joints[1,2] or based on the assumption of simultaneous welding on the two sides[3,4,5]. Apparently, no modelling work has been carried out on the sequential welding of the two fillet welds although this is what usually happens in engineering practice. The complexity of the modelling process may have contributed to this apparent lack of analytical results.

In this chapter, thermal and structural FEM models of a sequentially welded two-sided T-joint were generated and the corresponding welding process simulated. The methods used in this simulation are similar to those used in the simulation of a butt weld, presented in Chapter 3 of this thesis. The main features of the essentially 2D analysis are ramped heat input function, temperature-dependent material properties and element death and re-birth technique. The geometry, material properties, and the welding process data were similar to those associated with the parallel experimental investigation presented in Chapter 5 so that temperature histories obtained from the experiment can be used to calibrate certain thermal inputs of the FE model. A symmetric FE model, representing simultaneous fillet welding on both sides of the weld, was also developed and run under identical conditions in order to assess the effect of sequential welding on residual stress calculations. Through further comparison with limited published analytical and experimental data, the developed simulation method is shown to be a reliable and versatile analytical tool for obtaining not only qualitative but also quantitative information on welding-induced residual stresses and distortion. This information is essential to both researchers and designers for assessing the failure behaviour of welded joints and structures under low applied

load, such as fatigue failure. The generated model could be further used to assess the effect of various parameters such as welding speed, thermal boundary conditions, material properties and fit-up on residual stresses developed due to welding.

6.2 Finite element modelling procedure

As for the butt weld simulation, 2-D FE analysis was applied to the T-joint model presented in this chapter. A 2-D transient thermal analysis was carried out first to obtain the global temperature history generated during the welding process. A quasi-static stress analysis was then developed with the temperatures obtained from the thermal analysis entered as loading to the stress model. The general-purpose FE package ANSYS [6] was used for both thermal and stress analysis performed sequentially with the appropriate combination of elements. A decoupled thermal-stress analysis is commonly used in simulations of the welding process since the stress development affects very little the heat transfer process. Such an analysis is not only faster and computationally more economical, but also allows for all useful features of individual thermal and stress analyses available in FE packages to be applied.

The geometry of the FE model was similar to the tested specimen WT1 apart from the sizes and profiles of the two fillet welds, which were assumed to be the same in the FE model although they were different in the test specimen, as shown in Fig. 5-8. As discussed in Chapter 5, Section 5.2.3, relatively big variations in weld size were found along the weldment. Visually inspection also clearly revealed that the weld profile varied along the weld length. Various defects were found in the WT1 specimen, as shown in Fig. 5-19, and these defects were not uniformly distributed along the weldment. It is thus impossible to simulate precisely the actual profiles of the weld and HAZ area in the FE model. The profiles of the weld and HAZ were thus simplified and idealised as shown in Fig. 6-1. The temperature development is not expected to be affected significantly by not including the defects, however, the residual stress results, especially within the weld area, may be different if defects are modelled.

A four-node quadrilateral thermal solid element was used. Based on the mesh sensitivity study presented in Chapter 3 for a similar thermal-mechanical analysis, 0.5 mm was chosen to be the size of the elements in and near the weld and HAZ areas where temperature and residual stress are expected to have sharp gradients, as shown in Fig. 6-2. The heat transfer between the surfaces of the attachment plate and the base plate, i.e. through the fit-up, was modelled using 2-D conduction bar elements, LINK32, which were converted to 2-D node-to-node contact elements CONTAC12 in the stress analysis.

6.2.1 Thermal analysis

The non-linear transient heat flow analysis accommodated the temperature-dependent thermal properties and predicted the temperature development during the welding process.

The steel plate used was BS 4360 – 43A grade steel the chemical composition of which is specified as C: ≤ 0.25%; Si: ≤ 0.5%; Mn: ≤ 1.6%; P & S: ≤ 0.05%. This type of steel has thus a similar chemical composition to those given in Table 3.3 and so the thermal properties of the steels listed in Table 3.3 can be used for this steel. The temperature-dependent thermal properties adopted were essentially within the ranges discussed in Chapter 3, Section 3.3.2. As observed in the parametric studies presented in Chapter 3, variations of the temperature-dependent thermal properties within the range given in the literature for structural steel has no significant effect on the final residual stress results. Thus, the temperature-dependent enthalpy was taken from Brown and Song[1] and the conductivity from Hong et al.[8] The temperature variations of these quantities are given in Fig. 3-5 and Fig. 3-6.

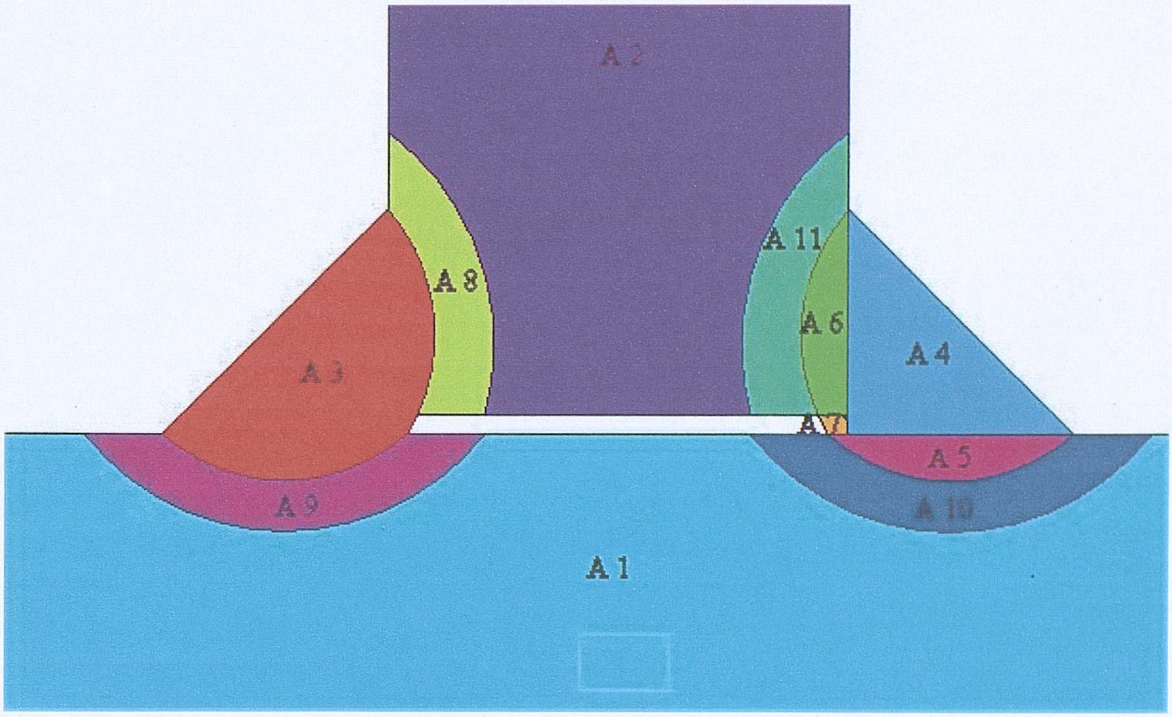

Fig. 6-1 Solid model showing area numbering

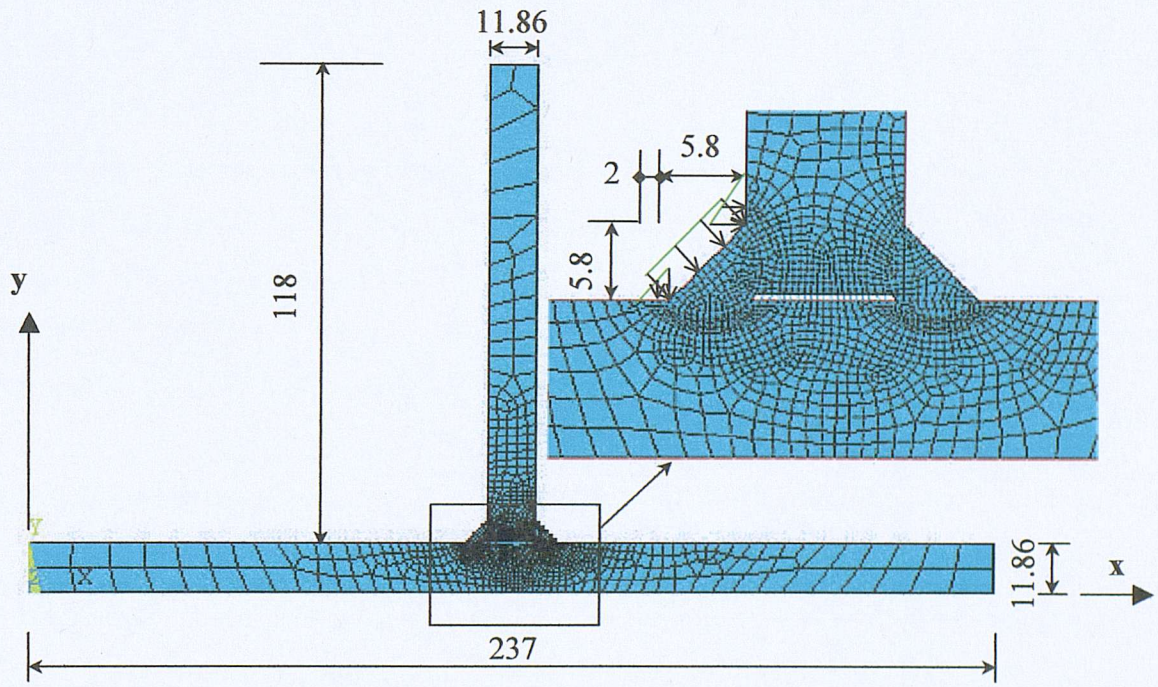

Fig. 6-2 Geometry and mesh map of the FE model, dimensions in mm

Heat source model

The total heat input into the specimen was calculated from Eqn (3-3) in Chapter 3, where the voltage, V was taken as 27 V, the current, I as 190 A. For the MIG welding process which is that used in this study, the arc efficiency, η_a is between 0.66-0.85[7]. The arc efficiency was initially assumed to be 0.75. Thus the total heat input rate, Q was found approximately equal to 3.8 kW, which is equivalent to 1907 kJ/m for the welding speed applied, $v = 2.02$ mm/s. The total heat input was assigned to the model in the form of surface load Q_s and body load Q_b. Their ratio can be adjusted to achieve an accurate representation of the fusion zone. In this study, Q_s/Q_b = 0.15/0.85 was found to give temperature distributions that best fitted the fusion zone modelled. As in Chapter 3, Section 3.3.2, the surface heat flux in this study was assumed to be uniformly distributed over the top surface of the weld metal and linearly varied over a short distance on the adjacent surfaces of the parent metal, as shown in Fig. 6-2 by the green lines. The body heat generation rate Q_b was applied uniformly to the volume of the weld metal.

Loading steps

In this 2-D simulation of an essentially 3-D welding process, the cross-section studied is somewhere in the middle region of the weldment transverse to the welding direction. To include the effect of out-of-plane heat input as well as to avoid numerical divergence problems which may be caused by a sudden increase in temperature, Hong et al.[8] applied a ramped heat input function. This method was adopted in this study as well. The heat was input in four load steps for each pass as shown in Fig. 6-3, where $t_1 = t_3 = t_5 = t_7 = 0.1$ s, $t_2 = t_6 = 0.4$ s, $t_4 = 677$ s and $t_8 =$ 14,700 s. These times roughly correspond to the welding and cooling periods measured during the welding of the test pieces. During pre-heat, the first pass weld area, Area 3 in Fig. 6-1, was considered absent and heat applied to the adjacent areas, Area 8 and 9, in the form of both surface heat flux and body heat. The same was applied to the second weld: heat was first applied to Areas 5 - 6 and 10 - 11 in load step 5. During the short post-welding step, the previously applied surface and body heat load was assumed to reduce linearly to zero.

In most practical cases, the two sides of a T-joint are welded sequentially. In this study, this sequential welding process was simulated. As ANSYS does not allow the generation of new elements between load steps, the element death and rebirth features of the program were used to simulate the fact that during the first welding pass, the elements representing the second fillet weld do not exist. In addition, this technique was also used to achieve the pre-heat load step (load step 1 and 5) where heat was applied to the HAZ area (Area 8 and 9 in load step 1; Area 5-6 and 10-11 in load step 5, refer to Fig. 6-1 for area numbering) while elements in the weld area (Area 3 for the first pass and Area 4 and 7 for the second pass weld) were killed and re-activated from the next load step. This element death and rebirth technique works in a way that the full model is generated first and those elements not initially present are "killed" by multiplying their thermal and mechanical properties by a severe reduction ratio. Temperatures of those killed elements were constrained at room temperature until they were reactivated in later load steps.

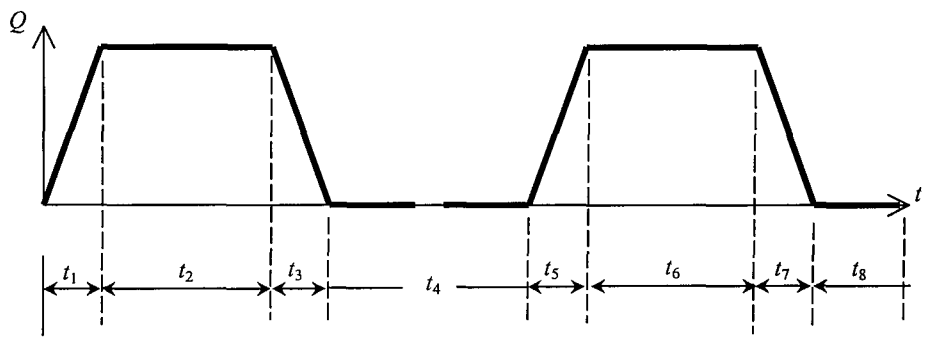

Fig. 6-3 Loading steps in the thermal analysis

Initial and boundary conditions

As discussed in Chapter 3, when the melting temperature is used, the amount of heat used to melt the electrode should be deducted from the total heat input into the model. In this simulation, this procedure was adopted and the melting temperature was used as the initial temperature.

Convection was applied to all free surfaces of the specimen with a temperature-dependent heat convection coefficient taken from Brown and Song[1] (h_1) as shown in

Fig. 3-7. In order to account for the fact that the specimen was welded on top of a thick steel plate through which heat was lost through conduction as well as convection, the convection coefficient for the bottom surface of the specimen was adjusted to include this effect (h_2, see Fig. 6-4). Furthermore, after the first pass on the right side had finished, the specimen will be distorted so that the left side of the specimen will not be in intimate contact with the supporting plate and less heat will be conducted through it (h_3, see Fig. 6-4). After the second pass, the specimen tends to deform in the opposite direction so that, this time, part of the bottom surface on the right side of the specimen will leave the supporting plate. Thus the convection coefficient was varied during the different stages of the welding process to account for these changes in real boundary conditions.

Radiation was not considered in this model as the study presented in Chapter 3 found it to have a very limited effect on the final residual stress results while including it would make the already complicated modelling computationally more difficult.

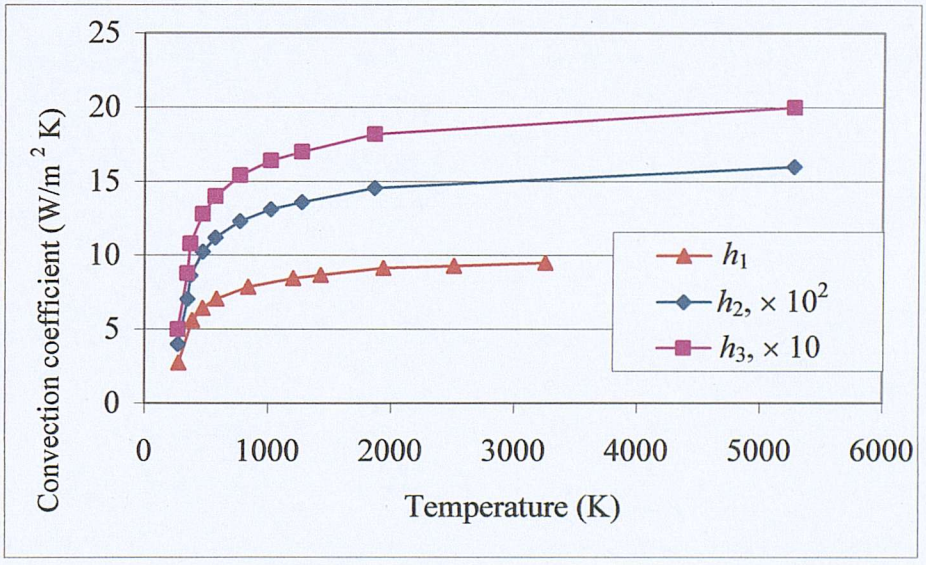

Fig. 6-4 Temperature-dependent convection coefficients adopted over various specimen surfaces

6.2.2 Stress analysis

A 2-D non-linear quasi-static stress analysis was subsequently conducted to calculate the welding-induced residual stresses. The thermal element was converted to the corresponding plane strain structural element available in ANSYS. Thus the mesh used in stress analysis was identical to that in the thermal analysis. It can be seen in Fig. 6-2 that this mesh is sufficiently refined in the weld and HAZ areas to capture stress variations due to significant temperature spatial gradients. The conduction bar elements (LINK32) through the fit-up gap were changed to 2-D node-to-node structural contact elements (CONTAC12), which are only capable of supporting compression in the direction normal to the surfaces and shear in the tangential direction. The nodal temperature solutions obtained from the thermal analysis were read as loading into the stress analysis. In order to capture the residual stresses induced due to the heating and cooling cycle, the temperature history needed to be read at a sufficiently large number of time points, especially where the temperature gradient is large. The temperatures were read in load steps. However, the greater the number of the thermal solution steps used, the more the computational time and the larger the store space required. One way to improve efficiency is to identify the time points when the temperature gradient is low and remove some of the corresponding solution steps. The model was constrained at the middle of the bottom surface to prevent free-body movement.

The temperature-dependent Young's modulus was taken from Brown and Song[1], which is within the range given in the literature (see Fig. 3-11) and thermal expansion coefficient taken from Hong et al.[8] (see Fig. 3-13). As discussed in Chapter 3, Section 3.5.4, the effect of variation of thermal expansion coefficient on the final residual stress results is not significant. The plastic properties of the base metal and the deposited weld metal at room temperature were experimentally determined as presented in Chapter 5; these values were found in Chapter 3 to have the most significant effect on the residual stresses results. The temperature dependence of these properties was deduced in the same way as in Chapter 3, Section 3.3.3 for the butt weld simulation based on the room temperature values. Fig. 6-5 shows the stress-temperature relation adopted.

As discussed in Chapter 3, Section 3.3.3, it is more realistic to use kinematic strain hardening since the material in and near the fusion zone experiences a cycle of compressive plastic strain and then tensile. A multi-linear kinematics strain-hardening model was adopted which was based on the stress-strain curves shown in Fig. 6-6. The stress-strain curves for the base metal and the weld metal are average values from the tensile tests carried out in Chapter 5. The stress-strain curve for the HAZ was based on that determined for the base metal and weld metal but scaled according to the relative hardness values of the HAZ and base/weld metal. However, the stress-strain curve for the HAZ was initially taken to be the same as that of the base metal since no experimental results from the hardness tests were available when the FE model was first generated. The stress-strain curve shown in Fig. 6-6 was adopted later and results compared with the previous model to assess the effect of HAZ on the local residual stress distribution.

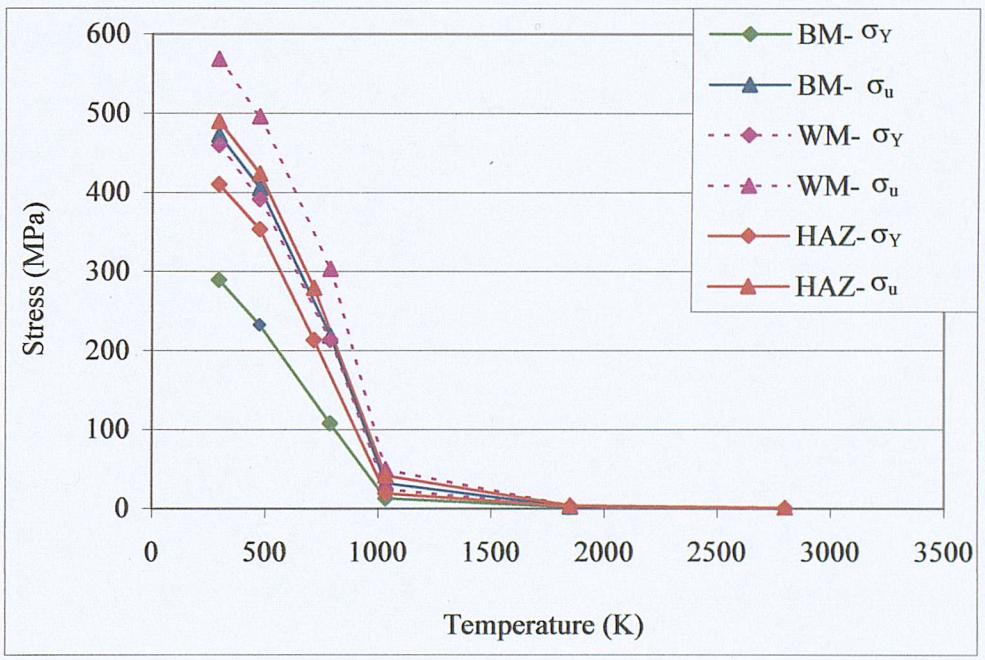

Fig. 6-5 Temperature-dependent plastic properties used in FE model

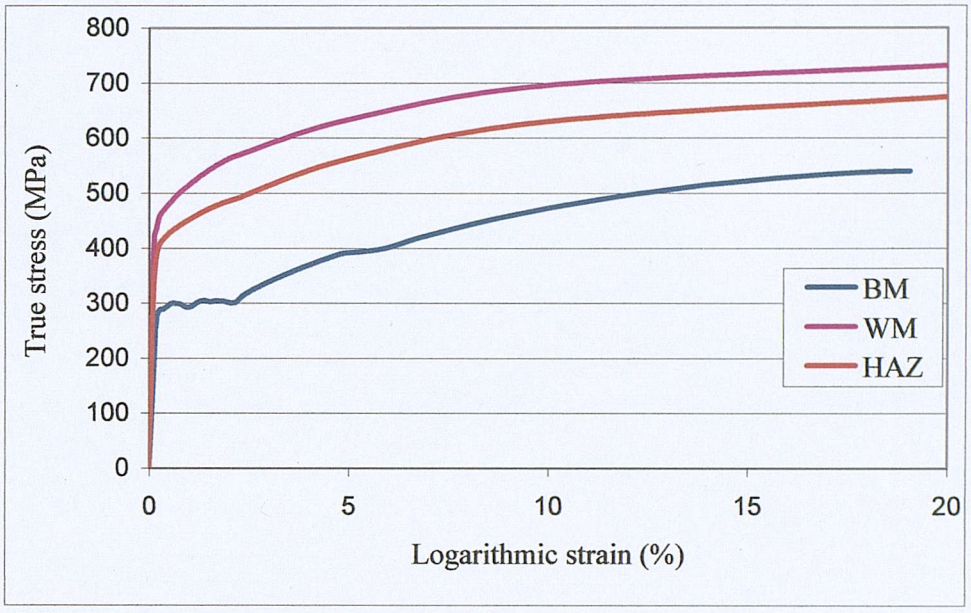

Fig. 6-6 True stress-logarithmic strain curves adopted in the FE model for WM, BM, and HAZ at room temperature

The element kill and rebirth technique was used in stress analysis as well to simulate the deposition of each weld at the respective temperature loading step. Appropriate material property changes were also imposed between steps. The elements belonging to the first fillet weld were activated at the end of the pre-heat phase ($t = t_1$) to simulate the deposition of the weld metal after pre-heat. The elements representing the second pass were also activated after the pre-heat in welding the second pass.

In order to simulate the fact that the weld metal is deposited in its fluid state and no expansion of this weld metal occurs, the thermal expansion coefficient of weld metal was decreased by a hundred times and changed back to normal from the time point identified from the thermal analysis where the temperature of the weld metal started to drop.

For elements in Area 5 and 6 as shown in Fig. 6-1, the material properties were assigned to be the same as those of the base metal during the first pass welding. They

were then changed to those of the weld metal during the deposition of the second weld.

6.3 Symmetric model

A symmetric model simulating a simultaneous welding of the two passes was also generated. The modelling process is much simpler than the sequential one. The mesh map is shown in Fig. 6-7. The mesh density was the same as that of the sequential model. The material properties and welding process data were identical to that of the sequential model.

6.3.1 Thermal analysis

The heat input model and initial temperature applied in this model were the same as in the sequential model. There is a slight difference in modelling convection. The convection coefficient used for the support plate was not changed during the welding process as only one pass welding was simulated. Only four load steps were applied with heat applied in the same ramped function as the sequential model for the first three steps, but the forth step was the final cooling down step, as shown in Fig. 6-8. Element kill and re-birth is only necessary for the pre-heat when the weld metal has not yet been deposited.

6.3.2 Stress analysis

The temperature-dependent material properties, conversion of element types, and temperature reading in as load, were all the same as for the sequential model. Symmetric boundary conditions were applied along the symmetry axis (see Fig. 6-7). The centre point at the bottom surface of the plate was also constrained in the vertical direction, as shown in Fig. 6-7. Appendix I section I-3 lists some important commands used for these models.

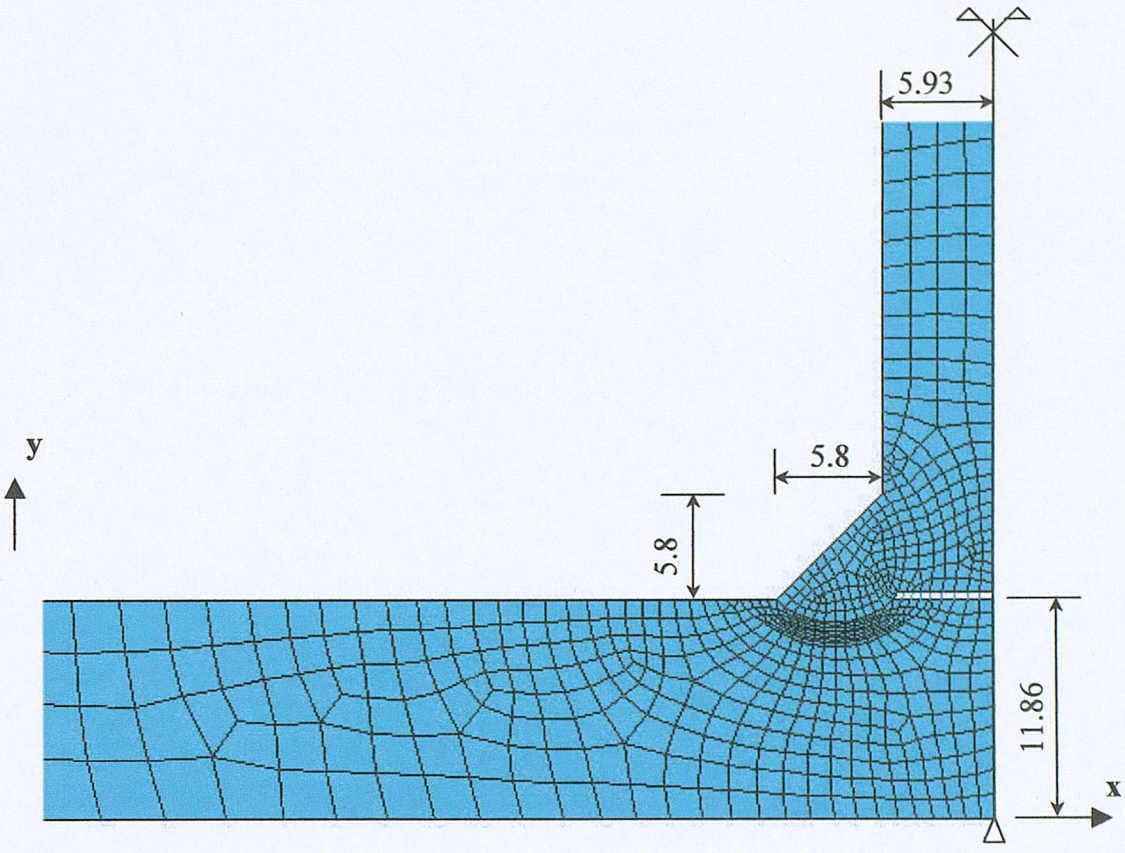

Fig. 6-7 Geometry and mesh map of the symmetric model, dimensions in mm

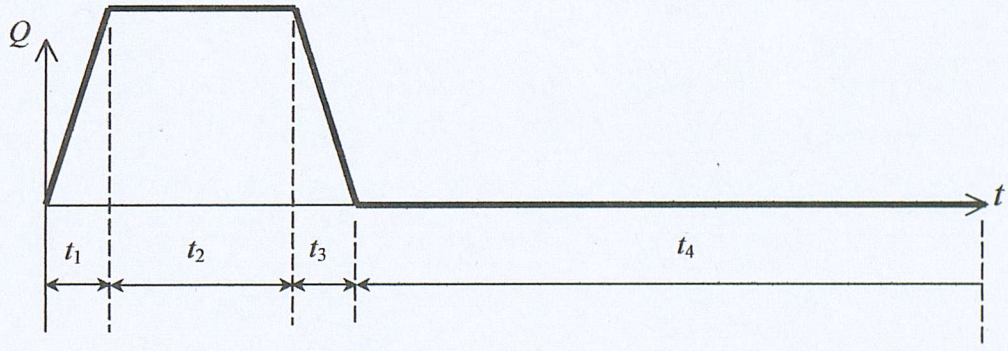

Fig. 6-8 Loading steps for the symmetric model

6.4 Results and discussion

The same method as that used for the mesh sensitivity study for the butt weld residual stress simulation presented in Chapter 3, Section 3.3.2 and 3.3.3, was applied and Fig. 6-2 shows the final FE mesh corresponding to a converged solution.

6.4.1 Temperature history

In general, good agreement between analytical results and experimental measurements on temperature history was achieved by most of the researchers in this area[3,8,9,10,11,12]. It was demonstrated in Chapter 3 that variations in thermal properties within the range adopted by various researchers in this area has little effect on the final residual stress results, but they do affect the temperature development slightly. As there are uncertainties regarding thermal properties at high temperature as well as the exact value of arc efficiency and boundary conditions, it is common in this research area that the measured temperature histories at a few discrete locations are used to calibrate the thermal analysis input by adjusting the values of certain parameters, within their practical range, so that the predicted temperature development agrees with the measured one as closely as possible[1,11,13].

The temperature histories at a few positions were measured in the experiment using thermocouples, as presented in Chapter 5, Section 5.2. Temperature measurements were used to calibrate the arc efficiency and convection of the bottom surface where the uncertainty of heat loss through the steel table underneath is more significant. Thermocouples TC6, TC2 and TC4, shown in Fig. 5-2 in Chapter 5, obtained from both the experiment and the FE analysis are shown in Fig. 6-9. A good agreement between experiment and FE was achieved with an arc efficiency of 0.78 and a convection coefficient, h_2 (as shown in Fig. 6-4), for convection when the bottom surface of the joint is in contact with the supporting table, and h_3 (see Fig. 6-4) when the bottom surface deforms upwards after welding. Fig. 6-10 shows the temperature history obtained from the original model (labelled FE1) and the calibrated model

(labelled FE). The maximum temperature difference between the original and the calibrated model is about 6.5%, which from the study presented in Chapter 3, is not expected to have significant effect on the final residual stress results.

Careful examination of the predicted temperature distribution over the weld and the area surrounding it at various critical stages of the simulation confirmed the validity of the solution. The fusion zone above the melting temperature 1803 K was, for instance, predicted to be close to the assumed weld area shape, as shown in Fig. 6-11.

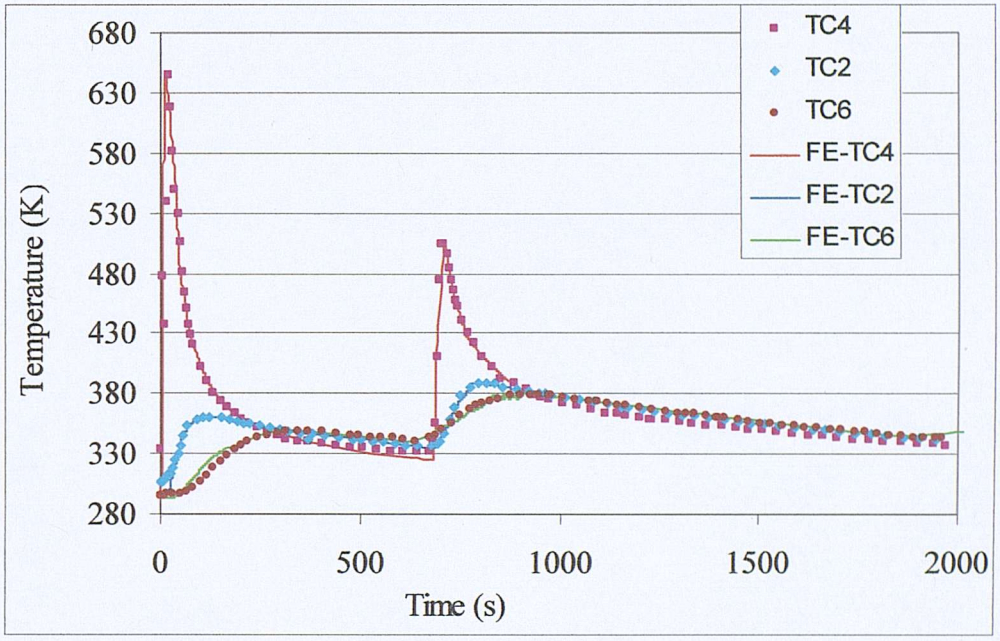

Fig. 6-9 Temperature histories from experimental measurement and predicted by the model using calibrated heat input parameters

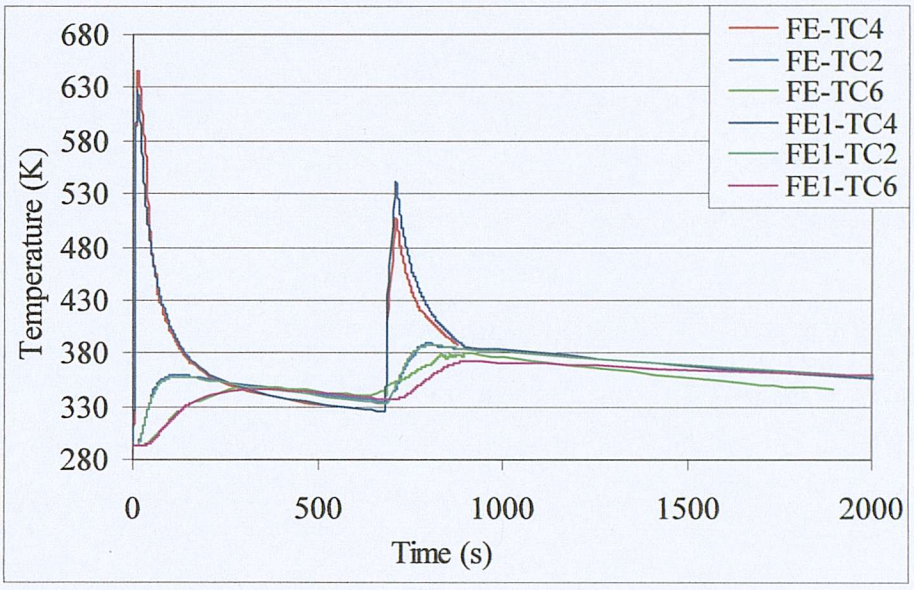

Fig. 6-10 Temperature history from the original (FE1) and calibrated (FE) model

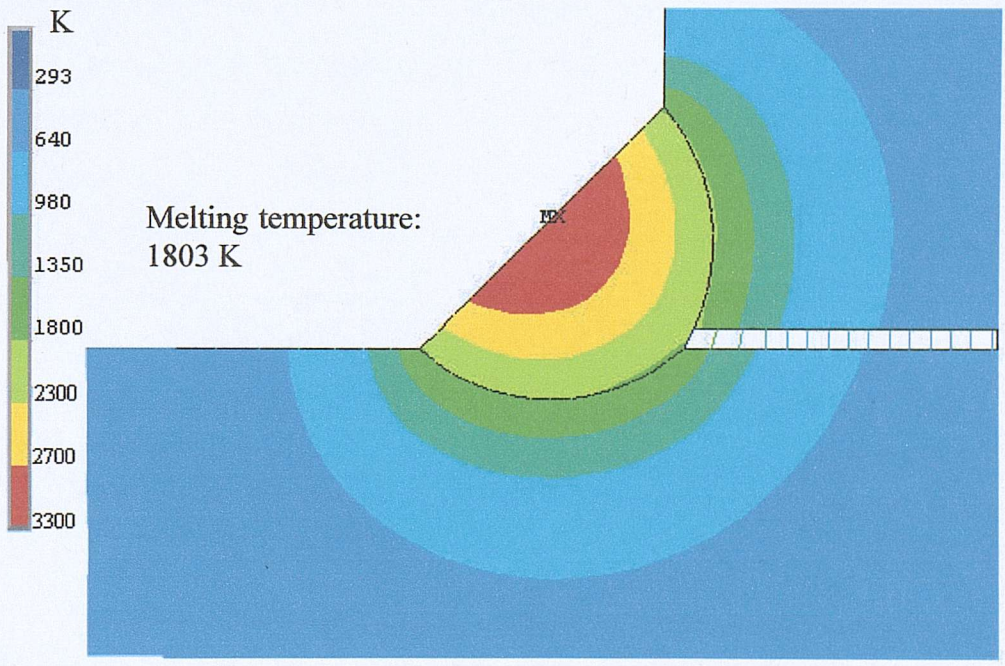

Fig. 6-11 Temperature distribution showing the predicted fusion zone

6.4.2 Residual stress distribution and distortion

The stress analysis results were monitored throughout the simulation in order to ensure a rational mechanical response to every stage of temperature input. Compressive stresses were observed in the heated areas counterbalanced by tensile ones away from them, as shown in Fig. 6-12, during the load step in the stress analysis when the HAZ was heated while elements in the weld metal area were "killed". This pattern was gradually reversed during cooling. Despite the differences in weld profiles between the FE model and specimens, the distorted shape predicted after welding was similar to that of the specimen. The value of the final distortion according to the FE prediction was measured to be 86.3°. This is comparable with the experimental measurement as listed in Chapter 5, Table 5-3.

The final results for certain variations of residual stresses are presented as curves labelled "No HAZ" in Fig. 6-13 to Fig. 6-14. Fig. 6-13 shows the longitudinal stress (σ_z) distribution over the surfaces of the base plate and Fig. 6-14 in the attachment. As in Chapter 3, Section 3.4.2, the longitudinal stress was obtained by deducting the mean stress σ_z^m over the cross section area calculated from Eqn. (3-11) to account for the over-constraint opposed by the plane strain assumed in the FEM analysis. The longitudinal stress distribution was compared with patterns determined experimentally by other investigators[14] for a fillet welded T-joint, reproduced in Fig. 6-15. The longitudinal stress distribution of the base plate from both the FE model and the experimental measurement show a similar shape. Towards the end of the main plate the compressive residual stress continue to increase in the experimental measurements. This may be due to the constraints applied in the experiment, as demonstrated by the study on the effect of constraints on residual stresses in a butt weld presented in Chapter 3, Section 3.5.7. Since the dimensions and material properties of the experimental specimen (σ_Y = 244 MPa, dimensions see Fig. 6-15) were different from that of the FE model (σ_Y = 290 MPa, dimensions see Fig. 6-2), the magnitude of the residual stresses is not comparable. However, residual stresses of the magnitude of the yield stress of the material used were obtained from both methods. Comparing Fig. 6-14 with Fig. 6-15, a discrepancy was found in the longitudinal residual stress distribution along the surface of the attachment plate

further away from the weld. The experimentally determined compressive residual stress turns to tensile and then compressive again at a distance about half the length of the attachment plate. However, in the length of approximately the attachment plate in the FE model (Fig. 6-2), as marked in Fig. 6-15, the distributions for the attachment plate from the FE model and the experiment study are similar. This difference in length of attachment plate between the FE model and the experiment specimen is thought to be the reason for the discrepancy. This is also evidence in the same experimental study carried out by Rao et al.[14], that the longitudinal residual stress distribution in a joint with a shorter length of attachment plate shows the same trend of variation.

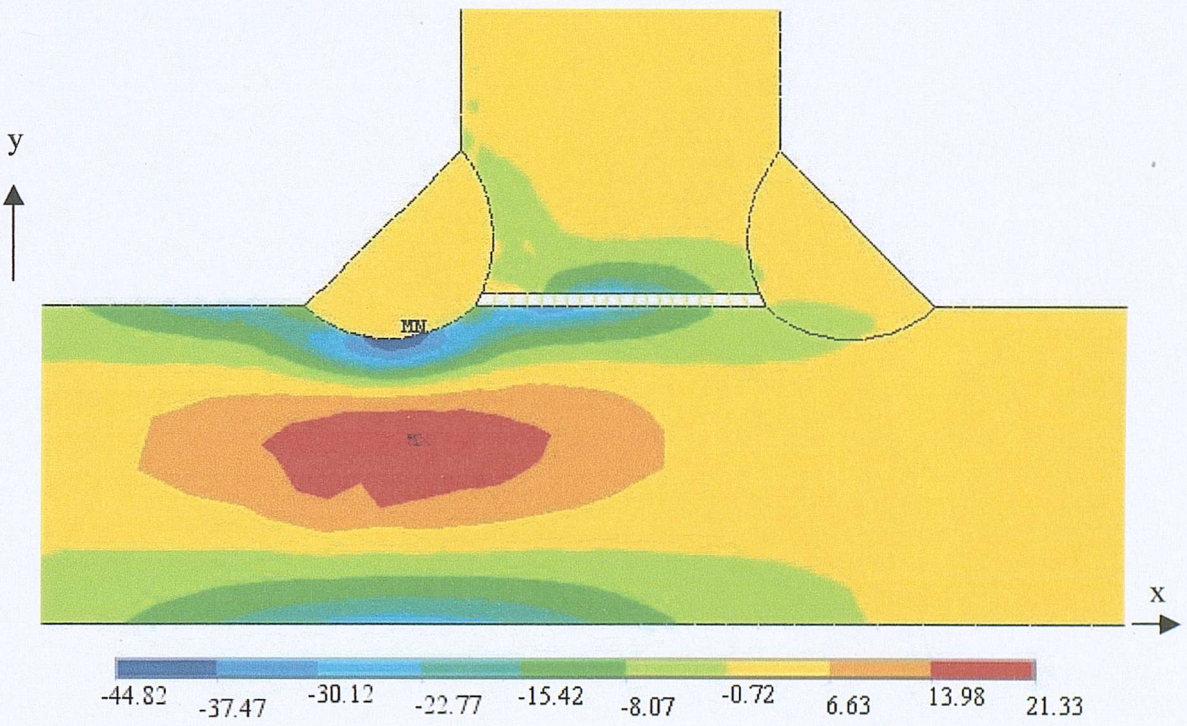

Fig. 6-12 Stress (σ_z) distribution developed after the first load step of stress analysis, stress units in MPa

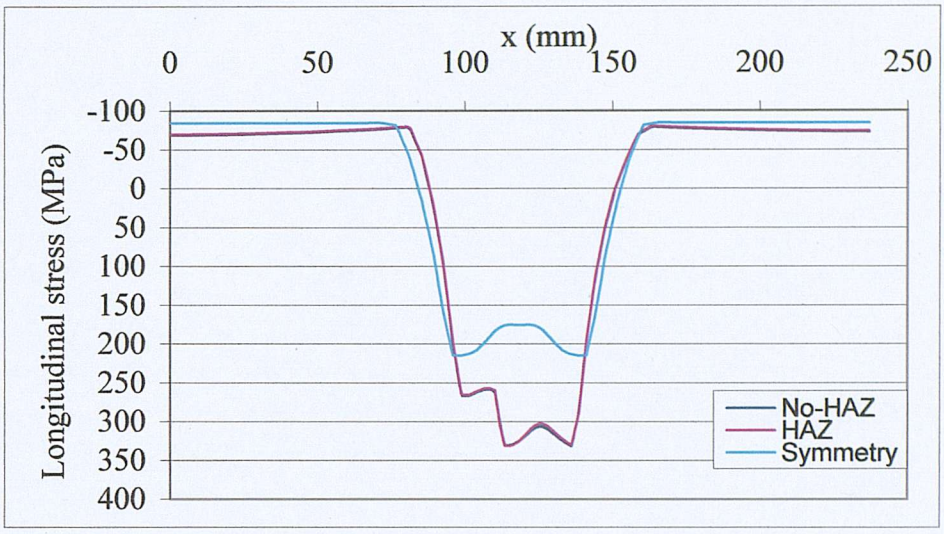

Fig. 6-13 Longitudinal residual stress (σ_z) over the bottom surface of the base plate

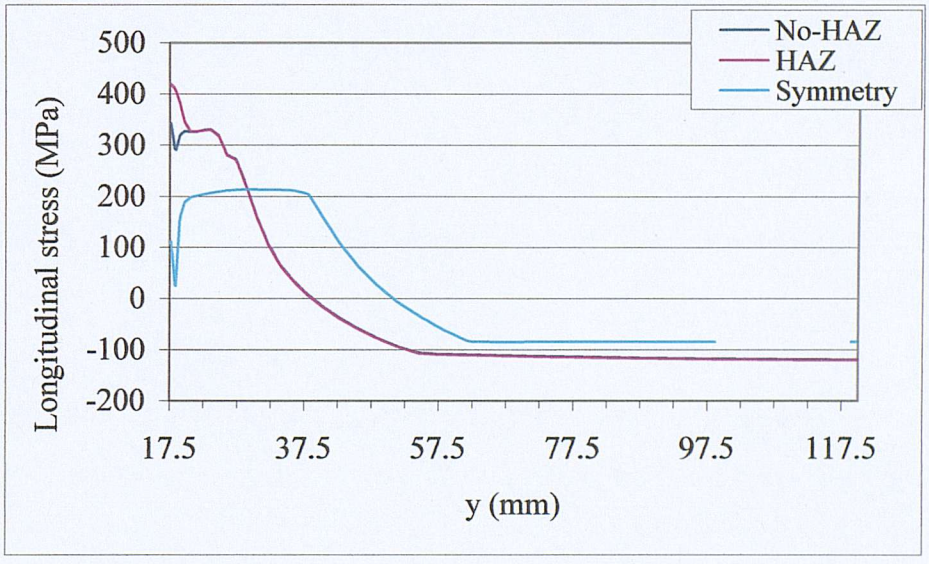

Fig. 6-14 Longitudinal residual stress (σ_z) patterns over the left surface of the attachment plate

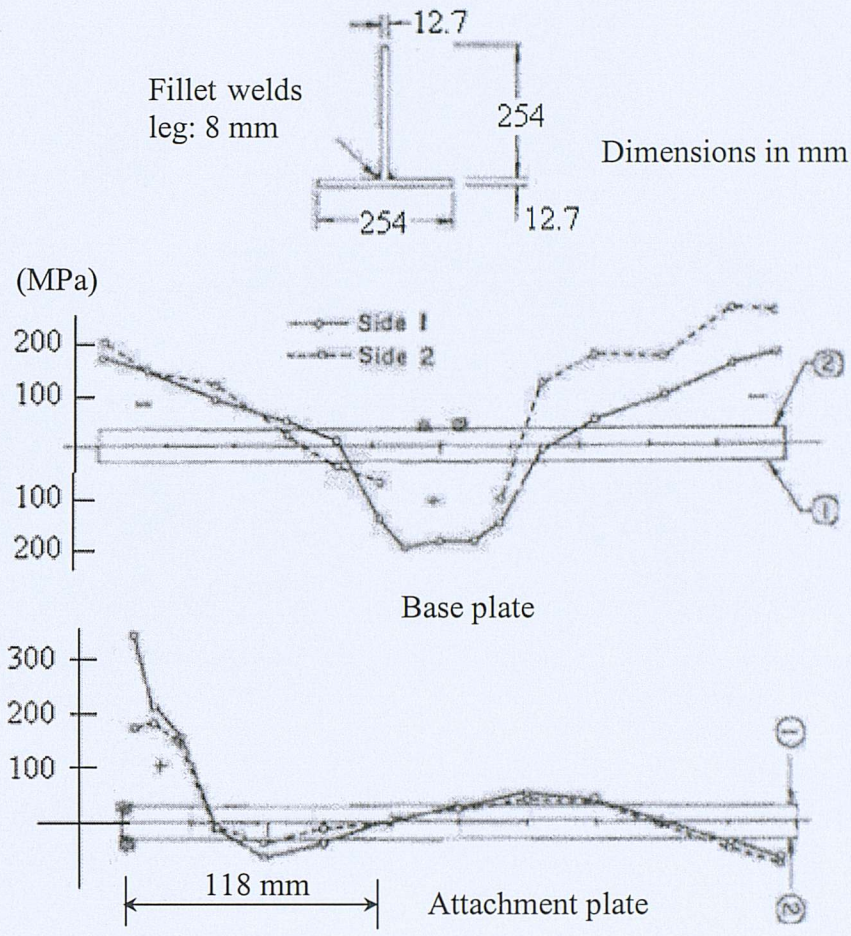

Fig. 6-15 Longitudinal residual stress (σ_z) distribution from experiment[14]

The focus in the present investigation has been on the in-plane stress distribution, which can be associated with brittle or fatigue fracture if amplified by external action transmitted through the structure. The results for σ_x in the first and the second pass fillets are presented in Fig. 6-16.

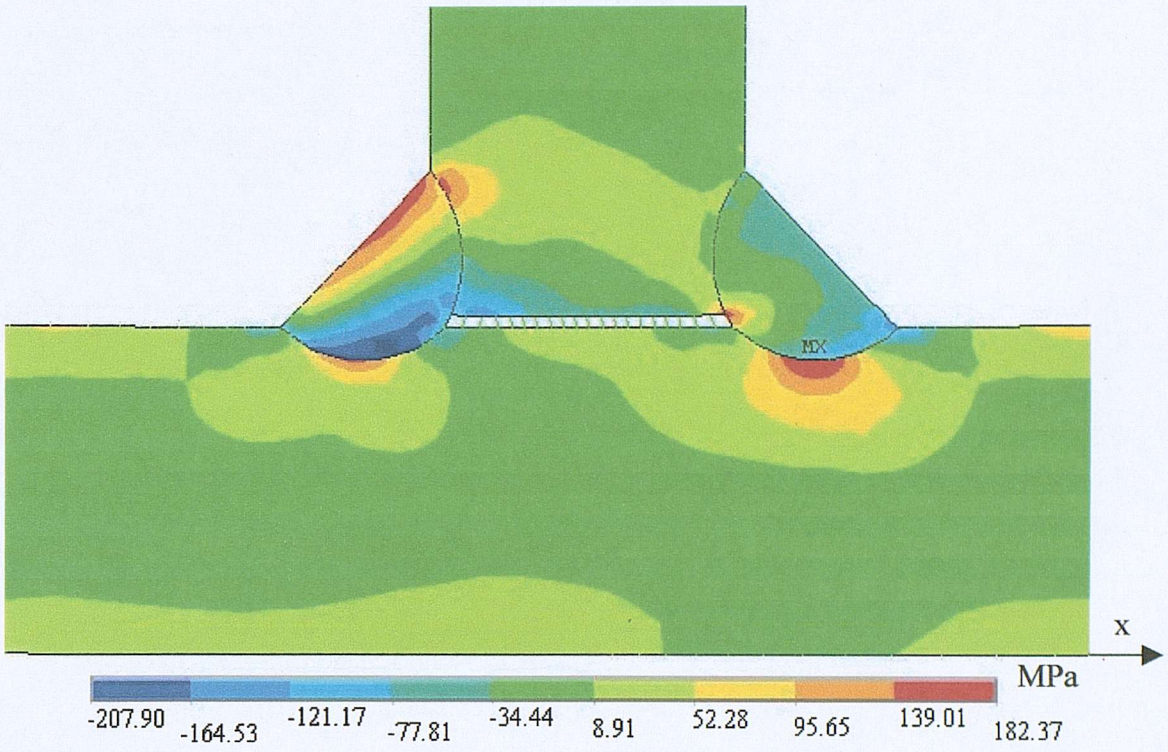

Fig. 6-16 Transverse residual stress σ_x assuming HAZ has the same material properties as BM

6.4.3 Accuracy of symmetric analysis

For comparison with previous analyses[4], the simulation was repeated for the symmetric case of simultaneous welding on both sides. The result for σ_x from the symmetric analysis is shown in Fig. 6-17 . This is similar to that found by Sarkani et al.[4] and hence helps to assess the present model. However, comparison with the results from the sequential simulation reveals that the stress distribution obtained from the symmetric model is similar to that for the second pass weld while very different from that for the first pass weld.

The longitudinal residual stress distribution over the bottom surface of the main plate and the left surface of the attachment plate obtained from this study are also presented in Fig. 6-13 and Fig. 6-14 as the curves labelled "Symmetry" for comparison. The difference between sequential welding and the symmetric model is

clearly seen. This difference is reasonable since, for the sequential model, the first pass weld acts as extra constraint when welding the second pass. This cannot be taken into account by the symmetric analysis.

In the symmetric simulation, the residual stresses predicted for the two passes are obviously the same, while as can be seen from Fig. 6-16 the stress distribution predicted by the sequential model is different for the two passes. There should be no distortion in the horizontal direction in the symmetric model along the symmetry axis; however, it is known from engineering and experimental practice that this is not true. The sequential model actually predicted this distortion. It thus can be concluded that a symmetric model is not adequate for predicting the residual stresses of a sequentially welded T-joint.

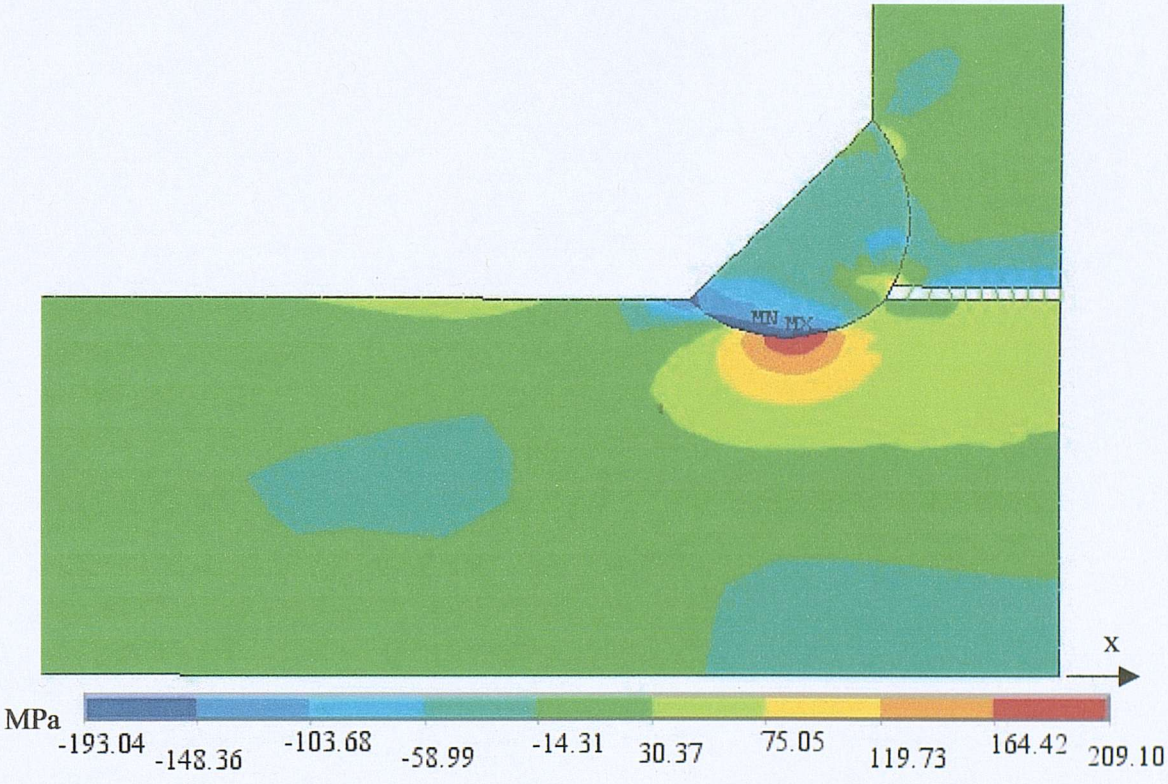

Fig. 6-17 Transverse residual stress σ_x in the fillet weld for a symmetric process

6.4.4 Effect of HAZ on the final residual stress results

The yield and ultimate strength for elements in Areas 8-11 (see Fig. 6-1) were changed from BM to HAZ (see Fig. 6-6) and the welding process simulated again. Fig. 6-18 and Fig. 6-19 show the longitudinal and transverse residual stresses, respectively, obtained from this analysis. The longitudinal stress distribution over the bottom surface of the plate and the left surface of the attachment plate are shown as the pink curve labelled "HAZ" in Fig. 6-13 and Fig. 6-14, respectively. It is obvious that considering different material properties for the HAZ has little influence on the longitudinal stress except locally, in the area neighbouring the HAZ.

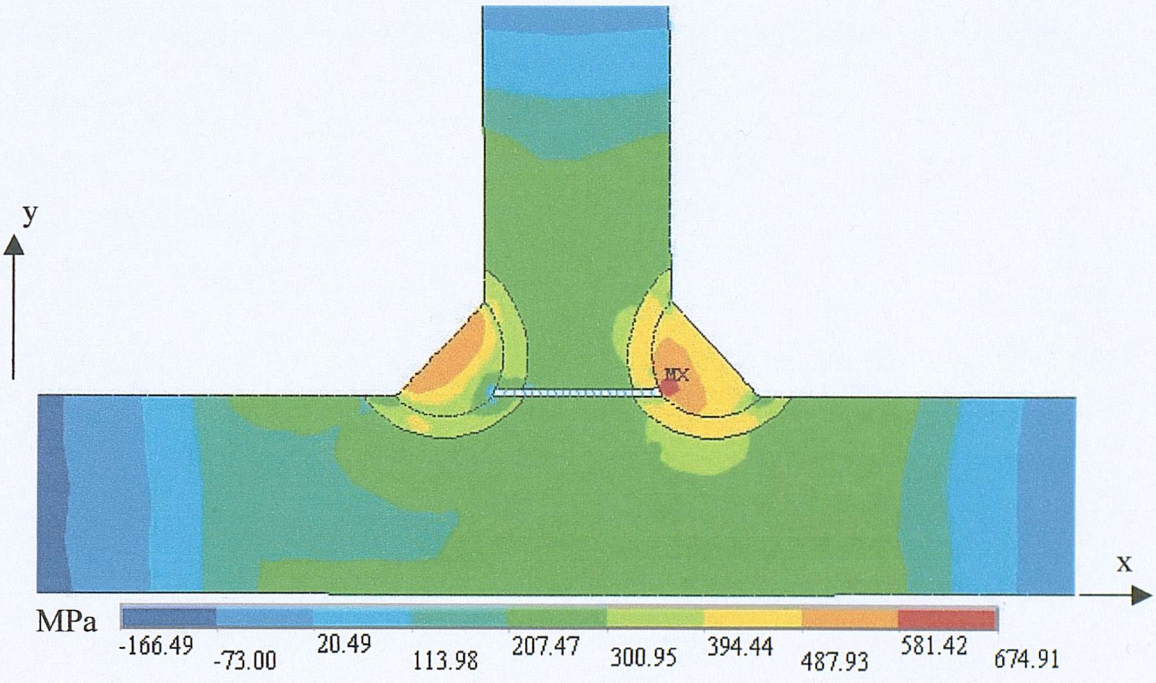

Fig. 6-18 Longitudinal stress (σ_z) distribution with material properties of HAZ

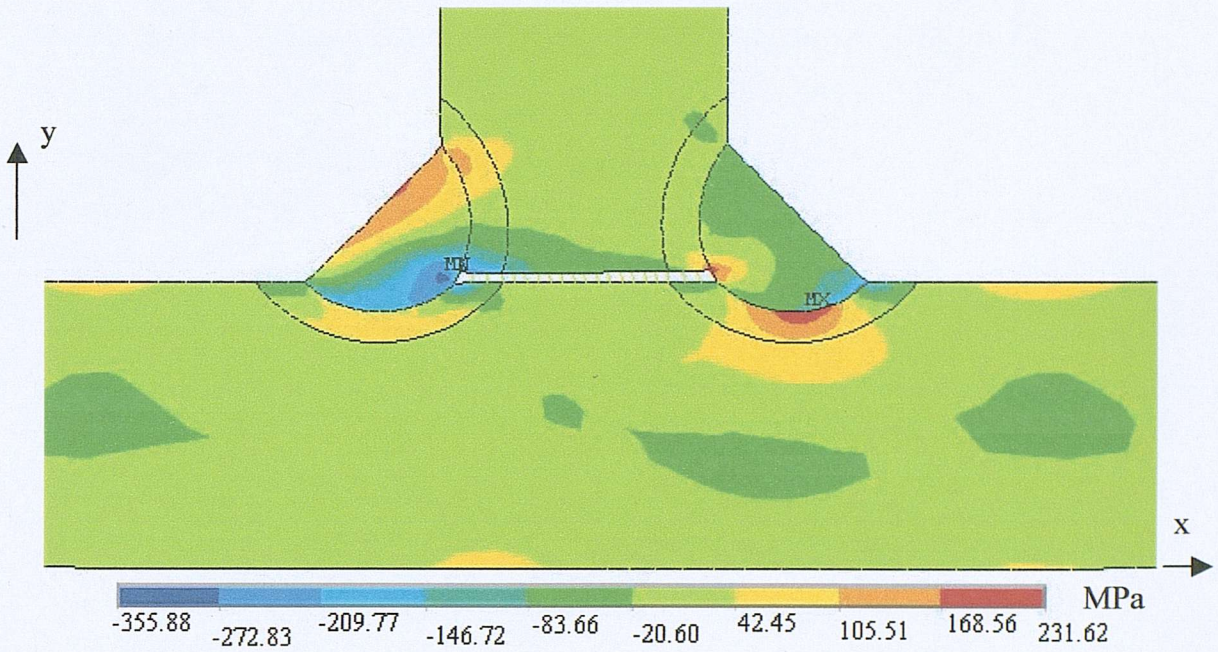

Fig. 6-19 Transverse residual stress (σ_x) distribution with material properties of HAZ

6.5 Summary

For a welded T-joint, most FE residual stress analyses presented in the literature either adopted a symmetric model simulating simultaneous welding of the two passes or only the first pass due to the complexity of the problem. The symmetric model simplifies the problem but is not accurate enough as the real constraint conditions during the second pass have been changed due to the presence of the first weld. This study provides a reasonable method of simulating the sequential welding process which is what really happens in real life.

The FE simulation of the welding process presented in this chapter provided new information on the residual stress magnitude and distribution over the weld area of a sequentially welded T-joint. A reliable thermal analysis is a prerequisite to the accurate prediction of residual stresses. The thermal analysis was calibrated by comparing the temperature history with that obtained from experiment. Good agreement of temperature results between FE models and experimental measurements are often achieved by most researchers in this area. However, the

residual stress results are extremely difficult to verify experimentally due to the small size of the area of interest and the experimental difficulties of measuring residual stresses during the welding operation. Every effort was made, however, to ensure a rational correlation between the stresses developing and the corresponding temperature history. Comparing the results with limited information including the angular distortion obtained from experiments presented in Chapter 5 of this thesis and in the literature[14] and the results of another FE simulation[4], the modelling methodologies adopted in this study are believed to give acceptable results.

Accurate representation of the material properties of the HAZ has little effect on the residual stress distribution away from that area, but a localised effect is evident which may affect the assessment of the fracture and fatigue behaviour of welded T-joints.

The same methodology can be applied to the WT2 sample to predict the residual stresses present in that weldment once dimensions and material properties are inputted. The predicted residual stresses can then be used as the initial condition to which external loads are applied. Hence the effect of residual stresses on the load carrying behaviour of a welded T-joint can be assessed. This is presented in Chapter 7.

Limitation of the FE model

The validation of the model developed is limited by the amount of experimental results available in the literature. Measurement of residual stresses is, unfortunately not practical at the present stage due to limitations of apparatus available.

The profiles of the weld and HAZ areas did not precisely represent the experimental specimens due to the variations noted and the various defects in the actual specimens.

As for the butt weld simulation presented in Chapter 3, the material properties at high temperatures were not obtained from direct experiment for the steel plate used. The

values used by other researchers were adopted based on a detailed comparison and reliability assessment, as presented in Chapter 3. From the sensitivity study carried out in Chapter 3, the variation of thermal properties within the range given for structural steel were found to have little influence on the final residual stress results. In addition, in this study certain input of the thermal analysis was calibrated by comparing the predicted temperature histories with those measured experimentally so that uncertainties arising from these input were limited.

As discussed in Chapter 3, Section 3.8, transformation plasticity, temperature-history dependency, plasma pressure, and the fluid movement in the weld pool were not included in this model either.

References

[1] Brown, S.B., Song, H., Implications of three-dimensional numerical simulations of welding of large structures, *Welding Journal Research Supplement*, **71**(2), pp55s-62s, 1992

[2] Brown. S.B., Song, H., Rezoning and dynamic substructuring techniques in FEM simulations of welding processes, *Journal of Engineering for Industry – Transactions of the ASME,* **115**(11), pp415-423, 1993

[3] Michaleris P., DeBiccari, A., Prediction of welding distortion, *Welding Journal Research Supplement,* **76**(4), pp172s-181s, 1997

[4] Sarkani S., Tritchkov V., and Michaelov G., An efficient approach for computing residual stresses in welded joints, *Finite Element in Analysis and Design,* **35**(3), pp247-268, 2000

[5] Teng T-L., Fung C-P., Chang P-H., Yang W-C., Analysis of residual stresses and distortions in T-joint fillet welds, *International Journal of Pressure Vessels and Piping*, Vol.**78**, pp523-538, 2001

[6] ANSYS 5.6, SAS IP, Inc., Canonsburg, PA (1999)

[7] Christensen N., Davies V. de L., Gjermundsen K., Distribution of temperatures in arc welding, *British Welding Journal*, **12**(2), pp54-75, 1965

[8] Hong J.K., Tsai C. –L, Dong P., Assessment of numerical procedures for residual stress analysis of multipass welds, *Welding Journal Research Supplement*, **77**(9), pp372s-381s, 1998

[9] Andersson B. A. B., Thermal stresses in a submerged-arc welded joint considering phase transformations, *Journal of Engineering Materials and Technology, Transactions of the ASME*, **100**, pp356-362, 1978

[10] Shim Y. L., Feng Z., Lee S., Kim D., Jaeger J., Papritan J. C., Tsai C.-L., Determination of residual stresses in thick-section weldments, *Welding Journal* **71**(9), pp305s-312s, 1992

[11] Jonsson M., Karlsson L., Lindgren L.-E., Deformation and stresses in butt-welding of large plates, Numerical Methods in Heat Transfer, Vol. III, Edited by Lewis R. W., *John Wiley & Sons Ltd*, pp35-58, 1985

[12] Argyris J. H., Szimmat J., Willam K. J., Finite element analysis of arc-welding processes, Numerical Methods in Heat Transfer, Vol. III, Edited by Lewis R. W., *John Wiley & Sons Ltd*, pp 1-35, 1985

[13] Withers P. J., Measurement and prediction of residual stresses, Residual Stresses- Their Origin, Measurement and Application, *Personal Development Seminar and Workshop*, London, 2002

[14] Rao N.R.N., Estuar F.R., Tall L., Residual stresses in welded shapes, *Welding Journal Research Supplement*, **43**(7), pp295s-306s, 1964

7. Finite element analysis of T-joints under loads

7.1 Introduction

In order to study experimentally the effect of a particular parameter, the size of the HAZ for example, on the behaviour of a welded T-joint, joints with different HAZ sizes need to be made and tested. This is both time-consuming and expensive. Finite element analysis provides a very efficient and economic alternative provided a satisfactory degree of confidence in its result has been established. In addition, detailed stress and strain distributions can be obtained from finite element models which give better insights into the behaviour of the joint. In this chapter, the FE modelling of T-joint specimens under bending was initially developed without considering residual stresses and using the same methodologies as that for the cruciform joint. The dimensions and material properties of those models were similar to the experimental specimens described in Chapter 5. Results from the experimental study and the finite element modelling were compared and the FE model assessed. The effect of geometry on the local stress distribution in the weld area was studied. From these results, the variation of failure mode observed in the experiments was explained. A preliminary study on the effect of defects has also been carried out based on FE models of imperfect welded specimens.

Although it is known that residual stresses have no significant effect on the failure load of welded joints due to the re-distribution of stresses after yielding of the joint under external loading, it has been found that the presence of residual stresses affects the yielding load of the joint depending on the directions of both the residual stresses and the external loadings. As discussed in Chapter 4, Section 4.4, Fessler and Pappalettere[1] carried out an experimental study on a main plate strip in a fillet welded cruciform joint with both the two side plates and the four welds removed and then loaded under tension. Yielding was found to occurr at a load of only 78% of the nominal yield load under tension. This was attributed to the presence of tensile residual stress due to welding. Many studies have been carried out on simulating welding process and load-carrying behaviour of welded joints, however, little has been done on combing them together to study the effect of detailed residual stress

distribution on the load-carrying behaviour of the joints. This effect could be significant for failures that occur at low loads, such as brittle fracture, of welded joints. As a first attempt, this study demonstrates the feasibility of combining residual stress simulation with a load-carrying study of welded joints by applying the residual stresses obtained from a welding process simulation, using the modelling methodology developed in Chapter 6, as the initial conditions to the joint subjected to external loading.

7.2 T-joints under bending

7.2.1 Models of WT2 specimens

Geometry of the FE models

Geometry of the joint

It has been found from the etched specimens that there is a slight variation in the profile and size of the weld area and HAZ along the welding direction. This variation was thought to be one of the reasons for the differences in failure path reported in Chapter 5 section 5.4.5. It is for this reason that the detailed profile of the welds was modelled. In the FE simulation, the profile and size of the weld area and HAZ, as shown in Fig. 7-1, were obtained from an etched specimen. The etched cross section, see Fig. 5-20, of the weld area was first scanned and points traced using a computer program. The other dimensions were taken to be the same as those of Specimen F, which failed in the weld metal area during the test. A second model with a profile and size more similar to that of Specimen A, which failed in the attachment plate in the experiment, was then generated to study the effect of geometry variation on the failure behaviour of the joints. The dimensions of these two T-joint specimens can be found in Appendix H, Table H-1, with the symbols as shown in Fig. 5-25 in Chapter 5.

Geometry of the supporting system and loading point

As shown in Fig. 7-1, the T-joint was supported by a plate with cross-sectional dimensions 120 × 38 mm, simulating the vertical part of the L-shaped plate used in the test. The dimensions of the clamp plate is 23.5 × 13 mm, also identical to the

plate used in the test. The loading beam was simulated by a steel block with a round tip as shown in Fig. 7-1. A rigorous modeling of the support system was adopted in order to account for any additional deflections due to its compliance. The overall model can be easily simplified if such deflections are found negligible.

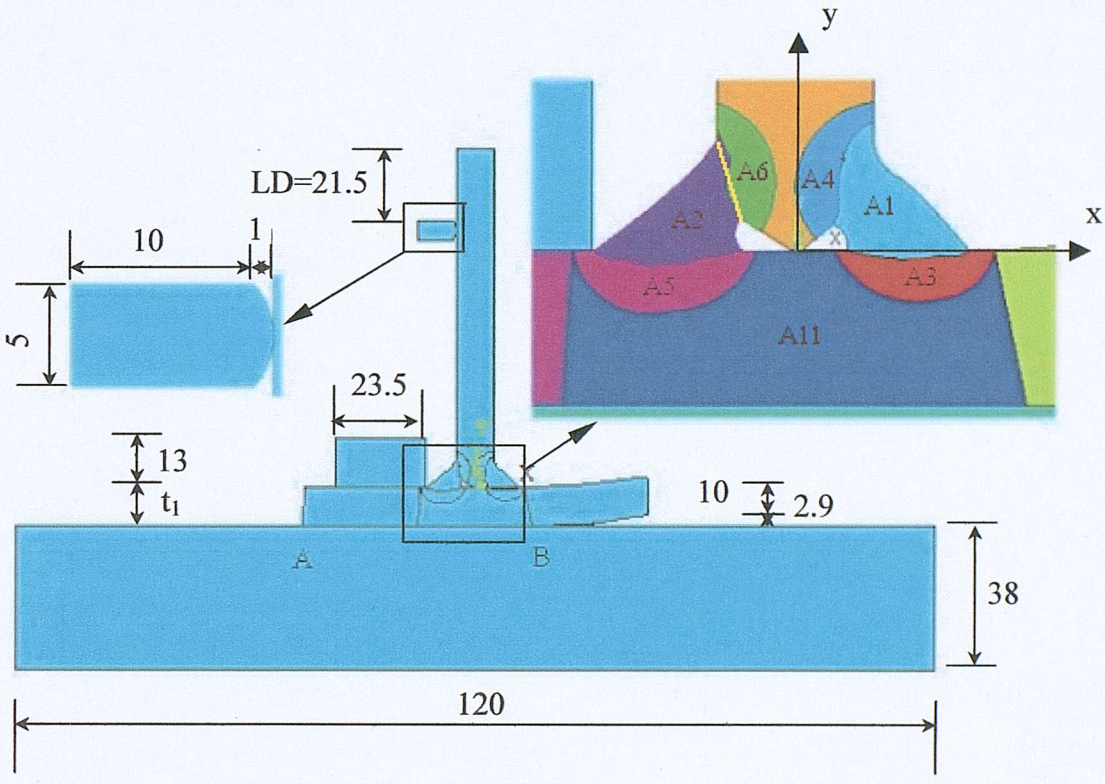

Fig. 7-1 Geometry of the FE model, dimensions in mm

Material model

The average values of the mechanical properties obtained from the tensile tests described in Chapter 5, Section 5.3 were assigned to the base metal and weld metal areas. The stress-strain curve for the HAZ was based on that determined for the base metal and weld metal but scaled according to the relative hardness values (see Table 5-10) of the HAZ and base/weld metal. The multi-linear kinematic strain hardening model was adopted. The true stress-logarithmic strain curves for the three materials are shown in Fig. 7-2.

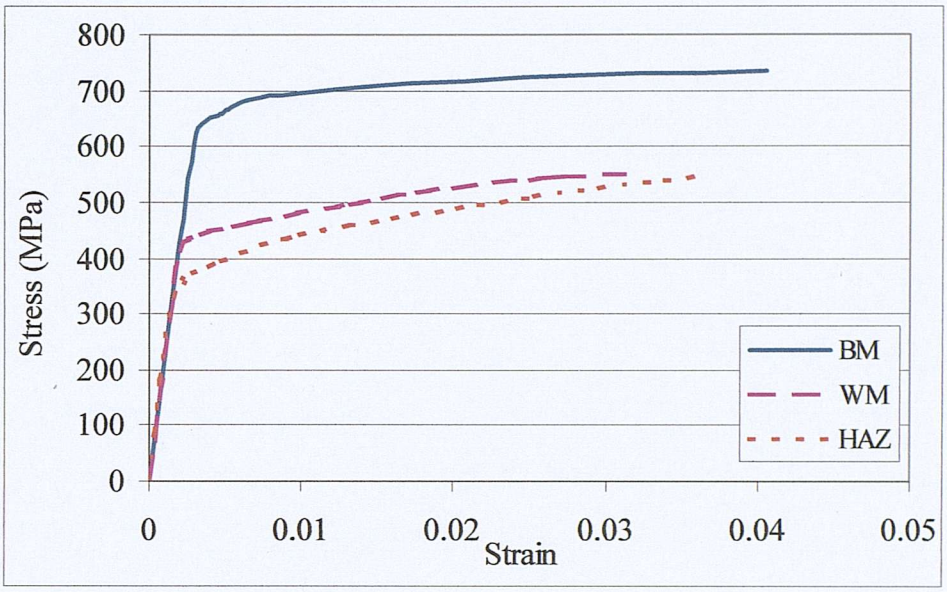

Fig. 7-2 Stress-strain curves for the three areas of the FE model

Element types and meshing

Four different types of elements were used in this model. The 4-node, 2-D structural solid element Plane42 was used for the joint as well as for the supporting and loading plates. Plane stress with thickness was applied as the joint was cut in 12 mm thick slices. However, different thickness, i.e. 120, 100 and 12 mm, were entered for the support, clamp plate and the loading beam, respectively, to simulate the test geometry. Point-to-point contact element Contac12 was generated across the contact surfaces between the clamp plate and the joint, the joint and the support plate (from point A to point B as shown in Fig. 7-1), as well as the attachment plate and the base plate of the joint, where there is reasonable certainty that no sliding between contact surfaces would occur during the application of the load. The surface to surface contact element combination, Conta171 and Targe169, was used to simulate the contact behaviour between the joint and the support plate from point B to the right end of the joint base plate, and between the loading beam and the attachment plate of the joint where the location and distribution of contact nodes change with the load applied. These surface-to-surface contact elements are also advantageous to this study in supporting large deformation efficiently, having no restrictions on the shape

of the target contact surfaces, and allowing different numbers of elements for potential contact surfaces. The contact problem is labelled flexible to flexible as both contact surfaces are deformable. Friction is allowed between the surfaces with the coefficient of friction set to be 0.3, a typical value for steel. As explained below, a minimum amount of friction is required for the stability of the support.

A uniaxial tension-compression element LINK1 was also used to simulate the bolts used to connect the clamp, support plate and the joint. The link element simulating the bolt was given an initial strain of 0.0006 working together with the friction between the two surfaces of the support and clamp plate and the joint to prevent sliding. If a smaller coefficient of friction is assumed, the initial strain of the bolt may have to be increased to ensure fixity of the joint.

As demonstrated in Chapter 4, Section 4.2.5, element sizes of 0.5 mm in the weld and HAZ area was satisfactory for the cruciform joint under bending. In this model the weld and the HAZ areas are the most interesting locations. In addition, in the area corresponding to where the strain gauges were attached in the experimental specimens, a finer mesh is preferable in order to find a better correlation in strain measurement locations between FE and experiment. An element size of 0.35 mm was thus used for the weld and HAZ areas. The areas adjacent to the contact surface between the loading beam and the attachment plate were also finely meshed in order to obtain a satisfactory contact result. As for the cruciform joint presented in Chapter 4, another model with element sizes of 30% finer was also analysed and the resulting von Mises stress compared. Very similar results was found for the two models with a 0.1% difference in the maximum stress. The final mesh map is shown in Fig. 7-3. The pink line shows where the link element is applied.

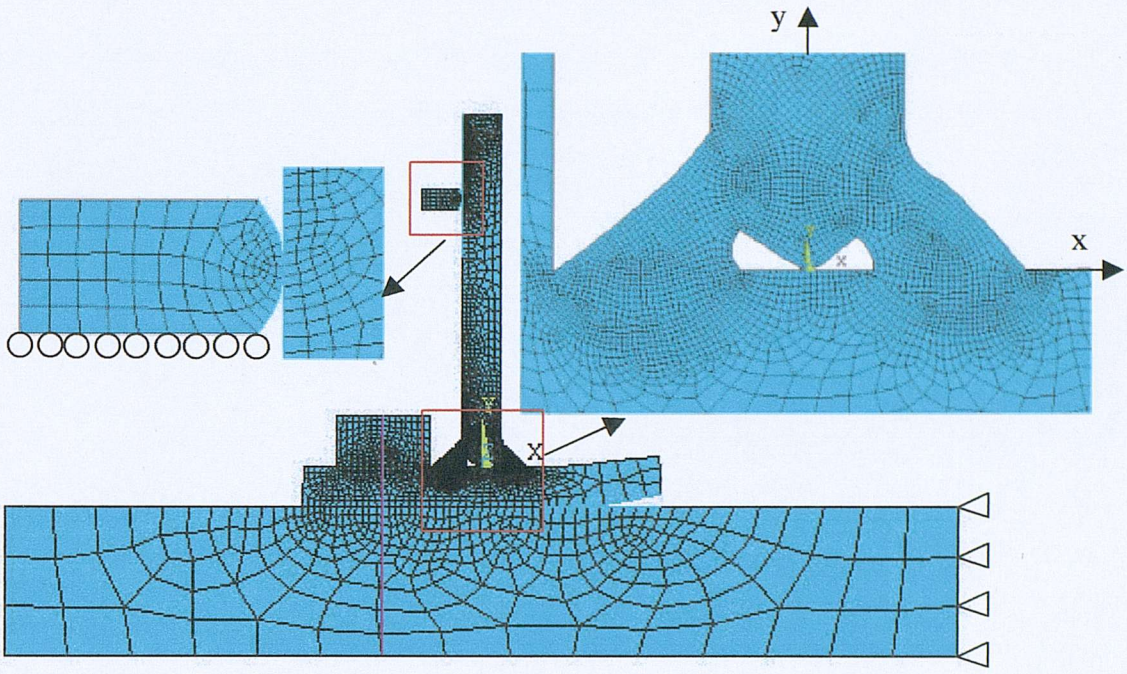

Fig. 7-3 Mesh map of the FE model for WT2 weldment

Boundary and loading conditions

The right side of the support plate was fully fixed to prevent rigid body movement, as shown in Fig. 7-3. In the FE model, the load cannot be accurately simulated simply by a force applied continuously to the same point, while in the experiment, the load was applied through the movement of the INSTRON loading beam which moves only in the vertical direction. Since the attachment plate of the joint was subjected to a large deformation, the loading point moved along the left edge of the attachment plate with the loading direction remaining constant throughout the test. The tip of the loading beam was modelled as deformable solid, constrained in the horizontal direction, the *y*-axis in the FE model, and assigned a displacement in the vertical direction, that is, along the *x*-axis in the FE model, to simulate this loading process in the test.

7.2.2 Models of WT1 specimen

Despite the poor quality of this weldment, the WT1 joint exhibited considerable resistance when tested under bending as described in Section 5.4.5. The purpose of this analysis is to simulate this behaviour and highlight the influence of the defective

features of this joint. Apart from the dimensions of the joint (see Appendix H, Table H-2) and the values of material strength (see Chapter 5 Section 5.3, Tables 5-4 and 5-7), the modelling process for the WT1 specimen is the same as that for the WT2 specimen. The dimensions of the supporting system are the same as those for the WT2 model. As described in Chapter 5, Section 5.2.3, the profile of the welds (as shown in Table 5-2) and the types of defects vary along the length of the WT1 weldment. The geometrical details around the weld areas were taken from an etched specimen and modelled, as shown in Fig. 7-4 (b). Other dimensions were similar to those of the tested specimen B, as listed in Appendix H, Table H-2 and shown in Fig. 7-4 (a). The mesh map for the WT1 specimen is shown in Fig. 7-4. This model is slightly more complex than that developed in Chapter 6 for the determination of residual stresses because it includes defects, which dominate the failure behaviour of the WT1 joints.

Node - node and surface - surface contact elements were applied to all possible contact surfaces in the gaps between the attachment plate and welds and are highlighted through blue lines and red lines, respectively, in Fig. 7-4.

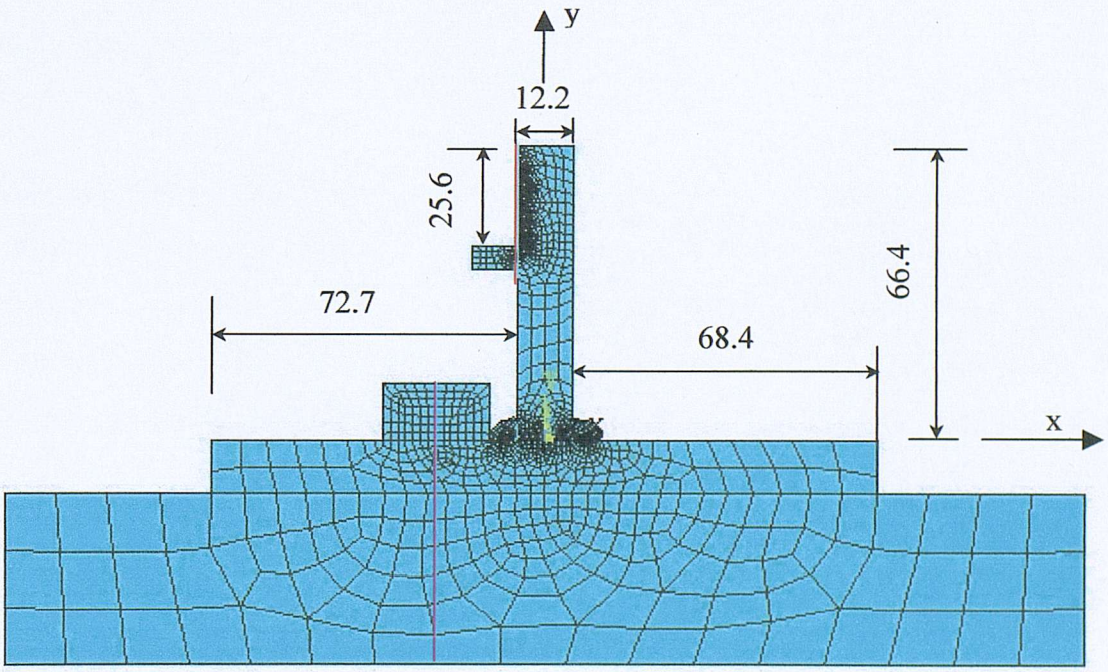

(a) Mesh map of the whole model, dimensions in mm

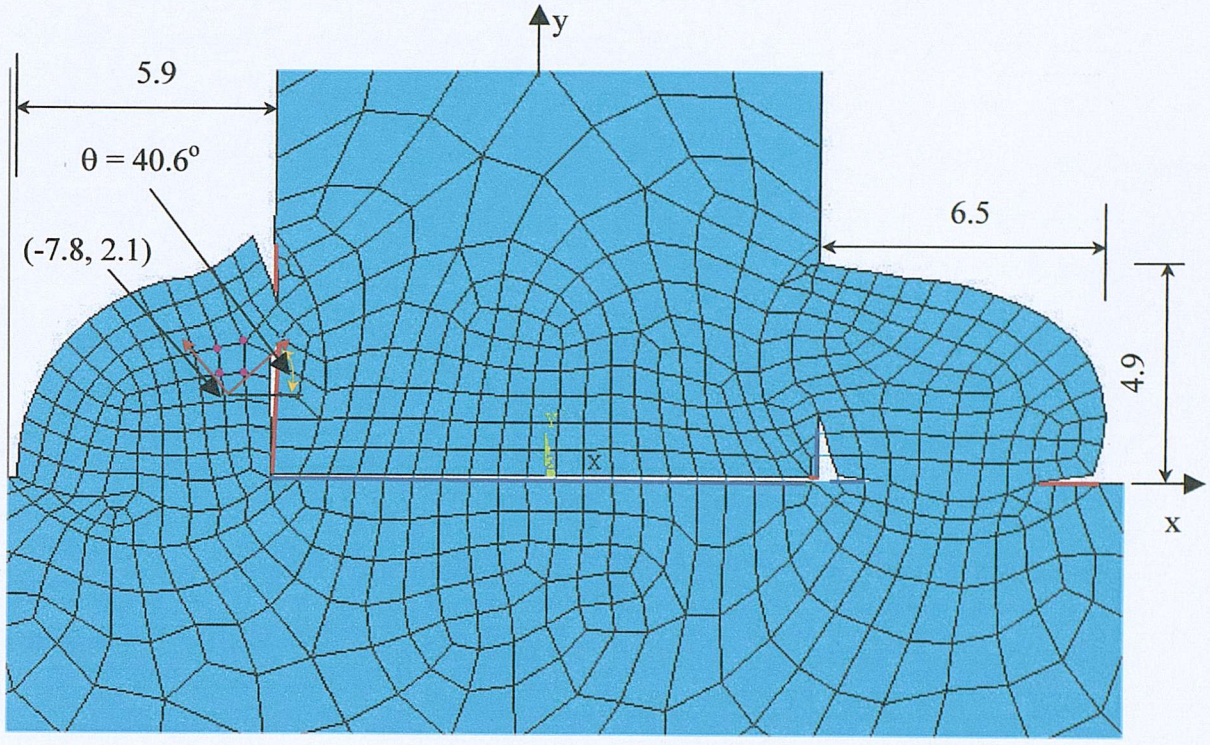

(b) Mesh detail around the weld areas, dimensions in mm

Fig. 7-4 Mesh map of WT1 model where the left weld was in tension

7.2.3 Strain results

WT2 weldment

Experimental load-strain relations were obtained for the positions where the strain gauges were attached and have been shown in Fig. 5-29 in Chapter 5. These results were first re-produced by the FE model and compared with the experimental results. The positions of the left bottom corner as well as the rotation angle of the strain gauges were measured from experiment. In the FE model, a local co-ordinate (as shown by the pink lines in Fig. 7-5) was defined with an origin corresponding to the bottom-left point of the strain gauges and nodes within the gauge grid and length (1.0 × 1.1 mm for the rosette strain gauge on the left weld area and 1.2 × 2 mm for the single strain gauge on the attachment plate) were selected, as shown in Fig. 7-5, by the pink colour dots. As the strain gauge covers a small area rather than a single point, strain results were obtained as averages of those corresponding to nodes selected.

The load from the FE model was calculated as the sum of the reaction forces of all the contact elements between the loading beam and the attachment plate of the joint. Due to the incremental nature of the solution, the results file produced by ANSYS could be very big, it is however necessary to store results from a sufficient number of intermediate steps in order to obtain the development of the load and strain results during the loading process for generating the numerical load-strain curves. For the location of the rosette strain gauge used in the experiment, principal strains were calculated from the strain data obtained from the three gauges and compared with the corresponding FE results. However, for the locations of the other single strain gauges used, it is not possible to obtain the principal strains so that results from the FE model were calculated from the x-y co-ordinate strains for the position and direction of the strain gauges, which are sensitive to the accurate measurement of the respective strain gauge directions.

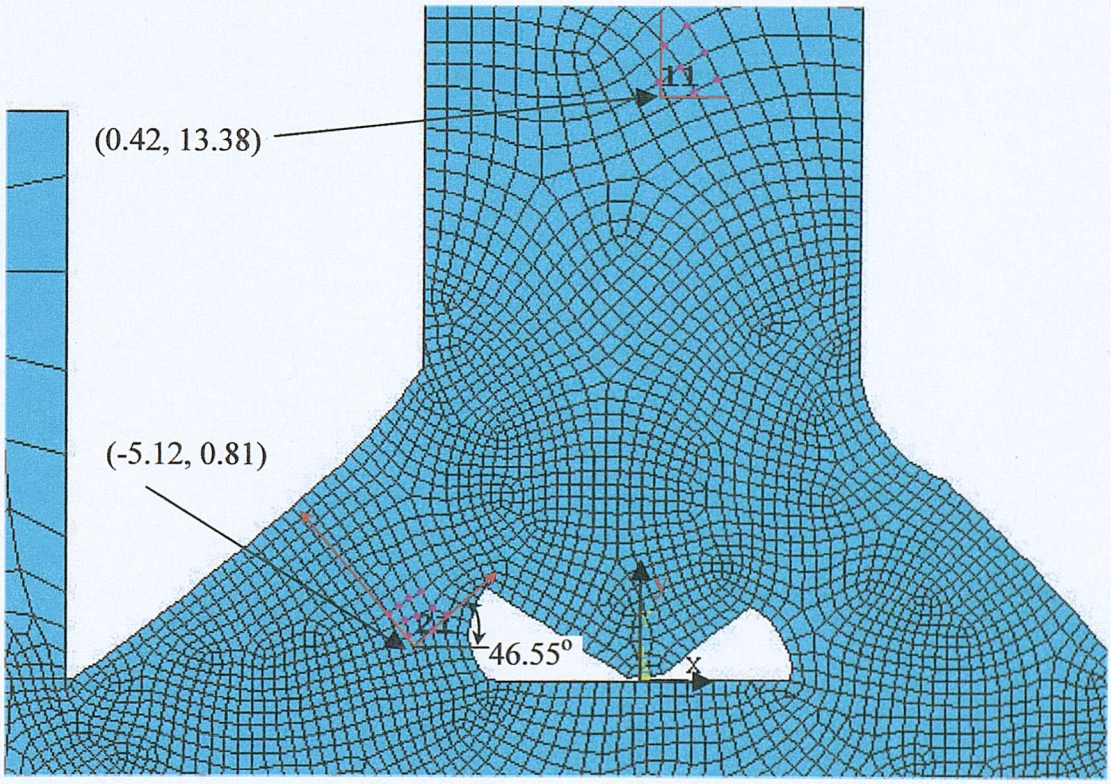

Fig. 7-5 Strain gauge positions for WT2 specimen B

A comparison between the load-principal strain (ε_1 and ε_3) results from the FE model and those of the experiment can be made by reference to Fig. 7-6 for the rosette strain gauge in the left weld area, and Fig. 7-7 for the single strain gauge on the attachment plate surface (see Fig. 7-5 for the strain gauge positions). In the elastic range, the weld area strains measured through the rosette gauge are considerably smaller than the predicted ones. This illustrates the difficulty of capturing accurately the strain over a small area due to the highly non-uniform strain distribution in the weld. With the onset of plasticity, stresses and strains become more uniform so that the experimental and analytical results seem to merge. The strain in the attachment plate has a smoother variation; hence the results shown in Fig. 7-6 are in better agreement in both elastic and plastic ranges.

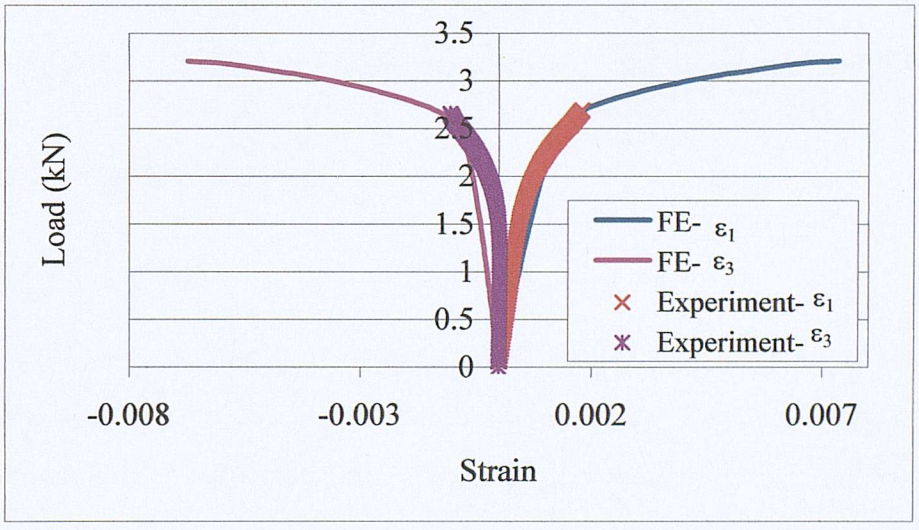

Fig. 7-6 Comparison of experimental and FEA load-strain curves at left weld (Specimen F, see Fig. 7-5)

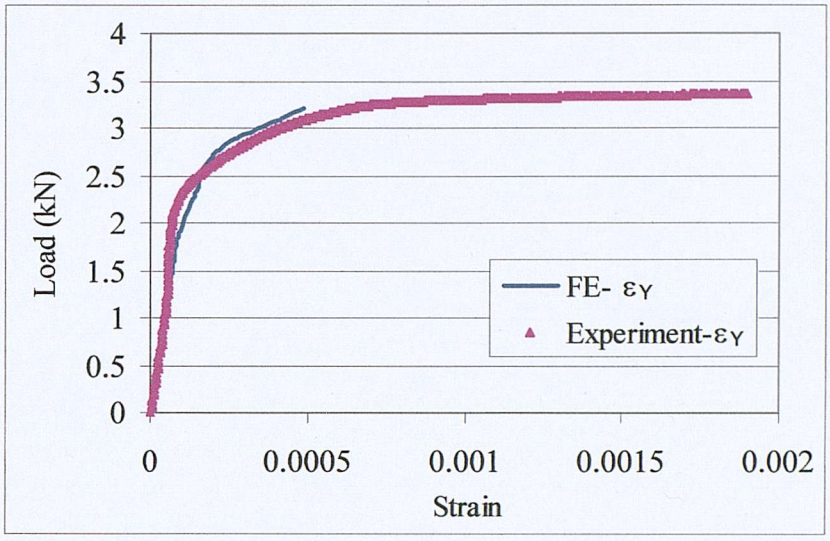

Fig. 7-7 Comparison of load-strain curves at the attachment position (Specimen F, see Fig. 7-5)

Based on this partially assessed FE model, the geometry has been changed as detailed in Section 7.3 to study the effect of weld dimensions on the behaviour of the joint under various loads.

WT1 weldment

The same procedure as that described in the previous section for the WT2 specimen was applied to the WT1 specimen to obtain, from the respective FE model, the load-strain relation at the various strain gauge positions (see Fig. 7-4). Fig. 7-8 shows the load-principal strain relations obtained from the FE model at the rosette strain gauge position in the left weld of Specimen B together with the respective experimental results for comparison. The discrepancies between the FE and experiment results may due to the nodes selected in the FE model not being exactly in the strain gauge area in the test specimen and experimental errors.

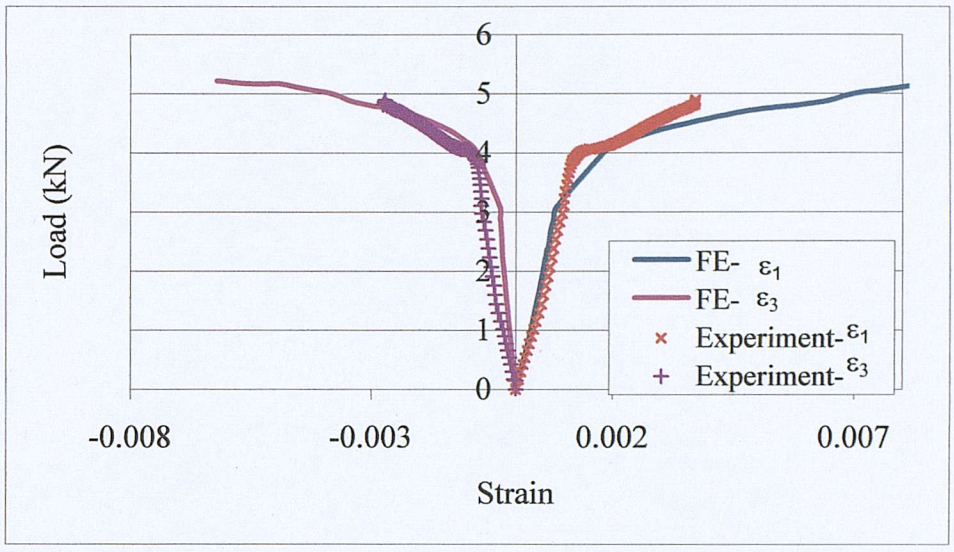

Fig. 7-8 Comparison of experimental and FEA load-strain curves at left weld for WT1 specimen B (Fig. 7-4)

7.3 Effect of geometry on the behaviour of the T-joint under bending

As mentioned in Chapter 5, it has been observed in the experiment that there are two types of failure path in the WT2 specimens tested although they were cut from the same weldment. Stress and strain development was carefully examined through the FE model in an attempt to explain this difference. One reason for this may be the shape and size of the weld. In this study, the effect of the distance from the weld toe to the top left corner of the weld root for the weld in tension, as indicated by the yellow line in Fig. 7-1, was considered. This dimension in specimen A was greater by 0.97 mm than that in Specimen F. Fig. 7-9 and Fig. 7-10 show the total von Mises equivalent strain distribution in joint Specimen F when the applied displacement of the loading beam was 3 and 5 mm respectively. High strain has developed at the weld toe and root. A comparison of Fig. 7-9 and Fig. 7-10 shows that, as the displacement of the loading beam increases, a clear path with high strain values appears in the weld (Fig. 7-10). It can thus be anticipated that a crack will first start near the weld toe or root and propagate along the indicated path so that failure occurs through the weld.

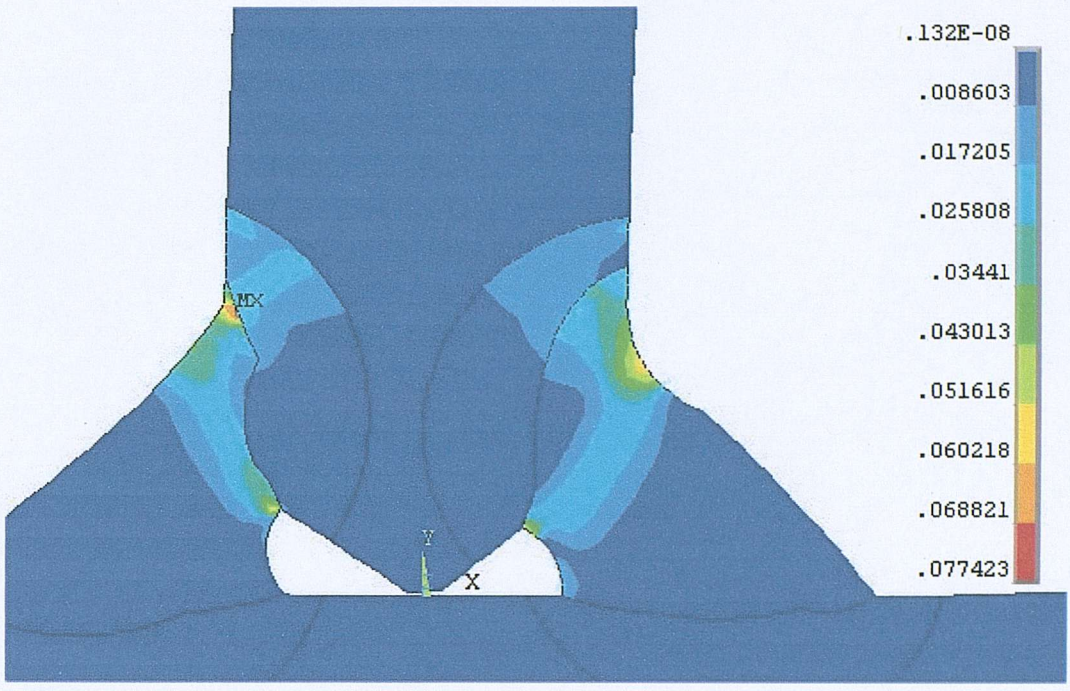

Fig. 7-9 Total von Mises strain distribution in WT2-F specimen under bending for a displacement of 3 mm

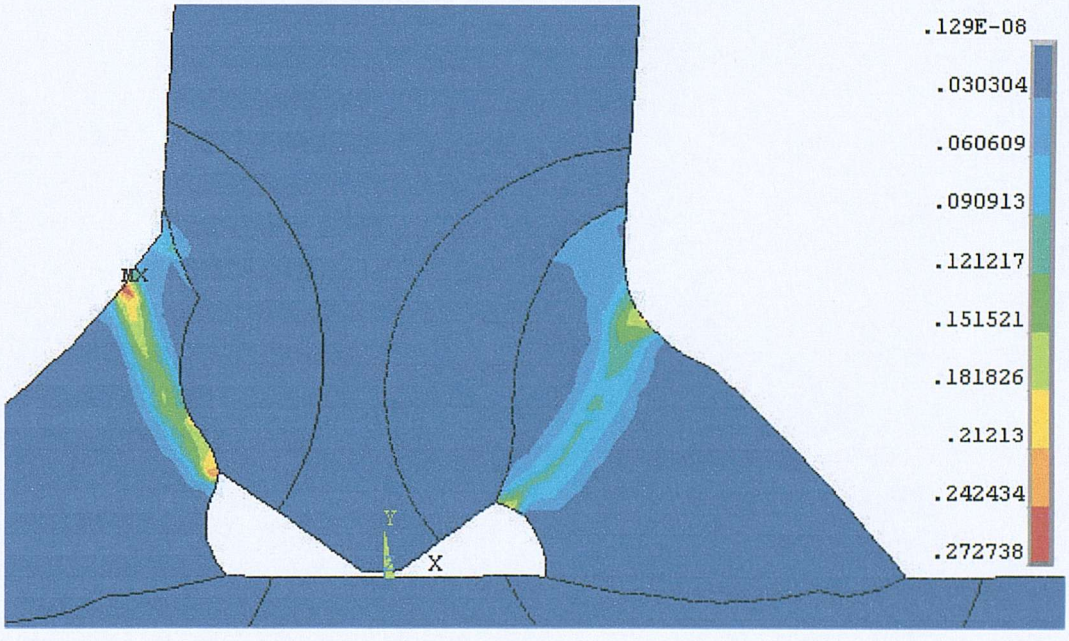

Fig. 7-10 Total von Mises strain distribution of WT2-F specimen under bending for a displacement of 5 mm

The FEM analysis was then applied to Specimen A and the respective von Mises equivalent strain distribution is shown in Fig. 7-11 when the loading beam displacement was 3.7 mm and in Fig. 7-12 when the loading beam displacement was 5 mm. It can be seen that high strain, of values up to the base metal elongation at failure, was developed at the weld toe and extended within the attachment plate, in its thickness direction, while the strain was still under three percent in the weld area away from the weld toe. High strain continued to develop across the thickness of the attachment plate as the displacement of the loading beam increased, as shown in Fig. 7-12. It is thus predicted that failure would happen in the attachment plate starting from the weld toe. The FE results thus clearly indicate that a larger size of weld area, especially the distance between the weld toe and root, could be the reason why failure of Specimens A and E occurred in the attachment plate rather than in the weld itself as happened in Specimen F [see Fig 5-31 (a) and (b)].

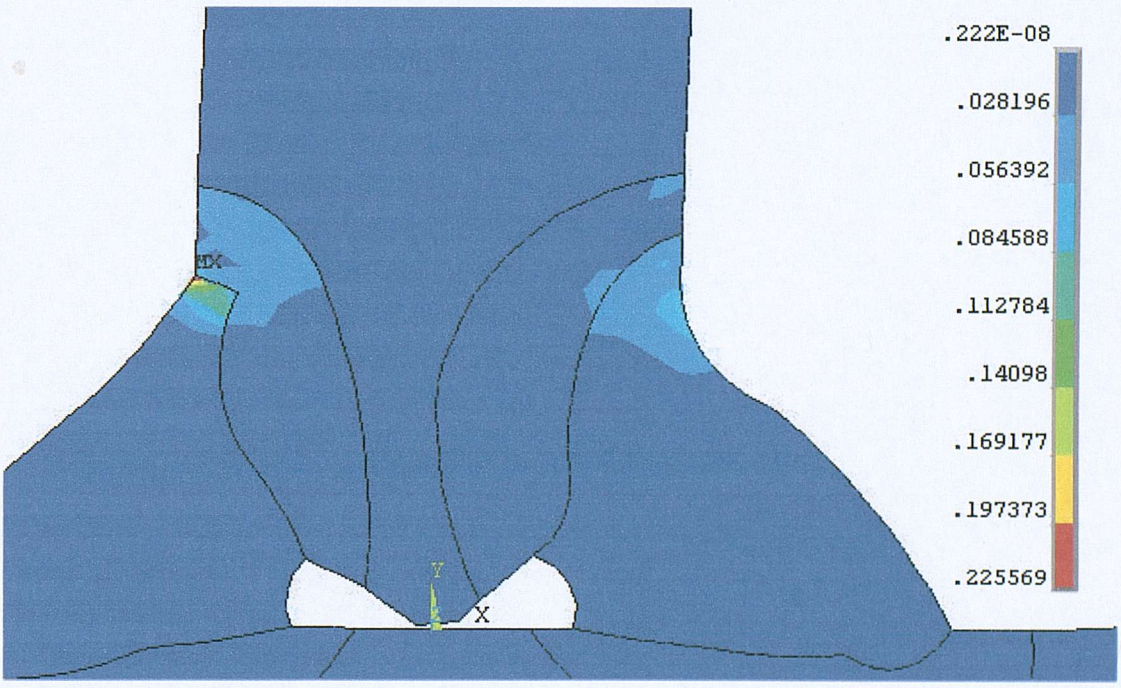

Fig. 7-11 Model WT2-A von Mises equivalent strain distribution for a loading displacement of 3.7 mm

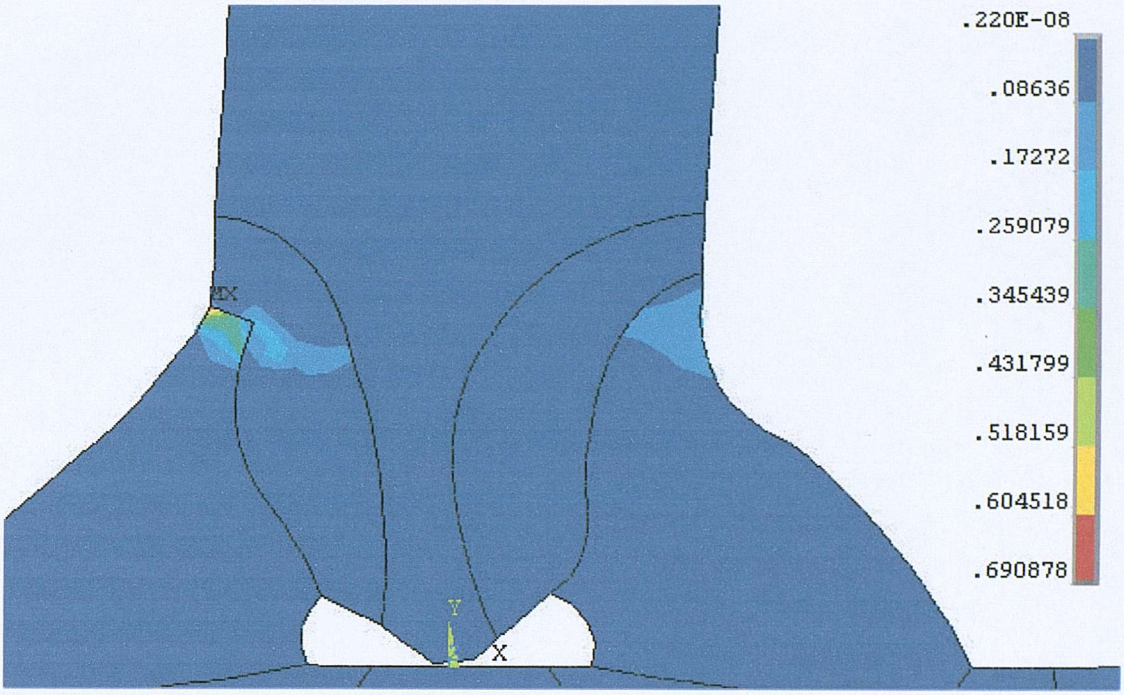

Fig. 7-12 Model WT2-A von Mises equivalent strain distribution for a loading displacement of 5 mm

7.4 Effect of defects

Fig. 7-13 shows the von Mises equivalent strain distribution in the model, named WT1-B, when the displacement of the loading beam is 3 mm. The load was applied in the same direction as on Specimen B in the experiment, but there may be a slight difference between the geometrical details of specimen and model around the weld areas. High strain concentration has been predicted in the left weld where defects are causing sharp changes in geometry. The maximum strain went up to 60% compared to less than 10% predicted for the WT2 specimen for the same 3 mm displacement of the loading beam. It is expected that the weld would have failed along the path shown by the red line in Fig. 7-13, as actually happened in the experiment with Specimen B (see Chapter 5, Section 5.4.5, Fig. 5-39).

Fig. 7-13 Total von Mises strain distribution of model WT1-B for an applied displacement of 3 mm

Bending was also applied to the same joint geometry, in the opposite direction generating tension to the right weld, as shown in Fig. 7-14. This loading condition is similar to that of Specimen A in the experiment, thus the FE model was named WT1-A.

The total von Mises equivalent strain distribution of model WT1-A when the applied displacement was 3 mm is shown in Fig. 7-15. Strain concentration was predicted to develop at the weld toe of the right weld. However, since crack-like defects exist in the weld root, failure was more likely dominated by crack propagation. Fig. 7-16 shows the x-direction normal stress distribution and Fig. 7-17 the y-direction normal stress. For the vertical crack, crack V shown in Fig. 7-16, the horizontal stress was compressive at the crack tip. However, for the horizontal crack, crack H shown in Fig. 7-17, a high tensile stress is present at the crack tip providing high crack driving force. It can thus be predicted that the horizontal crack would propagate prior to the

vertical crack. Photographs (Fig. 5-38) taken during the loading process of WT1 Specimen A show a similar failure process.

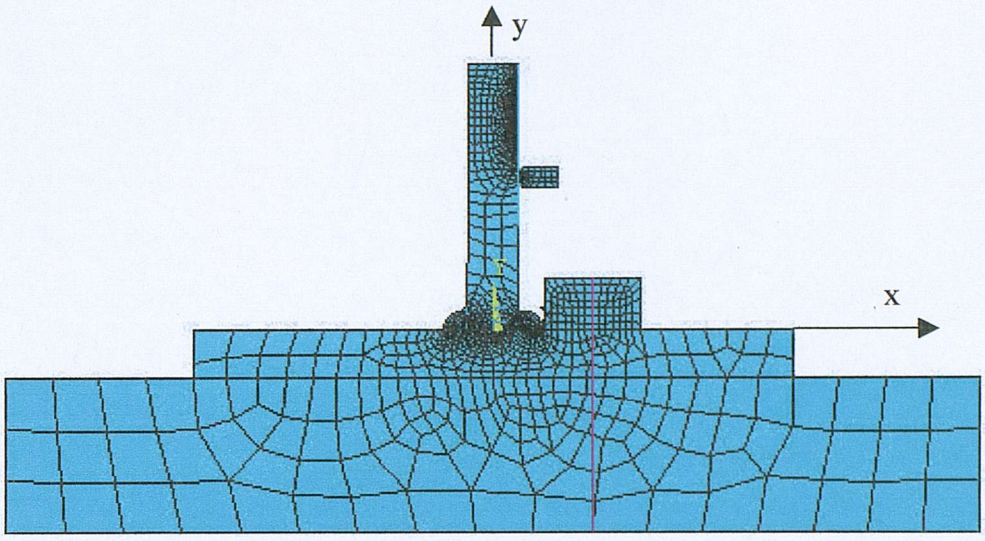

Fig. 7-14 Mesh map of FE model WT1-A

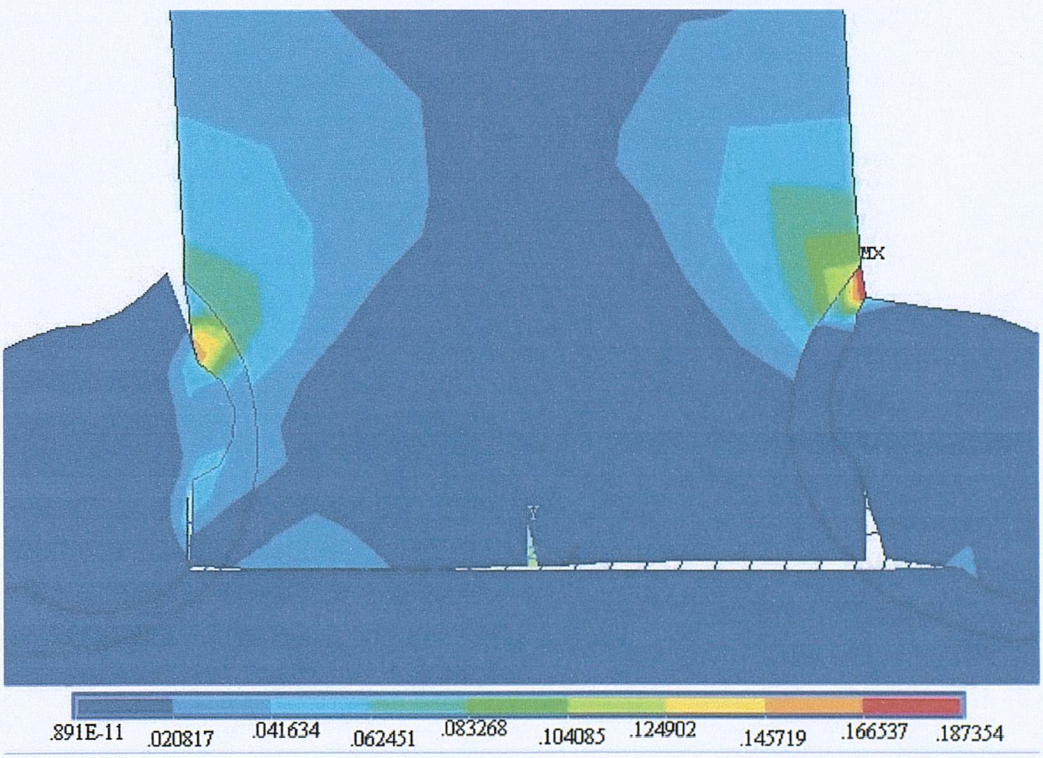

Fig. 7-15 Total von Mises equivalent strain distribution of model WT1- A for an applied displacement of 3 mm

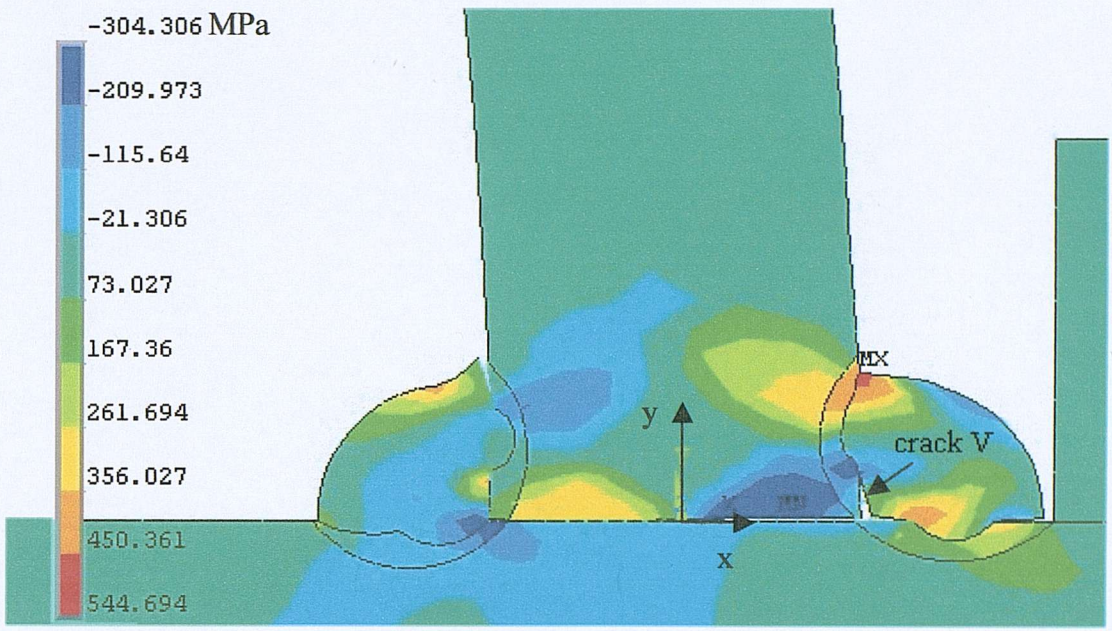

Fig. 7-16 Distribution of σ_x in model WT1-A

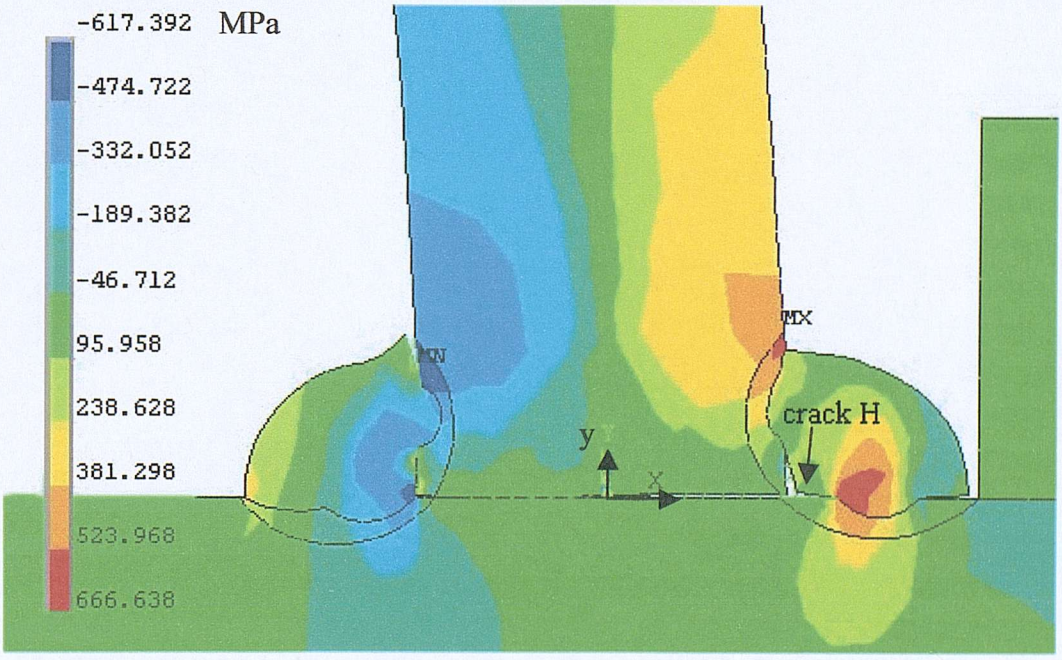

Fig. 7-17 Distribution of σ_y in model WT1-A

The existence of a defect and the type of the defect can thus play an important role in the failure of welded joints. The effect of a defect depends also on the particular loading on the joint itself.

7.5 Combined FEA for residual and static load stresses

It is recognised that the effect of residual stress decreases as the level of load applied increases in a butt weld subjected to uniform tension and this effect becomes negligible when the applied stress has been increased beyond the yielding point due to stress re-distribution. However, as discussed in Chapter 4, Section 4.4, in the experimental study carried out by Fessler and Pappalettere[1] on the main plate of a cruciform joint loaded under tension after the side plates and the welds had been removed, yielding was found to have occurred in the HAZ area with the yield stress of the plate only 78% of the nominal yield stress of the material due to the presence of tensile residual stresses in the HAZ area. However, the stress re-distribution under bending is more complicated than under uniform tension. Moreover, residual stress and strain affect significantly those phenomena that occur under a low applied stress, such as brittle fracture, as pointed out by Masubuchi[6]. It is thus important to be able to include detailed welding induced residual stresses in a load-carrying analysis of a welded joint. A large number of FE analyses have been carried out to simulate the welding process[2,3,4]. However, few studies[5] were found in the literature to have utilised these detailed residual stresses results obtained from a welding process simulation as input in load-carrying analysis. The complexity of the analysis itself may contribute to this paucity. Attempts were made in this study to combine the FE analysis of the welding process simulation with a load-carrying analysis on a welded T-joint in order to demonstrate the feasibility of including quantitatively residual stresses results obtained directly from a welding simulation.

One straightforward way to study the effect of residual stresses on a T-joint under external load is to perform the welding simulation first in order to obtain the distributions of residual stresses and, subsequently, apply additional external loads to the same model as new load steps. However, as ANSYS does not allow new

elements to be generated between load steps, the elements needed for simulating all the load steps must be generated at the residual stress analysis stage. The boundary conditions for the welding process simulation and those for the load-carrying model may not be the same and often, those for the load-carrying models are more complicated. Although elements can be "killed" and re-activated when necessary, this inevitably complicates the simulation and may cause convergence problems in addition to increasing the computation time. Moreover, not all element types support the "dead and rebirth" feature. Another drawback of this method is that the database and result files from the residual stress analysis, which are required to perform the additional load-carrying analysis, are significantly large and awkward to transfer around.

An alternative way of dealing with this problem is to utilise the initial stress feature supported by ANSYS. Subsequent to the welding process simulation, a different model can be generated for the static analysis with the residual stresses entered as initial stresses. ANSYS allows initial stresses to be read from an external file and applied to all or a subset of elements. The welding process simulation can be first carried out and the residual stresses obtained and then written into a file in the required format, which is the initial stress input file. The only requirement is that the mesh for the joint itself in the load-carrying model must be identical to that in the residual stress model. This can be easily achieved by getting the node coordinate and element node numbering from the residual stress model for the joint and applying to the load-carrying model. In this study, the initial stress rather than the integrated multi-step analysis method was used in order to save time and avoid convergence problems. This method has however a major disadvantage related to the omission of the plastic strains developed during the welding process. On application of initial stresses, the corresponding elastic strains are immediately obtained but these results are associated with the initial, unloaded state of the joint, that is, any previous strain history is ignored. This means that changes in the yield stress, i.e. strain hardening or strain softening, are not detected. Therefore, the results subsequently obtained for the loaded joint should be interpreted taking this limitation into consideration. Appendix I, Section I-4 lists the main commands used for models presented in this chapter.

7.5.1 Residual stresses in WT2 weldment

The same modelling methodologies as those presented in Chapter 6 for simulating the welding process of the WT1 weldment were applied to the WT2 specimen. The thermal material properties were taken to be the same as those of the WT1 specimen as no particular information on the WT2 weldment was available. Previous investigations have however indicated that these properties do not vary considerably between the various grades of steel and values within the range given in the literature have no significant effect on the final residual stress results. The amount of heat input was adjusted to give a fusion zone of reasonable similarity to the actual one whose size and shape could be assessed visually (see Fig. 5-20). Temperature-dependent yield and ultimate strength were scaled from those of the WT1 specimen based on the properties at room temperature for WT1 and WT2 specimens obtained from experiments. Fig. 7-18 shows the contour plot of the transverse residual stress (σ_x) distribution obtained.

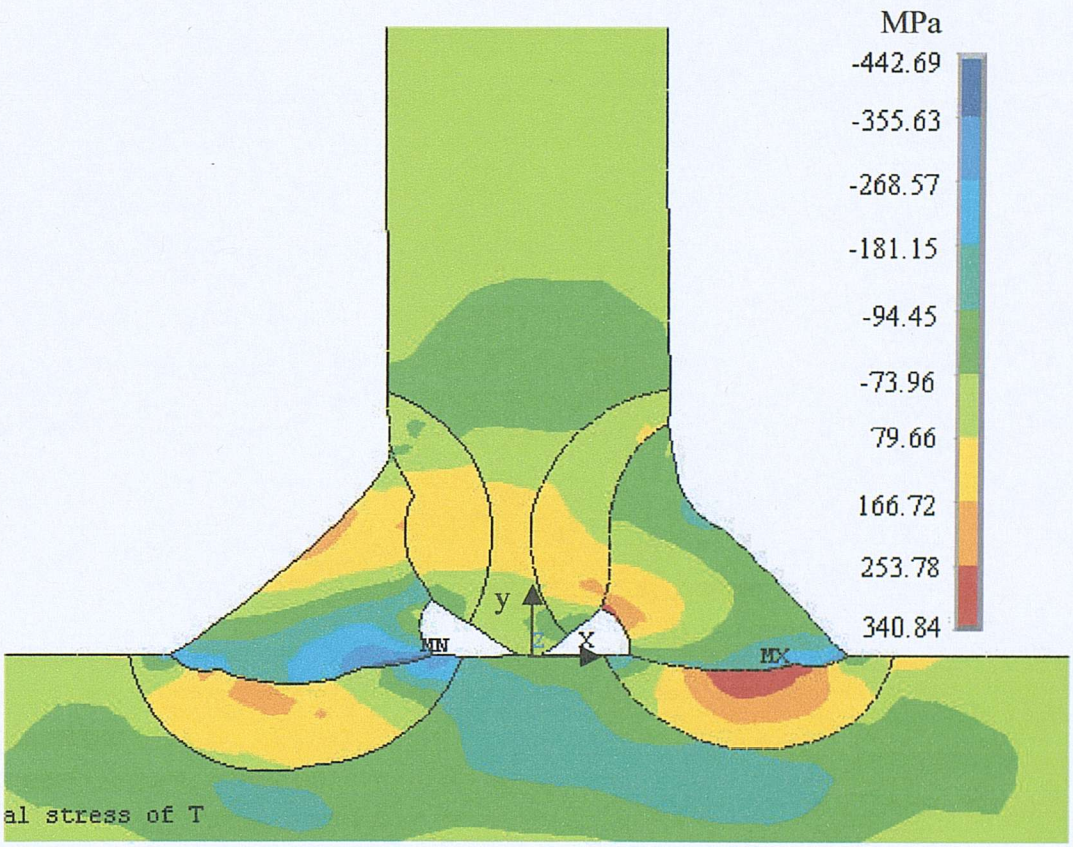

Fig. 7-18 Transverse residual stress (σ_x) distribution for the WT2 weldment

7.5.2 WT2 specimen with residual stresses under bending

The same FE model as that presented in Section 7.2 of this chapter was generated. The complete solution for the residual stresses was obtained from the welding process simulation presented in Section 7.5.1 and was read into the structural T-joint model prior to applying the bending load. It should be noted that the residual stress model was plain strain while the bending model was plain stress. Thus the predicted longitudinal residual stress (z direction in the FE models) must be removed to simulate the stress relief that occurred when the weldment was cut into 12 mm thick bending specimens. However, no rigorous such analysis was performed since the x and y direction residual stresses are not expected to be significantly affected by this operation. The remaining residual stresses were input into the bending specimen as initial stresses.

Results and discussion

Fig. 7-19 shows the load-strain curves obtained at the left weld strain gauge position where a comparison can be made between the results from the model with (lines labelled "resi") and that without (lines labelled "noresi") residual stresses. The first ($-\varepsilon_1$), and the third principal ($-\varepsilon_3$) strains predicted by the model with the residual stresses as initial stresses all show an around 10% lower yield load while there is little effect on the elastic behaviour and the ultimate failure load. This is in accordance with the expected behaviour as residual stresses are self-equilibrating and agrees well with comments made by Masubuchi[6] based on his review of relevant experimental and analytical studies. The initial residual plastic strains present along the same direction may lead to even lower yield loads if the material behaves according to the kinematic strain hardening model. The contour plots of the von Mises strain shown in Fig. 7-20 confirm that the specimen is expected to fail along the same failure path. These results were obtained for a load corresponding to a 3 mm displacement of the loading beam.

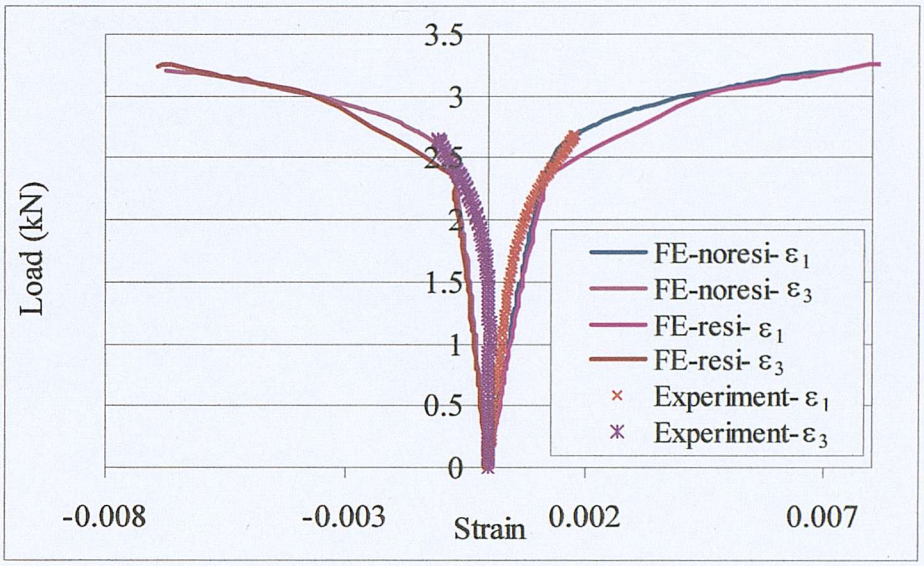

Fig. 7-19 Effect of residual stresses on load-strain behaviour at the WT2 specimen left weld strain gauge position

Fig. 7-21 shows the contour plots of von Mises stress distribution in both models, that is, with and without residual stresses as initial stresses, for the same applied 3 mm displacement of the loading beam. The maximum stress in the model without residual stresses is about 15% lower but the overall pattern is very similar for the two models. The difference of the local stress distribution at the weld toe and root is also evident. By comparing the results in Fig. 7-20 and Fig. 7-21 it becomes obvious that residual stresses are beneficial in certain regions while they are detrimental in others with regard to possible fatigue crack initiation. These effects would be more pronounced if the residual plastic strains are accounted for in a sequential residual stress/loading stress analysis. Stress-load curves at the toe of the left and right weld were checked and are shown in Fig. 7-22 and Fig. 7-23, respectively.

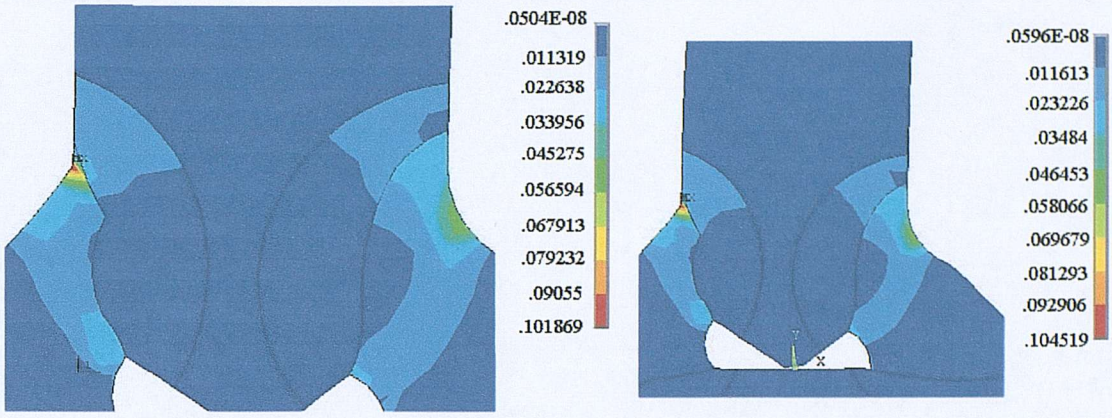

(a) Without residual stresses (b) With residual stresses

Fig. 7-20 Contour plot of the von Mises equivalent strain for a displacement of 3 mm

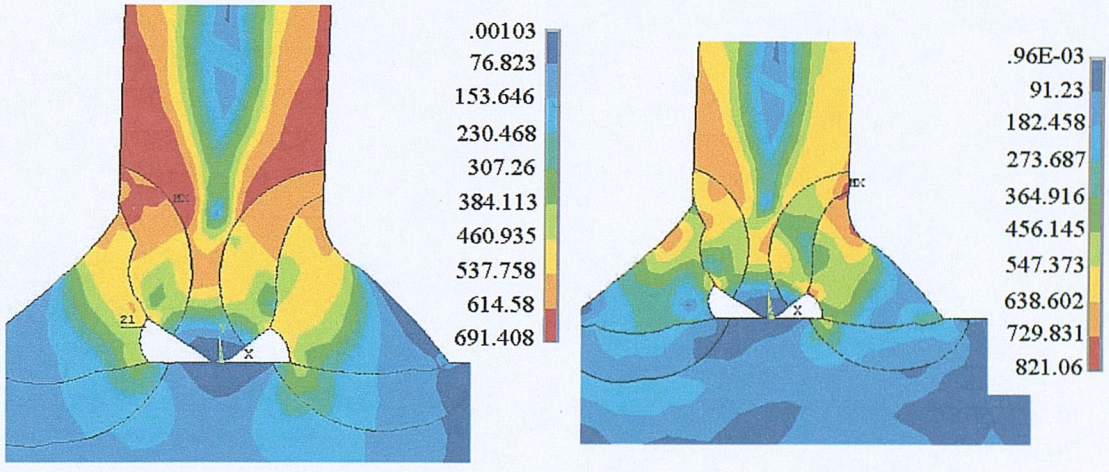

(a) Without residual stresses (b) With residual stresses

Fig. 7-21 Comparison of von Mises stress distribution (MPa)

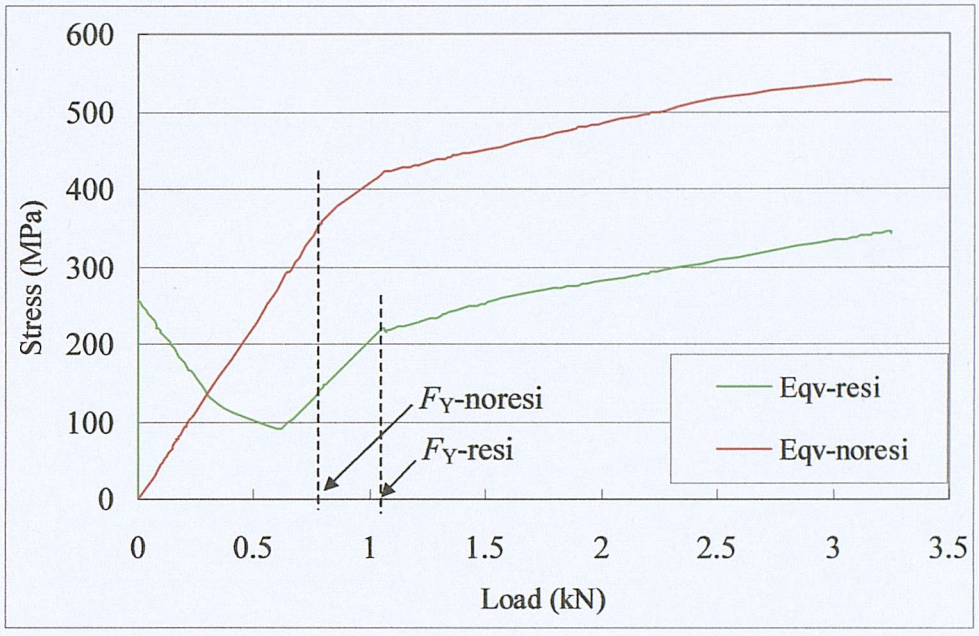

Fig. 7-22 Effect of residual stresses on predicted von Mises stress-load curves at the toe of the left weld

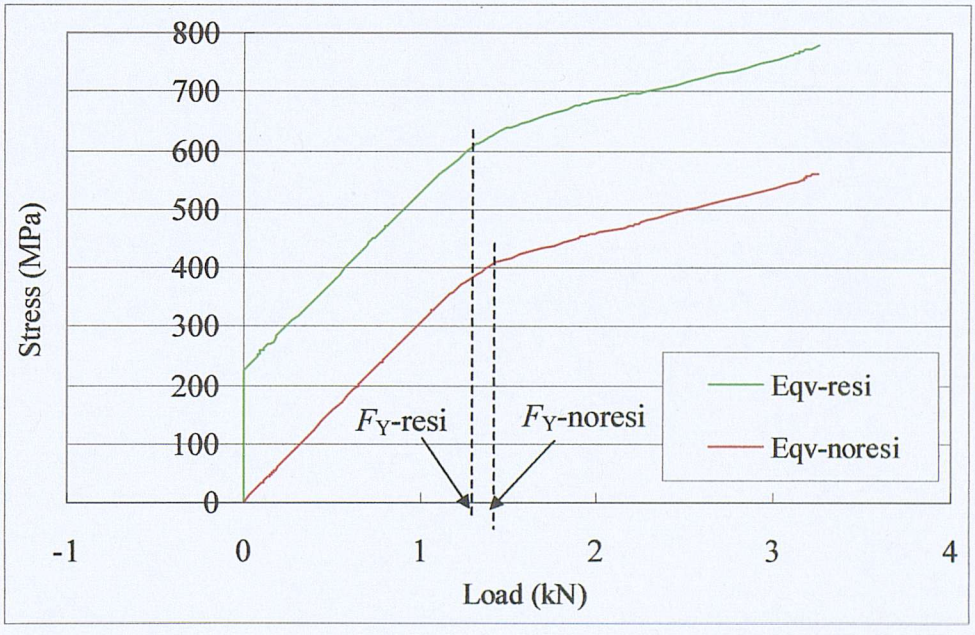

Fig. 7-23 Effect of residual stresses on predicted von Mises stress-load curves at the toe of the right weld

At the toe of the left weld, as shown in Fig. 7-22, the model with residual stresses (curve Eqv-resi) started with an initial stress but this stress decreases as the applied load increases until the load is up to around 0.6 kN. This means that the sign of the predominant stress locally is actually reversed, most likely from a residual compressive to tensile as the load increases. In such a case the yield load is expected to increase and this is confirmed by the results of Fig. 7-22 (F_Y-resi is the yield load for the model with residual stresses and F_Y-noresi the yield load for model without residual stresses).

At the toe of the right weld, as shown in Fig. 7-23, however, the von Mises stress resulting from the model with residual stresses (curve Eqv-resi) are much higher than those from the model without residual stresses (curve Eqv-noresi). In this case therefore a residual compressive stress seems to increase as the load applied, which causes compressive stress in this location, increases and a drop of yield load is expected. This is confirmed by the results of Fig. 7-23. Thus it is obvious that the effect of residual stresses on the final stress distribution depends on the residual stress distribution as well as the external load condition applied. This effect decreases with decreasing magnitude of residual stresses. The residual stresses have a significant effect on the stress distribution around the weld area, and this effect depends on the magnitude and sign of residual stresses as well as external load conditions applied. This effect is localised and appears to have little effect to the final failure load in terms of the integrity of the whole joint if plastic analysis is applied. This observation may have to be revised if residual plastic strains are accounted for and their effect quantified.

7.6 Summary

Finite element models of T-joints under bending have been generated in this chapter to study the behaviour of loaded welded T-joints. The performance of these models have been examined by comparison of predicted load-strain relations at certain positions with corresponding measured ones from experimental models presented in Chapter 5. This assessment is limited by the available results from experiment. In

addition, the meshing adopted in the areas where strain gauges were attached did not precisely map the strain gauge size and shape although a relatively fine mesh was generated. Due to the sharp gradient of strain in the weld area, the strain results obtained from the FE model show some discrepancies from the experimental results. A better correlation between the FEM results and the experimental measurements can be achieved if nodes and elements under the strain gauge area were generated based on the actual strain gauge size and profile, which, however, will inevitably complicate the modelling process and is not necessary if the failure behaviour of the joint is of main interest.

The effect of geometry variations of the weld area on the failure behaviour of the loaded T-joint was studied in Section 7.3. Based on the detailed stress and strain distributions obtained from these models, the presence of two different types of failure path observed in the experiments was explained. The effect of defects on the joint behaviour was studied and the results were found to be consistent with experimental observations. The effect of the welding-induced residual stresses has also been studied. However, The effect of welding-induced residual plastic strain was not included in the combined residual stress and load carrying model due to the limitation of the computing resources and time needed although the modelling method is rather straightforward.

The following observations can be made on the results obtained from these models:

1. Welded T-joints behave elastically under bending up to a load when a certain amount of yielding has occurred at the weld toe. The joint yield load lies between the loads corresponding to the start of yield at the weakest and strongest part of the base metal, weld metal and HAZ. After this local yielding, the joint can continue to carry load but with rapidly increasing deformation.

2. A crack is expected to start at the position of high stress concentration, that is, weld toe or root and the final failure occurs along the weakest path the location and orientation of which depends on the combination of weld size and material properties of the three weld areas. In the case studied here, an increase of about

18% of the distance from the weld toe to the weld root resulted in a different failure path. However, there is not much difference in the final failure load corresponding to these two failure modes. The size of a weld should be considered together with the strength of the materials to design a connection with a proper balance between the weld and base metals and thus economically utilise material.

3. Weld defects can significantly reduce the strength of welded joints. The effect of weld defects depends also on the defect profile and loading conditions of the joint with defects.

4. The effect of residual stresses on the load carrying behaviour of a welded joint can be studied quantitatively by inputting detailed residual stress results obtained from a welding process simulation to a structural joint analysis. This method could be particularly useful in FEM assessments of fracture and fatigue limits of welded connections.

5. Residual stresses can decrease the yield load of welded joints under bending but have no significant effect on the ultimate failure load if large plastic deformation is allowed. However, residual stresses affect significantly the stress distribution at certain key positions such as weld toe and root, and this effect increases with increasing residual stress magnitude. It is thus expected that residual stresses will have more significant effect on failures occurring at a relatively low stress level such as fatigue fracture. The combined residual stress and load carrying behaviour model is thus more meaningful in the analyses of welded joints under low-load failure behaviour such as fatigue and brittle fracture. Fatigue and other types of brittle fracture were not covered in this study. The methods presented here for modelling the welding process in order to obtain detailed residual stress and strain distribution and combining resulting residual stresses with load-carrying analysis models, however, is applicable.

References:

[1] Fessler H., Pappalettere G., Fillet welds under bending and shear, *5th International Conference on Pressure Vessel Technology*, pp47-61, Sept. 1984
[2] Sarkani S., Tritchkov V., Michaelov G., An efficient approach for computing residual stresses in welded joints, *Finite Elements in Analysis and Design*, vol. **35**, pp247-268, 2000
[3] Mackerle J., Finite element analysis and simulation of welds: a bibliography (1976-1996), *Modelling Simulation of Materials Science and Engineering*, **4**, pp501-533, 1996
[4] Mackerle J., FEM and BEM analysis and modelling of residual stresses: A bibliography (1998-1999), *Finite Elements in Analysis and Design*, **37**(2), pp253-262, 2001
[5] Mok D. H. B., Pick R. J., Finite element study of residual stresses in a plate T-joint fatigue specimen, *Journal of Mechanical Engineering Sciences*, Vol. **204**, pp127-134, 1990
[6] Masubuchi K., Analysis of Welded Structures, *Pergamon Press*, 1980

8. Conclusions and further work

8.1 Summary and conclusions

1. A literature review has been carried out on welding induced residual stresses, design methods for welds and the behaviour of welded joints with emphasis on finite element simulations. Although considerable research has been done on this subject, the behaviour of a welded joint is still not fully understood due to its complexity. The static strength of welds in welded structures is conventionally designed to be higher than that of other components of the structure, in the real world however a large percentage of fracture failures are found to be in the weld. Microstructure and material property variations in the weld, across the HAZ to the base metal, defects, and welding induced residual stresses and distortion are among the most important factors that may affect significantly the behaviour of welded joints.

   The final microstructures, hence the material properties in the weld and HAZ, are affected by many factors including the maximum temperature reached during the welding process, the cooling rate, and chemical composition of both the base plate material and the filler metal. More studies need to be performed to look at the effect of this non-uniformity of material property distribution by considering more realistic assessments of material properties.

   It is very difficult, if not impossible, to eliminate completely the presence of defects inherent in welds. The effect of defects is, however, not fully quantified and depends on the properties of the surrounding material, defect type, and loading conditions as well as residual stresses.

   It has also been established that welding residual stresses can play an important role in the fracture behaviour of welded structures. Residual stresses may cause initial distortion the presence of which can make it difficult to maintain

dimensional tolerances during weld fabrication and any misalignment in the welded joints may result in reaction stresses not considered at the design stage. Although it is well known that the effect of residual stresses decreases with increasing external loading due to stress re-distribution, this effect has not been quantified. In addition, the yield load of the welded joint may be affected. Residual stresses may affect significantly those failure mechanisms that occur at low loads such as fatigue fracture and buckling. There is no simple calculation method for the magnitude and distribution of residual stresses that is applicable to welded joints of any geometry and welding process. FEM simulation of welding process in order to obtain the residual stress and distortion results is thus still a very active research area. To study quantitatively the effect of residual stresses on the behaviour of welded joints and structures, detailed residual stress magnitude and distribution should be considered in a load-carrying analysis. However, very few analyses were found in the literature combining the simulation of the welding process with the assessment of the load-carrying behaviour of the joint although considerable work has been done on predicting residual stresses using FEM and simulating load-carrying behaviour of welded joints separately. The complexity of the simulation may have contributed to this.

Fillet welded T-joints have received relatively much less attention compared to simple butt welds or fillet welds in lap joints. Little has been done on the prediction of the static strength of welded T-joints using FEM. No consideration was given in such analyses to the possible variation of mechanical properties across the various material zones of the joint. No work has been found on simulating sequential welding of T-joints although this is what really happens in practice.

2. FEM models of a fillet welded cruciform joint have been generated and the reliability of the FEM models was examined by solving a benchmark problem, carrying out a mesh sensitivity study and comparing the strain-moment relation with experimental measurements.

The emphasis in this work was on the modelling of mechanical property variation in the base metal, weld metal and HAZ detected by hardness tests, which has not been addressed in the literature. It has been found from this modelling process that the strain distribution within and adjacent to the HAZ is very sensitive to the accurate representation of the gradual change of material properties in this area. Such variation should therefore be accounted for when detailed knowledge of strain distribution is vital to the assessment of joint failure mechanisms, for example, when assessing the possibility of crack initiation, which is normally expected to start at the weld toe, as well as crack propagation behaviour.

Subsequent parametric studies based on the same model have indicated that, as expected, the strength of the joint increases with increasing weld size and weld penetration. This finding is consistent with the prediction of design codes. The size of the HAZ has some effect on the local stress distribution within and around the weld and HAZ areas but not a significant one on the strength of the joint. It is thus recommended that in addition to the material property variation discussed above in this section, attention should be given to the size of the HAZ when assessing the joint failure behaviour at relatively low stress levels, in the case, for example, of fatigue fracture.

It must be pointed out that comparison with published experimental results was hampered by the limited information provided. Uncertainty on the accuracy of the experimental results is another problem which makes the comparison difficult. A 3.3% lower yield strength, a 1.6% smaller plate thickness, and applying a gradual change of material properties cross the HAZ to the base metal were found to produce a closer agreement with the experimental measurements. Welding induced residual stresses were not included in this model. Such stresses may have some effect on the yielding behaviour of the joint depending on the directions of residual stresses as well as loading.

3. A finite element simulation of the welding process has been carried out for a butt weld. The model has been assessed by comparison of its prediction with published experimental residual stress and empirical deformation results. This exercise demonstrated the capacity of the available software (ANSYS) to deal with the particular requirements of a rather complex thermo-mechanical problem, such as phase change and temperature-dependent material properties. It also provided the opportunity for a methodical investigation into the importance of the various input parameters. It is generally difficult to measure experimentally the thermal and mechanical material properties at high temperatures for every steel used in welding and the exact value of the arc efficiency which is needed to calculate the amount of heat input. Values of these input parameters used by other researchers in this area were collected and compared. Based on this comparison those appearing to be more reliable and more relevant to the simulated welding process were initially chosen for the current study. Sensitivity studies were carried out to investigate quantitatively the effect of these input parameters on both the temperature and residual stress results so that the dependence of the reliability of the simulation on these uncertainties can be obtained. The effect of boundary conditions on the final residual stress results was also studied. Various conclusions can be drawn from this simulation:

   (a) Residual stress results are not sensitive to a reasonable variation of heat input so that a value of arc efficiency within the range given in the literature for a specified welding process is sufficient to give residual stress results with acceptable accuracy. When the melting temperature is employed as the initial temperature for the weld metal, the amount of heat used to melt the electrode should be deducted from the total heat input into the model.

   (b) The variation of thermal material properties with temperature within the given range in the literature for structural steels has no significant effect on the final residual stress results.

(c) Yield strength is the most important factor that affects the residual stress results developed due to welding. Ultimate strength is another factor that affects the longitudinal residual stress results significantly. Yield strain at high temperatures was also found to affect the transverse residual stress and distortion results. Care should be taken to define these values as realistically as possible.

(d) The thermal expansion coefficient affects the longitudinal residual stress results by less than 3.1% compared with results obtained from the two extremes given in the literature for structural steel which have a maximum 33% difference.

(e) The heat loss through contact with other surfaces, such as those, for instance, providing support to the welded plates, was found to have significant effect on the final residual stress results. This type of boundary conditions should also be modelled as accurately as possible.

(f) Constraints may affect significantly the stress results especially transverse stress induced during the welding process. It is thus recommended that the constraint conditions should be modelled as accurately as possible in welding process simulations.

(g) The variation of radiation and convection parameters within practical limits has no significant effect on the final longitudinal residual stress distribution. It is not, therefore, necessary to take into account the radiation effect if the residual stresses are of main interest while convection coefficient values within the range of those given in the literature can be used without causing significant inaccuracy to the residual stress results.

As for the cruciform joint model, the assessment of the FEM code was hampered by the limited experimental results available and uncertainties about the accuracy of the experimental measurement itself.

4. Experiments have been carried out on two welded T-joints with very different manufacturing and geometric characteristics to compare, qualitatively, their

behaviour under load as well as to provide data for assessing respective FE models. The material properties of the base metal, weld metal, and the HAZ of each joint were determined from tensile and hardness tests as well as through examination of the microstructure. Comparing the strength values for the base metal of WT1 specimens obtained from hardness tests with those from tensile tests indicates that the values obtained from hardness tests were only 6.6% higher. The hardness test can thus provide a reasonably good approximation for yield and ultimate strength and can be used to approximately estimate the yield and post-yield strength of the HAZ since it is difficult to extract a tensile test specimen from such a small area. The monitoring of temperature variation during the welding of the in-house weldment, WT1, showed that, except from the regions near the ends of the plate, the majority of the cross-sections are at a quasi-steady thermal state. The WT1 fillet weld was sized so that failure will occur in the weld area as the strength of the weld is the main interest of this study. Although the WT1 specimen has various defects the quality of which is normally not accepted in practice, it provides useful information on geometry, material properties, boundary conditions and results for generating and assessing an FE model. The WT2 weldment is yield strength under-matched but combined with the weld size, resulted in an approximately even-matched weldment. Two failure paths have been found in the subsequent bending tests on the WT2 weldment but the final failure loads are very similar. It has also been found that, in welded T-joints under bending,

(a) cracks most likely initiate from the weld toe and/or weld root where there is stress concentration;
(b) failure in a good quality welded T-joints is ductile under bending and the joint undergoes large deformation before final failure;
(c) codes underestimate the strength of the properly welded T-joint WT2 under static loading by 30-40% and the actual failure plane is not the throat area as assumed by the codes;
(d) the presence of multiple defects greatly reduces the load-carrying capacity of weldments, as indicated by the behaviour of WT1, a low-quality weldment.

As shown in Tables 5-13 and 5-14, the WT1 specimens failed at a load only half of that predicted by codes. In comparison, the good-quality WT2 specimens failed at a load 30-40% higher than that predicted by the codes.

5. The FE simulation of the sequential welding process of the WT1 T-joint has been successfully carried out. Comparing the distortion results with those obtained from the experiments presented in Chapter 5 and the residual stress distribution in the literature as well as another FE simulation reported in the literature, the modelling methodologies adopted in this study were seen to give results of acceptable accuracy. As practiced by other investigators in this research area, the temperature histories measured at a few positions from the experiment were used to calibrate the values of the arc efficiency and heat loss through the bottom surface of the base plate thus the uncertainties presented in the thermal analysis were reduced. This simulation provided new information on the residual stress magnitude and distribution over the weld area of a T-joint. Such detailed information is extremely difficult to verify experimentally due to the small size of the area of interest and the extreme environmental conditions prevailing during the process. The predicted history of developing strains and stresses was however carefully examined and re-assessed so that it rationally correlated with the corresponding heat input and temperature histories. The main conclusions from this study are as follows:
   (a) A reliable thermal analysis is a prerequisite to the accurate prediction of residual stresses.
   (b) A symmetric model is not adequate to simulate a sequentially welded T-joint.
   (c) A more detailed representation of the material properties of the HAZ, i.e. accounting for their variation, has little effect on the residual stress distribution away from that area, but a localised effect is evident which may largely affect the assessment of the fracture and fatigue behaviour of welded T-joints.

6. Finite element models of T-joints under bending have been generated and the performance of these models have been examined by comparison of predicted load-strain relations at certain positions with corresponding measured ones from experimental models presented in Chapter 5. Based on the detailed stress and strain distributions obtained from these FE models, the two different failure paths observed in the experiments were explained as the combined effect of different weld sizes and material properties of the weld metal, base metal and the HAZ being one of the possible reasons. The effect of defects on the joint behaviour was also studied and the results were found to be consistent with the experimental observations.

As already pointed out, very few analyses were found in the literature combining the simulation of the welding process with the assessment of the load-carrying behaviour of the joint due to the complexity of the combined simulation. As a first attempt, this study demonstrates the feasibility of combining residual stress simulation with a load-carrying study of welded joints by applying the residual stresses obtained from a welding process simulation on WT2 weldment, as the initial conditions to the joint subjected to external loading. As expected, the residual stresses were found to have no significant effect on the final failure load if large plastic deformation is allowed due to stress-redistribution. However, residual stresses decrease the yield load at certain key positions such as the weld toe and root and the stress distribution under bending in the weld areas may be changed due to the presence of residual stresses. It is well-known that residual stresses have a more significant effect in the case of failures occurring at a low stress levels such as fatigue fracture. The method developed for combining residual stresses results and load-carrying analysis for static loading is also applicable to such fracture analysis.

The assessment of the model is limited by the available results from experiment. In addition, the meshing adopted in the areas where strain gauges were attached did not precisely map the strain gauge size and shape although a relatively fine

mesh was generated. Due to the sharp gradient of strain in the weld area, the strain results obtained from the FE model show some discrepancies from the experimental results. A better correlation between the FEM results and the experimental measurements can be achieved if nodes and elements under the strain gauge area were generated based on the actual strain gauge size and profile, which, however, will inevitably complicate the modelling process and is not necessary if the failure behaviour of the joint is of main interests. The effect of welding-induced residual plastic strain was not included in the combined residual stress and load carrying model due to the limitation of the computing resources and time needed for this task although the modelling method is rather straightforward.

It has to be emphasized that uncertainties in certain input parameters exist in generating the FE models presented in this thesis due to limited available information. The assessment of the FE models is also limited by the available analytical and experimental results and the reliability of those results themselves. Sensitivity study on those uncertain input parameters have been carried out to ensure that most important factors are taken into account.

It is clear from the above discussion that the work presented in this thesis is only the first step towards a comprehensive analytical tool that would be useful in design practice. The generated complex joint FE models cannot realistically be part of a global structural analysis. They however could be the basis of relatively simple joint models that incorporate, to an acceptable accuracy, the various features and effects identified in the full models.

As a summary, the work presented in this thesis has provided new knowledge and contributed to the following areas:

1. The detailed sensitivity studies presented in chapter 3 provide quantified variations of temperature development and residual stress results on various

input parameters such as the temperature-dependent thermal and mechanical material properties with temperature, the value of arc efficiency and convection coefficient as well as modelling of thermal and mechanical boundary conditions. Points that need particular care were identified through the simulation of the simple butt weld process. As these input parameters are normally difficult to obtain, advantages can be taken from this study for any future modelling to save time and gain confidence by paying more attention to the most important factors.

2. The reliability of utilising the commercial program ANSYS for simulation of welding process has been assessed and a simplified modelling procedure with acceptable accuracy has been recommended.

3. Simulation of a sequentially welded T-joint, which is what happens in practice, has been carried out. A symmetric model, which was used in the literature by most investigators on welded T-joints, was proved to be not adequate for sequential welding. This provides new information on residual stress distribution and distortion results.

4. The importance of taking into account the gradual change of material properties from the weld metal across the HAZ to the unaffected base metal, which is present in a real weldment but has not been addressed in the literature, has been demonstrated by the model of a cruciform joint. This information is very useful particularly for studies on failure mechanisms under low applied loads, such as fatigue fracture.

5. Experimental results on welded T-joints under bending indicated that codes underestimate the strength of a good quality weld by 30-40%. This together with detailed stress-strain development information obtained from corresponding FE models, allow more accurate and economic partial safety factors to be proposed for the design of welded joints.

6. The work presented in this thesis provides a very useful base for further generation of FE models on welded joints, either for research or solving a practical problem. As the models presented in this thesis were all generated using parametric language, models of different geometry, material properties and boundary conditions can be easily generated based on these codes.

8.2 Further work

Finite element models have been successfully generated in this research and assessed by available experimental and analytical results. Parametric studies have been carried out on these models. However, these studies are focused on particular joint types under specific load conditions. Given more time, the same methodologies developed here in this research could have been used to analyse other types of welded joints with various geometries and loading conditions. Thus wider and more comprehensive information on the behaviour of welded connections could have been obtained. It should be noted that the FE models have been generated using the parametric language provided by ANSYS with most parameters individually defined. This facilitates their modification and use in parametric studies since dimensions and property values can be changed easily.

With regard to detailed material information on the various areas of a weld (base metal, weld metal and HAZ), it is worth noting that another research programme[1], run parallel to this one, aimed at developing a characterisation procedure based on indentation data from an instrumented hardness tester. It is hoped that these characterisation results could be used as inputs to the models described in this thesis.

It has also become obvious that the FE modelling of welded joints would benefit from further experimentation and more detailed measurements of developing temperatures, strains and displacements in the weld area. It was noted that the detailed stress and strain distribution in the weld area of the FEM of a sequentially

welded T-joint was not fully validated due to lack of such data. Given more experimental information, the models could be better validated to give more accurate results and increased confidence in their reliability. The FE model of the cruciform joint and the welding process simulation of the butt weld were assessed by comparison with the results from the work of others, where available details are limited. Experiments should also be carried out, given more time and resources, on specimens manufactured under high-quality control welding conditions and covering a wider range of geometric configurations and material properties. Based on such results as well as a wider range of predictions from FEA models, reliability analysis could then be developed leading to recommendations for improvement of the current design codes.

Based on the current work, several areas for further analysis were identified.

1. FEA should be applied to additional joint types and parametric studies carried out on material properties, geometry and loading conditions, to provide sufficient information for further reliability analysis or to generate a database with a realistic ranges of material properties and geometries so that it could be directly applicable for the design of welded joints in practice.

2. In practice, it is often the case that the plates to be welded together are not free ended. The welding process can therefore be simulated using the same methodologies as those adopted in this research but under different, more realistic boundary conditions to study further the effect of various constraints on residual stresses.

3. Typical welding defects can be introduced as cracks into the FE models and the relevant fracture mechanics concepts and methodology applied to simulate crack propagation and thus study the fracture behaviour of welded joints. In addition to elastic-plastic material properties, fracture toughness is also needed for such analysis.

4. The FEA for assessing the effect of welding-induced residual stresses on the load-carrying behaviour of welded T-joints can be carried out adopting the alternative, integrated approach, as described in Chapter 7, section 7.5, which takes into account also the residual plastic strains in addition to the stresses. This would lead to a more reliable assessment of failure mechanisms.

5. Improved modelling of welded joints based on the present work can be incorporated into structural FE models. Two possible ways may be adopted to achieve this. One of them is to make use of the sub-modelling and/or the sub-structuring techniques provided in ANSYS. Sub-models for welded connections could be easily generated by changing the dimensions and material properties of those already generated and validated in this research. Another method is to generate a special type of "weld joint element" in structural models taking into account the most important features that the weld connections bring to the overall structural behaviour such as residual stress, material variation in WM and HAZ, and distortion etc. The first method is more straight-forward and specific details of the welded joint in question can be taken into account in the sub-model/sub-structure. However, this may require considerable computational time and thus prove expensive. By using a simplified "weld element" according to the second method, the computational time can be significantly reduced and the overall structural model easy to generate, but this model is limited in the details of the welded joint itself to be considered and its features are restricted by what ANSYS permits.

6. This "weld joint element" would enable the ultimate strength analysis of a welded construction to be undertaken as part of fracture analysis. The failure sequence could be derived by FEA which, aided by fractographic examination, would allow both a qualitative and quantitative assessment of the reasons for failure of a welded structure. Based on such a comprehensive failure analysis, safer structure could then be designed with optimised safety factors.

References

[1] H. Habbab, Post-yield characterisation of welds based on instrumented hardness tester data, PhD Thesis (to be submitted), University of Southampton, 2004

Appendix A: Weld defects

Welds often contain various types of defects. Table A-1 and Fig. A–1 illustrate typical weld defects.

Table A-1 Types of weld defects and their causes

Type of defect	Causes
Porosity	Poor welding technique; Incorrect setting; Lack of cleaning Electrodes not dried
Slag inclusions	Poor welding technique; Insufficient interpass cleaning
Tungsten inclusions	Welding current too high; Electrode contamination
Incomplete fusion	Poor welding technique; Current too low; Welding speed too high
Incomplete penetration	Poor arc control; Current too low; Welding speed too low Root opening too narrow
Excess penetration	Poor arc control; Current too high; Welding speed too low Root opening too wide
Undercut*	Poor welding technique; Current too high
Underfill	Insufficient weld layers deposited
Arc strikes	Poor welding technique
Cracks**	Poor welding technique; Incorrect termination of the welding arc

* Undercut: This term is used to describe a groove melted into the base metal adjacent to the toe of a weld and left unfilled by the weld metal. It also describes the melting away of the sidewall of a welding groove at the edge of a layer of bead, thus forming a sharp recess in the sidewall in the area to which the next layer or bead must fuse.

** Cracks: Cracks result from ruptures of metals under stress. Although sometimes large, they are often very narrow separations in the weld or adjacent base metal. Cracks are one of the most harmful of welding defects and are prohibited by most specifications. However, small cracks, often called fissures or microfissures, may not reduce the service life. Specifications are reluctant to specify an allowable maximum crack size; rather, they tacitly admit that any cracks too small to be resolved by the required inspection procedure are permitted.

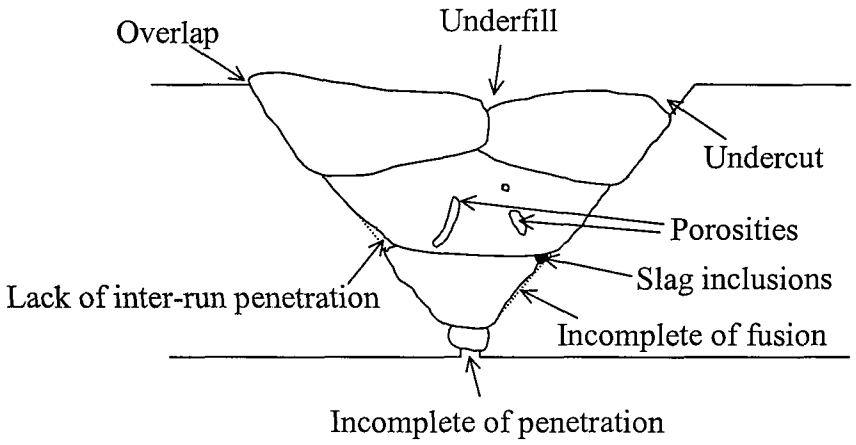

Fig. A-1 Typical weld defects

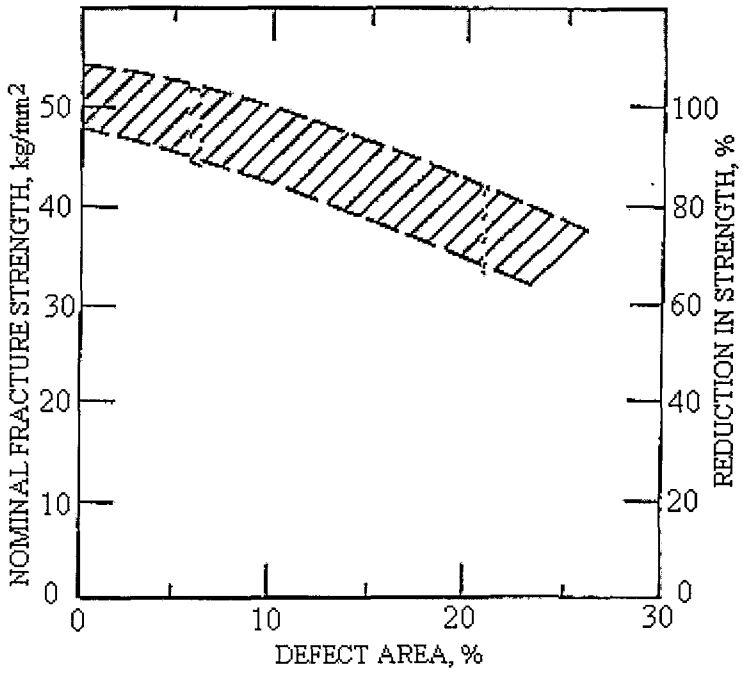

Fig. A-2 Reduction of static strength due to defects in welds (reproduced from Kahara[1])

[1] Kahara H., Tada Y., Watanabe M., Ishii Y., Nondestructive Testing of Welds and their Strength, 60th Anniversary Series, 7, *The Society of Naval Architects of Japan*, Tokyo, 1960

Appendix B: Summary of welding process simulation in the literature

A summary of published simulations of welding process, including the publication year, FEM programme used, 2D or 3D simulation, geometry of the model, type of material, temperature-dependency of material properties input, heat input function and experimental method used, is listed in Table B-1

Notations in the table

c	specific heat
k	thermal conductivity
HF	convection coefficient
Em	emissivity
ρ	density
S_Y	yield stress
E	Young's modulus
Et	Tangent modulus
υ	Poisson's ratio
α	thermal expansion coefficient
η	arc efficiency
V	voltage
I	current
v	electrode travel speed
HS	heat source mode
TF	temperature-dependent and values given in figures
THF	temperature-history dependent and values given in figures
TN	temperature-dependent but no values given
NM	not mentioned
N	no
Y	yes or given
G	Gaussian distribution
R	ramped heat input function
PC	phase change
S-S	solid-solid phase change considered
S-L	solid-liquid phase change considered
BHD	blind hole drilling
NSS	Neutron strain-scanning
ABX	Abrasive bore +X-ray

Table B-1 Summary of some of the welding simulation in the literature

Pub. Year	Program		Geome-try	Material	Material properties										Heat input					Rad.	PC	Experiment-al validation		Agreement
					C	*k*	*HF*	*Em*	ρ	S_Y	*E*	*Et*	*v*	α		η	Value	V, I,v	M					
1999		2D	Butt					TN														Y	X-ray	Good
			Girth(Mu)	SS 304 l																				
1997	ABAQUS	2D	T-stiffened	SAE 1020	TF	TF	TF	0.2	N	TF	TF		TF	TF		N	0.307-717	N	DE	Y	247KJ/KG.C	Y	BHD	Good
1998	ABAQUS	2D	Butt(Mu)	ASTM A36	TF	TF	NT		N	TF	TF			TF	N	0.85	Qs+Qb	Y	G,R	N	N	Y		
			Girth(Mu)	SS304	TF	TF			N	TF	TF	TF	TF	TF	N					N	N	Y	Brust	
1992	ABAQUS	3D							N															
1993	ABAQUS	2/3 D	Butt(Mu)	ASTM A36	TN											N	Qb	Y	R	NM	NM	Y	BHD	Good
1993	ABAQUS	2D	Butt(Mu)	ASME A36	TF	TF	NM	NM	N	TF	TF	NM	NM	TF	N		Qb+Qs	Y	G,R	NM	N	N		
1992	ABAQUS	2D	Butt(Mu)	ASTM A36	TF	TF	NM	NM	N	TF	TF	NM	NM	TF	N	0.85	Qb+Qs	Y	G,R	NM	NM	Y	BHD	Good
2000	ABAQUS	2/3 D	Butt	NM	TN						TN				N	0.75	Qb	Y		NM	NM	N		
			MF-C	A36,A572-Gr50-														Y						
1994	Self-gene	3D	Edge butt	AISI 1020	TN						TN					0.7	0.32	N	DE	NM	TP	Y	SSM	Good
2000	COSMO	2D	Butt	NM, MPs	TN				Y		NA								G,E	Y	Y	Y		
1994	In house code	2D	D-shape hollow	SS142132 SS142172	TF	TF	NT	NM	N	THF	TF	TF	TF	THF	N	0.8	0.993	v	R	NM	Y, S-S		NSS	
2000	ABAQUS	3D	Butt	S460M	NM	NM	NM	NM	NM	TN	TN	TN	0.3					Y	G	NM	N	Y	BHD	
1985		2D	Butt+tack		TF	TF				TF	TF	THF	TF	TF	Y	0.72	1.6	v			Y	Y	BHD	
1996			T+I fillet																					
1999	in-house SiMPle	2D	Butt(Mu)	SIS2134, AISI 1524-	TF	TF	NT	0.5	NM	TF	TF		TF	TF	Y	NM	NM	NM	NM	Y	S-S,S-L,	Y	BHD	Good
1985	NM, susp. In-house	2D	Butt	Sy=360MPa	TF	TF	NT	N	NT	TF	TF	0	TF	THF	Y	0.72	1.6mj/m	v	Qs	N	S-S+S-L, VC	Y	BHD	Good
1985	SMART II	2D	Butt	St 37	TF	TF	TF	TF	NM	TF	TF	TF	TF	TF	N	N	1680J/s	v	Qs, G	Y	VC, TP	Y	ABX	Good

Appendix C: FEM fundamentals

The finite element method is an approximate method of analysis. The basic principles underlying it are simple. To obtain the distribution of an unknown variable in a body, the body is first divided into an assembly of subdivisions (elements) interconnected by nodes. The distribution of the unknown variable is then assumed over each element. The number and type of elements are chosen so that the variable distribution over the whole body is adequately approximated by the combined elemental representations. The governing equation for each element is calculated and assembled to obtain the system equations, which describe the behaviour of the body as a whole. The number of equations involved in the system equations are normally very large and can be solved with the help of modern advanced computers.

Stress analysis

The system equations of stress problems generally take the form

$$[K]\{U\} = \{F\} \tag{C-1}$$

where $[K]$ is the stiffness matrix; $\{U\}$ the vector of nodal displacement; and $[F]$ the vector of nodal forces.

By applying the minimum potential energy theory, the stiffness matrix can be calculated from

$$[K] = [B]^T [D][B] \int_V dV \tag{C-2}$$

where $[D]$ is the stress-strain matrix, and depends on material properties such as Young's modulus, Poisson's ratio, and as in

$$\{\sigma\} = [D](\{\varepsilon\} - \{\varepsilon^{th}\}) \tag{C-3}$$

where $\{\sigma\}$ is the stress vector; $\{\varepsilon\}$ the total strain vector; and $\{\varepsilon^{th}\}$ the thermal strain vector, calculated from the thermal expansion coefficient and the temperature change; $[B]$ is the strain-displacement matrix as in

$$\{\varepsilon\} = [B]\{u\} \tag{C-3}$$

where $\{u\}$ is the nodal displacement vector.

The boundary conditions (constraints or other known displacements to $\{U\}$, forces to $[F]$, etc.) will then be incorporated into the system equations and the system equations Eqn. (C-1) solved to obtain the displacement results at each node, from which the element strain and stress can be calculated.

Heat flow analysis

The mathematical analysis of transient heat flow in a weldment is essentially based on the following partial differential equation

$$\rho c \frac{\partial T}{\partial t} = q_G + \left[\frac{\partial}{\partial x}\left(k\frac{\partial}{\partial x}\right) + \frac{\partial}{\partial y}(k\frac{\partial}{\partial y}) + \frac{\partial}{\partial z}\left(k\frac{\partial}{\partial z}\right)\right]T \tag{C-4}$$

From Fourier's law

$$\{q\} = -[D]\{L\}T \tag{C-5}$$

where $\{q\}$ is the heat flux vector;

$[D] = \begin{bmatrix} K_{xx} & 0 & 0 \\ 0 & K_{yy} & 0 \\ 0 & 0 & K_{zz} \end{bmatrix}$, the conductivity matrix; and

$$\{L\} = \begin{Bmatrix} \dfrac{\partial}{\partial x} \\ \dfrac{\partial}{\partial y} \\ \dfrac{\partial}{\partial z} \end{Bmatrix}$$, the vector operator,

Eqn. (C-4) can then be re-written as

$$\rho c \frac{\partial T}{\partial t} + \{L\}^T \{q\} = q_G \tag{C-6}$$

Now considering the three types of boundary conditions:

1. Specified temperatures, T^* acting over surface S_1,

$$T = T^* \tag{C-7}$$

2. Specified heat flows, q^* acting over surface S_2

$$\{q\}^T \{\eta\} = -q^* \tag{C-8}$$

where $\{\eta\}$ is the unit outward vector;

3. Specified convection acting over surface S_3

$$\{q\}^T \{\eta\} = h\,(T\text{s}-T_\text{B}) \tag{C-9}$$

where h is convection coefficient, Ts and T_B the bulk temperature of the adjacent fluid (air in this study) and temperature at the surface of the model, respectively

Premultiplying Eqn. (C-6) by a virtual change in temperature, δT, and integrating over the volume of the element, combining Eqn. (C-5) and (C-8) to (C-9),

$$\int_V \left(\rho c \delta T \frac{\partial T}{\partial t} + \{L\}^T (\delta T)([D]\{L\}T) \right) dV =$$

$$\int_{S_2} \delta T q^* dS_2 + \int_{S_3} (\delta T) h (T_B - T) dS_3 + \int_V (\delta T) q_G dV \qquad \text{(C-10)}$$

For transient analysis, variable temperature, T varies with both space and time,

$$T = [N]^T \{T_e\} \qquad \text{(C-11)}$$

where $[N]$ is element shape functions; $\{T_e\}$ is the nodal temperature vector of element.

$$\dot{T} = \frac{\partial T}{\partial t} = [N]^T \left\{ \dot{T}_e \right\} \qquad \text{(C-12)}$$

$$\delta T = \{\delta T_e\}^T [N] \qquad \text{(C-13)}$$

$$\{L\}T = [B]\{T_e\} \qquad \text{(C-14)}$$

where $$[B] = \{L\}[N]^T \qquad \text{(C-15)}$$

Substitute Eqns.(C-11)-(C-15) to Eqn. (C-10),

$$[C]\ \{\dot{T}\} + [K]\ \{T\} = \{Q\} \qquad \text{(C-16)}$$

where $[C] = \rho \int_V c\{N\}\{N\}^T dV$,

$[K] = \int_V [B]^T [D][B] dV + \int_{S_3} h\{N\}\{N\}^T dS_3$, and

$\{Q\} = \int_{S_2} \{N\} q^* dS_2 + \int_{S_3} T_B h \{N\} dS_3 + \int_V q_G \{N\} dV$

Method used by ANSYS to solve non-linear problems

ANSYS employs the "Newton-Raphson" approach to solve nonlinear problems. For each load step applied, which is assumed to vary linearly with time, it is divided into substeps (load increment), for each substep, the program performs equilibrium iterations until a converged solution is obtained. If convergence cannot be achieved, the program attempts to solve with a smaller load increment.

For the geometric non-linearity encountered in this study, i.e., large strain/large deflection, a feature provided by ANSYS has to be activated which accounts for the change of stiffness matrix due to the change of element shape and orientation. For material nonlinearity, for example, elastic-plastic material behaviour adopted in this study, the true stress-true strain curves have to be input following one of the material hardening models provided by ANSYS, for example, bi/multi-isotropic (see Fig. C-1), bi/multi-kinematic (see Fig. C-2), etc. The program will respond to plasticity after the fact, by reducing the load step size after a load step in which a large number of equilibrium iterations was performed or in which a plastic strain increment greater than 15% was encountered.

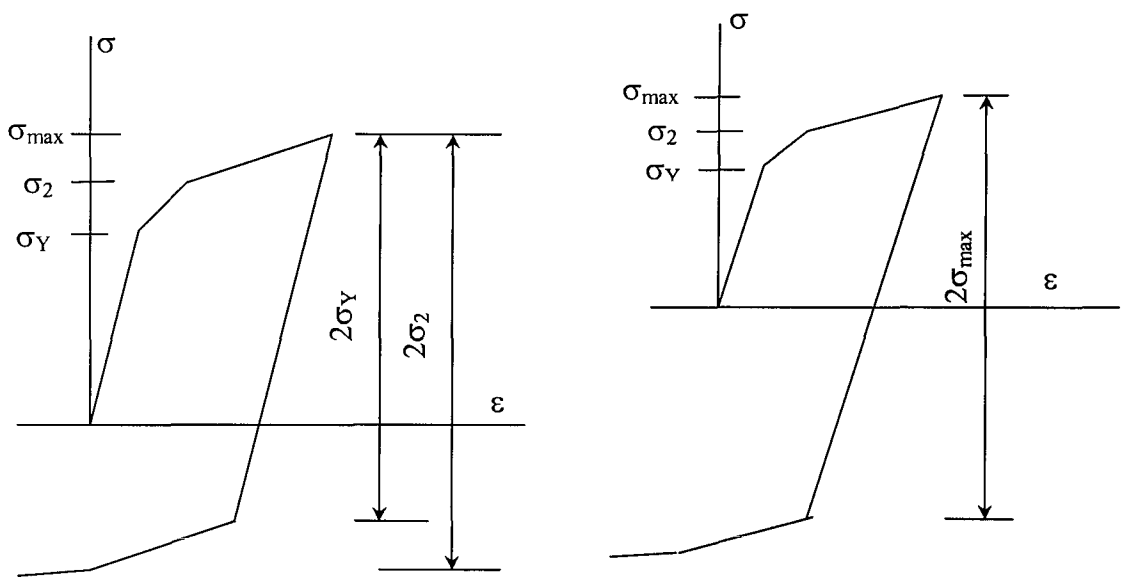

Fig. C-1 Strain hardening model

FEM sources of errors

Systematic errors:

As already pointed out at the beginning of this appendix, FEM is an approximate method of analysis, and the choice of element (type, i.e., interpolation function and density) as well as how close the real loading and constraint conditions are represented in the FE model, will influence the accuracy of FEM. In general, as the number of elements increased, i.e., the size of the element reduced, the results will be closer to the real values. Use of complex or multiplex high order elements would also improve the accuracy. In a non-linear analysis, the smaller the load increment, the closer the results towards the real values. However, the smaller the element size and the load increment, the longer the duration hence more expensive the computation would cost. In practice, the number of elements is never infinite thus the results from FE are not the exact real values. A trade-off between the size of element and load increment and the cost must be decided. High mesh density should be used where there is an expected rapid change in the unknown variable.

Software errors

It should be emphasised that the accuracy and reliability of the FE program in dealing with the problem in question will also influence the accuracy of the FE results. For widely used commercial FE packages, their accuracy and reliability may well have been verified for common problems such as stress analysis. Solving a benchmark problem is commonly used to verify the FE program, which may be provided with the program so that the user can validate the implementation on his own machine.

Human errors

The computer only calculates based on the data the engineer input into it. As the FE programs are tend to be more complex, given the program is reliable, the accuracy of the FE results relies also on the engineer to apply the program correctly. It is vital that the model is generated as close as possible to the real situation, and input data such as

material properties, loading and constraint conditions, as accurate as possible. Considerable engineering judgement may be required to generate the model as well as to interpolate the results.

Elements used in this thesis

2-D line element (as shown in Fig. C-2)

LINK 1: is a uniaxial tension-compression element with two degrees of freedom at each node: translations in the nodal x and y directions. As in a pin-jointed structure, no bending of the element is considered.

LINK32: is a uniaxial element with the ability to conduct heat between its nodes. The element has a single degree of freedom, temperature, at each node point.

CONTAC12 represents two surfaces which may maintain or break physical contact and may slide relative to each other. The element is capable of supporting only compression in the direction normal to the surfaces and shear (friction) in the tangential direction. The element has two degrees of freedom at each node: translations in the nodal x and y directions.

The interpolation functions for LINK1 are:

$$u = 0.5\,[u_i\,(1\text{-}s) + u_j\,(1\text{+}s)] \tag{C-17}$$

$$v = 0.5\,[v_i\,(1\text{-}s) + v_j\,(1\text{+}s)] \tag{C-18}$$

and for LINK32 is

$$T = 0.5\,[T_i\,(1\text{-}s) + T_j\,(1\text{+}s)] \tag{C-19}$$

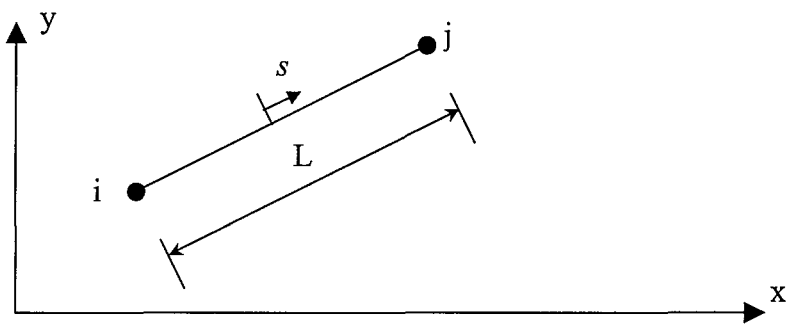

Fig. C-2 Line element geometry

2-D solid element (as shown in Fig. C-3)

PLANE2: is a 6-node triangular element. The element has a quadratic displacement behaviour. The element is defined by six nodes having two degrees of freedom at each node: translations in the nodal x and y directions. The element can be used as a plane element (plane stress or plane strain) or as an axisymmetric element. The element also has plasticity, creep, swelling, stress stiffening, large deflection, and large strain capabilities.

PLANE42: 2-D linear quadrilateral, is used for 2-D modelling of solid structures. The element can be used either as a plane element (plane stress or plane strain) or as an axisymmetric element. The element is defined by four nodes having two degrees of freedom at each node: translations in the nodal x and y directions. The element has plasticity, creep, swelling, stress stiffening, large deflection, and large strain capabilities.

PLANE55: can be used as a plane element or as an axisymmetric ring element with a 2-D thermal conduction capability. The element has four nodes with a single degree of freedom, temperature, at each node. The element is applicable to a 2-D, steady-state or transient thermal analysis

The interpolation functions (in Natural coordinate) for PLANE2 are

$$u = u_i (2L_1\text{-}1) + u_j (2L_2\text{-}1) + u_k (2L_3\text{-}1) + u_l (4L_1 L_2) + u_m (4L_2 L_3) + u_n (4L_3 L_1)$$
$$v = v_i (2L_1\text{-}1) + v_j (2L_2\text{-}1) + v_k (2L_3\text{-}1) + v_l (4L_1 L_2) + v_m (4L_2 L_3) + v_n (4L_3 L_1)$$

The interpolation functions for PLANE42 are

$$u = 0.25 [u_i (1\text{-}s) (1\text{-}t) + u_j (1+s) (1\text{-}t) + u_k (1+s) (1+t) + u_l (1\text{-}s) (1+t)]$$
$$v = 0.25 [v_i (1\text{-}s) (1\text{-}t) + v_j (1+s) (1\text{-}t) + v_k (1+s) (1+t) + v_l (1\text{-}s) (1+t)]$$

and for PLANE55 are

$$T = 0.25 [T_i (1\text{-}s) (1\text{-}t) + T_j (1+s) (1\text{-}t) + T_k (1+s) (1+t) + T_l (1\text{-}s) (1+t)]$$

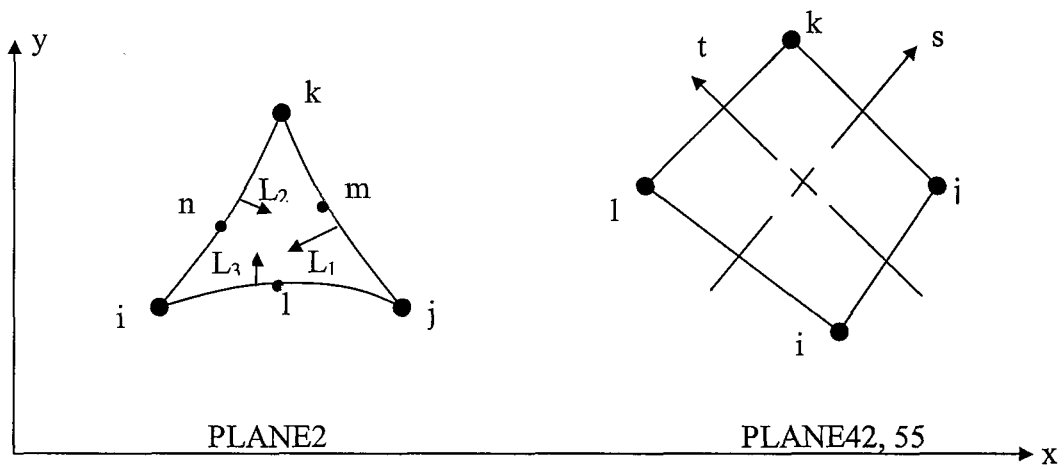

Fig. C-3 2-D solid element geometry

Appendix D: Generation of elasto-plastic stress-strain curves from a set of material parameters

Fig. D-1 shows a typical nominal stress-train as well as true stress-logarithmic strain curve for a structural steel. The true stress, σ, and true strain, ε, can be calculated from:

$$\varepsilon = \ln(1+\varepsilon_n) \qquad \text{(D-1)}$$

$$\sigma = \sigma_n(1+\varepsilon_n) \qquad \text{(D-2)}$$

where, ε_n is the nominal strain and σ_n the nominal stress. In the plastic region, the stress-strain relation can be assumed to have the form:

$$\sigma = K\varepsilon^n \qquad \text{(D-3)}$$

where, K is the strength coefficient and n the strain-hardening exponent.

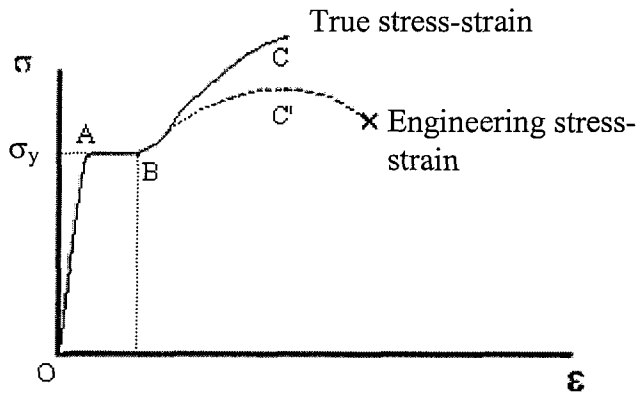

Fig. D-1 Stress strain curves of structural steel

Tabulated information from tensile tests usually consists of the yield stress σ_y, the ultimate stress σ_u, the yield point elongation ε_y, the elongation at ultimate stress ε_u and the reduction of area at fracture A_r. The application of Eqns. (D-1) and (D-2) converts σ_y, σ_u, ε_y, ε_u, to the corresponding true and logarithmic values. Then, the conditions

$$\sigma_y = K(\varepsilon_y)^n \qquad \text{(D-4)}$$

and

$$\sigma_u = K(\varepsilon_u)^n \qquad \text{(D-5)}$$

provide a system of equations for the determination of the parameters K and n. Thus part OAB of the stress-strain curve in Fig. D-1 can be drawn directly based on the Young's modulus and the information given while BC is represented by Eqn. (D-3). Finally A_r can be used to calculate the nominal strain at fracture according to:

$$\varepsilon_f = \frac{A_r}{1 - A_r}$$

which can also be converted to logarithmic using Eqn. (D-1). If the fracture load has been recorded, the true fracture stress σ_f can also be estimated. Parameters K and n can then be further adjusted so that the curve BC lies as closely as possible to point (σ_f, ε_f).

The procedure described above was applied to the weld materials in Chapter 4 (see Table 4-1 for the material properties for BM, WM and HAZ).

Steel plate:

$\sigma_y = 387\,\text{MPa}$; $\sigma_u = 536\,\text{MPa}$; $A_r = 0.66$

Assuming that the nominal strain ε_u, at σ_u is 18%, the respective logarithmic strain and the true ultimate stress can be calculated from Eqns. (D-1) and (D-2) as:

$\varepsilon_u = \ln(1.18) = 0.1655$
$\sigma_u = 536 \times 1.18 = 632\,\text{MPa}$

Assuming that the yield point elongation is $\varepsilon_y = 0.02$, Eqns. (D-4) and (D-5) give:

$$\left.\begin{aligned} 387 &= K \times 0.02^n \\ 632 &= K \times 0.1655^n \end{aligned}\right\} \Rightarrow \quad n = 0.232,\ K = 959\,\text{MPa}$$

The true stress strain relation for the steel plate in the plastic region is thus:

$$\sigma = 959\varepsilon^{0.232},\ \varepsilon \geq 0.02$$

Engineering strain at fracture: $\varepsilon_f = \frac{A_r}{1 - A_r} = \frac{0.66}{1 - 0.66} = 1.941$, $\Rightarrow \varepsilon = \ln(2.941) = 1.08$

Weld metal

$\sigma_y = 398$ MPa; $\sigma_u = 529$ MPa; $A_r = 0.63$

The same procedure as that used for the weld metal, with strength values as listed above, results in the values 0.212 and 911 MPa for n and K, respectively.

HAZ

$\sigma_y = 468$ MPa; $\sigma_u = 579$ MPa; $A_r = 0.35$

Assuming a similar reduction of strain at σ_u for steel plate and the HAZ:

$$\varepsilon = 0.1655 \times \frac{0.431}{1.08} = 0.066 \ (\text{nominal } \varepsilon_u = 7.4\%)$$

Hence

$$\left(\frac{0.066}{0.02}\right)^n = \frac{579 \times 1.068}{468} \quad \Rightarrow n = 0.233$$

$$K = \frac{468}{0.02^{0.233}} = 1165 \text{ MPa} \quad \Rightarrow \sigma = 1165\varepsilon^{0.233}$$

Strain at fracture: nominal $\varepsilon_f = \frac{A_r}{1-A_r} = \frac{0.35}{1-0.35} = 0.538$, $\Rightarrow \varepsilon_f = \ln(1.538) = 0.431$

Appendix E Sizing of WT1 weld

The size of the WT1 weld was designed based on a simple approximate method to ensure that failure occurs in the weld in order to study the strength of the weld itself. In addition, the weld should also be large enough to enable a tensile test specimen to be extracted from the weld area.

As shown in Fig. E-1, load F was applied to the attachment plate to produce a combined shear and bending moment to the joint. The bottom of the main plate was fixed.

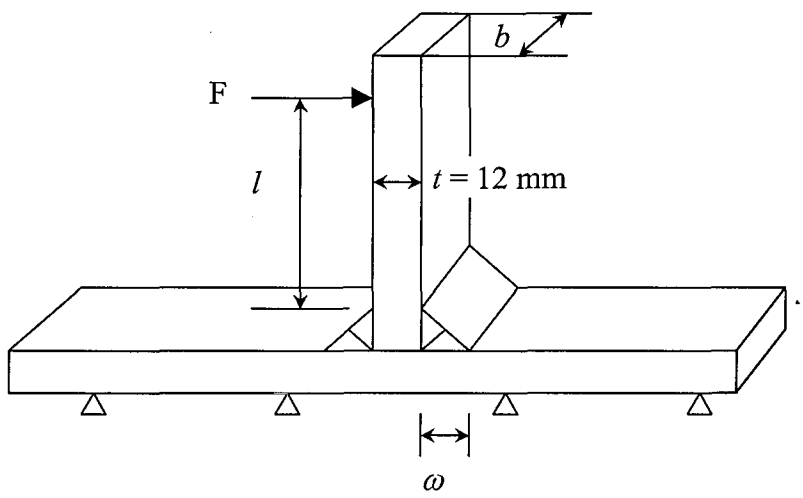

Fig. E-1 Loading of T-joints

Weld having a leg size ¾ of the base plate thickness is considered to be a full strength weld[1]. In this experiment, the plate thickness is 12 mm, hence the leg length should be less than 9 mm for failure to occur in the weld.

For the simplest calculation, assume that the throat is in shear for all types of load, and the shear stress in the throat is the load divided by the throat area. The plate thickness should be larger than the combined weld throat area for failure to occur in the weld. For an equal leg length weld, its leg length should thus be less than 8.5 mm if the strength of the weld metal is assumed to be the same as the base metal. Assuming a 15% higher strength of the weld metal, the weld leg length is then 7.4 mm.

After consulting the technicians for the minimum size required for extracting a tensile test specimen from the weld area, 7 mm was chosen to be the size of the weld to be welded for the WT1 weldment.

References

[1] The Lincoln Electric Company, The Procedure Handbook of Arc Welding, 30th Edition, 1995

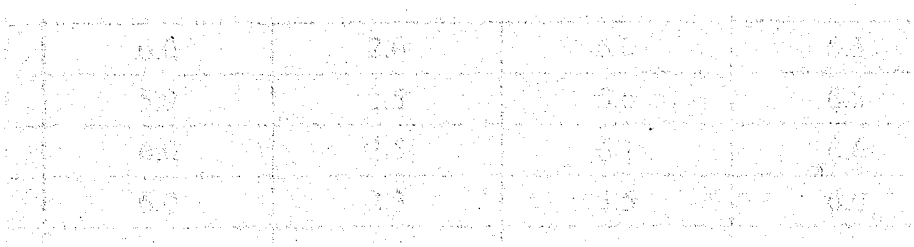

Appendix F: Size of weld throat and leg length of the WT1 weldment

The weld leg length and throat dimensions at different positions along the longitudinal length of the WT1 weldment for the two weld passes, measured every 10 mm, is listed in Table F-1.

Table F-1 Measured weld leg length and throat

Distance from start of weld run (mm)	First weld		Second weld	
	Leg, mm	Throat, mm	Leg, mm	Throat, mm
10	6.8	3.0	7.0	6.0
20	6.0	3.0	6.3	6.0
30	4.7	2.0	6.0	6.0
40	6.7	2.0	6.1	6.0
50	5.3	2.0	5.4	6.0
60	5.3	2.0	5.8	6.0
70	5.6	2.0	5.2	5.7
80	5.0	2.0	6.0	5.9
90	7.0	2.5	5.8	6.0
100	6.8	3.0	6.0	6.0
110	6.2	2.0	6.2	6.0
120	5.9	3.0	6.3	6.1
130	5.8	2.9	5.9	6.0
140	5.5	2.8	6.0	6.0
150	6.2	2.0	6.0	6.0
160	5.9	2.0	5.5	6.0
170	6.0	2.0	6.0	6.5
180	5.9	2.5	5.6	6.5
190	6.0	2.5	6.1	6.6
200	6.0	2.3	5.5	6.0
210	5.9	2.9	6.3	6.4
220	5.7	2.5	6.2	6.2
230	6.6	3.0	6.5	6.1

240	5.8	2.2	6.1	6.2
250	6.3	2.5	6.2	6.2
260	6.9	3.2	5.8	6.2
270	6.0	2.6	6.8	6.9
280	6.0	2.5	5.6	6.2
290	6.0	2.9	6.0	6.1
300	6.0	3.0	5.8	6.2
310	7.0	4.0	5.9	6.1
320	6.8	3.5	6.2	6.9
330	7.0	3.2	5.9	6.8
340	7.0	4.0	5.8	6.0
350	7.2	3.8	6.3	6.2
360	6.8	3.5	5.9	6.4
370	7.0	3.0	5.8	6.3
380	8.0	4.1	5.9	6.1
390	7.0	3.8	5.6	6.2
400	6.5	3.0	5.9	6.0
410	7.3	4.0	6.0	6.2
420	6.8	3.5	5.9	6.6
430	6.3	3.0	6.0	6.5
440	6.0	3.1	5.9	6.0
450	5.8	3.0	6.0	6.4
460	7.0	3.5	5.8	6.3
470	6.5	3.1	6.0	6.0
480	6.0	2.5	6.0	6.4
490	6.0	3.0	6.4	6.5

Appendix G Dimensions of specimens and apparatus used in the tensile tests

WT1 specimen base metal

Fig. G-1 shows the specimen used in the tensile test for WT1 specimen. The dimensions of the samples were measured and are listed in Table G-1.

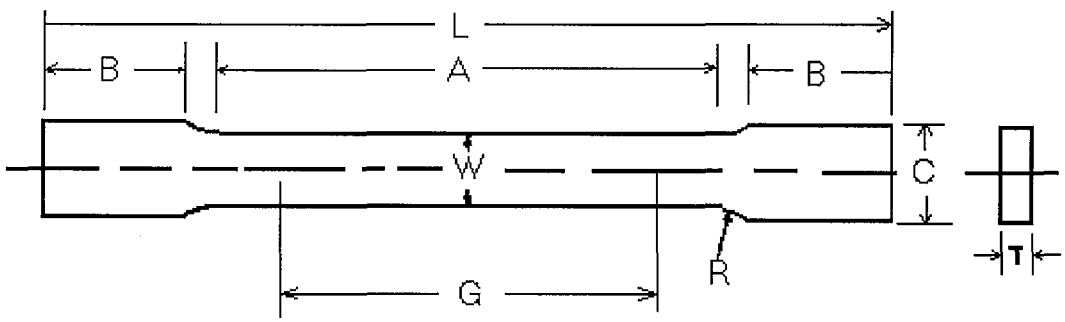

G-Gauge length, 50.0±0.1; W-Width, 12.5± 0.2
T-Thickness; R-Radius of fillet, 12.5
L-Overall length, 200;
A-Length of reduced section, 57
B-Length of grip section, 50; C-Width of grip section, 20

Fig. G-1 Rectangular tensile test specimen, dimensions in mm

Table G-1 Tensile test specimen dimensions for WT1 base metal

Specimen	W (mm)	T (mm)	A_0 (mm^2)
A	12.585	12.630	158.949
B	12.218	12.689	155.038
C	12.156	12.623	153.442
Average	12.320	12.647	155.809
Standard deviation	0.23	0.04	2.83

Apparatus

An M&W micrometer and a Vernier calliper were used to measure the dimensions of the specimens. The tensile tests were carried out at room temperature using an INSTRON 2511-320 machine. A 50 mm gauge length extensometer was used to measure strain in the sample. Along with the chart recorder a Hewlett Packard Data logger was connected to collect digitally the strain and load values.

WT2 specimen base metal

The specimen used in the tensile test for WT2 specimen is shown in Fig. G-2. The dimensions of the specimens are listed in Table G-2. All values in the table are in mm.

Apparatus:

Except that the extensometer used in these tests has a 25 mm gauge length with a 12.5 mm travel distance, the experimental procedure used was the same as that for the WT1 specimen.

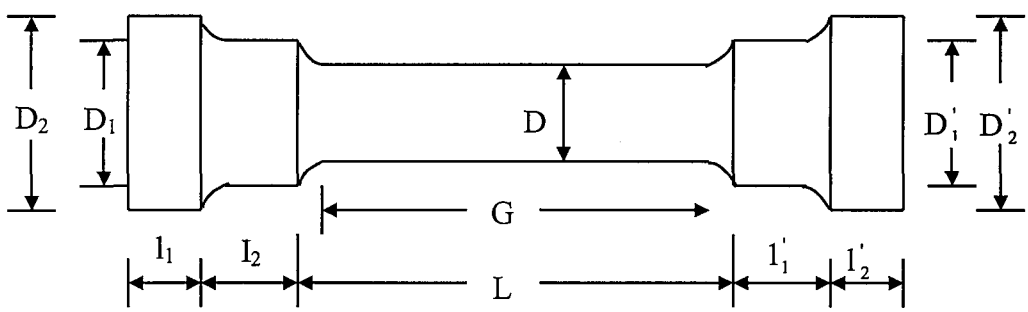

Fig. G-2 Standard round bar tensile test specimen

Table G-2 Dimensions of the tensile specimens for the WT2 weldment steel plate

Specimen	A	B	C	Average
D	5.00	5.02	5.01	5.01
D_1	6.94	6.93	6.93	6.93
D_2	10.04	10.00	10.03	10.02
D_1'	6.97	6.96	6.95	6.96
D_2'	10.10	9.79	9.96	9.95
L	28.59	28.78	28.51	28.63
l	26.83	26.91	26.92	26.89
l_1	6.33	5.40	5.07	5.60
l_2	5.43	4.71	6.04	5.40
l_1'	4.21	5.62	5.32	5.05
l_2'	5.59	5.65	4.80	5.35
D'	5.00	5.00	5.02	5.01
D''	5.02	5.02	5.04	5.03
G	24.75	25.04	25.45	25.08

WT1 specimen weld metal

Standard round bar specimen as shown in Fig. G-2 was used for the tensile test of both WT1 and WT2 weld metal. The dimensions of these specimens are listed in Tables G-3 and G-4 for the WT1 and WT2 specimens, respectively.

Apparatus:

The apparatus used and the experimental procedure was the same as that for the WT2 specimen base metal.

Table G-3 Dimensions of the WT1 weld metal tensile specimens (in mm)

Specimen	A	B	Average	Standard deviation
D	3.54	3.56	3.55	0.016
D_1	5.02	5.09	5.05	0.049
D_2	7.61	8.03	7.82	0.299
D_1'	5.09	5.00	5.04	0.062
D_2'	8.00	7.91	7.95	0.062
L	27.18	26.39	26.79	0.559
l	25.76	26.91	26.34	0.818
l_1	3.52	4.20	3.86	0.483
l_2	2.44	3.50	2.97	0.750
l_1'	4.34	3.85	4.10	0.344
l_2'	4.35	2.73	3.54	1.140

Table G-4 Dimensions of the WT2 weld metal tensile specimens, dimensions in mm

Specimen	A	B	Average	Standard deviation
D	3.47	3.58	3.52	0.077
D_1	5.04	4.96	5.00	0.057
D_2	7.73	7.84	7.79	0.078
D_1'	5.01	4.90	4.95	0.075
D_2'	7.85	7.89	7.87	0.028
L	27.00	26.75	26.88	0.177
l	25.86	25.56	25.71	0.210

Appendix H Dimensions of the WT1 and WT2 bend specimens

The dimensions describing the geometry of the various specimens tested are given in Tables H-1 and H-2. These dimensions are defined in Figs. 5-25 and 5-20 for the WT2 and WT1 specimens, respectively.

Table H-1 Dimensions of WT2 bend specimens, dimensions in mm

	t_1	t_1'	t_2	h	l_1	l	L	LLH	LLV	RLH
A	10.03	10.04	10.03	12.16	83.06	89.00	89.63	6.54	5.75	8.51
B	10.09	10.08	10.07	10.68	82.01	90.00	89.84	8.35	6.02	8.85
C	9.95	9.94	9.94	10.40	81.50	89.50	89.63	6.23	6.49	7.61
D	10.00	9.97	9.96	10.59	82.49	89.57	89.76	7.92	5.75	6.38
E	9.92	9.91	9.70	11.06	81.90	90.06	89.77	7.95	5.81	6.22
F	10.05	10.04	9.98	10.95	81.90	90.06	89.77	7.96	5.78	7.80

Table H-2 Dimensions of WT1 bend specimens, dimensions in mm

	t_1	t_1'	t_2	l_1	l_2	L	LLH	LLV	RLH	RLV	h
A	11.83	11.79	11.89	64.28	65.86	147.87	7.06	5.27	6.13	4.92	9.98
B	12.37	11.98	12.16	68.39	66.41	141.13	6.43	4.78	6.03	4.28	10.01

Appendix I: FE modelling input commands

I.1 Commands for the welding simulation of a butt weld

```
!THERMAL ANALYSIS
/prep7

!DEFINE ELEMENT TYPES
et, 1, plane55                    ! 4-node quadrilateral with DOF of temp

!RADIATION ELEMENT
et, 2, surf151
keyopt, 2, 4, 1
keyopt, 2, 5, 1
keyopt, 2, 9, 1
r, 1,1,5.67e-11

!DEFINE TEMP-DEPENDENT MATERIAL PROPERTIES(MP)

*do, n, 1, 3
mp, dens, n, 7.860e-9

! THERMAL CONDUCTIVITY
mptemp, 1, 277.5, 341.9, 412.7, 556.1, 672.6, 808.6
mptemp, 7, 954.4, 1070.3, 1256.8, 1523, 1732.2, 1813.1
mptemp, 13, 2073.9, 3273.7, 8000
mpdata, kxx, n, 1, 51.7, 51.5, 50.21, 44.85, 42.82, 38.4
mpdata, kxx, n, 7, 32.51, 25.97, 26.96, 30.57, 33.94, 119.7
mpdata, kxx, n, 13, 119.72, 119.76, 119.8
mptemp

!ENTHAPY
mptemp, 1, 279.6, 318.4,636.25,876.46, 970.9, 1025.8
mptemp, 7, 1143, 1543.4, 1753, 1803, 2273, 5273
mptemp, 13, 8273

mpdata, enth, n, 1, 0, 123, 1424, 2740, 3356, 3812
mpdata, enth, n, 7, 4626, 6672.6, 7869.4, 10209, 12986.8, 30716.6
mpdata, enth, n, 13, 48446.4
mptemp

!CONVECTION COEFFICIENT
mptemp, 1, 273.4, 307, 343.2, 359, 372, 457.8
mptemp, 7, 573.2, 733.2, 890.4, 1094.8,1543,1831.8
mptemp, 13, 2028.4, 2461.2, 2931.3, 3257,6000
mpdata, hf, n, 1, 0.00263,0.00346,0.00444,0.0051,0.00547,0.0063
mpdata, hf, n, 7, 0.00705,0.00762, 0.00797,0.00834,0.00882,0.00909
mpdata, hf, n, 13, 0.00919,0.00928, 0.0094,0.00947,0.0095
```

```
mptemp
*ENDDO

!CONVECTION COEFFICIENT FOR THE BASE SURFACE
mptemp, 1, 277.5, 341.9, 412.7, 556.1, 672.6, 808.6
mptemp, 7, 954.4, 1070.3, 1256.8, 1523, 1732.2, 1910
mptemp, 13, 2073.9, 3273.7, 5000
mpdata, hf, 5, 1, 51.7/100, 51.5/100, 50.21/100, 44.85/100, 42.82/100, 38.4/100
mpdata, hf, 5, 7, 32.51/100, 25.97/100, 26.96/100, 30.57/100, 33.94/100, 36.9/100
mpdata, hf, 5, 13, 40/100, 62.7/100, 93/100
mptemp

!EMISSIVITY
mptemp,1, 273,373,473,573,773,1023
mptemp,7,1273,1863,5273
mpdata,emis,10,1, 0.2,0.4,0.45,0.475,0.54,0.58
mpdata,emis,10,7,0.59,0.6,0.65
mptemp

!..... define all other thermal material properties
:
:
*enddo

! GEOMETRY OF THE MODEL - V-WELD
! left half assuming symmetry
! L = total plate width
! T = plate thickness
! b = weld width - bottom
! B = weld width - top
! h = overfill height
! w1 = width of bm to be applied surface heat on top surface
! w2 = haz width on bottom surface
*dim, geo, , 9
!       L/2   T   b   B    h   w1   w2 RU  RL
geo(1) = 127, 12.7, 2, 16.665, 1, 1.2, 0.6, 50, 30
x2 = geo(1)-geo(3)/2
x5 = geo(1)-geo(4)/2
y7=geo(2)+geo(5)
x8=(x5+geo(1))/2
y8=geo(2)+geo(5)*0.6
x9=geo(1)-4*geo(2)
x11=geo(1)-geo(3)/2-geo(7)
x12=x5-geo(6)

!define key points
k, 1
k, 2, x2, 0
```

```
k, 3, geo(1), 0
k, 4, geo(1), geo(2)

:
:
!define lines from key points
l, 1, 9          !l1
l, 2, 5          !l2
l, 10, 6 !l3
:
:
!define areas from lines
al, 1, 11, 3, 4
al, 5,6,7,8,2
al,11,9,13,10
al,13,12,2,14

!define mesh size and mesh
esize,5
lesize, 9,1.5,,,0.15
lesize, 2,0.5,,
lesize, 10,1.4,,,12

lesize, 5,,,3
lesize, 6,0.5
lesize, 7,0.5
lesize, 8,0.5
lesize, 12,,,3
lesize, 13,0.5
lesize, 14,,,3

!mesh
mat, 1
amesh, 1, free
amesh,3,4
mat, 2
amesh, 2, free

!GENERATE RADIATION ELEMENT
n, 5000, geo(1)/2, geo(8)
n, 5500, geo(1)-geo(4)/2, geo(8)
n, 6000, -geo(9), geo(2)/2

mat,10
type, 2
real, 1
nsel, s, loc, y, geo(2)
nsel, r, loc, x, 0, x5
```

```
esurf, 5000
allsel

lsel,s,line,,8
nsll,s
esurf,5500
allsel

nsel, s, loc, x, 0
esurf, 6000
allsel
esel, s, type,,2
/color, elem, yell

check,esel,warn
/color,elem,red
allsel
eplot
:
:

mat,3
type, 2
real, 1
nsel, s, loc, y, geo(2)
nsel, r, loc, x, 0, x5
esurf, 5000
allsel
nsel, s, loc, x, 0
esurf, 6000
allsel
esel, s, type,,2
/color, elem, red
allsel
eplot

!CHECK BAD ELEMENTS AND SHOWN IN RED
check,esel,warn
/color,elem,blac
allsel
eplot

finish

!SOLUTION
/solu
antype, transient
solcontrol, on
```

```
nropt, full,, on

tunif, 293                    !assign initial uniform temp to all nodes
asel,s,area,,2          ! melting temperature as the initial temperature of the weld
nsla,s,1
ic,all,temp,1803
allsel
dl, 6, 2, symm                !symmetry constraints
dl, 7, 2, symm
d, 5000, temp, 293
d, 5500, temp, 293
d, 6000, temp, 293

! total heat input due to welding arc
ae = 0.75                     !arc efficiency for net heat-input
v = 40                        !arc voltage
i = 375                       !arc current
qa = 1000*0.5*ae*v*i          ! (half) total net heat-input to the model

! length of top weld surface (arc)
pi=acos(-1)
r=(geo(5)**2+(geo(4)/2)**2)/(2*geo(5))
agl=asin(geo(4)/(2*r))                !in radians
lar=r*agl

! weld area
a = (geo(3)+geo(4))*geo(2)/4+(agl*r**2/2-(r-geo(5))*geo(4)/4)

! heat to melt electrode
delth=10209-43.706
!den=7860
!deltt=1803-293
qm=4.318*delth*a

! net heat input to model
q=qa-qm

!heat input

qb=0.8*q/a              !body heat-input portion
asel, s, area, , 2      !uniform body heat-input
esla, s
bfe, all, hgen, , qb
allsel

qs= 0.2*q/(lar+geo(6))        !surface heat-input portion
sfl, 8, hflux, qs
sfl, 14, hflux, qs,0
```

```
!convection load
lsel, s, line, , 4          !select convection surface:all free surfaces
lsel, a, line, , 3
lsel, a, line, , 10
                                    !lsel, a, line, , 14
sfl, all, conv, -1, , 293
allsel

lsel, s, line, , 1          !select convection surface:all free surfaces
lsel, a, line, , 5
lsel, a, line, , 9
lsel, a, line, , 12
sfl, all, conv, -5, , 293
allsel


vs = 4.318      ! mm/sec

! first load step of thermal analysis
tm1 = 0.2/vs
time, tm1
autots, on
nsubst, 25, 5000, 10
outres, basic, all

solve

*get,nsul1, active, 0, solu, ncmss

! second load step of thermal analysis
timint, on
tm2 = 5*tm1
time, tm2
nsubst, 80, 50000000, 2

sfl, 8, hflux, qs
sfl, 14, hflux, qs,0

asel, s, area, , 2          !uniform body heat-input
esla, s
bfe, all, hgen, , qb
allsel
solve
*get,nsul2, active, 0, solu, ncmss

!and all other load steps
:
:
```

```
save
finish


!STRESS ANALYSIS
/prep7
etchg, tts
keyopt, 1, 3, 2
tref, 293

 ! MECHANICAL PROPERTIES

  ! YOUNG'S MODULUS AND POISSON'S RATIO
  *dim, exym,,9
  exym(1)=207.375e3, 198.31e3, 189.4e3, 183.1e3, 133.8e3, 91.16e3, 36.51e3,0.05e3, 0.0031e3

*do, n, 1, 3

  mp, nuxy, n, 0.3
  mptemp, 1, 293, 436, 571, 670, 846.5, 988
  mptemp, 7, 1268,1800, 6000
  mpdata, ex, n, 1, exym(1),exym(2),exym(3),exym(4),exym(5),exym(6)
  mpdata, ex, n, 7, exym(7),exym(8),exym(9)
  mpplot, ex, n

*enddo

! THERMAL EXPANSION COEFFICIENT FOR BASE AND WELD METAL
*do,n,1,2
   mptemp
   mptemp, 1, 273, 373, 473.7, 573.5, 674, 774.4
   mptemp, 7, 873.6, 993.6, 1102.5, 1275.8, 1800,1850
   mptemp, 13, 3000, 5000

   mpdata, alpx, n, 1, 6.7e-6, 9.26e-6,11.6e-6, 12.5e-6, 13.83e-6, 13.6e-6
   mpdata, alpx, n, 7, 14.06e-6, 14.5e-6, 10.6e-6, 12.8e-6, 17.4e-6,17.4e-6
   mpdata, alpx, n, 13, 17.4e-6, 17.4e-6
   mpplot, alpx, n
   mptemp
*enddo

mpamod, 1, 293
mpamod, 2, 293


!STRAIN HARDENING FOR BASE METAL

*dim, bmmp, , 9, 11                    !base metal mp
```

```
bmmp(1,1)= 293, 436, 571, 670, 846.5, 988, 1268,1800, 6000    !9 temp value
bmmp(1,2)= 244, 222, 199, 174, 91, 30, 20,5.6, 0.6             !s1
bmmp(1,3)= 317, 286, 246, 212, 116, 37,24.8,5.87,0.635         !s2
bmmp(1,4)= 424, 370, 315, 271, 148, 43, 30.2,5.95, 0.652       !s3
bmmp(1,5)= 517.5, 449.8, 385.9, 339, 179.7, 52, 35.1, 6.07, 0.66    !s4
bmmp(1,6)= 602, 525, 459, 400, 205, 71, 40, 6.11, 0.665        !s5

*dim, eyb,,9            !eyb: strain at yield for bm
*do, n, 1, 9
  eyb(n)=bmmp(n,2)/exym(n)
*enddo

bmmp(1,7)= eyb(1), eyb(2), eyb(3), eyb(4), eyb(5), eyb(6), eyb(7),eyb(8),eyb(9)   !e1
bmmp(1,8)= .029267,0.029267,0.029267,0.029267,0.029267,0.029267,0.029267,0.161,0.235
bmmp(1,9)= 0.07844, 0.07844, 0.07844, 0.07844, 0.07844, 0.07844, 0.07844, 0.22, 0.272
bmmp(1,10)= 0.1398, 0.1398, 0.1398, 0.1398, 0.1398, 0.1398, 0.1398, 0.284, 0.317
bmmp(1,11)= 0.21511, 0.21511, 0.21511, 0.21511, 0.21511, 0.21511, 0.21511,0.323, 0.369
!bmmp(1,13)= 4.24, 4.24, 4.24, 4.24, 4.24, 4.24, 4.24, 4.24, 4.24          !e6

!STRAIN HARDENING DEFINE

 tb, kinh, 1, 9, 5
 *do, i, 1,9
        tbtemp, bmmp(i,1)
        *do, n, 1, 5
          tbpt,,bmmp(i,n+6), bmmp(i,n+1)
        *enddo
 *enddo
 tbplot, kinh,1


!STRAIN HARDENING FOR WELD METAL

*dim, bpw, , 9, 11                    !weld metal mp
bpw(1,1)= 293, 436, 571, 670, 846.5, 988, 1268,1800, 6000    !9 temp value
bpw(1,2)= 342.4, 305, 270, 247, 135, 40, 5,0.002,  0.00001          !s1
bpw(1,3)= 362, 318,280, 257, 142, 42, 5.8,0.00215,0.0000107         !s2
bpw(1,4)= 446, 380, 327, 282, 157, 43, 6.6, 0.00225,0.000012        !s3
bpw(1,5)= 484, 413.8, 351.3, 304, 160.3, 45, 7, 0.00229,0.0.0000124      !s4
bpw(1,6)= 531, 460, 391, 336, 168, 49, 7.2, 0.00229,0.0000124       !s5

*dim, eyw, ,9           !eyw: strain at yield for wm
*do, n, 1, 9
  eyw(n)=bpw(n,2)/exym(n)
*enddo

bpw(1,7)= eyw(1), eyw(2), eyw(3), eyw(4), eyw(5), eyw(6),eyw(7),eyw(8),eyw(9)    !e1
bpw(1,8)= 0.00975, 0.00975, 0.00975, 0.00975, 0.00975, 0.00975,0.00975,0.098, 0.0066 !e2
```

```
bpw(1,9)= 0.062, 0.062, 0.062, 0.062, 0.062, 0.062, 0.062,0.22, 0.0437          !e3
bpw(1,10)= 0.1133, 0.1133, 0.1133, 0.1133, 0.1133, 0.1133,0.1133, 0.284, 0.093
        !e4
bpw(1,11)= 0.215, 0.215, 0.215, 0.215, 0.215, 0.215, 0.215,0.336, 0.113          !e5

!strain hardening define

 tb, kinh, 2, 9, 5
 *do, i, 1,9
        tbtemp, bpw(i,1)
        *do, n, 1, 5
          tbpt,,bpw(i,n+6), bpw(i,n+1)
        *enddo
 *enddo
 tbplot, kinh, 2
finish

!SOLUTION
/solu
antype, static
solcontrol, on
nropt, full,, on
nlgeom, on
!first load step

!DEFINE BOUNDARY CONDITIONS
time, 10001
dk, 3, uy, 0!, ,,,uy

dl, 6, 2, symm                !symmetry constraints
dl, 7, 2, symm
allsel

*do, n, 1, nsull
 ldread,temp,1,n,,,,rth
 autots, on
 kbc, 0
 nsubst, 50, 500000, 5
 solve
*enddo

!all other load steps
:
:
finish
save
!POST-PROCESSING
/post1
```

```
!OBTAIN ELEMENT Z-STRESS AND VOLUME
esel,all
etable,zstres,s,z
etable,elevolu,volu
smult,elefor,elevolu,zstres

*get,toelenum,elem,0,count

/page,,,2*toelenum
/output,eletable
pretab,zstres,elevolu,elefor
```

I-2 Programme file for the cruciform joint

```
/filnam, cross-bend
/title, analysis of a cross fillet welded joint
/prep7
thik = 10
et, 1, plane42
keyopt, 1, 3, 3
r, 1, thik

! contact element
rl = 2.07e6
fr = 0.3
ent3 = 0.0001

!loading magnitude
p1 = 0
p2 = -387

*dim, mapr,,15,20
mapr(1,1)=2.07e5,387,387,478.61,562.11,617.55,674.93,713.8,387/2.07e5,0.02,0.05,0.1,0.15,
0.22,0.28
mapr(1,2)=2.07e5,398,398,482.73,559.14,609.33,660.86,695.53,398/2.07e5,0.02,0.05,0.1,0.1
5,0.22,0.28
mapr(1,3)=2.07e5,468,468,579.68,681.28,748.78,818.67,866,468/2.07e5,0.01,0.05,0.1,0.15,0.
22,0.28
*do, n, 1,15
 mapr(n,4)=mapr(n,3)-(mapr(n,3)-mapr(n,1))/18
 mapr(n,5)=mapr(n,3)-(mapr(n,3)-mapr(n,1))/9
 mapr(n,6)=mapr(n,3)-(mapr(n,3)-mapr(n,1))/6
 mapr(n,7)=mapr(n,3)-2*(mapr(n,3)-mapr(n,1))/9
 mapr(n,8)=mapr(n,3)-5*(mapr(n,3)-mapr(n,1))/18
 mapr(n,9)=mapr(n,3)-(mapr(n,3)-mapr(n,1))/3
 mapr(n,10)=mapr(n,3)-7*(mapr(n,3)-mapr(n,1))/18
 mapr(n,11)=mapr(n,3)-4*(mapr(n,3)-mapr(n,1))/9
```

```
  mapr(n,12)=mapr(n,3)-(mapr(n,3)-mapr(n,1))/2
  mapr(n,13)=mapr(n,1)+4*(mapr(n,3)-mapr(n,1))/9
  mapr(n,14)=mapr(n,1)+7*(mapr(n,3)-mapr(n,1))/18
  mapr(n,15)=mapr(n,1)+(mapr(n,3)-mapr(n,1))/3
  mapr(n,16)=mapr(n,1)+5*(mapr(n,3)-mapr(n,1))/18
  mapr(n,17)=mapr(n,1)+2*(mapr(n,3)-mapr(n,1))/9
  mapr(n,18)=mapr(n,1)+(mapr(n,3)-mapr(n,1))/6
  mapr(n,19)=mapr(n,1)+(mapr(n,3)-mapr(n,1))/9
  mapr(n,20)=mapr(n,1)+(mapr(n,3)-mapr(n,1))/18
  !mapr(n,21)=mapr(n,2)+(mapr(n,3)-mapr(n,2))/2

*enddo
*do,n,1,20
 mp,ex,n,mapr(1,n)
 mp,prxy,n,0.3
 tb, kinh,n,,20
  *do,i,1,7
    tbpt,,mapr(8+i,n),mapr(1+i,n)
  *enddo
*enddo


!geometry
*dim, geo, , 9
!       t,   t,   l,  l,  leg,  hazw1, hazw2, hazd1,  hazd2
geo(1) = 12.5, 12.5, 50, 50, 12.5,   1,    2,    1.5,    3.5

y1 = geo(1)/2
y5 = y1 + geo(4)
x6 = geo(3)-geo(2)/2
:
:
k, 1, 0, y1
k, 2, 0, 0
k, 3, geo(3), 0
:
:

k, 100, 110, 0

l, 1, 2                    !l1
l, 2, 3                    !l2
:
:
al, 1, 2, 3, 11,14, 4
al, 12, 5, 6, 7, 16
:
:
```

```
lesize, 13,,,26
lesize, 15,,,26
:
:
mat, 1
amesh, 1
amesh,2
amesh,6
amesh,7

mat, 2
amesh, 3
amesh,8

mat, 3
amap,4,11,9,10,15
amap,5,10,31,7,8
amap,9,24,26,20,25
amap,10,22,23,25,32

!Change elements material properties
!left weld and adjacent areas
lsel,s,line,,13,15,2
nsll,s,0
esln,s,0
asel,s,area,,3
esla,r
emodif,all,mat,21
cm,ea31,elem
allsel

ne1=7
*dim,ea4,char,ne1

ea4(1)='a41','a42','a43','a44', 'a45','a46','a47'

lsel,s,line,,13,15,2
nsll,s,0
esln,s,0
asel,s,area,,4,5,1
esla,r
cm,%ea4(1)%,elem
nsle,s
esel,all
esln,s,0
esel,u,,,%ea4(1)%
esel,u,,,ea31
emodif,all,mat,4
```

```
cm,%ea4(2)%,elem
nsel,all

*do,n,1,ne1-2
nsle,s
esel,all
esln,s,0
asel,s,area,,4,5,1
esla,r
esel,u,elem,,%ea4(n)%
esel,u,elem,,%ea4(n+1)%
emodif,all,mat,n+4 !namp2+namp3+5
cm,%ea4(n+2)%,elem
nsel,all
*enddo
allsel
:
:
et, 2, contac12
keyopt,2,4,1
r, 2, 0, r1,,1.0,r1/100
r, 3, 180, r1,,1.0,r1/100
mp, mu, 50, fr

nsel, s, loc, y, y1
nsel, r, loc, x, x6, x21
nsel,u,loc,x,geo(3),x20
type, 2
real, 2
mat, 50
eintf, ent3
allsel

nsel, s, loc, y, -y1
nsel, r, loc, x, x6, x21
type, 2
real, 3
mat, 50
eintf, ent3
allsel

nsel, s, loc, y, y1
nsel, r, loc, x, geo(3),x20
type, 2
real, 2
mat, 50
eintf, ,,high
allsel
```

```
!ASSIGN DIFFERENT COLORS TO ELEMENT WITH DIFFERENT MAT NUMBER
*dim,ecolor,char,ne1+4
ecolor(1)='red','blue','yell','blac','gree','oran','ygre','mage','gcya','bmag','whit'

*do,i,4,13
  esel,s,mat,,i
  /color,elem,ecolor(i-3)
  allsel
*enddo
esel,s,mat,,21
/color,elem,oran
allsel
:
:
check,esel,warn
/color,elem,blac
allsel
eplot
finish

/solu
antype, static, new
solcontrol, on

nsel, s, loc, y, y5
d, all, ux, 0,,,, uy
allsel

lsel, s, loc, y, -y5
lsel,r,loc,x,x6,geo(3)
sfl, all, pres, p1, p2
allsel

lsel,s,loc,y,-y5
lsel,r,loc,x,geo(3),x21
sfl,all,pres,-p2,-p1
allsel

outpr,basic,all
autots, on
nsubst, 10, 500, 10
time, 1

solve
save
finish
```

I-3 Programme file for the simulation of a sequentially welded T-joint

```
/filname, haz-mptet
/title, residual stress of t
/config, nres, 10000

!THERMAL ANALYSIS
/prep7
!DEFINE ELEMENT TYPES, KEYOPTIONS, REAL CONSTANTS, AND MP
et, 1, plane55                    ! 4-node quadrilateral with dof of temp
:
:
!GEOMETRY OF THE MODEL

*dim, geo, , 9
! !geometry
!       t,  t,  1,  l,  leg,  hazw2, hazd1, gap, hazw3
geo(1) = 1.186,1.186,23.7,11.8,0.58,0.2,0.12,0.05,0.25

k, 1, 0, geo(1)
k, 2, 0, 0
:
:
!mesh
:
:
finish
!SOLUTION
/solu
antype, transient
solcontrol, on
nropt, full,, on

asel, s, area, ,4,7,3
asel,a,area,,3
esla, s
ekill,all
estif,10e-10
allsel
esel, s, live
nsle, s
nsel, inve
d, all, temp, 293
allsel
!DEFINE LOAD CONDITIONS
:
:
nsubst, 20, 50, 20
```

```
solve
*get,nsul1, active, 0, solu, ncmss

! second load step of thermal analysis
timint, on
tm2 = 6*tm1
time, tm2
asel,s,area,,3
esla,s
ealive,all
nsle, s
ddele, all,all
allsel

sfldele,11,hflux
:
:
asel,s,area,,8,9,1
esla,s
bfedele,all,hgen
allsel
SOLVE
*get,nsul2, active, 0, solu, ncmss
autots, on
nsubst, 30, 50000, 30
kbc,0
:
:
! sixth load step of thermal analysis
timint, on
tm6 = tm5+5*tm1
time, tm6

esel, s, live
esel, inve
ealive, all
nsle, s
ddele, all,all
allsel
:
:
finish

!STRESS ANALYSIS
!haz original mat number:1 in thermal analysis
!haz mat number is 11 in stress analysis
!haz mat11 interpolated from bm and wm from test data
!area5,6 change to haz at ls5 when heat input into haz
```

```
!area5,6 change to wm at ls6 when second wm deposited.

/prep7

etchg, tts
keyopt, 1, 3, 2
:
:

! contact element
r3 = 2.07e7
fr = 0.3
et, 3, contac12
keyopt,3,4,1
keyopt,3,7,1
r, 3, 0, r3
mp, mu, 5, fr
esel, s, type,,2
emodif, all, type, 3
emodif, all, mat, 5
emodif, all, real, 3
allsel
!MP
define temp-dependent expansion coefficient, etc.
:
:
!strain hardening for base metal

*dim, bmmp, , 6, 15                          !base metal mp
bmmp(1,1)= 293, 472, 785, 1033,1850,2800    !6 temp value
bmmp(1,2)= 290.1e2,233e2,108e2,13e2,2e2,0.1e2  !s1
bmmp(1,3)= 300.5e2,262e2,129e2,21e2,2.24e2,0.14e2  !s2
bmmp(1,4)= 303.4e2,264e2,136e2,27e2,2.4e2,0.16e2        !s3
bmmp(1,5)= 305e2,265e2,143e2,29e2,2.41e2,0.17e2         !s4
bmmp(1,6)= 392.8e2,333e2,189e2,31e2,2.45e2,0.19e2       !s5
bmmp(1,7)= 473e2,406e2,219e2,32e2,2.455e2,0.20e2        !s6
bmmp(1,8)= 510e2,432e2,222e2,33e2,2.46e2,0.2e2  !s7
bmmp(1,9)= 0.00139,0.001395,0.001102,0.001857,0.5,0.5  !e1
bmmp(1,10)= 0.006294,0.006294,0.007, 0.006294, 1.58, 2  !e2
bmmp(1,11)= 0.015211,0.015211,0.0149, 0.015211, 3, 3    !e3
bmmp(1,12)= 0.021822,0.021822,0.021822, 0.021822, 4, 4          !e4
bmmp(1,13)= 0.05,0.05,0.05, 0.05, 5, 5        !e5
bmmp(1,14)= 0.1,0.1,0.1, 0.1, 6, 6    !e6
bmmp(1,15)= 0.15,0.15,0.15, 0.15, 7, 7        !e7
:
:
!strain hardening for wm and haz
:
```

```
:
finish

SOLUTION
/solu
antype, static
solcontrol, on
nlgeom, on
nropt, full
outres,basic

asel,s,area,,4,7,3
asel,a,area,,3
esla, s
ekill, all
estif,10e-15
mpchg,31,all
allsel

asel,s,area,,8,11,1
esla, s
mpchg,11,all
allsel

stm1 = 1
time, stm1

nsel,s,loc,x,geo(3)/2
nsel,r,loc,y,0
d,all,ux,0,,,,uy
allsel
d,32,uy,0
allsel

tref, 293
mp, reft, 21, 1773
mp,reft,31,1773
mp,reft,3,1773
mp,reft,2,1773

*do, n, 1, nsul1
  ldread,temp,1,n,,,haz-mptet,rth
  autots, on
  nsubst, 30, 500000, 2
  solve
*enddo

!second load step
```

```
stm2 = stm1+1
time, stm2
nlgeom, on
asel,s,area,,3
esla,s
ealive,all
mpchg,2,all
allsel

*do, n, 1, nsul2
 ldread,temp,2,n,,,haz-mptet,rth
 autots, on
 kbc, 0
 nsubst, 50, 50000, 15
 solve
*enddo
!third load step
:
:
finish
```

I-4 Programme file for the simulation of load-carrying behaviour of welded T-joints

Bending model without residual stresses

```
/filname, fri2-tn-bed-geo2-3
/title, static analysis of fillet welded T-joint under bending
!geo2=length of attachment plate = 89 mm
! analysis is done in mm and Newton's.

/prep7

!define element types

jthik=12            !joint thickness
sthik=120           !support plate thickness
cthik=100           !clamp thickness
lbemt=12            !loading beam thickness
et, 1, plane42
keyopt, 1, 3, 3
r, 1, jthik
:
:
! BOLT CROSS-SECTIONAL AREA, DIAMETER 12MM
pi=acos(-1)
bcs = pi*(6**2)

et, 2, link1        !bolt
```

```
alink=2*bcs             !area
e0lik=0.0006            !initial strain
r, 21, alink, e0lik             !area !initial strain

!point-point contact element
r1 = 2.07e6
fr = 0.3          ! friction coefficient
ent3 = 0.0001

et, 3, contac12
keyopt,3,4,1
r, 10, 0, r1,,1.0,r1/100
r, 11, 180, r1,,1.0,r1/100
mp, mu, 10, fr

!RIGID-FLEXIBLE SURFACE CONTACT ELEMENT

et, 4, targe169
r,41,,lbemt!,10
r,42,,jthik!,10
et,5,conta171
keyopt,5,5,2
fr5=0.3
mp,mu,50,fr5

!DEFINE MATERIAL PROPERTIES

*dim, mapr,,15,15
mapr(1,1)=2.07e5,623.5,660.1,670.6,687.4,699.3,723.1,734.2,623.5/2.07e5,0.00477,0.00531,
0.00725,0.011,0.0246,0.0406
mapr(1,2)=2.078e5,414.4,437.0,457.4,496.7,516.8,541.4,549.4,414.4/2.078e5,0.0035,0.00663
,0.0133,0.0177,0.0256,0.0312
mapr(1,3)=2.0735e5,528.75,559.8,568.7,582.9,600,630,647,528.75/2.0735e5,0.00477,0.0053
1,0.00725,0.011,0.0242,0.0406
!multi-linear strain hardening
*do,n,1,3
 mp,ex,n,mapr(1,n)
 mp,prxy,n,0.3
 tb, kinh,n,,15
  *do,i,1,7
    tbpt,,mapr(8+i,n),mapr(1+i,n)
  *enddo
*enddo

! BUILD GEOMETRY

*dim, geo, ,10
! geo(1)= length of bottom line of the gap
```

```
!geo(2)= right hoz leg
!geo(3)= right vert leg
!geo(4)= thickness of the attachment plate
!geo(5)= right hoz haz width
!geo(6)= right vert haz width
!geo(7)= left hoz leg
!geo(8)= left vert leg
!geo(9)= left hoz haz width
!geo(10)= left vert haz width

geo(1) = 6.91/2, 7.8, 7.40, 10, 1.65, 2.21, 8, 6, 1.43 ,1.77

!geometry origin: middle point of the bottom line of the gap between attachment and base
plate

! right fillet area
x1=geo(1)+geo(2)
:
:
*dim, cgeo,,3
!cgeo(1,2)=clamp plate length, height,
!cgeo(3)=distance of the plate right lower corner to weld toe
cgeo(1)= 23.5,13,0.2
:
:
! CREATE NODES AT THE BASE PLATE AND A LINK ELEMENT FOR THE BOLT

type, 2
mat, 1
real, 21
nsel,s,loc,x,(x110+x112)/2
nsel,r,loc,y,y110
*get,liki,node,,num,max
allsel
ksel,s,kp,,150
nslk,s
*get,likj,node,,num,max
allsel

e, liki, likj

! CREATE CONTACT ELEMENTS BETWEEN THE JOINT AND CLAMPS

type, 3
mat, 10
real, 10

nsel, s, loc, y, 0
```

```
nsel, r, loc, x, x110, x112
eintf, ent3
nsel,all

real,11
nsel,s,loc,y,y85
nsel,r,loc,x,x84,x85
eintf, ent3
allsel

!DEFINE TARGET SURFACES AND ASSIGN TARGET ELEMENTS
!joint-support plate
type,4
real,42

lsel,s,line,,64
lmesh,all
allsel

!loading beam-joint
type,4
real,41
lsel,s,line,,77
lmesh,all
allsel

!define contact surface and assign contact elements
!joint-support plate
type,5
real,42

lsel,s,line,,52,58,6
lmesh,all
allsel
!loading beam-joint
type,5
real,41
lsel,s,line,,42,45,3
lmesh,all
allsel

check,esel,warn
/color,elem,red
allsel
eplot
finish

!SOLUTION
```

```
/solu

antype, static, new
solcontrol, on,on
nlgeom,on

! apply boundary conditions
!support plate
nsel,s,loc,x,ggeo(1)
d, all, all, 0
allsel

lsel,s,line,,76
nsll,s,1
d,all,uy,0
allsel

dbend=3
lsel,s,line,,77
nsll,s,1
d,all,ux,dbend
allsel

kbc,0
autots, on
nsubstep, 50,5000,10
time, 1
outres,all,all
solve
save
finish
```

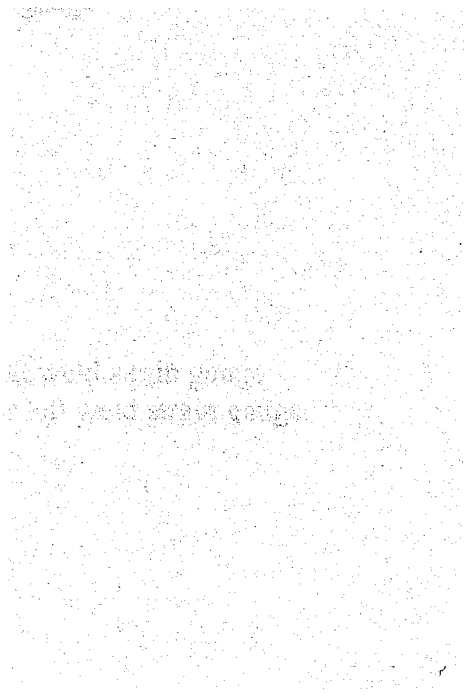

Get strain results at the strain gauge position and load

This file is an independent file: **getresult-left.txt**. It was read into the resumed .db and .rst files using the following command:

```
/input, getresult-left, txt,,line,0

!GET STRAIN AT STRAIN GAUGE POSITIONS in the weld
! strain gauge 1 in left weld
! Define a local coordinate sysytem

xori=x35-(19.0835-17.4233)
yori=(17.1243-16.3174)
local,21,0,xori,yori,0,43.45,,,

!select nodes under the strain gauge area
```

```
nsel,s,loc,x,0,1
nsel,r,loc,y,-0.1,1.1
csys,0

!get node number for the selected nodes
!numnodel=number of nodes selected under the left weld strain gauge
!nsnl = node number under the left weld strain gauge

*get,numnodel,node,0,count
*dim,nsnl,,numnodel
*get,nsnl(1),node,0,num,max
*do,n,2,numnodel,1
 *get,nsnl(n),node,nsnl(n-1),nxtl
*enddo

! get strain data for selected nodes
!e1nl = first principal strain for nodes under left weld strain gauge
!e2nl = second principal strain for nodes under left weld strain gauge
*get,numset,active,0,solu,ncmss
nset=nint((numset-20)/6)+36
*dim,e1nl,,nset,numnodel
*dim,e2nl,,nset,numnodel
*dim,e3nl,,nset,numnodel

*do,n,1,16
 set,,,,,,,n
 *do,i,1,numnodel
  *get,e1nl(n,i),node,nsnl(i),epto,1
  *get,e2nl(n,i),node,nsnl(i),epto,2
  *get,e3nl(n,i),node,nsnl(i),epto,3
 *enddo
*enddo
:
:
*do,n,1,nset-36
 set,2,11+6*(n-1)
 *do,i,1,numnodel
  *get,e1nl(n+26,i),node,nsnl(i),epto,1
  *get,e2nl(n+26,i),node,nsnl(i),epto,2
  *get,e3nl(n+26,i),node,nsnl(i),epto,3
 *enddo
*enddo
:
:
!WRITE STRIAN DATA TO FILE STRAIRSTL.TXT
!file strairstl=result file stores strain data for left weld strain gauge

*cfopen,istrairstl3,txt,,append
```

```
*vwrite,'number of nodes selected'
%c
*vwrite,'numnodel=',numnodel
(a,f6.0)
*vwrite,'selected nodes'
%c
*vwrite,nsnl(1)
(f8.1)
*vwrite,'***************'
%c
*vwrite,'principal strains'
%c
*vwrite,'*****************'
%C
*do,n,1,numnodel
 *vlen,1
 *vwrite,'node=',nsnl(n)
  (a,f5.0)
 *vwrite,'***************'
  %c
 *vwrite,'set=','','istrain',' ','iistrain',' ','iiistrain'
 (a,a,a,a,a,a,a)
 *vwrite,'***************'
 %c
 *vlen
 *vwrite,sequ,e1nl(1,n),e2nl(1,n),e3nl(1,n)
 (f6.0,f14.8,f14.8,f14.8)
*enddo
allsel
:
:
```

Bend model with residual stresses

```
!OBTAIN RESIDUAL STRESSES FOR EACH ELEMENT FROM
!THE WELDING PROCESS SIMULATION
! AND WRITE INTO A .IST FILE IN THE FORMAT REQUIRED BY ANSYS.

*CFOPEN, resistre0.9,txt,,APPEND

*get,nuele,elem,0,count

*dim, sxresi,,nuele
*dim, syresi,,nuele
*dim, szresi,,nuele
*dim, sxyresi,,nuele

*do,n,1,nuele
  etable,sxresi(n),s,x
```

```
  etable,syresi(n),s,y
  etable,szresi(n),s,z
  etable,sxyresi(n),s,xy
*enddo

*dim,resisx,,nuele
*dim,resisy,,nuele
*dim,resisz,,nuele
*dim,resisxy,,nuele
*dim,isx,,1310
*dim,isy,,1310
*dim,isz,,1310
*dim,isxy,,1310

*do,n,1,nuele
 *get,resisx(n),elem,n,etab,sxresi
 isx(n)=0.9*resisx(n)/100
 *get,resisy(n),elem,n,etab,syresi
 isy(n)=0.9*resisy(n)/100
 *get,resisz(n),elem,n,etab,szresi
 isz(n)=0!.9*resisz(n)/100
 *get,resisxy(n),elem,n,etab,sxyresi
 isxy(n)=0.9*resisxy(n)/100
*enddo

*do,n,nuele+11,1310
 isx(n)=0
 isy(n)=0
 isz(n)=0
 isxy(n)=0
*enddo
*do,n,1,1310
 *vwrite,'eis,',n
 (a,f6.0)
 *vlen,1
 *vwrite,isx(n),',',isy(n),',',isz(n),',',isxy(n)
 (f12.5,a,f12.5,a,f12.5,a,f12.5)
*enddo

!OBTAIN GEOMETRY FROM THE WELDING SIMULAITONA and,
!INPUT INTO THE PROGRAM FILE FOR FURTHER LOAD-CARRYING
!ANALYSIS
!GET NODE COORDINATE FROM THE RESIDUAL STRESS MODEL

*get,nunode,node,0,count
*dim, nodeloc,,nunode,3

*dim,xn,,nunode
```

```
*dim,yn,,nunode

*do, i,1,nunode
  *get,xn(i),node,i,loc,x
  *get,yn(i),node,i,loc,y
*enddo
*do,n,1,nunode
nodeloc(n,1)=n
nodeloc(n,2)=xn(n)*10
nodeloc(n,3)=yn(n)*10
*enddo

!get element nodal number
*get,nuele,elem,0,count
*dim,nn1ele,,nuele
*dim,nn2ele,,nuele
*dim,nn3ele,,nuele
*dim,nn4ele,,nuele

*do,n,1,nuele
  *get,nn1ele(n),elem,n,node,1
  *get,nn2ele(n),elem,n,node,2
  *get,nn3ele(n),elem,n,node,3
  *get,nn4ele(n),elem,n,node,4
*enddo

!write node location and element node number into file

*CFOPEN,isgeometry,TXT,,APPEND

  *vwrite,'n,', nodeloc(1,1),',',nodeloc(1,2),',',nodeloc(1,3)
 (a,f6.0,a,f14.8,a,f14.8)

*vwrite,'e,', nn1ele(1),',',nn2ele(1),',',nn3ele(1),',',nn4ele(1)
 (a,f8.0,a,f8.0,a,f8.0,a,f8.0)
```

T-JOINT UNDER BEND WITH RESIDUAL STRESSES

```
/FILNAME, resi-F0.9-3
/TITLE, fillet welded T-joint under bending with residual stresses
! Analysis is done in mm and Newtons.
!residual stresses as initial stress
!residual stresses read from file: resistre-0.9mm.ist
!node and element were copied from the isgeometry.txt file
/PREP7
!Define element types, material properties, geometry etc. and mesh
:
:
```

```
finish

SOLUTION

/SOLU
antype, static, new
solcontrol, on,on
nrop,unsym

esel,s,elem,,1,1310,1
isfile,read,resistre,ist
allsel

!support plate
nsel,s,loc,x,ggeo(1)
d, all, all, 0
allsel

lsel,s,line,,18
nsll,s,1
d,all,uy,0
allsel

kbc,1
nlgeom,on
autots, on
nsubstep, 150,500000,10
time, 1
outres,all,all

solve

dbend=3
lsel,s,line,,19
nsll,s,1
d,all,ux,dbend
allsel

kbc,0
nlgeom,on
autots, on
nsubstep, 150,500000,10
time, 2
outres,all,all

solve
save
finish
```